N00014-85-C-0857
MCR-89-506

②

AD-A213 712

Final
Report

May 1989

Damping
Characteristics
of Metal Matrix
Composites

DTIC
ELECTE
OCT 2 7 1989
S D
C&D

Prepared for:

6 105

MARTIN MARIETTA

REPORT DOCUMENTATION PAGE

1a. REPORT SECURITY CLASSIFICATION		1b. RESTRICTIVE MARKINGS
Unclassified		AD-A213 712

2a. SECURITY CLASSIFICATION AUTHORITY	3. DISTRIBUTION/AVAILABILITY OF REPORT
	Unclassified/Unlimited
2b. DECLASSIFICATION/DOWNGRADING SCHEDULE	

4. PERFORMING ORGANIZATION REPORT NUMBER(S)	5. MONITORING ORGANIZATION REPORT NUMBER(S)
MCR-89-506	

6a. NAME OF PERFORMING ORGANIZATION	6b. OFFICE SYMBOL (If applicable)	7a. NAME OF MONITORING ORGANIZATION
Martin Marietta Space Systems		

6c. ADDRESS (City, State and ZIP Code)	7b. ADDRESS (City, State and ZIP Code)
P. O. Box 179 Denver, CO 80201	

8a. NAME OF FUNDING/SPONSORING ORGANIZATION	8b. OFFICE SYMBOL (If applicable)	9. PROCUREMENT INSTRUMENT IDENTIFICATION NUMBER
Office of Naval Research (ONR)		N00014-85-C-0857

8c. ADDRESS (City, State and ZIP Code)	10. SOURCE OF FUNDING NOS.			
Department of the Navy 800 N. Quincy St. Arlington, VA 22217	PROGRAM ELEMENT NO.	PROJECT NO.	TASK NO.	WORK UNIT NO.

11. TITLE (Include Security Classification) (Unclassified)
Damping Characteristics of Metal Matrix Composites

12. PERSONAL AUTHOR(S)
Suraj P. Rawal, Joseph H. Armstrong, and Mohan S. Misra

13a. TYPE OF REPORT	13b. TIME COVERED	14. DATE OF REPORT (Yr., Mo., Day)	15. PAGE COUNT
Final	FROM 9/15/85 TO 5/14/89	May 25, 1989	181

16. SUPPLEMENTARY NOTATION

17.	COSATI CODES		18. SUBJECT TERMS (Continue on reverse if necessary and identify by block number)
FIELD	GROUP	SUB. GR.	Damping, Metal Matrix Composites, Graphite/Aluminum, Graphite/
			Magnesium, KiA, MiA, Hidamet, Heat Treatment, Residual Stress
			Hashin, Granato-Lucke, Temperature-dependence, Strain

19. ABSTRACT (Continue on reverse if necessary and identify by block number)

In the present investigation of damping characteristics of metal matrix composites, the objectives were to:

1) Develop an understanding of energy dissipation mechanisms in Gr/Al composites,
2) Characterize fiber/matrix interface structure,
3) Define the role of interfaces in damping, and
4) Identify and evaluate potential high damping metal matrix composite

To accomplish these objectives, initially damping measurement techniques were established to obtain reproducible and reliable test data of Gr/Al composites. These data obtained at different frequency and strain amplitude levels, were analyzed to develop an understanding of damping mechanisms in Gr/Al composites. Damping at low strain amplitudes ($< 10^{-5}$) was nearly constant, but at intermediate strain levels damping increased with

20. DISTRIBUTION/AVAILABILITY OF ABSTRACT	21. ABSTRACT SECURITY CLASSIFICATION
UNCLASSIFIED/UNLIMITED ☒ SAME AS RPT. ☐ DTIC USERS ☐	Unclassified

22a. NAME OF RESPONSIBLE INDIVIDUAL	22b. TELEPHONE NUMBER (Include Area Code)	22c. OFFICE SYMBOL
Dr. Steven G. Fishman, Manager, Non Metallics, ONR	(202) 696-0285	

DD FORM 1473, 83 APR   EDITION OF 1 JAN 73 IS OBSOLETE.

18. (Continued)

dependence, dislocation substructure, intercalation, centrifugal casting, acoustic emission, damping test techniques.

19. (Continued)

increasing strain amplitude. Data analyses indicated that fiber, matrix and interfaces, each contributed to the damping response of Gr/Al composite. Fiber-matrix interfacial regions were examined by TEM to determine the nature of bond and dislocation substructure. The role of interfaces in damping was further examined by acoustic emission (AE), Moire interferometry and stress pattern analysis by thermal emission (SPATE) techniques.

Based on the data analysis and understanding of damping mechanisms, cast Gr/Mg - 0.6% Zr and Gr/Mg 1% Mn composites were identified as high damping MMC primarily because of enhanced energy dissipation characteristics of matrix alloys. Flat plates of these Gr/Mg composites were cast and test specimens were prepared to measure damping at different frequency, temperature and strain amplitudes. A few of the specimens were also heat treated to obtain large grain size because damping in Mg alloy increases with increasing grain size. Damping response of both as-cast and heat treated Gr/Mg composites as a function of vibrational strain amplitude was similar to Gr/Al. At low strains ($<10^{-6}$) measured specific damping capacity of Gr/Mg was between 1-3%, and at intermediate strains varied between 3 to 7%. Enhancement of damping capacity was limited, as the grain size in the matrix alloy could not be increased high enough (because of interfiber spacing) to yield maximum damping contribution from the Mg matrix alloy.

The damping behavior of Gr/Mg composites, and the characteristics of interface structure are described in this report. To provide the background, major features of previous work related to the development of reliable test techniques and damping mechanisms of Gr/Al composites have also been included. Also included during this study of damping characteristics of MMC were tasks related to residual stress measurements and centrifugal casting of high damping Gr/Mg tubes.

Accesion For		
NTIS CRA&I		☒
DTIC TAB		☐
Unannounced		☐
Justification		
By		
Distribution /		
Availability Codes		
Dist	Avail and/or Special	
A-1		

Final
Report   May 1989

Damping Characteristics of Metal Matrix Composites

FOREWORD

This final report covers work conducted under the Office of Naval Research (ONR) Contract N00014-85-C-0857 from 9/15/85 to 5/14/89. The effort was directed to identify damping mechanisms and to develop a metal matrix composite (MMC) with higher damping than conventional structural alloys. ONR technical monitor of this contract was Dr. Steven G. Fishman.

This study was performed at Martin Marietta Space Systems, Denver, CO, by the Materials and Structures Group of Research and Technology. Various tasks were subcontracted in the areas of damping measurement, damage characterization, transmission electron microscopy, and centrifugal casting. Team members, their tasks and organization are listed below:

Team Members:

Name	Task	Organization
Dr. Mohan S. Misra	Program Manager	Martin Marietta Space Systems
Dr. Suraj P. Rawal	Co-Principal Investigator	Martin Marietta Space Systems
Dr. Joseph H. Armstrong	Co-Principal Investigator	Martin Marietta Space Systems
Dr. Vikram K. Kinra	Task Leader: Damping Measurements	University of Texas A&M
Dr. Steve H. Carpenter	Damping and Acoustic Emission Testing and Analysis	University of Denver
Dr. Marvin A. Hamstad	Acoustic Emission Testing and Analysis	University of Denver

Table of Contents

1

TABLE OF CONTENTS

Glossary

FFT.............................Fast Fourier Transform
V_f.............................Fiber Volume
FFF.............................Free-Free Flexure
f.............................Frequency
G-L.............................Granato-Lucke Theory of Dislocation Damping
Gr.............................Graphite
Gr/Al.............................Graphite-Reinforced Aluminum-Matrix Composite
Gr/Mg.............................Graphite-Reinforced Magnesium-Matrix Composites
K1A.............................Graphite-Reinforced Magnesium-0.6%Zirconium Matrix Composite
M1A.............................Graphite-Reinforced Magnesium-1.0%Manganese Matrix Composite
Hz.............................Hertz
kHz.............................Hertz x 10^3 (Kilohertz)
HP.............................Hewlett-Packard
hcp.............................Hexagonal Close Packed Crystalline Structure
hr.............................Hour
E_I.............................Imaginary Component of Modulus
in.............................Inches
μ in..............................Inches x 10^{-6} (Microinches)
IR&D.............................Independent Research and Development
K.............................Kelvin
LPSS.............................Large Precision Space Structures
Pb.............................Lead
q.............................Load Intensity
δ.............................Log Decrement
ϕ.............................Loss Angle
η.............................Loss Factor
Mg.............................Magnesium
Mn.............................Manganese
ρ.............................Mass Density
MMC.............................Metal Matrix Composites
m.............................Meter
μm.............................Meter x 10^{-6} (Micrometers or Microns)
mm.............................Meters x 10^{-3} (Millimeters)
nm.............................Meters x 10^{-9} (Nanometers)
min.............................Minute
Λ.............................Mobile Dislocation Density
E.............................Modulus
E_{11}.............................Modulus (Axial) of the Composite
E_f.............................Modulus of the Fiber Reinforcement
E_m.............................Modulus of the Matrix Alloy

Mo	Molybdenum
NASA	National Aeronautics and Space Administration
N	Newton
kN	Newtons x 10^3 (Kilonewtons)
NDE	Nondestructive Evaluation
Ω	Orientation Factor
K	Orientation Factor Connected with Resolved Shear Stress for Dislocation Breakaway
β_n	Parameter Related to Vibratory Mode
kPa	Pascals x 10^3 (Kilopascals)
MPa	Pascals x 10^6 (Megapascals)
GPa	Pascals x 10^9 (Gigapascals)
ε_p	Peak in Strain Amplitude Dependent Damping
Δf	Peak Width at Half Maximum Intensity
PC	Personal Computer
π	Pi
PCO	Piezoelectric Composite Oscillator
P55Gr	Pitch 55 Graphite Fiber
ksi	Pounds per Square Inch x 10^3
Msi	Pounds per Square Inch x 10^6
Q	Quality Factor of a Dynamic System
rad	Radians
E_R	Real Component of Modulus
rpm	Revolutions per Minute
f_n	Resonant Frequency of nth Mode of Vibration
rms	Root-Mean Squared
s	Second
Si	Silicon
SiC	Silicon Carbide
SiO_2	Silicon Dioxide Fiber Coating
ψ	Specific Damping Capacity
L	Specimen Length
h	Specimen Thickness
b	Specimen Width
ε	Strain Amplitude
ψ_H	Strain Amplitude Dependent (Hysteretic) Damping
ψ_I	Strain Amplitude Independent Damping
$\mu\varepsilon$	Strain Amplitude x 10^{-6} (Microstrain)
$\varepsilon(x,z)$	Strain as a Function of Position on a Cantilever Beam Specimen
ε_{root}	Strain Measured at Root of Cantilever Beam Specimen

$\varepsilon_{measured}$ ....Strain Measured by Strain Gage on Cantilever Beam Specimen

σ ....Stress

σ_f ....Stress Borne by the Fiber

σ_m ....Stress Borne by the Matrix

SPATE ....Stress Pattern Analysis by Thermal Emission

$d(x)$ ....Tangential Displacement of Cantilever Beam Specimen as a Function of Position

Th ....Thorium

t_o ....Time of Flight for Initial Cycle of Torsional Pendulum

t_n ....Time of Flight for nth Cycle of Torsional Pendulum

Sn ....Tin

a_t ....Tip Amplitude of Shaker Table Experiment

Ti ....Titanium

Ψ_{total} ....Total Measured Damping

TEM ....Transmission Electron Microscopy

UTTC ....Uniaxial Tension-Tension Cycling

kV ....Volts x 10^3 (Kilovolts)

mV ....Volts x 10^{-3} (Millivolts)

λ ....Wavelength

f_z ....Zener Frequency

Zn ....Zinc

Zr ....Zirconium

LIST OF TABLES

LIST OF FIGURES

LIST OF FIGURES (CONTINUED)

LIST OF FIGURES (CONTINUED)

LIST OF FIGURES (CONTINUED)

LIST OF FIGURES (CONTINUED)

LIST OF FIGURES (CONTINUED)

LIST OF FIGURES (CONTINUED)

LIST OF FIGURES (CONTINUED)

1.0 Introduction

CHAPTER 1.0
INTRODUCTION

Advanced metal matrix composites (MMC) with attractive mechanical and physical properties are candidate structural material for large space structures (LSS). A critical design concern for LSS is suppression of vibrations, caused by onboard and hostile threat-related disturbances during acquisition pointing and tracking (APT) phases of maneuvering. Various active and passive control measures can be incorporated in the designs of such structures (Fig. 1.0-1) to damp vibrations and achieve dynamic dimensional precision in space missions [Refs 1, 2, and 3]. In active control measures, the role of material and structural damping is generally omitted, although passive control measures via enhanced material damping would improve the dynamic stability of a system (Fig 1.0-2). If the inherent material-damping capacity of metal matrix composites can contribute significantly to passive control methodology (Fig. 1.0-1), then it will lead to reduction in weight and improved performance of LSS. Preliminary investigation by Misra and LaGreca indicated that graphite aluminum (Gr/Al) and graphite magnesium (Gr/Mg) composites exhibit higher damping than a matrix alloy [Ref 4]. From the mechanism point of view, it was suggested that interfaces play a dominant role in the damping behavior of metal matrix composites.
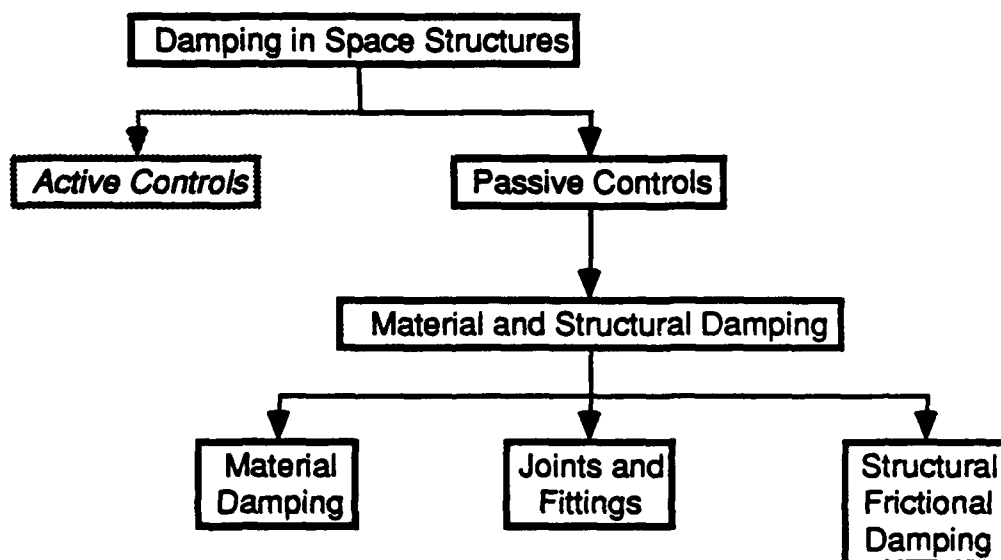
Figure 1.0-1 Vibrational Control in Space Structures
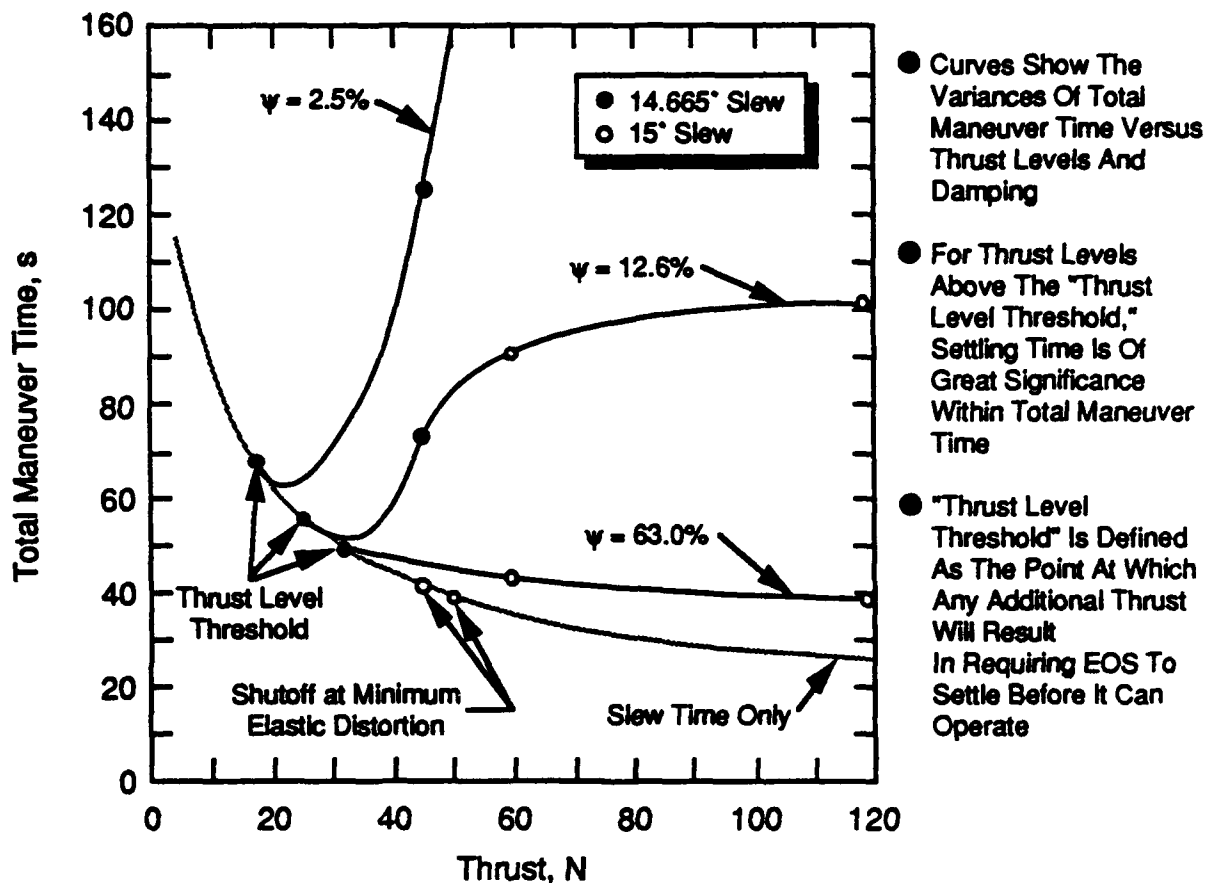
Figure 1.0-2 *Role of Structural Damping in Reducing Total Settling Time During the Maneuvering of an Earth Observation Spacecraft (EOS)*

Therefore in the present investigation of damping characteristics of metal matrix composites, the objectives were to:

1) Develop an understanding of energy dissipation mechanisms in Gr/Al composites,

2) Characterize fiber/matrix interface structure,

3) Define the role of interfaces in damping, and

4) Identify and evaluate potential high damping metal matrix composite.

To accomplish these objectives, initially damping measurement techniques were established to obtain reproducible and reliable test data of Gr/Al composites. These data obtained at different frequency and strain amplitude levels were analyzed to develop an understanding of damping mechanisms in Gr/Al composites. Damping at low strain amplitudes ($\leq 10^{-5}$) was nearly constant, but at intermediate strain levels damping increased with increasing strain amplitude. Data analyses indicated that fiber, matrix and interfaces each contributed to the damping response of Gr/Al composite.

Fiber-matrix interfacial regions were examined by TEM to determine the nature of bond and dislocation substructure. The role of interfaces in damping was further examined by acoustic emission (AE), Moire interferometry and stress pattern analysis by thermal emission (SPATE) techniques.

Based on the data analysis and understanding of damping mechanisms, cast Gr/Mg - 0.6% Zr and Gr/Mg 1% Mn composites were identified as high damping MMC primarily because of enhanced energy dissipation characteristics of matrix alloys. Flat plates of these Gr/Mg composites were cast and test specimens were prepared to measure damping at different frequency, temperature and strain amplitudes. A few of the specimens were also heat treated to obtain large grain size because damping in Mg alloy increases with increasing grain size. Damping response of both as-cast and heat treated Gr/Mg composites as a function of vibrational strain amplitude was similar to Gr/Al. At low strains ($\leq 10^{-6}$), measured specific damping capacity of Gr/Mg was between 1-3%, and at intermediate strains varied between 3 to 7%. Enhancement of damping capacity was limited, as the grain size in the matrix alloy could not be increased high enough (because of interfiber spacing) to yield maximum damping contribution from the Mg matrix alloy.

The damping behavior of Gr/Mg composites, and the characteristics of interface structure are described in this report. To provide the background, major features of previous work related to the development of reliable test techniques and damping mechanisms of Gr/Al composites have also been included. Also included during this study of damping characteristics of MMC were tasks related to residual stress measurements and centrifugal casting of high damping Gr/Mg tubes.

1.1 SUMMARY OF RESEARCH EFFORT

During the determination of dynamic response of graphite-reinforced metal matrix composites, significant accomplishments were made in the following tasks of measurement and analyses of damping. The accomplishments of each task are summarized below while details are presented in the subsequent chapters:

Task	Title	Chapter
1	Damping Test Techniques	2.0
2	Damping of Gr/Al Composites	3.0
3	High-Damping Magnesium Alloys	4.0
4	Damping of Gr/Mg Composites	5.0
5	Effect of Heat Treatment on Damping of Gr/Mg	6.0

1-3

After identifying Gr/Mg as a potentially high damping metal matrix composite, the next logical step was to fabricate structural components. Consequently, the final task of this investigation was

1.1.1 Damping Test Techniques

In general, an overall choice of test techniques should bear a relationship to the stress state, frequency, specimen geometry, and temperature to be encountered in the material application. Damping test data can be expressed in many different parameters which are interrelated at low damping values. Although no single test method can be used to obtain material damping data over a wide frequency and strain amplitude range, it must be recognized that a common (fundamental) measure of damping can be agreed upon by investigators in various disciplines. Such a measure will reduce confusion and lead to a systematic approach of comparing damping data of a structural material.

A thorough understanding was developed for the damping nomenclature and the background for each test method. A variety of damping test techniques were evaluated for use with metal matrix composites. Flexural, extensional, and torsional modes of vibration were employed to measure the damping as a function of frequency, strain amplitude, and temperature. Extraneous energy losses were eliminated or minimized to enhance the reliability of each test technique. At low strain amplitudes ($\varepsilon \leq 10^{-5}$), damping values of MMC from each of the test techniques provided damping data that were compatible. Techniques were developed to obtain data at intermediate strain amplitudes.

1.1.2 Damping of Gr/Al Composites

Reliable damping measurements of unidirectional single-ply P55Gr/6061Al composites were obtained by three different test techniques: free-free flexure, clamped-free flexure, and tension-ten-

sion fatigue. Both flexural and extensional mode tests were conducted at 1×10^{-6} — 800×10^{-6} strain levels within 0.1 Hz and 150 Hz frequency range.

Damping response of Gr/Al indicated that beyond a critical strain amplitude, damping increases with increasing strain amplitude. In the strain amplitude independent region, the measured damping capacity is consistent with the values predicted by the moduli-weighted rule of mixtures for damping (Hashin Theory). Extensional mode test data of Gr/Al were also analyzed in terms of the Granato-Lucke (G-L) model which is based on energy dissipation due to oscillatory dislocation motion. Strain amplitude dependence is also predicted by this model as a result of dislocation breakaway from minor pinning points. Mobile dislocation density predicted by G-L analysis ($\approx 10^{12}$ $1/m^2$) was also consistent with the measured average dislocation density (4×10^{14} $1/m^2$) obtained from various TEM images of the interfiber matrix regions. These dense dislocation networks have been attributed to differential contractions between the fiber and matrix, and the attendant residual stress state. Both test results and analyses indicate that damping characteristics of Gr/Al are influenced by contributions from fiber, matrix, residual stress state, and the associated dislocation substructure near the fiber-matrix interface.

1.1.3   High Damping Magnesium Alloys

Based on the damping data of Mg alloys in the literature, Mg-1.6% Zr, and Mg-1% Mn were selected as a high damping matrix for the composite. The damping capacity of these alloys varies between 30% - 80% at different strain levels and frequencies. It was recognized that their high damping was associated with a large equiaxed grain size (≥ 20 μm) microstructure obtained by a casting process. If such a matrix microstructure could be retained in the cast composite, then the damping contribution from matrix will result in a high damping Gr/Mg composite.

1.1.4   Damping of Gr/Mg Composites

Damping measurements of pitch 55 graphite fiber reinforcement in high-damping Mg-0.6%Zr (K1A) and Mg-1.0%Mn (M1A) alloys exhibited a transition from strain amplitude independent to dependent response at strain levels above 10^{-6}. Damping measurements of these materials in the strain amplitude independent region as a function of temperature indicated a contribution from a phase transformation between rhombohedral and hcp structures in the graphite fiber at 200K (-99.4°F). Above room temperature, the temperature dependent damping response was typical of that

found in the matrix alloy alone. Comparison of predicted and measured composite damping capacity at low strain amplitudes yielded an *in situ* matrix damping contribution of 9% which was substantially lower than the damping capacity of cast Mg alloys. Low *in situ* matrix damping in the composite could be attributed to the fine grain structure near the fiber-matrix interface.

The strain amplitude dependent response was explained in terms of the Granato-Lucke (G-L) model, suggesting that dislocation damping is the likely energy dissipation mechanism. Also, mobile dislocation densities predicted by G-L theory were consistent with the average dislocation densities measured from various transmission electron micrographs near the fiber-matrix interface. The strain amplitude dependence also predicted the presence of the damping peaks, and gave a reasonable approximation for the dislocation loop length. After substitution of appropriate material constants, a four to five order of magnitude lower mobile dislocation density was observed than that measured by TEM, which was explained by the limited slip systems for dislocations in hcp metals, and consequently, the small percentage of total dislocations that are mobile under a low applied stress.

1.1.5   Effect of Heat Treatment on Damping of Gr/Mg

Damping measurements of as-cast $[0°]_8$ P55Gr/Mg-0.6%Zr (Gr/K1A) and P55Gr/Mg-1.0%Mn (Gr/M1A) composites exhibited a transition from strain amplitude independent to dependent damping at about $\varepsilon = 10^{-6}$. Damping of the Gr/K1A and Gr/M1A composites were higher than those measured for Gr/Al under similar circumstances. Unlike $[0°]$ P55Gr/6061Al specimens tested earlier, the Gr/K1A and Gr/M1A specimens possessed a peak in the strain amplitude dependent damping.

From the strain amplitude independent region, it was determined that the matrix contributed only 3.1% of the total specific damping capacity (ψ) for the Gr/M1A specimens, although damping values in the literature for these alloys were as high as $\psi = 30\%$. Metallographic analysis of these materials indicated that the grain size of the matrix was as low as 2 μm, whereas the high damping exhibited in the literature was for a grain size in excess of 20 μm. Therefore, Gr/Mg specimens were heat treated to increase the matrix grain size, thereby enhancing the contribution of the matrix to the total damping.

Prior to damping measurements, both Gr/M1A and Gr/K1A were heat treated at 450°F for 6 hours, and at 800°F for 4,8, and 16 hours in an argon atmosphere, followed by an oven cool. Damping test data analysis indicated that strain amplitude independent contributions from the matrix increased as

a result of heat treatment (3.59% and 6.24% for 450°F, 6 hr and 800°F, 4 hr heat treatment respectively). Further heat treatments at 800°F for longer durations did not result in any significant increase in damping, although micrographs indicated a coarsening of elemental precipitates in the matrix.

Data analysis of the strain amplitude dependent damping of heat treated Gr/Mg indicated the strain amplitude dependent damping can be described by the Granato-Lucke theory of dislocation damping. Strain amplitude dependence is modeled by a dislocation breakaway from minor pinning points. Average dislocation loop length (L_C) between minor pinning points increased systematically with longer heat treatment (3.57 x 10^{-8} m, 4.76 x 10^{-8} m, and 17.4 x 10^{-8} m for as-cast, 450°F, 6 hr and 800°F, 4 hr heat treatment respectively). Approximate predicted values of mobile dislocation density was on the order of 6 x 10^9 1/m^2, which was far lower than the average dislocation density observed in various TEM images of 10^{14} 1/m^2. This large difference can be attributed to the limited slip systems in hcp structure materials, consequently limiting the number of dislocations that can become mobile in response to an applied cyclic stress.

1.1.6 Role of Residual Stresses in Damping in Gr/Al

Damping measurements of as-fabricated unidirectional P55/6061 Al specimens indicated that beyond a critical strain amplitude, damping increased with increasing strain amplitude. Data analysis in terms of Granato-Lucke theory, combined with transmission electron microscopy observations, suggested that movement of dislocations in the tangled networks near the interfaces was the operative energy dissipation mechanism at these strain levels. These dense and tangled dislocation networks were associated with the thermal residual stresses that are generated by the differences in thermal expansion of graphite fiber and aluminum matrix.

Residual stress state near the fiber-matrix interface was modified by appropriate heat treatment procedures. As-fabricated Gr/Al specimens subjected to cryogenic quench treatment to relieve residual stresses through yielding showed the disappearance of strain amplitude dependent damping when measured both by piezoelectric composite oscillator and uniaxial tension-tension cycling test methods. When the stress-relieved specimens were heated to diffusion-bonding process temperature (588°C) and slowly cooled to room temperature, their damping response exhibited the reappearance of strain amplitude dependent behavior at strains below 4 x 10^{-4}. A tensile component of residual stress along the axis of vibration induces strain amplitude dependent damping response at stress levels much lower than those observed in stress-relieved specimens. These observations of as-fabricat-

ed and heat treated Gr/Al indicated that residual stresses play a significant role in the damping behavior of composites.

1.1.7 Acoustic Emission Analysis of Metal Matrix Composites

Acoustic emission (AE) technology has been utilized to monitor the initiation and progression of damage in Gr/Al and Gr/Mg composites. During tensile loading, operative damage mechanisms include matrix yielding, interfacial degradation, and fiber breakage. A low amplitude AE rms voltage peak which appears immediately after loading was indicative of matrix yielding and interfacial degradation. Initiation of this peak in Gr/Al composite wires at low loads was possible because of a static tensile preload contributed by residual stresses. A higher amplitude rms peak was attributed to fiber breakage. This two-peak behavior changed dramatically as damage was introduced into the specimens by shear deformation, where the event rate increased by virtue of the weaker fiber-matrix interface. Fiber breakage was virtually eliminated as an AE mechanism as evidenced by the elimination of the second, high amplitude peak.

Residual stresses are an important aspect in metal matrix composites because they affect their mechanical and dynamic behavior. Because AE mechanisms in metal matrix composites are stress-activated, phenomenon such as residual stresses near the fiber-matrix interface can affect AE response of deformation mechanisms. By using a reproducible AE mechanism such as matrix yielding, attempts were made to quantify the amount of residual stresses in the composite. Estimated residual stress values for the [0°] P55Gr/6061Al system ranged from 35.2 MPa to 124.8 MPa (5.1 ksi to 18.1 ksi), depending on matrix temper (6061-0 or 6061-T4 respectively). The higher range of residual stress values agree well with results from the literature. Similar analysis of the [0°] P55Gr/Mg-0.6%Zr (Gr/K1A) resulted in a residual stress value of only 24.6 MPa (3.53 ksi). These experiments suggested that AE analysis can be used to provide a reasonable estimate of residual stresses in metal matrix composites where yielding of the matrix alloy produces a distinct AE signature.

1.1.8 High Damping Graphite Fibers

An increase in fiber damping would provide a significant contribution to the total damping of a graphite fiber reinforced metal matrix composite because the fibers are sites of the highest strain energy. Preliminary experiments have indicated that intercalated (brominated) graphite fibers exhib-

it an order of magnitude increase in damping when compared to as-processed pitch fibers. Bromi-nated pitch fibers were plated with electroless nickel at Martin Marietta in an attempt to seal the intercalants at low temperatures prior to preparing precursor wires. Damping capacity of the plated-intercalated fiber was measured in the flexural test setup at NASA Lewis Research Center. Prelimi-nary test measurement at different temperature indicated that baseline damping capacity of coated fibers were comparable to unintercalated fibers, and still showed the characteristic peak at about -70°C. The low damping could be due to the nickel sheath which experiences the maximum strain during flexural vibration. Also, it is likely that residual intercalant level in the coated fiber is less than as-brominated fiber, if the intercalant can escape slowly even at 100°C. Therefore, to exploit the high damping of intercalated fibers in a composite, innovative methodologies must be developed to seal the carrier species within the fiber, before incorporation into a metallic matrix.

1.1.9   Interfacial Characterization of Interfaces In Metal Matrix Composites

Fiber-matrix interfaces in metal matrix composite include voids, impurities, second phase precipi-tates and dense dislocation substructure. These interfacial features could also provide various sources of vibrational energy dissipation during cyclic loading.

Interfacial regions in diffusion bonded Gr/Al and cast Gr/Mg composites were successfully exam-ined by transmission electron microscopy. Various TEM images revealed the nature of interfacial bond, where the fiber coating was far more adherent to the matrix as compared to the fiber, during interfacial separation or debonding. Interface region in both composites also revealed dislocation substructure which are associated with residual stresses generated due to differences in thermal expansion between fiber and matrix during composite processing conditions. In Gr/Al composite, these dislocations have the characteristic Burger's Vector a/2 [110] for the face centered cubic Al system, and the dense tangled networks are made of the different variants. Near the interface in Gr/Mg composite, dislocations are generally linear and correspond to available basal slip systems in hcp Mg matrix. Dislocation density measurements were made using the weak beam imaging tech-nique, and an average dislocation density in Gr/Al was 4×10^{14} $1/m^2$ and Gr/Mg composites between 1.6×10^{13} and 1.6×10^{14} $1/m^2$. These measurements of dislocation density indicate that enough mobile dislocations are present to contribute to the damping mechanisms (Granato-Lucke model) in each composite.

1.1.10 Damping Test Data Comparison: Interlaboratory Testing

Damping capacity of MMC at low strain amplitudes is quite small. Therefore, extraneous losses during the damping measurement must be minimized to obtain reliable data. Damping measurements of test specimens from the same Gr/Al and Gr/Mg panes were performed at five different laboratories that are involved in determining the dynamic response of metal matrix composites. These measurements were performed within the frequency range ($16 < f < 2500$ Hz) and strain amplitude range ($1 \times 10^{-6} - 200 \times 10^{-6}$). At low strain levels when damping is a function of temperature and frequency only, measured values from all of these test sites were in excellent agreement.

1.1.11 Development of Centrifugal Casting Techniques to Fabricate Gr/Mg Tubes

Fabrication processes such as diffusion bonding, pultrusion and filament winding-vacuum casting have been successfully used to produce 1-3 in. dia. 50-in. long tubes. But any scaleup to produce large tubes from these will be very tedious and expensive. Therefore, a fabrication process combining two well established technologies: 1) filament winding and 2) centrifugal casting was evaluated because it has potential to produce large tubes using state-of-the-art equipment.
Laboratory scale experiments were conducted to demonstrate the feasibility of fabricating tubes by filament winding-centrifugal casting (FWCC) process. Filament wound P55 fiber tubular preforms were placed inside a centrifugal mold setup that was held on a lathe machine for mold rotation. In each casting experiment, Gr/Mg tube had various regions that showed excellent matrix infiltration and in the remaining tube fibers were trapped between the molten magnesium. The visual and microstructural observations indicated that if binder was completely removed without any degradation of coating, and optimum combination of melt superheat and mold-preform temperature was maintained then the casting showed good matrix infiltration. With an improved design to preheat the preform under the protective atmosphere, good matrix infiltration could be attained in the entire tube. Therefore, the observations of well infiltrated regions in the cast tube demonstrate that filament winding centrifugal casting technique could be developed to produce large Gr/Mg tubes.

1.2 References

1   H. Ashley, "On Passive Damping Mechanisms in Large Space Structures," AIAA Paper No. 82-0639, 23rd Structures, Structural Dynamics and Materials Conference, April 1982, p. 56.

2   "Passive and Active Control of Space Structures," Technical Operating Report MCR-84-541, Martin Marietta Denver Aerospace, April 1984.

3   C.D. Johnson and D.A. Kienholz, "Finite Element Prediction of Damping in Structures with Constrained Viscoelastic Layers," Paper No. 881-0486, 22nd Structures, Structural Dynamics and Materials Conference, April 1981, p. 17.

4   M.S. Misra and P.D. LaGreca, "Damping Behavior of Metal Matrix Composites," Vibration Damping 1984 Workshop Proceedings, AFWAL-TR-84-3064, Nov. 1984, p. U-1.

2.0 Damping Test Techniques

CHAPTER 2.0
DAMPING TEST TECHNIQUES

Internal friction, or damping, has been used to study the inherent vibrational energy dissipation due to microstructural and micromechanical phenomenon in materials for many years. Consequently, a number of test techniques have been developed to measure damping in test materials, all of which require the vibration of the specimen. Each technique has particular frequency and vibratory strain amplitude ranges, and damping can be measured either during free decay or during a continuous driving force at a given frequency and/or strain amplitude. Because damping is often measured in different modes of vibration, namely 1) extensional, 2) torsional, and 3) flexural, careful attention must be given to the data from each test in order to obtain valid data comparison.

2.1   MEASURES OF DAMPING

Internal friction, or damping, is the inherent ability of a vibrating material to convert its vibrational energy into heat, even when the material is isolated and energy losses to its surroundings are negligible. A phase lag always exists between an applied stress and the resultant strain, and as such, energy is dissipated in the complete stress cycle. Such dynamic hysteresis at low stress levels has been explained in terms of anelasticity, in which Hooke's law is extended to include time as a variable in the stress-strain relationship, and modulus of elasticity is expressed as a complex quantity.

It has been established [Ref 2-1—2-6] that fundamental mechanisms which lead to energy dissipation involve changes in the atomic configuration from a nonequilibrium state to an equilibrium state under an applied stress. Damping, as an engineering property, is used in the analysis and design of machines and structures subjected to cyclic loading conditions. Dynamic test measurements have also been used as a nondestructive inspection tool, based on empirically-observed correlations between damping and other material properties, such as hydrogen embrittlement, fatigue, and creep.

Experimental results have been expressed in terms of various parameters used as a measure of damping which can be confusing to a reader unfamiliar to damping terminology, to understand the engineering significance of quantitative results. Though the significance of having common terminology in this field has been suggested by various investigators [Ref 2-3,2-7,2-8], no specific measure has been agreed upon as yet. Almost all of the measures of damping are derived from the response of linear mechanical systems consisting of a dashpot in parallel with a totally-elastic spring

having a single degree of freedom. These mathematical models lead to the definitions of various measures of damping which are described below.

2.1.1 Logarithmic Decrement (δ)

In terms of the logarithmic decrement, or log decrement, the damping is defined in the following manner:

$$\delta = \left(\frac{1}{j-i}\right) \ln \left(\frac{a_j}{a_i}\right) \tag{2-1}$$

where a_i and a_j are the peak displacement, velocity, or acceleration in the ith and j^{th} decay cycles. Thus, greater the damping of the material, the more rapid the vibratory decay.

2.1.2 Complex Modulus (E*), Loss Angle (φ), and Loss Factor (η)

The modulus of a material is a complex quantity (E*) that can be described in terms of its real (E^R) and its imaginary (E^I) parts in the following manner:

$$E^* = E^R + iE^I. \tag{2-2}$$

Its loss angle φ and loss factor ν are related to the complex modulus in the following manner

$$E^* = E^R (1 + i\eta) \tag{2-3}$$

$$\eta = E^I/E^R = \tan \phi \tag{2-4}$$

E^R is known as the storage, or elastic modulus, as it is related to the stored energy per unit volume, and E^I is defined as the loss, or dissipation, modulus because it is related to the energy dissipation per unit volume [Refs 2-1,2-2, and 2-3].

2.1.3 Half-Power Bandwidth (Δf)

Damping may also be described in terms of the breadth of the resonance peak at half maximum intensity (Δf) as shown below

$$Q^{-1} = 1/Q = (f_2 - f_1) / f_n = \Delta f / f_n. \tag{2-5}$$

where f_n is the associated resonant frequency.

2.1.4 Specific Damping Capacity (ψ)

The specific damping capacity is defined as the ratio of energy lost (ΔW) to the maximum vibrational energy stored (W) per cycle per unit volume, i.e.

$$\psi = \Delta W/W. \tag{2-6}$$

2.1.5 Relationship Among Damping Parameters

As described earlier, a number of terms have been used to describe material damping. Often these quantities may be interrelated, provided that the magnitude of the material damping is small (i.e. $\tan \phi \le 0.1$ where $\phi \equiv$ phase, or loss angle between the applied stress and resultant strain) which is often the case with most metallic materials. Material damping may be described in the following manner:

$$\delta/\pi = \eta = \tan \phi \approx \phi = E^I/E^R = Q^{-1} = \psi/2\pi = \Delta W/2\pi W = 2\zeta \tag{2-7}$$

where: η $\equiv$ loss factor,

Q $\equiv$ quality factor,

δ $\equiv$ log decrement,

ψ $\equiv$ specific damping capacity,

ΔW $\equiv$ energy lost per cycle,

W $\equiv$ energy stored per cycle, and

ζ $\equiv$ damping ratio.

An additional parameter, the damping ratio ζ has been included which is defined as the ratio of actual damping coefficient to the critical one. The terms ζ, $\Delta W/W$, and ψ are quite often expressed in percentages. Therefore in quantitative terms, 1.0% specific damping capacity (ζ) is equivalent to 0.079% damping ratio (ζ), 0.00159 loss factor (η) and inverse quality factor (Q^{-1}).

2-3

2.2   EXPERIMENTAL PROCEDURES

Damping can be measured by various experimental techniques, but no single method can be used to measure damping over the entire frequency range 10^{-3} — 10^{10} Hz. Experimental procedures and there limitations are well documented in the literature [Ref 2-1-2-3, 2-8-2-10]. Material damping is primarily a low energy loss process. Therefore, the major problem in measurement involves extraneous energy losses in the apparatus because of support friction, air drag, acoustic radiation, transducer mounting, and wire movement. In all of the damping measurements, the specimen support and the method for driving and measuring specimen vibration play an extremely important role. The various experimental techniques for the determination of material damping are described below:

2.2.1 Decay of Free Vibration

In this test, a specimen is excited in a desired resonant vibratory mode by some means. Once the desired mode has been established, the excitation device is cut off and the ensuing free vibration decay is measured by a transducer to determine damping in terms of logarithmic decrement (δ). The decay test can be conducted in extensional, flexural, or torsional modes of vibration.

2.2.2 Resonant Dwell Test

In this technique, a double cantilever beam specimen, clamped at its midpoint (base), is excited at resonance by a sinusoidal force, normally supplied by an electrodynamic shaker. The loss factor (η) is related to the ratio of measured base amplitude (a_b) to tip amplitude (a_t) at a resonant mode.

2.2.3 Half-Power Band Width Technique

This technique is also a forced-vibration technique. In recently-developed Random and Impulse excitation techniques [Ref 2-11], all resonant frequencies are excited simultaneously, as compared to resonant sine-dwell techniques in which each mode is excited individually. These techniques make use of a frequency-domain transfer function of a material specimen which is found from the ratio of the Fourier transforms of excited and response signals via a fast Fourier transform (FFT) analyzer. The purpose of the FFT is to convert a time domain signal into a combined real and imaginary representation of the signal in the frequency domain. A typical transfer function shows several resonant peaks and the loss factor (η) is obtained with the half-power bandwidth technique

$$\eta = \Delta f / f_n \tag{2-8}$$

where Δf is the bandwidth at half-power, and f_n is the resonant frequency of the nth mode.

2.2.4 Hysteresis Measurements

In this method, a test specimen is loaded cyclically in the extensional mode at subresonant frequencies (< 20 Hz). The specific damping capacity (ψ) is determined from the measured hysteresis loops as the ratio of energy dissipated per cycle (ΔW) to the energy stored (W) at maximum vibratory displacement.

2.2.5 Wave Propagation Techniques

The basic premise behind this technique is that the amplitude of a wave propagating at the speed of sound in a material will diminish as a result of material damping. These test techniques consist of a drive transducer that supplies an ultrasonic pulse to a material, and a gage transducer that monitors the wave as it exits the material. Both pulse and continuously-driven configurations are possible; the most common of continuously-driven systems is the piezoelectric composite oscillator technique.

2.3   DESCRIPTION OF TEST

Five testing techniques have been utilized in this investigation, namely a) clamped-free flexure, b) free-free flexure, c) uniaxial tension-tension cycling, d) piezoelectric composite oscillator, and e) torsional pendulum. Figure 2.3-1 illustrates the relationship between these test techniques as a function of temperature, strain amplitude, and frequency. Table 2.3-1 contains the operational parameters for each of these test technique. In this section a detailed description of damping test techniques in each of the three vibratory mode categories will be given.
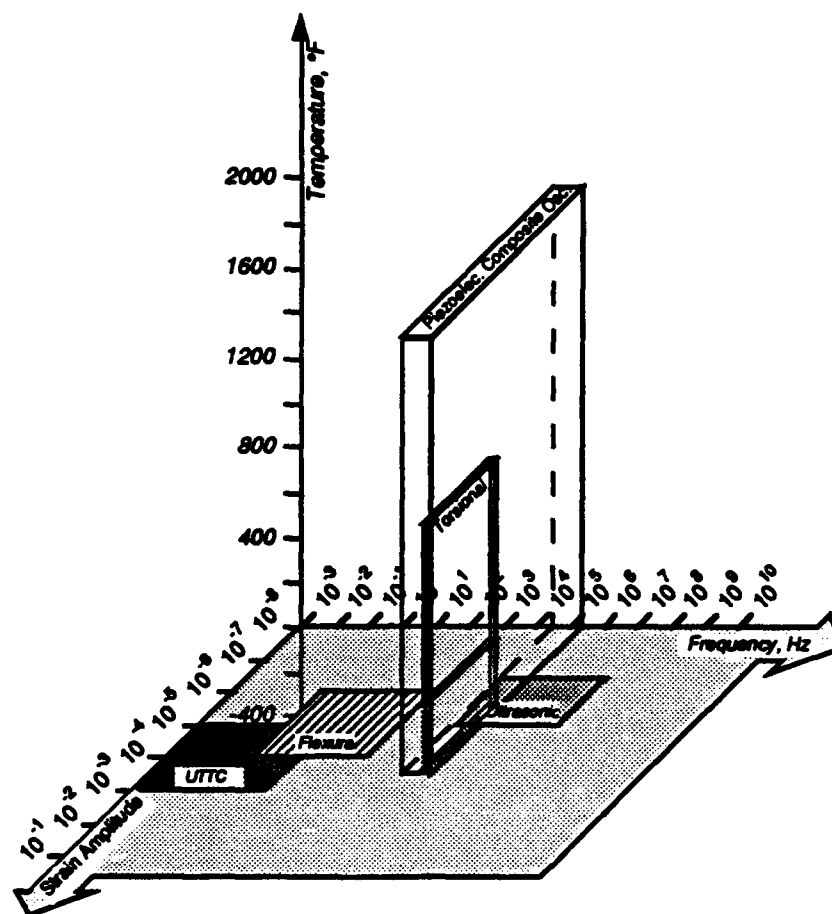
Figure 2.3-1 Relationship Between Various Test Techniques as a Function of Frequency, Temperature, and Strain Amplitude [Ref 2-12]

Table 2.3-1 Operational Parameters of the Damping Techniques Used in This Investigation

Test Technique	Mode of Vibration	Frequency Range (Hz)	Strain Amplitude Range
Clamped-Free Flexure (CFF)	Flexural†	10 — 1000	$5 \times 10^{-6} - 5 \times 10^{-4}$
Free-Free Flexure (FFF)	Flexural†	< 20	$4 \times 10^{-6} - 2 \times 10^{-5}$
Uniaxial Tension-Tension Cycling (UTTC)	Extensional	0.1 — 10	$3 \times 10^{-5} - 5 \times 10^{-4}$
Piezoelectric Composite Oscillator (PCO)	Extensional	80,000 — 10,000	$10^{-9} - 10^{-3}$
Torsional Pendulum	Torsional†	< 1	$\approx 10^{-6}$

† In Vacuum

2-6

2.3.1 Flexural Damping Test Techniques

One of the most common vibration modes used to measure the damping is flexure. Both free-decay and forced oscillation techniques are possible in flexure mode, thereby allowing a wide range of tests to be conducted. Also, data acquisition from flexural techniques can be be simpler than other techniques, thereby making it one of the most favored vibratory modes for testing. Difficulties with flexural tests include 1) inherent parasitic energy losses at the specimen support(s), 2) energy dissipation from aerodynamic drag, and 3) nonuniform strain (stress) amplitude distribution throughout the specimen. Any noble attempt at using flexural mode test techniques must address each of these concerns, as well as other related problems with the particular chosen apparatus.

Two flexural test techniques were chosen for investigation, namely 1) clamped-free flexure and 2) free-free flexure. Both methods were investigated thoroughly to address the aforementioned concerns of energy losses and nonuniformity. Each technique will be discussed below in greater detail.

2.3.1.1 Clamped-Free Flexure — The flexural technique most frequently cited is the cantilever beam, or clamped-free flexure (CFF) arrangement. In this method, one end of the specimen is held in place, usually in a vise-like gripping arrangement, while the other end of the specimen is allowed to move freely to respond to manual displacement or induced vibration. Most commonly, this specimen tip is displaced and released, but it is also possible to drive the specimen vibration continuously by using either noncontact transducers or a shaker table arrangement. Measurement of the damping require the recording of the vibratory history of the specimen, including specimen displacement and also the force input for continuously-driven systems. Note must be taken of the position from which the data are taken, namely the distance from the clamped end, or root, of the specimen. Displacement history is commonly measured by metal foil strain gages or accelerometers, but as concerns of tip-mass anomalies and parasitic losses due to electrical connections increase, greater emphasis has been placed on noncontact methods for displacement measurement. Though these methods have few inherent problems, such as nonlinearity, but these can be solved with the flexibility of real-time data acquisition systems.

In this investigation, three separate CFF experimental setups were employed to measure the damping over a wide range of frequencies. Each setup will be discussed below, along with measures taken to ensure high-quality data.

2.3.1.1.1 Clamped-Free Flexure in Vacuum with Manual Displacement — Initial damping tests were conducted at Martin Marietta with a manual-displacement CFF apparatus as shown schematically in Figure 2.3.1.1.1-1 [Ref 2-13]. A large stainless-steel grip held the specimen vertically in a vacuum chamber. An electromechanical displacement arm was used to grasp the specimen and pull it away from its equilibrium position. Once the desired initial strain amplitude was achieved (as measured by a metal foil strain gage mounted on the surface of the specimen one inch from the root), the displacement arm was lifted to release the specimen, allowing free decay to occur. Data were recorded on high-speed stripchart recorders and peak amplitudes for each cycle were recorded. Damping data were obtained for each initial strain amplitude by a least-squares fit of the peak amplitude data over a minimum of 20 cycles.
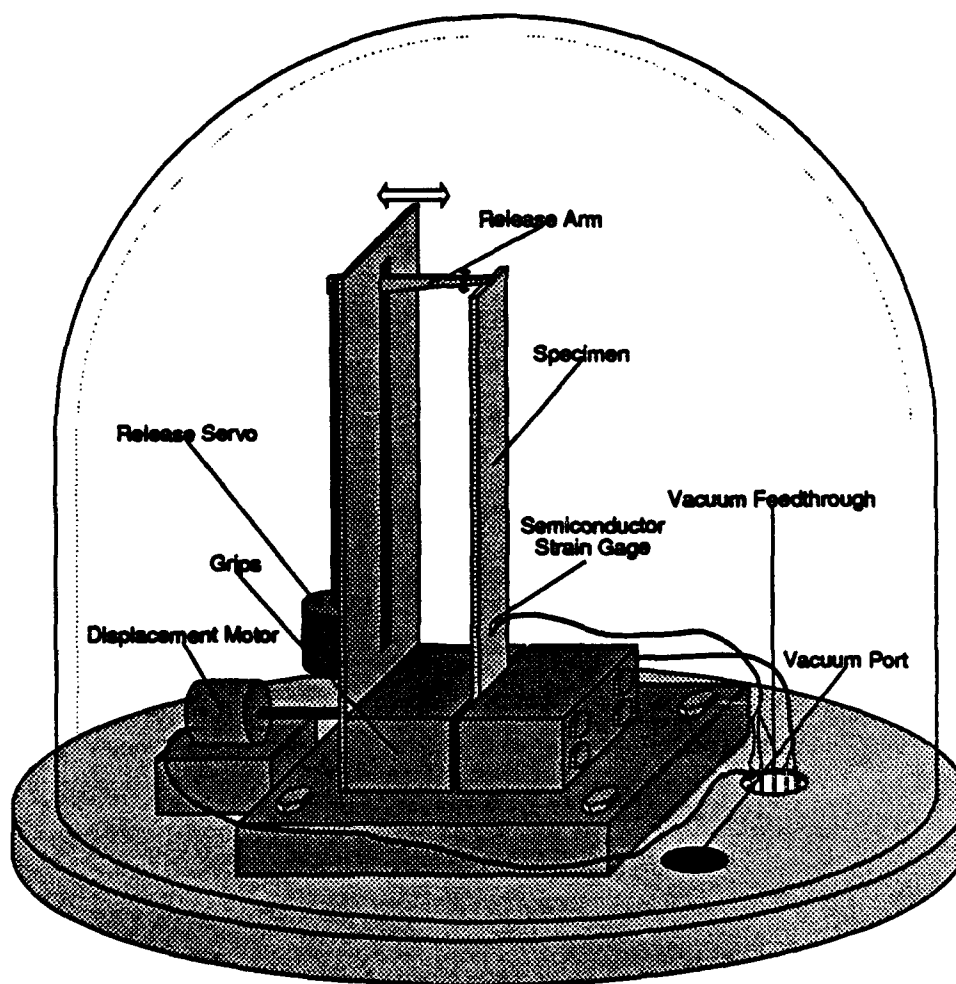
Figure 2.3.1.1.1-1 Schematic of Clamped-Free Flexure (in Vacuum)
Apparatus with Manual Specimen Displacement

Two problem that were identified with the this CFF apparatus was the possibility of parasitic losses derived from motion of the strain gage wires, as well as additional vibratory modes introduced by nonoptimized displacement of the specimen. Great care was taken during data acquisition to minimize these problems.

2.3.1.1.2 Clamped-Free Flexure in Vacuum with Noncontact Transducers — The second CFF apparatus, shown schematically in Figure 2.3.1.1.2-1, was developed at Texas A&M University, Department of Aerospace Engineering, by Dr. Vikram Kinra [Ref 2-14]. Energy dissipation from aerodynamic drag was reduced by placing the entire apparatus in a vacuum. Parasitic energy losses were reduced by the use of noncontact transducers. A Bruel and Kjaer (B&K) MM0002 magnetic transducer was used to induce the specimen into vibration, either by displacement by a specific amount for free-decay measurements, or by continuous vibration. Tip displacement was measured by a B&K MM0004 capacitive transducer. Data were recorded by a Data 6000 transient recorder, and the results analyzed by an HP computer.
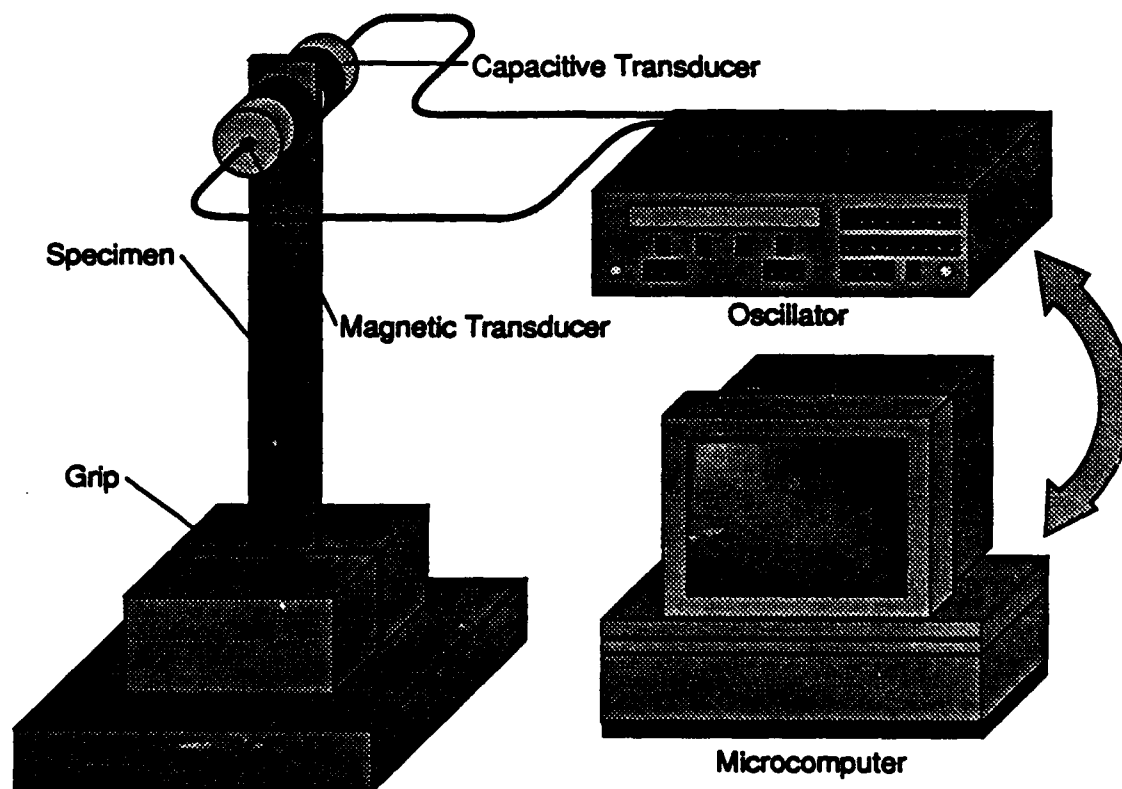
Figure 2.3.1.1.2-1 Schematic of Clamped-Free Flexure (in Vacuum) Apparatus with Noncontact Transducers

2.3.1.1.3 Intermediate-Frequency Clamped-Free Flexure in Vacuum — Measurement of the damping capacity of fibers and small specimens in the low kilohertz range as a function of temperature was made with an apparatus developed by Dr. J.A. DiCarlo, NASA Lewis Research Center, Cleveland, OH (Fig. 2.3.1.1.3-1). Clamped-free flexure specimens of 1/8 inch wide maximum were tested in a high-vacuum cryostat-furnace. The driving frequency was selected as one of the flexural resonant frequencies, thereby making the specimen length shorter than 2-1/2 inches.
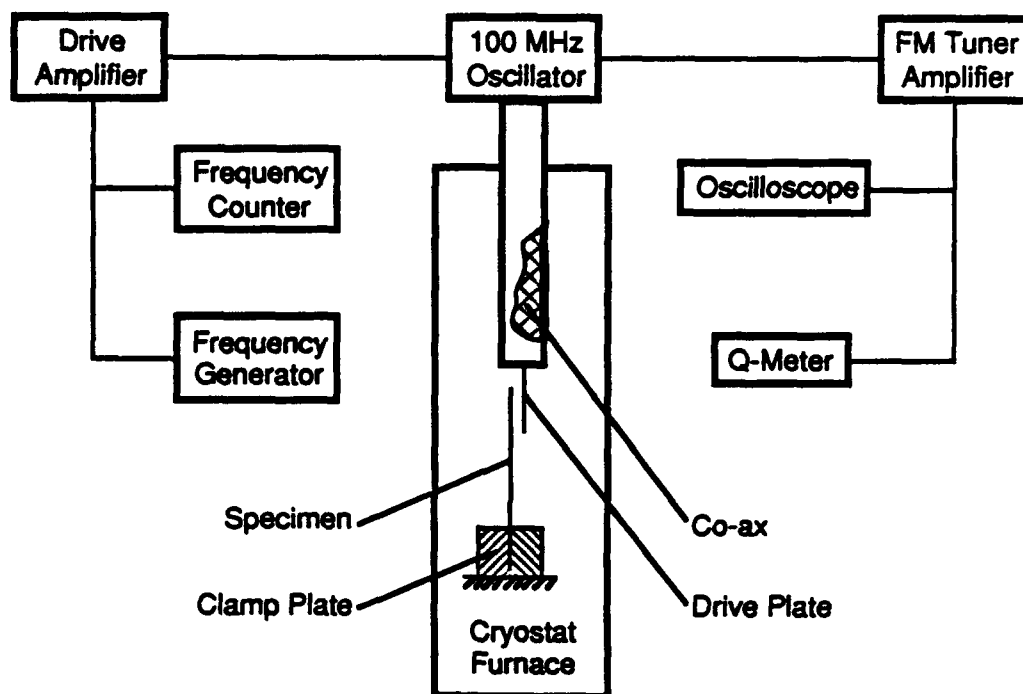
Figure 2.3.1.1.2-1 Schematic of an Intermediate Clamped-Free Flexure
(in Vacuum) Apparatus

2.3.1.2 Free-Free Flexure Technique — A concern with the clamped-free flexure apparatus is the parasitic energy losses at the grip, or root, of the specimen. Furthermore, theoretical considerations indicate that the nonideal gripping arrangement disturbs the wavetrain. Consequently, another flexural test technique called free-free flexure (FFF) has been developed to measure damping while the specimen is vibrated in a standing wave configuration while being suspended by threads at two points along its length which correspond to displacement nodes. First, these fine threads support the specimen without significant parasitic energy losses, and second, the standing wave method of damping is more theoretically sound.

An apparatus for noncontact data acquisition of free-free flexure damping tests was developed at Texas A&M University, Department of Aerospace Engineering, by Dr. Vikram Kinra [Ref 2-14]. As shown in Figure 2.3.1.2-1, the electronics for the FFF apparatus were nearly identical to that of the CFF apparatus discussed earlier in Section 2.3.1.1.2. Transducers could be moved along the length of the specimen to allow different vibratory modes to be excited with the transducers located at the antinodes (i.e. for the first mode, the transducers can be located at the center of the specimen. Location of the support threads was determined analytically prior to specimen mounting. In the case of the FFF apparatus, the specimen was typically tested in continuous vibratory mode, with either the half-power or phase angle methods being chosen for data reduction.
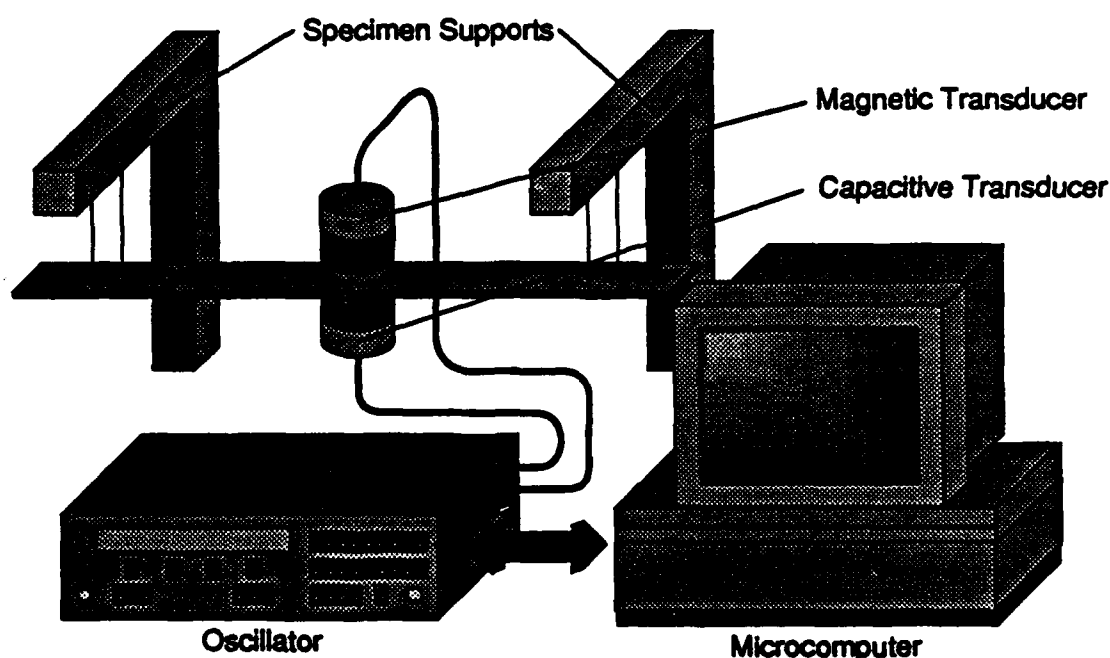
Figure 2.3.1.2-1 Schematic of Free-Free Flexure (in Vacuum) Apparatus with Noncontact Transducers

2.3.2 Parasitic Losses from Aerodynamic Drag by Flexural Testing in Air

While all of the data from the aforementioned flexural damping test techniques were conducted in vacuum to minimize the effects of aerodynamic drag upon the damping, it is important to understand the contribution of air damping when comparing the results of this program with others measured in air.

As a result of the work of Baker, et. al. [Ref 2-15], two expressions were obtained to describe the effects of aerodynamic drag upon the damping of flexural specimens:

$$\delta_a' = \pi C_s \frac{\rho_a}{\rho} \frac{1}{h} \qquad (2\text{-}9)$$

$$\delta_a = \frac{4}{3} \frac{\rho_a}{\rho} C_d \beta_n \frac{A_n}{h} \qquad (2\text{-}10)$$

where: δ_a $\equiv$ air damping for large tip displacement,

δ_a' $\equiv$ air damping for small tip displacement,

ρ_a $\equiv$ air density around the test apparatus,

ρ $\equiv$ specimen density,

C_d, C_s $\equiv$ drag coefficients,

β_n $\equiv$ parameter related to the normal mode shape function which is dependent upon the vibrational mode selected ($\beta_1 = 1.473$, $\beta_2 = 1.300$, $\beta_3 = 1.270$, $\beta_4 = 1.252$, $\beta_5 = 1.252$),

A_n $\equiv$ tip amplitude of the nth mode,

1 $\equiv$ specimen length, and

h $\equiv$ specimen thickness.

These analytical results were verified by Baker, et. al. (Figures 2.3.2-1 and 2.3.2-2) and indicate that for low-density, thin specimens that are commonly used in metal matrix composite damping experiments, air damping can contribute significantly to the measured damping of flexure specimens tested in air, even with extremely-low tip displacements.

2.3.3 Incorporation of Nonuniform Stress Effects in Flexural Test Techniques

One of the major problems with flexural damping data is that the strain (stress) amplitude throughout the length of a specimen is not uniform. The stresses at the root of the specimen displaced from equilibrium are greater than those at the tip, and also the side of the specimen opposed to the displacement is under tension while the other side is undergoing compression. Obviously, the strain amplitude independent damping data are of no concern as they are not affected by discrepancies in stress concentration. However, as these metal matrix composites often exhibit significant strain amplitude dependent damping behavior, it is essential that some common type of data analysis be developed to correlate flexural data between investigators, or with data obtained from other test techniques with different stress (strain) distributions.

2-12
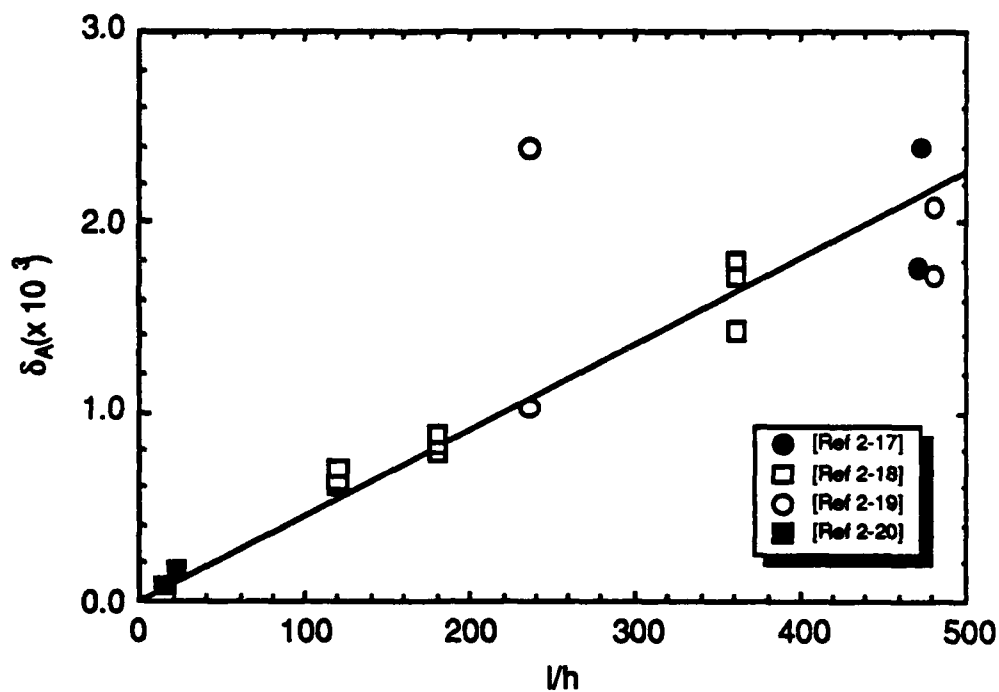
Figure 2.3.2-1 Verification of Small Tip Displacement Air Damping
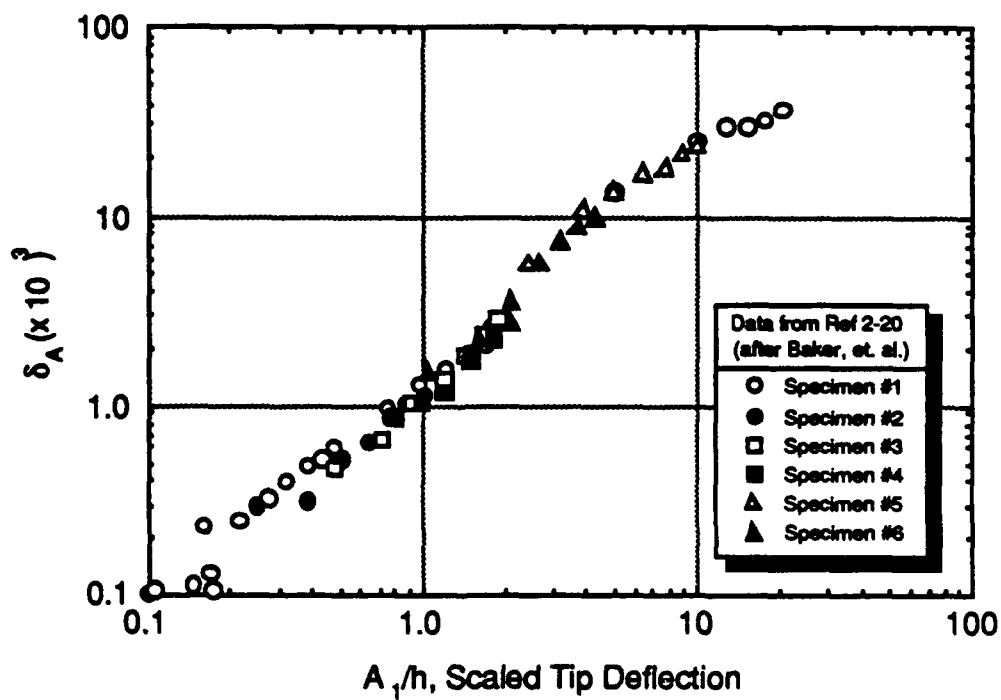
Figure 2.3.2-2 Verification of Large Tip Displacement Air Damping

2.3.3.1 Relationships Between Tip Displacement and Measured Strain Amplitude — From beam theory, the strain observed at any point throughout a horizontal cantilever beam specimen, $\varepsilon(x,z)$, and the tangential displacement, $d(x)$, as defined in Figure 2.3.3.1-1 can be described by the following

$$\varepsilon(x,z) = \frac{6qx^2z}{bh^3E} \tag{2-11}$$

$$d(x) = \frac{q}{2bh^3E}(L-x)^2(3L^2 + 2Lx + x^2) \tag{2-12}$$

where: q = load intensity,
  b = specimen width,
  h = specimen thickness,
  E = elastic modulus of the beam, and
  L = specimen length.

All tests conducted at Martin Marietta measured strain amplitude one inch away from the root. Thus, equation 2-11 can be written as

$$\varepsilon_{measured} = \frac{3q(L-1)^2}{bh^2E} \tag{2-13}.$$

Another common way to describe the strain amplitude is to normalize the measurement with respect to the value at the root. Thus, equation 2-13 then becomes

$$\varepsilon_{root} = \frac{3qL^2}{bh^2E} \tag{2-14}.$$

By solving 2-13 and 2-14 simultaneously, one obtains the relationship

$$\varepsilon_{root} = \varepsilon_{measured}\left(\frac{L}{L-1}\right)^2 \tag{2-15}.$$

Conversely, the tip displacement can be related to the strain amplitude. The tip displacement, from equation 2-12, is given by

$$d_{tip} = \frac{3q}{2bh^3E}L^4 \tag{2-16}.$$

By solving 2-13 and 2-16 simultaneously, one then obtains

$$d_{tip} = \frac{L^2}{2h}\left(\frac{L}{L\text{-}1}\right)^2 \varepsilon_{measured} \qquad (2\text{-}17).$$

Thus, strain amplitude dependent damping data from these flexural investigation can be related to any data in the literature that are measured either by tip displacement or by surface strain at any position on the specimen.

2.3.3.2 Calculation of Intrinsic Damping of Flexural Specimens — It is often difficult to discuss strain amplitude dependence of materials when the specimens are tested under different modes of vibration (e.g. flexural versus extensional). Thus it is necessary to find "common ground" for flexural damping data. This may be accomplished by converting damping data to intrinsic values. According to Ritchie, et. al. [Ref 2-16], the intrinsic damping of a specimen ψ' (ε) as a function of strain amplitude ε is related to the data obtained from a cantilever beam test in the following manner

$$\psi'(\varepsilon) = \psi_s + \frac{7}{9}\varepsilon\frac{d\psi_s}{d\varepsilon_s} + \frac{1}{9}\varepsilon^2\frac{d^2\psi_s}{d\varepsilon_s^2} \qquad (2\text{-}12)$$
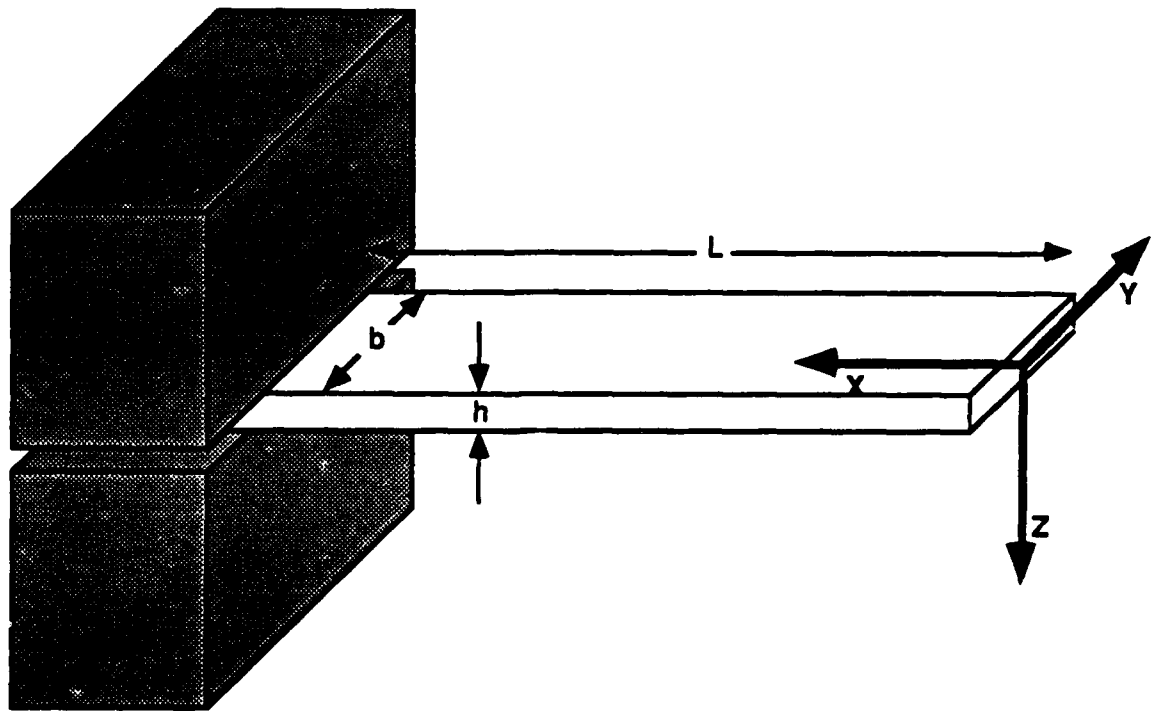
Figure 2.3.3.1-1 Schematic of Cantilever Beam and the Chosen Coordinate System

2-15

where the first and second derivatives of the original damping data ψ_s as a function of the original strain amplitude ε_s must be obtained, either graphically or numerically. Specific modification of the intrinsic damping for composite specimens requires complex analyses using strain energy modeling on computers and as such, was beyond the scope of this investigation.

2.4 EXTENSIONAL DAMPING TEST TECHNIQUES

Another common mode of vibration for damping tests is extensional. Typically, these techniques are driven oscillations at continuously-maintained strain amplitude and/or frequency. This mode also has the widest frequency range possible, from subhertz to megahertz levels. They may also be broken into resonant and subresonant techniques, where subresonant techniques make the specimen exhibit relatively uniform strain amplitude along its entire length, while resonant mode dictates that the specimen be vibrated in a standing wave configuration. In this investigation, two types of this technique were used, namely 1) subresonant uniaxial tension-tension cycling, and 2) piezoelectric composite oscillator. Both techniques are described below.

2.4.1 SUBRESONANT UNIAXIAL TENSION-TENSION CYCLING

A technique was developed at Texas A&M University, Department of Aerospace Engineering, by Dr. Vikram Kinra [Ref 2-13] to measure the damping of metal matrix composites undergoing sub-resonant constant strain amplitude uniaxial tension-tension cycling (UTTC). Tension-tension cycling eliminated both the possibility of specimen buckling that would occur as a result of tension-compression testing, and possible parasitic losses from aerodynamic drag. As shown in Figure 2.4.1-1, a servohydraulic machine was used to supply a cyclic load to the specimen. Semiconductor strain gages were used to measure the strain at the center of the gage length of the specimen because they allowed higher excitation voltages than conventional metal foil gages with no thermal instabilities, thereby resulting in higher signal-to-noise ratios. Fast fourier transform (FFT) analysis of the digitized stress (load cell) and strain signals by a microcomputer and digital oscilloscope resulted in the phase angle between the two signals to obtain the damping values. Large number of data (>1024 points) were obtained per cycle to enh⌐ce the resolution of the FFT. In all cases, additional phase angle changes from phase differences in all amplifiers, particularly the load cell, were characterized prior to testing to eliminate any contributions to the measured damping. Furthermore, damping data obtained from phase angle analysis were compared to data obtained from the area contained within the stress-strain hysteresis loop with excellent results.
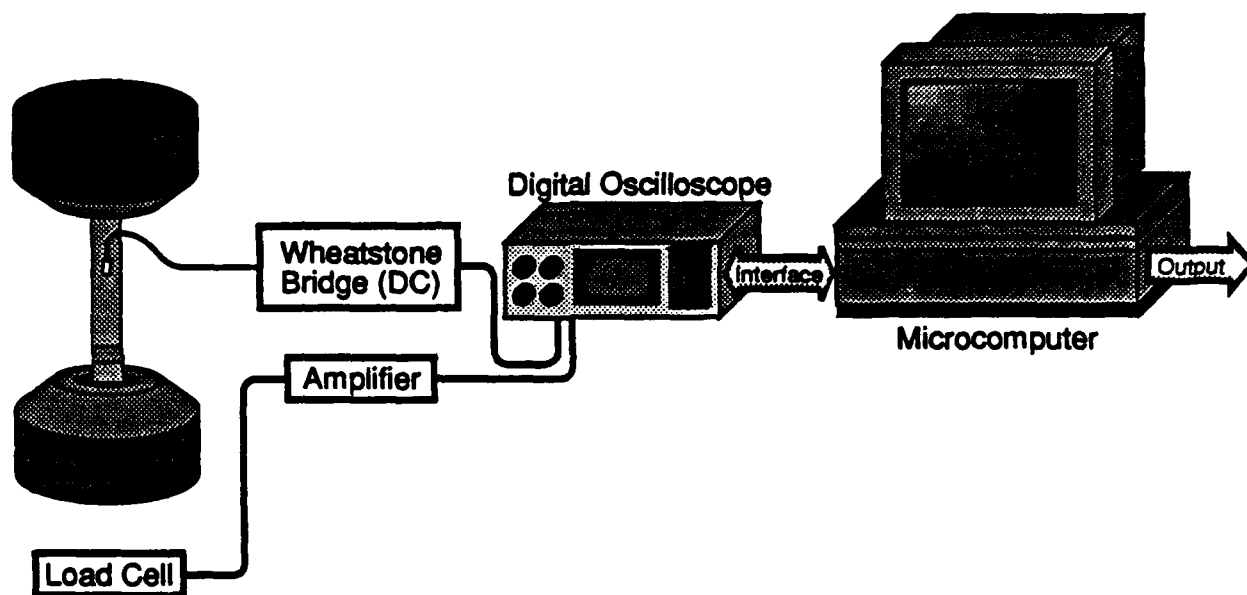
Figure 2.4.1-1 Schematic of Subresonant Uniaxial Tension-Tension Cycling Apparatus

Because the specimen is driven by a servohydraulic tensile machine, there is no restriction as to specimen length with UTTC as was observed with flexural testing. Furthermore, a significant contribution can be made to the study of very-low frequency (0.1 Hz — 1.0 Hz) damping of interest to SDI-related programs. While the strain amplitude range (50 $\mu\varepsilon$ — 600 $\mu\varepsilon$) is somewhat limited in comparison to the resonant piezoelectric composite oscillator discussed below, the advantages of nearly-uniform strain amplitude with respect to length for the analysis of strain amplitude dependent damping phenomenon is very important.

2.4.2 Resonant Piezoelectric Composite Oscillator

One of the most reliable damping test techniques available is the resonant piezoelectric composite oscillator (PCO). In use since the 1940's, it has been used to measure the damping and dynamic modulus of a variety of materials. A schematic of the testing apparatus is shown in Figure 2.4.2-1. A pair of quartz crystals, whose length is matched precisely to 1/2 wavelength each, is driven in a standing wave configuration at kilohertz frequencies by a closed-loop crystal driver. The center of each quartz bar is a displacement node, allowing for both electrical and structural connections. A specimen, whose length is precisely 1/2 wavelength for that particular material, is attached to the quartz bar assembly using E910 adhesive. The entire assembly is then vibrated in a standing wave

configuration, with the crystal driver adjusting the driving frequency and voltage to maintain resonance at a preselected strain amplitude (gage voltage). Because resonance of the entire system is maintained in the kilohertz range, this technique has also proven valuable in monitoring damage growth through very precise changes in modulus and damping [Ref 2-17].
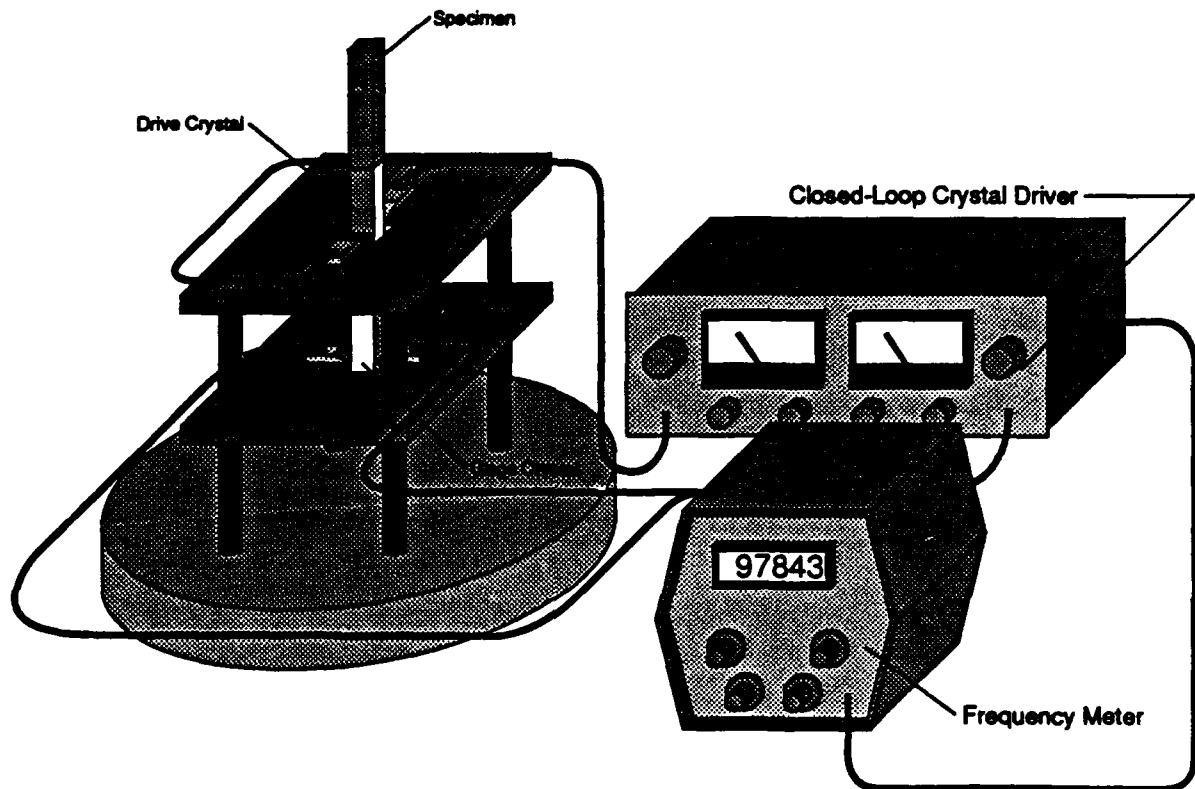
Figure 2.4.2-1 Schematic of Resonant Piezoelectric Composite Oscillator Technique

Like the flexural testing, the length of the specimen is restricted to the particular frequency of interest. However, the piezoelectric composite oscillator also allows for the largest strain amplitude range of any of the tests mentioned previously, namely 10^{-9} to 10^{-3}. The six orders of magnitude range of the strain amplitude allows for high-integrity strain amplitude dependent analysis of the damping data. Because strain amplitude dependent damping response is typically frequency independent, it is possible to compare the analyses of PCO data with those obtained from other tests, provided that the sinusoidal strain distribution with respect to length is acknowledged and the data treated accordingly.

2-18

2.5 TORSIONAL DAMPING TEST TECHNIQUE

A third mode of vibration employed to measure damping is torsion. This mode allows for temperature-dependence measurements of damping at very low frequency (< 1 Hz) of wire geometry specimens in vacuum. Thus, the temperature dependence of damping could be used to characterize the strain amplitude independent damping regime.

The torsional pendulum apparatus used in these investigations was developed at the University of Denver, Denver, CO, under the supervision of Dr. Steve Carpenter. As shown in Figure 2.5-1, a specimen was attached by jewler's vises at the rigid base and on the torsional carrier above. Initial displacement of the device was accomplished by magnetic solenoids, and measurement of the angular displacement was made by time-of-flight measurements by a three-element photocell arrangement. Cycles were counted by the center photocell, and the outer photocells measured the time-of-flight of a light beam reflected by a mirror placed atop the torsional carrier.
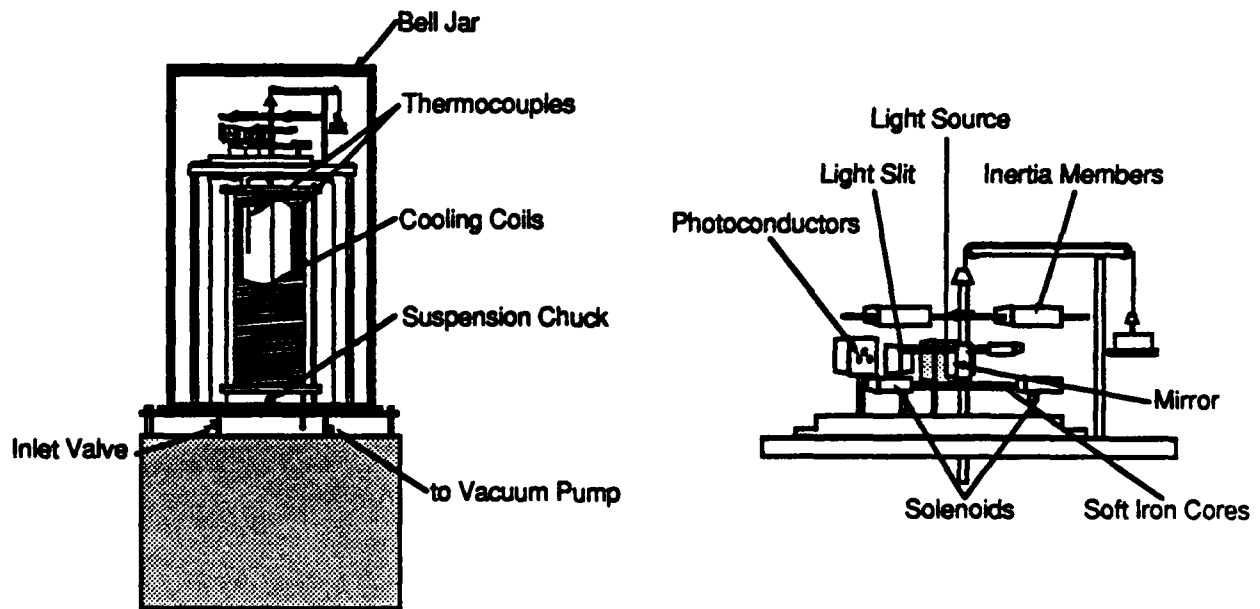
Figure 2.5-1 Schematic of Torsional Pendulum Damping Apparatus

Specific damping capacity (ψ) was obtained from the time-of-flight measurements during free decay by the following relationship

$$\psi = \frac{2}{n} \ln \left[\frac{\sin \omega t_n/2}{\sin \omega t_0/2} \right]$$ (2-13)

where: n = number of cycles measured,

ω = angular frequency of wire specimen, and

t_0, t_n = time-of-flight of reflected light path between outer photocells for initial and n^{th} cycles respectively

Accurate temperature was maintained by a three-zone furnace precision and multi-zone temperature controller which provided approximately 18 inches of uniform temperature with respect to temperature length. Time-of-flight and temperature data were then acquired, reduced, analyzed, and stored by a PC-based computer system.

2.6 SUMMARY

In general, an overall choice of test techniques should bear a relationship to the stress state, frequency, specimen geometry, and temperature to be encountered in the material application. Damping test data can be expressed in many different parameters which are interrelated at low damping values. Although no single test method can be used to obtain material damping data over a wide frequency and strain amplitude range, it must be recognized that a common (fundamental) measure of damping can be agreed upon by investigators in various disciplines. Such a measure will reduce confusion and lead to a systematic approach of comparing damping data of a structural material.

A thorough understanding was developed for the damping nomenclature and the background for each test method. A variety of damping test techniques were evaluated for use with metal matrix composites. Flexural, extensional, and torsional modes of vibration were employed to measure the damping as a function of frequency, strain amplitude, and temperature. Extraneous energy losses were eliminated or minimized to enhance the reliability of each test technique. At low strain amplitudes ($\epsilon \leq 10^{-5}$), damping values of MMC from each of the test techniques provided damping data that were compatible. Techniques were developed to obtain data at intermediate strain amplitudes.

2.7 REFERENCES

2-1   A.S. Nowick and B.S. Berry: Anelastic Relaxation in Crystalline Solids, Academic Press, New York (1972).

2-2   R. De Batist: Internal Friction of Structural Defects in Crystalline Solids, North Holland, Amsterdam (1972).

2-3   B.J. Lazan: Damping of Materials and Members in Structural Mechanics, Pergamon Press, Ltd., Oxford (1968).

2-4   C. Zener: Elasticity and Anelasticity of Metals, Univ. of Chicago Press, Chicago (1948).

2-5   K.M. Entwistle: Physical Examination of Metals, 2nd ed., by B. Chalmers and A.G. Quarrell, Edward Arnold, Ltd., London (1960).

2-6   D.N. Beshers: Techniques of Metals Research, Vol. VII, Part 2, John Wiley & Sons, New York (1976).

2-7   J.W. Mar: Vibration Damping 1984 Workshop Proceedings, Report #AFWAL-TR-84-3064, pp. A2-A23 (1984).

2-8   R. Plunkett: Structural Damping, ed. Ruzicka, ASME, 117-131, Dec. 1959.

2-9   C.W. Bert and R.R. Clary: "Composite Materials: Testing and Design", Third Conference, ASTM STP 546, 250-265 (1974).

2-10   R.F. Gibson and R. Plunkett: The Shock and Vibration Digest, Vol 9, No. 2, pp 9-17 (1977).

2-11   S.A. Suarez, R.F. Gibson, and L.R. Deobald: Experimental Techniques, Vol 8, No. 5, pp 19-24 (1984).

2-12   V.K. Kinra, private communications.

2-13   J.H. Armstrong, S.P. Rawal, and M.S. Misra: "Damping Measurements of Graphite-Aluminum Composites," Martin Marietta Report R86-48681-002, December 1986.

2-14   A.K. Ray, V.K. Kinra, S.P. Rawal, and M.S. Misra: "Measurement of Damping in Continu-
        ous Fiber Metal Matrix Composites," Role of Interfaces in Material Damping, eds. B.B.
        Rath and M.S. Misra, ASM, Metal Park, OH, pp 995-102, 1986.

2-15   W.E. Baker, W.E. Wollam and D. Young: International Journal of Mechanical Science, 9, p
        743 (1967).

2-16   I. G. Ritchie and H.L. Rosinger: Dynamic Elastic Properties of Materials, Materials
        Research in AECL, AECL-4842, Summer 1974.

2-17   J.H. Armstrong: Ph.D. Thesis, University of Denver Department of Physics, Denver, CO
        1985.

2-18   M. Uemura and M. Takehana, Tokyo Univeristy Report, Inst. Science and Technology, Vol 7,
        No. 2 (April 1953).

2-19   W.E. Baker and F.J. Allen, BRL Report No. 1033, Aberdeen Proving Ground, Md. (Oct.
        1957).

2-20   N. Granick and J.E. Stern, Shock and Vibration Bulletin, Vol 34, Part 5, pp. 177-195.

3.0 Damping of Gr/Al Composites

CHAPTER 3.0
DAMPING MECHANISMS IN CONTINUOUS Gr/Al COMPOSITES

Graphite fiber-reinforced metal matrix composites are candidate materials for large space structures (LSS) because of their high specific mechanical properties, high electrical and thermal conductivity, and near zero coefficient of thermal expansion. In addition to high stiffness and dimensional stability, a critical design and operational requirement for LSS is the reduction of settling time during acquisition, pointing and tracking (APT) maneuvers. Vibrational control can be achieved by various active controls and passive damping measures at low frequency (0.1 - 20 Hz) and low strain levels ($\varepsilon < 10^{-4}$) encountered by space structures. While the role of inherent material damping is frequently omitted in active control analyses, it may provide a significant source of passive energy dissipation to ensure successful stabilization of large, flexible space structures.

Enhancement of material damping in metal matrix composites is limited by insufficient knowledge of the operative damping mechanism(s). Damping in metal matrix composites must be influenced by the energy dissipation processes acting within the constituent fiber and matrix materials. Because damping is a structure-sensitive property, imperfections, voids and second-phase precipitates (particularly near the interfaces) may also act as sources of energy dissipation. In this section, the results of damping measurements by flexural and extensional mode test techniques have been analyzed to understand the operative damping mechanism in continuously-reinforced Gr/Al composites. It is believed that such an understanding of sources of energy dissipation in metal matrix composites will define an approach for enhancement of damping in these materials.

3.1   EXPERIMENTAL PROCEDURE

3.1.1   Material

Single-ply [0°] P55Gr/6061Al composite panels were fabricated by DWA Composite Specialties, Chatsworth, CA. Graphite/Aluminum precursor wires were consolidated between 88.9 μm (0.0035 in.) thick 6061 Al face sheets at 588°C (690°F) and 24 kPa (3.5 ksi) for 20 minutes, yielding a composite with 66.0 mm (0.026 in.) thickness and 39.2% fiber volume. Examination of the panels using X-radiography and optical microscopy indicated good bonding characteristics and fiber collimation. Elastic modulus for the composite was 158 GPa (22.9 Msi) and ultimate tensile strength was 531 MPa (77.0 ksi). In addition, specimens of 6061 aluminum alloy were fabricated as a reference spec-

imen to ascertain the reliability of the damping measurements as compared to data found in the literature.

3.1.2   Test Techniques

Damping characteristics of these composites were measured both in flexural and extensional mode by three test techniques: free-free flexure, clamped-free flexure and subresonant uniaxial tension-tension fatigue [Ref 3-1]. Flexural tests were conducted in a vacuum better than 10^{-4} to eliminate contributions to the measured damping from aerodynamic drag. The range of strain amplitudes and frequencies tested was dependent upon the test method ($10^{-6} < \epsilon < 10^{-5}$ at f ≈ 20 Hz for free-free flexure, $1 \times 10^{-5} < \epsilon < 5 \times 10^{-3}$ at f < 100 Hz for clamped-free flexure, and $1 \times 10^{-4} < \epsilon < 5 \times 10^{-4}$ at $0.1 < f < 10$ Hz for tension).

The specific damping capacity (ψ) of a material is interrelated to other parameters in the following way

$$\psi = \Delta W/W = 2\delta = 2\pi\zeta = 2\pi\phi = 2\pi\eta = 2\pi Q^{-1} \tag{3-1}$$

Log decrement (δ) values for the flexural tests were obtained by a least-squares fit of the strain history of the specimen vibrating at its fundamental resonant frequency. Damping values in the uniaxial tension-tension fatigue tests were derived initially from integration of the stress/strain hysteresis loop, which is related to the ratio $\Delta W/W$. At the same time, an alternate method for obtaining the loss angle ϕ from fast fourier transform (FFT) analysis was also found to be within ±5% of the values obtained from the integration method.

3.2   RESULTS

Damping test results from flexural and extensional mode tests at different frequency and strain amplitudes are described below.

3.2.1   In Vacuo Free-Free Flexure Test Method

Typical damping behavior of the reference 6061-0 aluminum alloy within the $10^{-6} — 10^{-5}$ strain range is given in Figure 3.2.1-1. Preliminary investigations have shown that values at low strain

3-2

amplitudes for free-free flexure correspond well for data obtained by *in vacuo* clamped-free flexure. Corresponding damping behavior for [0°] P55Gr/6061Al composites is shown in Figure 3.2.1-2. Both the composite and the matrix alloy exhibit nearly strain amplitude independent damping behavior within the strain amplitude range tested. Furthermore, specific damping capacity (ψ) values of the composite are noticeably lower than the 6061-0 Al alloy.
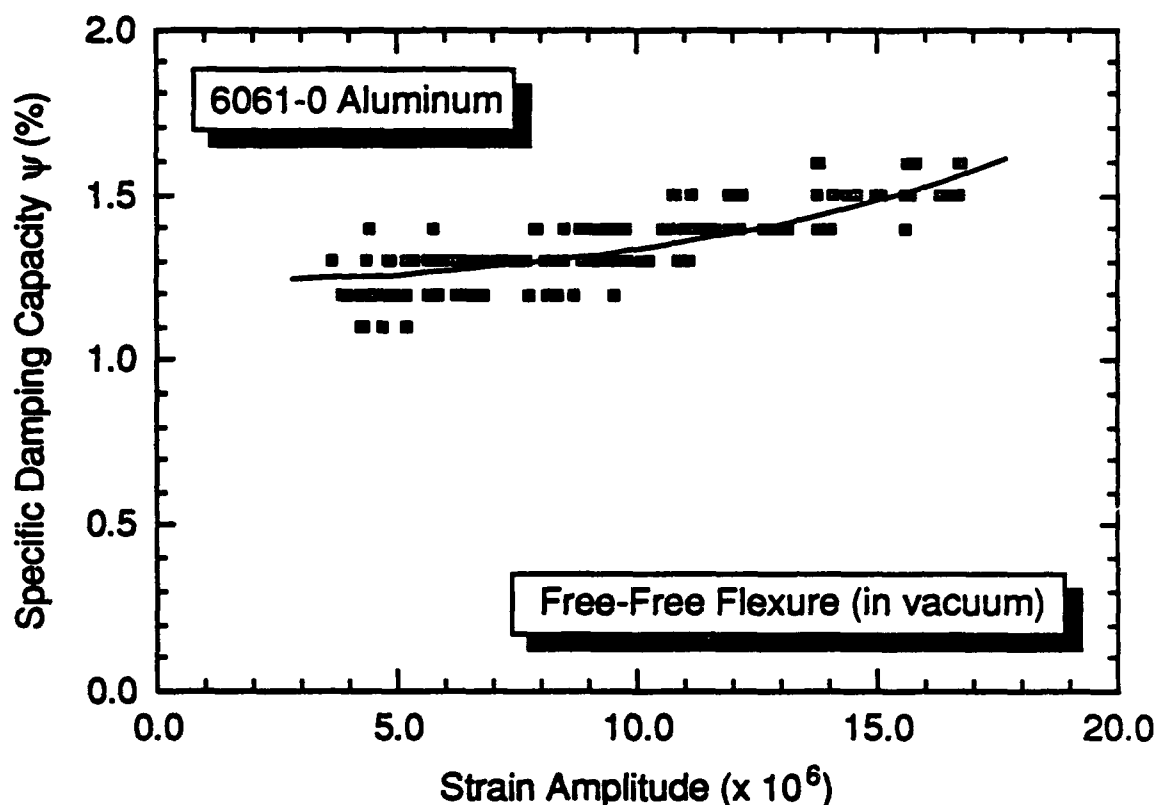
Figure 3.2.1-1 Typical Damping Response of 6061-0 Al as a Function of Strain Amplitude (Free-Free Flexure in Vacuum)

3.2.2 *In Vacuo* Clamped-Free Flexure Test Method

Typical damping behavior of [0°] P55Gr/6061Al in clamped-free flexure is shown in Figure 3.2.2–1. While in agreement with damping data from free-free flexure tests at comparable strain amplitude and vibrational frequency, clamped-free flexure data exhibit significant strain amplitude dependence at high strain ($\varepsilon > 10^{-4}$). Figure 3.2.2-1 also shows that specimens vibrated at higher frequencies exhibited higher damping.
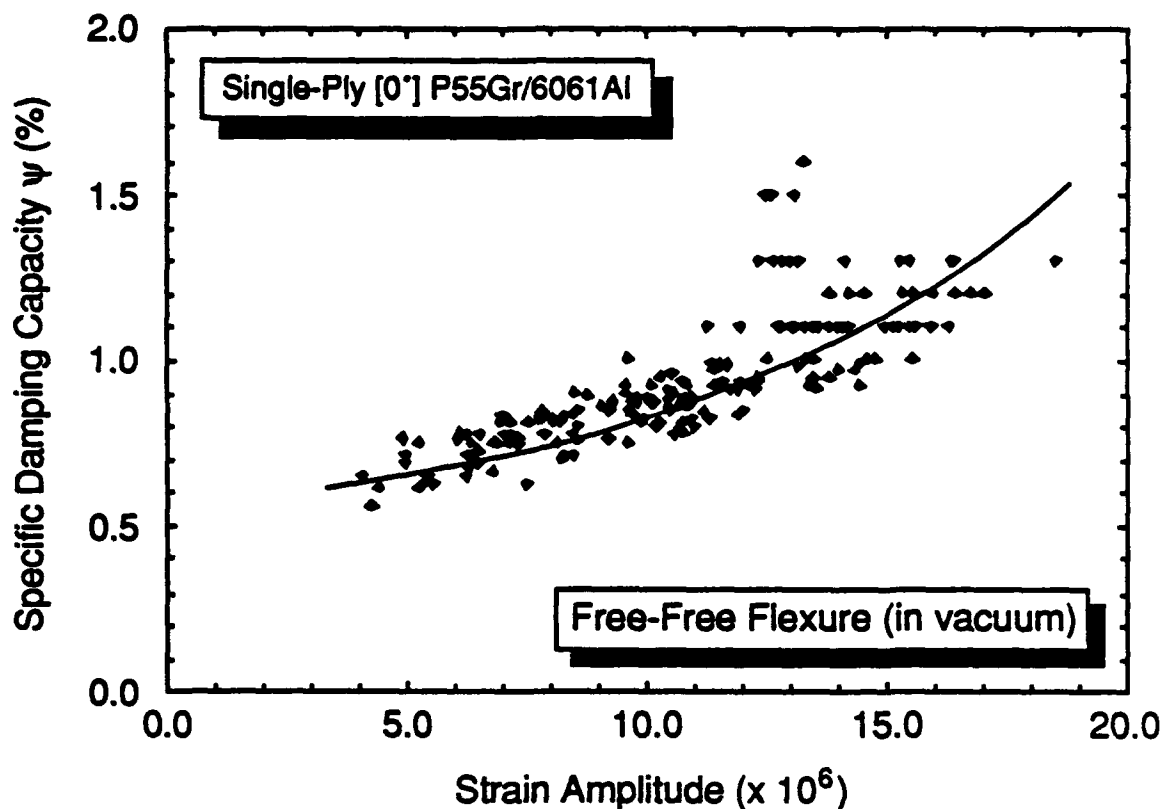
Figure 3.2.1-2 Typical Damping Response of Unidirectional [0°] P55Gr/6061Al as a Function of Strain Amplitude (Free-Free Flexure in Vacuum)

3.2.3   Uniaxial Tension-Tension Fatigue Test Method

Specific damping capacity and corresponding strain amplitude for [0°] P55Gr/6061Al specimens at 0.4 and 1.0 Hz are given in Table 3.2.3-1. A plot of these data, along with values for 6061-T625, shown in Figure 3.2.3-1, showed the damping level of the composite to be above that of the matrix alloy. Furthermore, damping behavior of the composite exhibited strong strain amplitude dependence within the 150 — 325 microstrain levels tested. In addition, measured damping in extensional mode were significantly higher compared to flexural damping tests (Figs. 3.2.1-2 and 3.2.2-1).
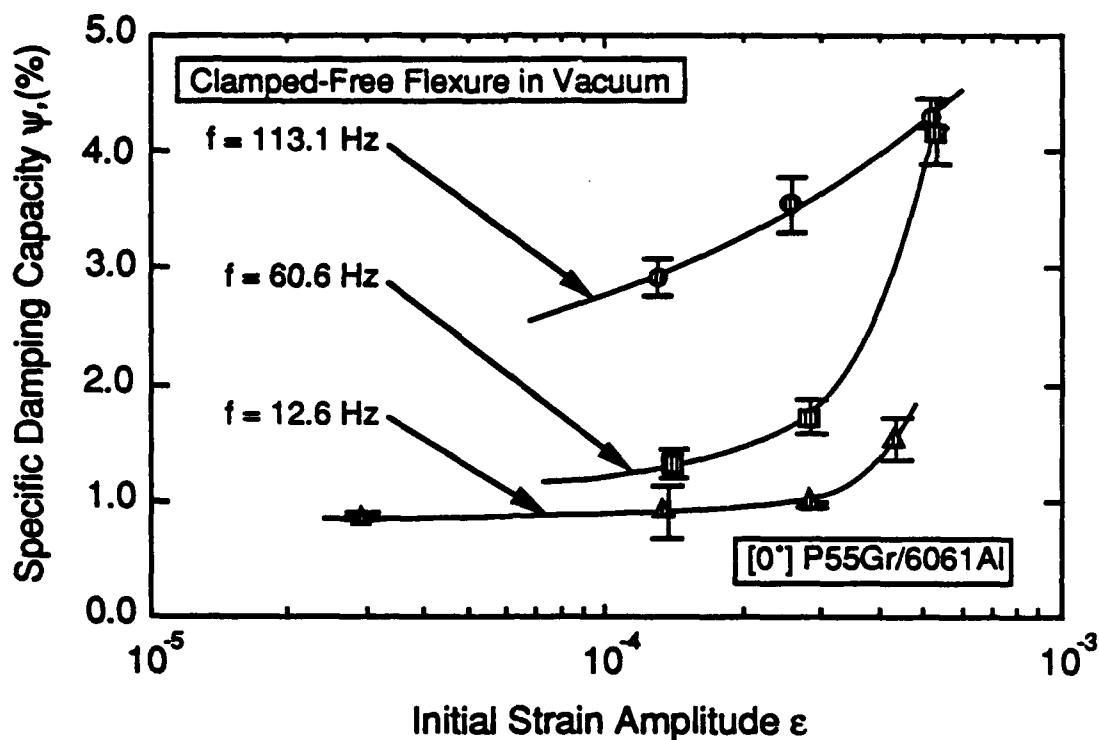
Figure 3.2.2-1 Damping Behavior of [0°] P55Gr/6061Al as Measured by
Clamped-Free Flexure in Vacuum

Table 3.2.3-1 Damping Measurements of [0°] P55Gr/6061Al Using
Uniaxial Tension-Tension Fatigue Apparatus

Strain Amplitude ε (μ in./in.)	Specific Damping Capacity Ψ, (%)				
	0.4 Hz	1.0 Hz	2.0 Hz	4.0 Hz	10.0 Hz
150	7.82	6.74	7.42	8.58	—
195	8.82	7.36	7.55	11.98	16.14
242	10.96	10.13	—	—	—
285	13.09	11.51	—	—	—
325	15.48	13.40	—	—	—

3.3   DISCUSSION

Damping behavior of Gr/Al composites exhibited strain amplitude dependent behavior similar to
that of metallic materials. Based on results from free-free flexure, clamped-free flexure, and uniaxi-

al tension-tension cycling test techniques, the specific damping capacity of these composites is nearly strain amplitude independent below 2×10^{-5}, but exhibits strong strain amplitude dependence above 10^{-4}. The total measured damping may be expressed as a sum of strain amplitude independent (ψ_i) and strain amplitude dependent (ψ_H,) or hysteretic, components, i.e. $\psi_{total} = \psi_i + \psi_H$. Operative mechanisms for these two damping components in MMC are discussed below.
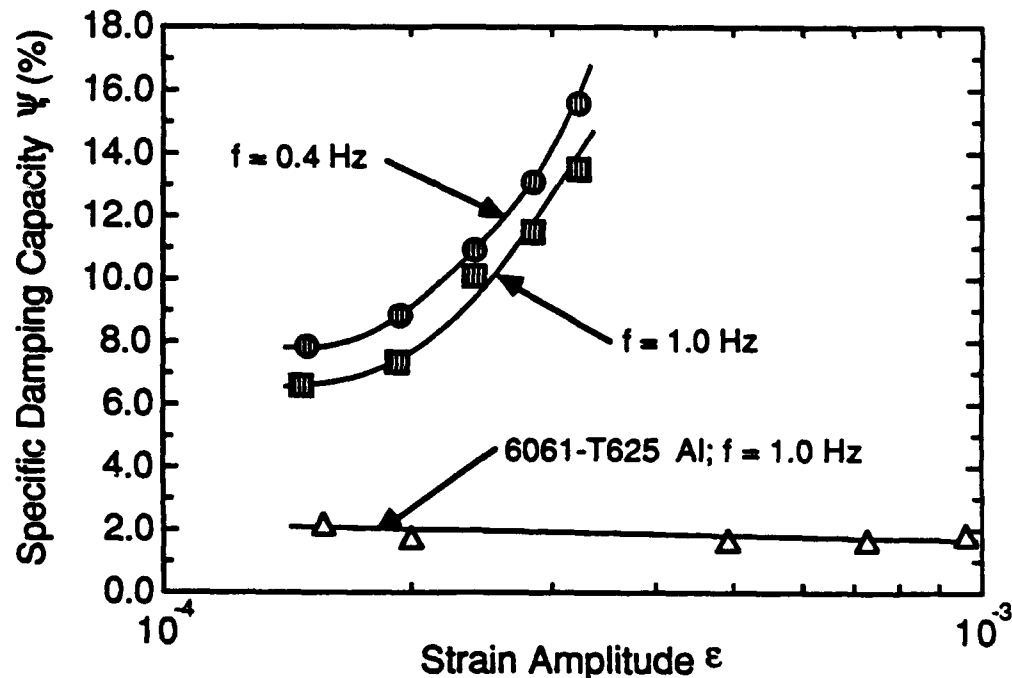
Figure 3.2.3-1 Damping Behavior of [0°] P55Gr/6061Al as Measured by Uniaxial Tension-Tension Fatiuge

3.3.1   Strain Amplitude Independent Damping

At low strain amplitude levels where material damping is nearly independent of strain, the energy dissipation is primarily attributed to anelastic relaxation mechanisms involving atomic diffusion, dislocation relaxation (Bordoni Peak), dislocation resonance and the Zener thermoelastic effect. It is most likely that the thermoelastic effect may be the primary mechanism of energy dissipation for both flexural and extensional modes of vibration at room temperature During flexural vibration the top and bottom surfaces of the composite beam undergo cyclic compressive and tensile stress states. The resulting strain is generally accompanied by a change in temperature; temperature rises under compressive loads, and declines under tensile loads. Energy dissipation processes result pri-

3-6

marily from heat transfer due to thermal gradients within the specimen. In the case of extensional (longitudinal) vibrations, heat flow within the specimen is minimal and most of the energy from the surface is lost to the surroundings. Zener thermoelastic damping effects are maximum at a relaxation frequency where the period of applied stress is comparable with the time taken for heat to flow across the beam. Zener relaxation frequency of P55Gr/6061Al test specimens was calculated to be $f_z = 108.17$ Hz (679.3 rad/s) at which the energy losses from the thermoelastic effect are a maximum. The calculated specific damping capacity contribution from thermoelastic relaxation at the Zener frequency was 0.13%, suggesting that other anelastic relaxation processes operative within the constituent fiber and matrix must lead to energy dissipation.

The dynamic response of a linear anelastic (or viscoelastic) composite in terms of their constituent properties can be predicted by Hashin theory [Ref 3-2]. Using a correspondence principal, Hashin has derived expressions to determine effective complex moduli of fiber-reinforced materials directly from the composite effective elastic modulus by replacing the elastic modulus of the phases by their complex moduli. For unidirectional composites, the axial specific damping capacity ψ_{11} can be expressed in the following form:

$$\psi_{11} = \left[\frac{E_f}{E_{11}}\right] \cdot \psi_f V_f + \left[\frac{E_m}{E_{11}}\right] \cdot \psi_m (1 - V_f) \qquad (3-2)$$

where
$$E_f \equiv \text{Fiber Modulus}$$
$$\psi_f \equiv \text{Fiber Damping}$$
$$E_{11} \equiv \text{Axial Composite Modulus}$$
$$\psi_f \equiv \text{Fiber Damping}$$
$$\psi_m \equiv \text{Matrix Damping}$$
$$V_f \equiv \text{Fiber Volume.}$$

Graphite fibers behave in a nearly elastic manner and are considered to have very low damping as compared to the matrix. Recently, DiCarlo obtained a maximum value of fiber damping (ψ_f) in Pitch 100 graphite fiber of 0.1% at room temperature [Ref 3-4]. Using this value, and $\psi_m = 1.2\%$ for 6061Al, Equation 3-2 yields ψ_{11} of 0.41%, as compared to the measured ψ_{11} value of 0.6% (minimum) obtained by the flexural test method. Although it is difficult to isolate contributions from extraneous losses in the measured ψ_{11}, the measured and predicted values are reasonably close. In addition, these results indicate that anelastic mechanisms operating in both fiber and matrix provide the sources of energy dissipation at low strain amplitudes.

3.3.2 Strain Amplitude Dependent Damping

At intermediate strain amplitude ranges ($10^{-5} > \varepsilon > 10^{-3}$) the specific damping capacity of as-fabricated P55Gr/6061Al composites increases with increasing strain. Strain amplitude dependent damping behavior of this material has been analyzed in terms of energy loss due to cyclic dislocation motion proposed by Granato and Lucke (G-L) 0 Kelvin model [Ref 3-4 and 3-5].

As shown schematically in Figure 3.3.2-1, dislocations are pinned at major pinning points, defined by dislocation tangles, precipitates, etc. Minor pinning points such as impurities or fine precipitates are distributed randomly along the dislocation network. Based on this vibrating string model, G-L theory provides two mechanisms of energy dissipation. At low strain amplitudes, the strain amplitude independent damping is explained in terms of dislocation vibration about minor pinning points in response to a cyclic applied load, often referred to as dislocation resonance damping. At intermediate strain amplitudes, damping is strain amplitude dependent and can be described in terms of dislocation breakaway from the minor pinning points and vibration about the major pining points, thereby providing hysteretic energy loss.

(a)   (b)   (c)   (d)   (e)   (f)
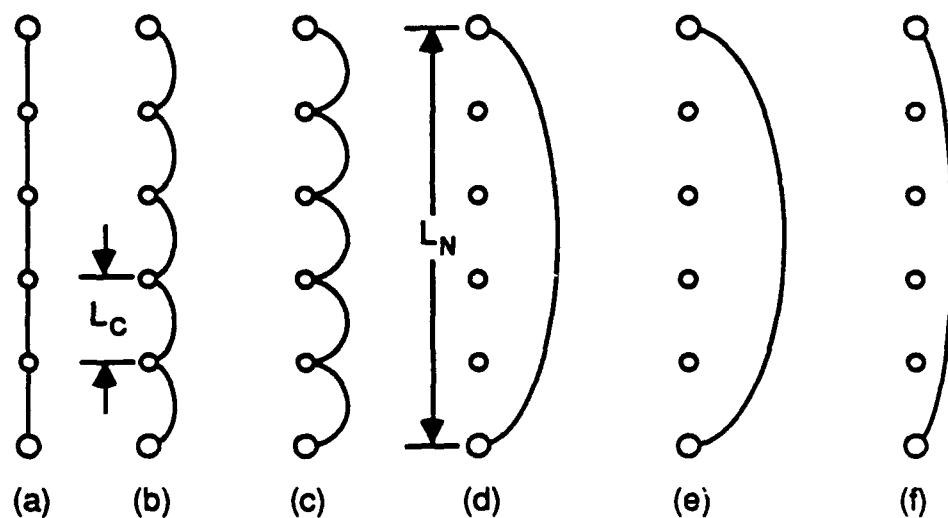
Figure 3.3.2-1 A Schematic Diagram of G-L Dislocation Damping Theory.
Dislocations with an Average Loop Length L_C Bow Out in Response to
Increasing Strain Amplitude (a,b,c). At a Critical Stress, Dislocations Break
Away From M̄ or Pinning Points, and Oscillate About its Network Length
L_N (d,e). With Decreasing Stress, Dislocations Collapse About Network
Length (f) until Repinning At Zero Stress (a) (after Granato-Lucke)

For a material subjected to a vibration in a uniform strain field exhibits a strain amplitude dependent, or hysteretic, contribution to the total damping (ψ_H) can be expressed as

$$\psi_H = \frac{C_1}{\epsilon} \cdot \exp\left[-\frac{C_2}{\epsilon}\right]$$ (3-3)

where C_1 and C_2 are constants in terms of material parameters:

$$C_1 \cong \frac{K\eta^* a}{L_C}$$ (3-4)

$$C_2 \cong \frac{2\Omega\Lambda L_N^3}{L_C \pi^2} \cdot \frac{K\eta^* a}{L_C}$$ (3-5)

where Ω and K are orientational constants, Λ is the mobile dislocation density, L_N is the dislocation network length, η^* is the Cottrell misfit parameter, a is the lattice spacing, and L_C is the average dislocation loop length. Therefore, if experimental data follow the strain amplitude dependence predicted by G-L theory, a plot of $\psi_H\epsilon$ vs. $1/\epsilon$ should be linear, the slope C_2 inversely proportional to L_c, which is a measure of pinning point density, and the intercept C_1 a measure of dislocation loop density Λ.

A G-L plot of data obtained by uniaxial tension-tension cycling is shown in Figure 3.3.2-2. By introducing appropriate material constants, the average dislocation loop length can be estimated as ≈ 212 Å (0.02 μm). This value of L_C is smaller than the average interfiber spacing (≈ 3.5 μm), indicating that impurities and fine second phase precipitates in the interfiber aluminum matrix region. Assuming the average network length of L_N ≈ 0.2 μm, the calculated mobile dislocation density is of the order 6 x 10^{13} 1/m^2. Experimental dislocation density values by quantitative image analysis of various transmission electron micrographs (Fig. 3.3.2-3) yielded 4 x 10^{14} 1/m^2. This dislocation density value is higher than the average dislocation density of unreinforced 6061 aluminum of 8 x 10^{12} 1/m^2. The increase in dislocation density has been attributed to the differential contraction of the matrix and fiber, and the attendant residual stress state at the interface originating during the fabrication process. Values of calculated mobile dislocation density are consistent with the measured total dislocation density, suggesting that energy dissipation by dislocation motion and breakaway is the operative mechanism in Gr/Al composites at intermediate strain amplitude levels.

3-9

Page 3-10 missing
not available

26 Jun 90

Unlike damping values from uniaxial tension-tension fatigue which is effectively the intrinsic measured damping, special consideration must be taken with strain amplitude dependent data from clamped-free flexure tests. Strain amplitude within a clamped-free flexure specimen varies from extension to compression across the thickness, and decreases from the clamped length along the specimen length. While this relationship is quite complex, the strain as a function of position $\varepsilon(x,z)$ can be approximated by the following relationship:

$$\varepsilon(x,z) = \frac{6qx^2z}{bh^3E} \tag{3-6}$$

where q is the load intensity, b is the specimen width, h is the specimen thickness, L is the specimen length, and E is the elastic modulus of the beam. Because only a small portion of the specimen experiences a strain amplitude as high as that measured at the surface by the strain gage, one would expect the intrinsic damping values to be higher than the measured damping. Using a treatment developed by Ritchie, et. al. [Ref 3-6], the intrinsic damping ψ^* in terms of the measured damping ys and strain amplitude es can be described by the following:

$$\psi^*(\varepsilon_s) = \psi_s + \frac{7}{9}\varepsilon\frac{d\psi_s}{d\varepsilon_s} + \frac{1}{9}\varepsilon^2\frac{d^2\psi_s}{d\varepsilon_s^2} \tag{3-8}$$

where the intrinsic damping depends upon the first and second derivative of the measured damping with respect to strain amplitude. By applying this relationship to the measured damping data presented earlier in Figure 3.3.2-1, one obtains the calculated intrinsic damping shown in Figure 3.3.2-4. As anticipated, the calculated intrinsic damping values are higher than the measured values with increased strain amplitude dependence. A Granato-Lucke plot of the calculated intrinsic damping is shown in Figure 3.3.2-5. The slope and intercept of this plot, and thus the dislocation loop length and density, agree well with those values obtained from the uniaxial tension-tension fatigue tests, thereby lending further support to energy dissipation from dislocation motion as the operative mechanism in strain amplitude dependent damping in Gr/Al composites.

3.4   SUMMARY

Reliable damping measurements of unidirectional single-ply P55Gr/6061Al composites were obtained by three different test techniques: free-free flexure, clamped-free flexure, and tension-tension fatigue. Both flexural and extensional mode tests were conducted at 1×10^{-6} — 800×10^{-6} strain levels within 0.1 Hz and 150 Hz frequency range.
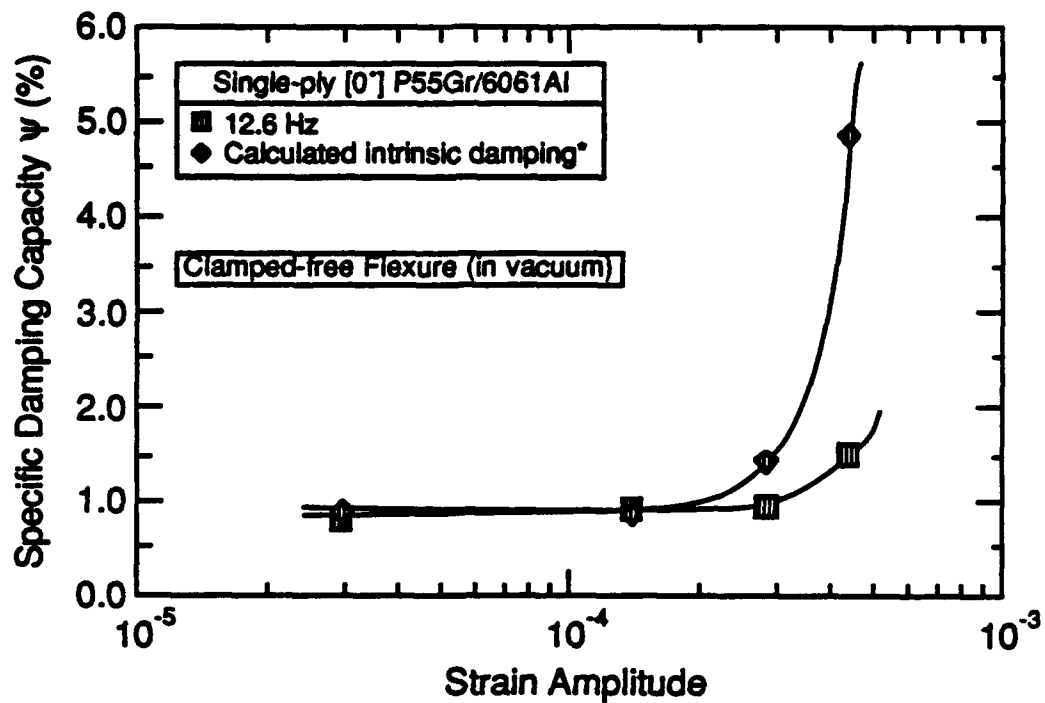
Figure 3.3.2-4 Calculated Intrinsic Damping Behavior of [0°] P55Gr/6061Al at 12.6 Hz as Measured by Clamped-Free Flexure in Vacuum
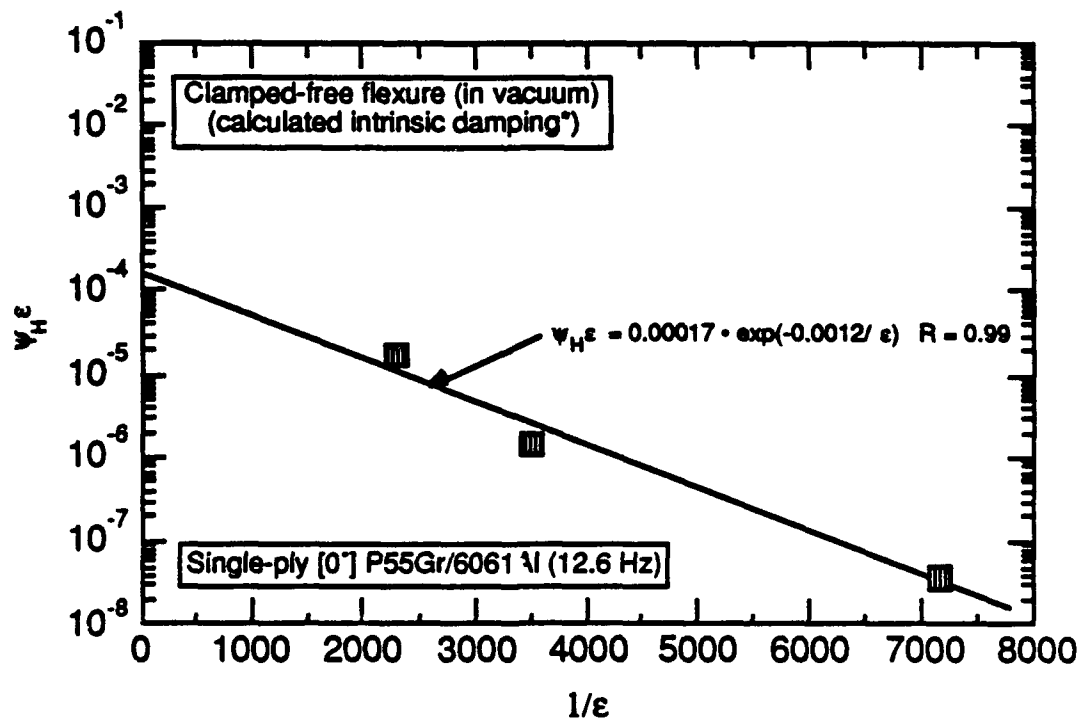
Figure 3.3.2-5 G-L Plot of the Calculated Intrinsic Damping Behavior Measured by Clamped-Free Flexure in Vacuum

Damping response of Gr/Al indicated that beyond a critical strain amplitude, damping increases with increasing strain amplitude. In the strain amplitude independent region, the measured damping capacity is consistent with the values predicted by the moduli-weighted rule of mixtures for damping (Hashin Theory). Extensional mode test data of Gr/Al were also analyzed in terms of the Granato-Lucke (G-L) model which is based on energy dissipation due to oscillatory dislocation motion. Strain amplitude dependence is also predicted by this model as a result of dislocation breakaway from minor pinning points. Mobile dislocation density predicted by G-L analysis ($\approx 10^{12}$ $1/m^2$) was also consistent with the measured average dislocation density (4×10^{14} $1/m^2$) obtained from various TEM images of the interfiber matrix regions. These dense dislocation networks have been attributed to differential contractions between the fiber and matrix, and the attendant residual stress state. Both test results and analyses indicate that damping characteristics of Gr/Al are influenced by contributions from fiber, matrix, residual stress state, and the associated dislocation substructure near the fiber-matrix interface.

3.5   REFERENCES

3-1   M.S. Misra, S.P. Rawal and J.H. Armstrong: "Damping Characteristics of Metal Matrix Composites," Final Report MCR-643, Office of Naval Research, 1986.

3-2   Z. Hashin: "Complex Moduli of Viscoelastic Composites - II Fiber Reinforced Materials," International Journal Solids and Structures, Vol. 6, No. 6, p. 797 (1970).

3-3   J. DiCarlo (personal communication)

3-4   A.V. Granato and K. Lucke: "Theory of Mechanical Damping Due to Dislocations," J. Appl. Phys., 27, 583 (1956a).

3-5   A.V. Granato and K. Lucke: Applications of Dislocation Theory to Internal Friction Phenomena at High Frequency," J. Appl. Phys., 27, 789 (1956b).

3-6   I. G. Ritchie and H.L. Rosinger: Dynamic Elastic Properties of Materials, Materials Research in AECL, AECL-4842, Summer 1974.

4.0 High-Damping Mg Alloys

CHAPTER 4.0
HIGH DAMPING MAGNESIUM ALLOYS

Specific damping capacity in magnesium alloys ranges from extremely low values ($\psi < 0.01\%$) to high ($\psi > 90\%$). Damping capacity in Mg alloys varies with composition and vibrating stress amplitude [Ref 4-1 — 4-8]. The increase of damping capacity with stress is qualitatively evident, but it is apparent that each alloy has individual characteristics in the stress sensitivity and magnitude of its damping capacity. These characteristics appear to be affected in complex ways by the composition, the microstructure, the metallurgical condition and other physical properties of the alloy.

Among metals, unalloyed magnesium in the cast condition exhibits the highest damping. It is also interesting to note that the damping capacity of cast magnesium is significantly higher than wrought magnesium. The reduced damping capacity in wrought magnesium alloys are attributed to fine grain structure and orientational dependence induced by rolling or extrusion processing methods.

Early research conducted at the Bureau of Mines Lab, U.S. Department of the Interior, Rolla MO, [Ref 4-1 — 4-4] has suggested that the damping in single crystals of magnesium is highest when the basal planes of the crystal are inclined at about 45 degrees to the direction of the vibration. This research also produced the evidence that the high damping capacity of pure magnesium is associated with the movement of dislocations in the slip systems that are parallel to the basal plane. The observations of the role of alloying elements and processing methods on the damping capacity are also consistent with the rationale that dislocation movements are the principal cause of damping in magnesium and its alloys.

4.1   DAMPING TEST DATA

Damping capacity data for sand-cast magnesium alloys are presented in Table 4.1-1. These results were obtained by torsion pendulum test method [Ref 4-3], and for the purpose of comparison, damping capacity values for cast magnesium and for a number of well-known commercial alloys such as cast irion, brass, and aluminum alloys are presented in Table 4.1-2.

These results show that unalloyed magnesium, and sand cast magnesium-manganese (Mg-1% Mn) and magnesium-zirconium (Mg-0.6% Zr) alloys show higher damping than other Mg alloys. Based on these results, it can be generalized that the magnesium base with moderate alloy content (3-9%)

had a lower damping capacity than did that containing a small amount (≤ 1%) of alloying elements. The decrease in damping capacity is associated with the solubility and the presence of a second phase. A magnesium alloy with silicon in equivalent weight percent than manganese or zirconium exhibits slightly lower damping. In Mg-Si alloy, typical microstructure consists of large grains of primary Mg surrounded by the eutectic mixture of Mg_2Si while zirconium and manganese have low solubility in molten magnesium at temperature just above the melting point of Mg. In Mg Zr alloy, the amount in solution increases slightly as solidification takes place through a peritectic reaction. Coring develops as the solid solution of Zr in Mg forms. In Mg-Mn alloys, small particles of elemental Mn generally precipitate in the grain and at the grain boundaries.

Table 4.1-1 Damping Capacity for Sand-Cast Magnesium Alloys

Alloy No.	Commercial Designation	Composition,[1] Percent	Rockwell Hardness	Yield Strength (0.2 pct offset), 1,000 psi	Tensile Strength, 1,000 psi	Specific Damping Capacity, Percent, At Stress Levels--					
						500 psi	1,000 psi	1,500 psi	2,000 psi	2,500 psi	3,500 psi
D17...	K1-F	0.6 Zr	19 E	6.8	22.0	49	61	65	67	69	72
D36...	K1X1-F	0.6 Zr	12 E	6.5	21.6	56	67	71	72	73	75
D21...	S1-F	0.7 Si	39 E	7.6	13.5	44	55	61	66	70	75
D39...	S1	1.4 Si	40 E	8.7	15.5	34	43	49	58	62	67
4060..	-	0.2 Si	49 H	-	10.3	51	63	(2)	-	-	-
D22...	M1-F	0.9 Mn	44 H	2.5	13.5	43	63	80	87	89	91
D38...	M1	1.4 Mn	51 H	-	10.8	46	85	(3)	-	-	-
D40...	AM100A-F	9.8 Al, 0.2 Mn	74 H	17.2	21.0	.044	.099	1.5	8.0	16	34
4059..	-	8.6 Li, 0.5 Si	30 E	-	-	1.9	2.3	2.9	4.6	7.9	16

1 - Nominal
2 - Modulus too low for sensitivity of test
3 - Severe plastic flow

Table 4.1-2 Comparison of the Damping Capacity of Conventional Magnesium Alloys

Alloy No.	Commercial Designation	Composition,[1] Percent	Hardness[2]	Yield Strength (0.2 pct offset), 1,000 psi	Tensile Strength, 1,000 psi	Specific Damping Capacity, Percent, At Stress Levels--					
						500 psi	1,000 psi	1,500 psi	2,000 psi	2,500 psi	3,500 psi
1...	Cast Mg	99.9+ Mg	30 R_H	3.0	10.0	73	89	(3)	-	-	-
2...	Aluminum 2S-F	99.+ Al	38 Bhn	17.0	20.0	-	.22	0.28	-	0.46	0.68
3...	Al Alloy 11S-T3	5.5 Cu, 0.5 Pb, 0.5 Bi	95 Bhn	47.0	53.0	-	.08	.10	-	.15	.19
4...	Al Alloy 17S-T4	4 Cu, 0.5 Mg, 0.5 Mn	105 Bhn	40.0	62.0	-	.022	.022	-	.022	.023
5...	Al Alloy 24kS-T4	4.5 Cu, 1.5 Mg, 0.6 Mn	120 Bhn	46.0	68.0	-	.025	.026	-	.027	.029
6...	Free-Cutting Brass, 1/2H	62 Cu, 35 Zn, 3 Pb	75 R_B	44.0	55.0	-	.14	.18	-	.28	.42
7...	Naval Brass, 1/4 H	60 Cu, 39 Zn, 1 Sn	78 R_B	46.0	69.0	-	.015	.015	-	.016	.017
8...	Gray Cast Iron	3.5 C, 0.3 P, 2 Si, 0.5 Mn	205 Bhn	-	36.0	-	4.1	5.3	-	7.5	9.3

1 - Nominal
2 - R_H, Rockwell H scale; Bhn, Brinell hardness number; R_B, Rockwell B scale
3 - Severe plastic flow

Table 4.1-3 lists the damping capacity of a few heat treated cast magnesium alloys. Again, the Mg-0.6% Zr exhibits higher damping than the alloys with relatively high alloy content. Damping capacity of wrought and cast Mg alloys is compared in Figure 4.1-1, which show that wrought and cast Mg alloys with high alloy content exhibit the lowest damping and cast pure Mg and Mg-0.6% Zr alloy exhibit the highest damping [Ref 4-2].

Table 4.1-3 Damping Capacity of Heat Treated Cast Magnesium Alloys

Alloy No.	Commercial Designation	Comp. ..n,[1] Percent	Hardness	Yield Strength (0.2 pct offset), 1,000 psi	Tensile Strength, 1,000 psi	Specific Damping Capacity, Percent, At Stress Levels--					
						500 psi	1,000 psi	1,500 psi	2,000 psi	2,500 psi	3,500 psi
D9...	AZ91C-T4	9 Al, 1 Zn, 0.4 Mn	66E	13,4	32.0	-	0.017	0.14	0.55	1.8	11
D10...	AZ91C-T6	9 Al, 1 Zn, 0.4 Mn	76E	17.0	32.0	0.042	.058	.12	.50	1.9	9.3
D11...	AZ81XA-T4	8 Al, 1 Zn, 0.2 Mn	63E	13.3	35.5	.003	.008	.025	.18	1.8	10
D12...	EK1A-T5	4 Ce, 0.7 Zr	66E	17.2	20.0	1.0	1.6	2.1	2.7	3.4	5.4
D13...	EK1A-T6	4 Ce, 0.7 Zr	68E	18.6	22.6	.34	.51	.71	.94	1.2	1.8
D14...	EZ33A-T5	3 Ce, 3 Zn, 0.7 Zr	66E	15.3	19.0	.26	1.6	4.4	7.9	12	19
D15...	HK31A-T6	3 Th, 0.7 Zr	67E	16.0	28.0	.28	.37	.48	.62	.83	1.4
D16...	ZH62XA-T5	6 Zn, 2 Th	80E	25.0	32.8	.11	.12	.13	.14	.14	.17
D18...	EK30A-T6	3 Ce, 0.4 Zr	59E	14.5	18.4	.88	1.2	1.6	3.2	3.2	6.9
D19...	AZ92A-16	9 Al, 2 Zn, 0.2 Mn	83E	18.8	29.0	.006	.028	.11	1.2	1.2	6.6
D20...	HZ32XA-T5	3 Th, 2 Zn, 0.7 Zr	66E	15.7	25.0	.45	1.9	4.4	11	11	17
D37...	K1X1-T4	0.6 Zr	5E (56H)	6.9	22.5	53	67	72	73	73	74

1 - Nominal

High damping capacity in cast pure Mg and Mg-Zr and Mg-Mn alloys is also associated with large grain size microstructure. Therefore, any heat treatment (e.g., 800°F for 1 hr) to enhance the grain size (Fig. 4.1-2) of sand-cast Mg-Mn and Mg-Zr alloys results in improved damping (Fig. 4.1-3). Measurement of flexural damping response of pure Mg single crystals by Sugimoto et al [Ref 4-6] also indicated their strain amplitude-dependent damping response. It was found that if only the basal slip system is operative, then Schmid's law holds for the orientation dependence of the break-away stress (σ_B) given from the damping versus stress amplitude curves. This suggests that the amplitude dependent damping is caused by the movement of basal dislocations. Further analysis of their data in terms of Granato-Lucke theory also indicated that the amplitude dependence is caused by the static hysteresis due to the interaction of basal dislocations with impurity atoms. Similar experiments using polycrystalline Mg showed that damping response was extremely sensitive to the crystallographic orientation of individual grains. Also, in a specimen of Mg with equiaxed grain, σ_B value was very small and therefore it displayed a large amplitude dependence of damping. These results suggested that Mg alloys with large equiaxed grain size (> 20 μm) and low alloying element (< 1%) exhibited high damping. If these high damping alloys could be incorporated as a matrix with

Gr fibers, then a high damping Gr/Mg composite could be designed. In contrast, Mg specimens with columnar grains whose longitudinal direction was almost parallel to the specimen axis had a much larger value of σ_B and displayed a very little amplitude dependence of damping.
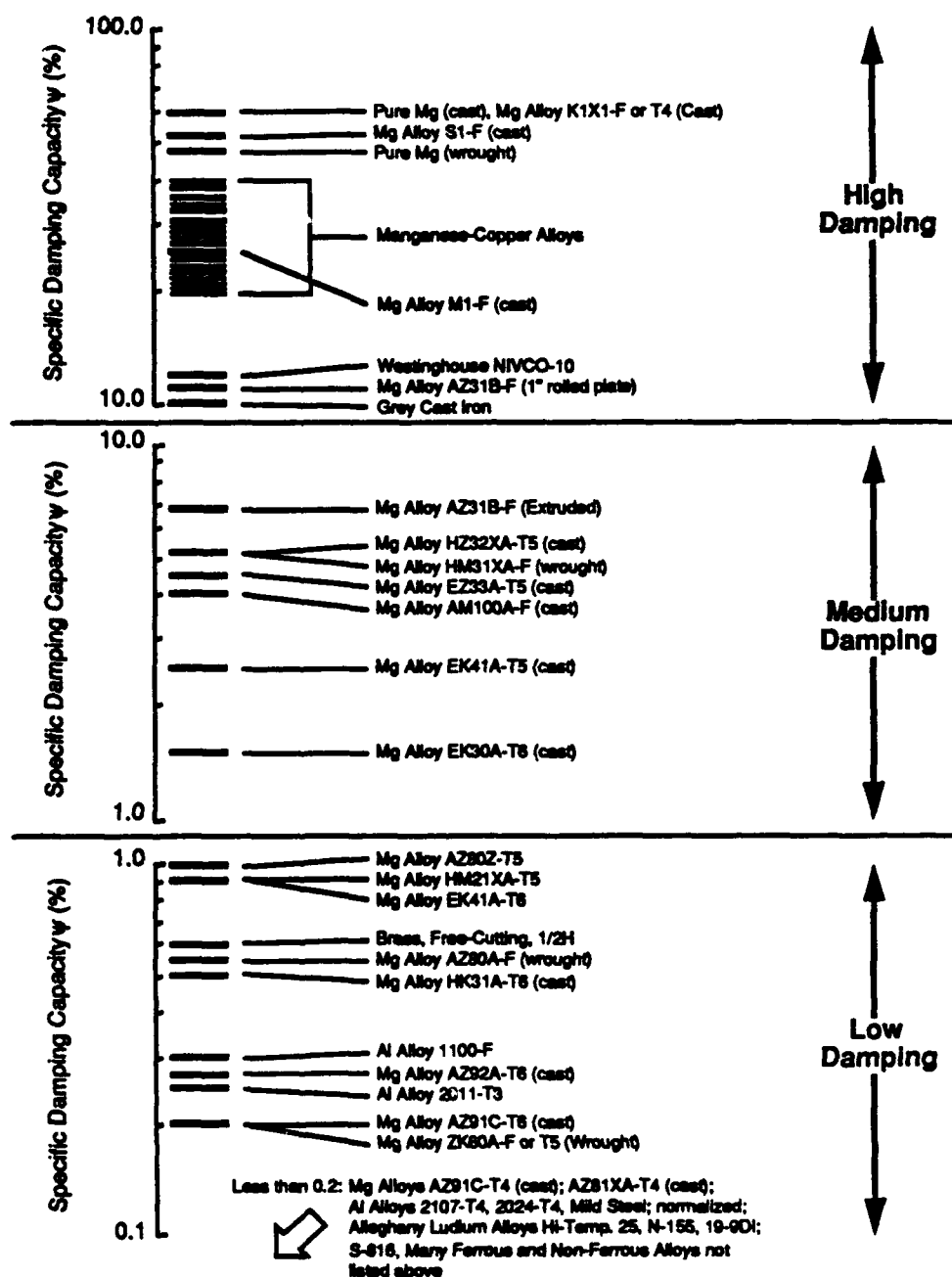
Figure 4.1-1 Comparison of Wrought and Cast Magnesium Alloys [Ref 4-2]
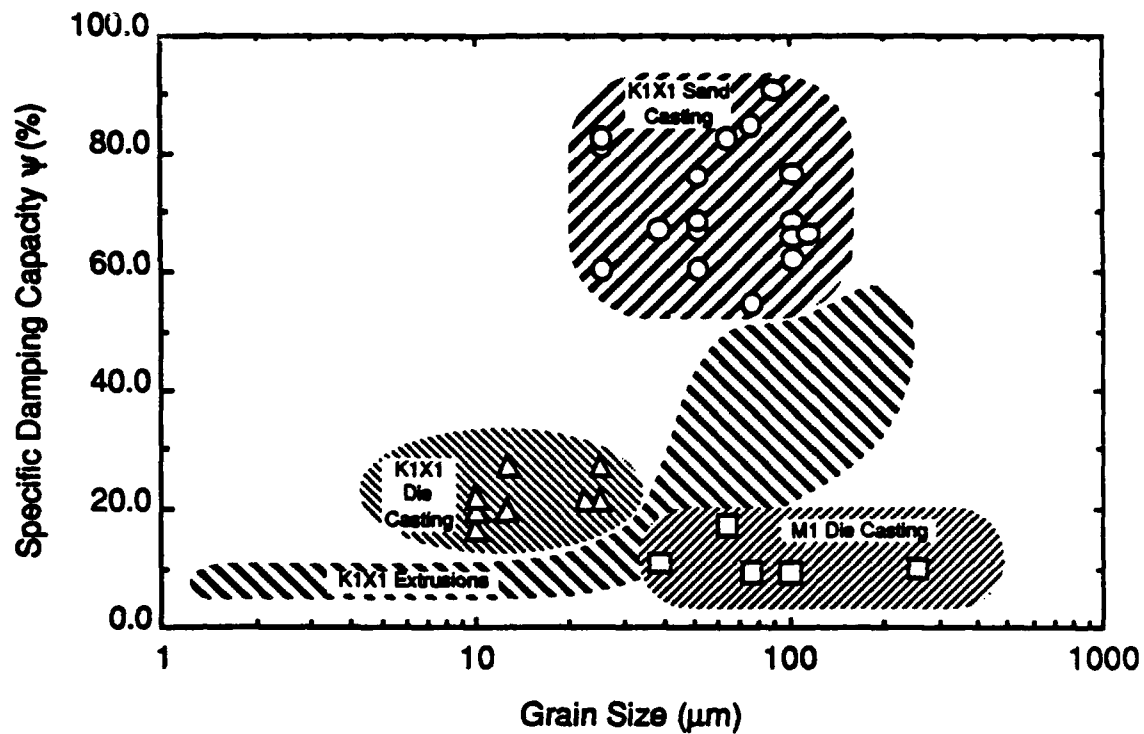
Figure 4.1-2 Effect of Grain Size on Damping Capacity of Mg-Zr (K1A) Alloys [Ref 4-3]
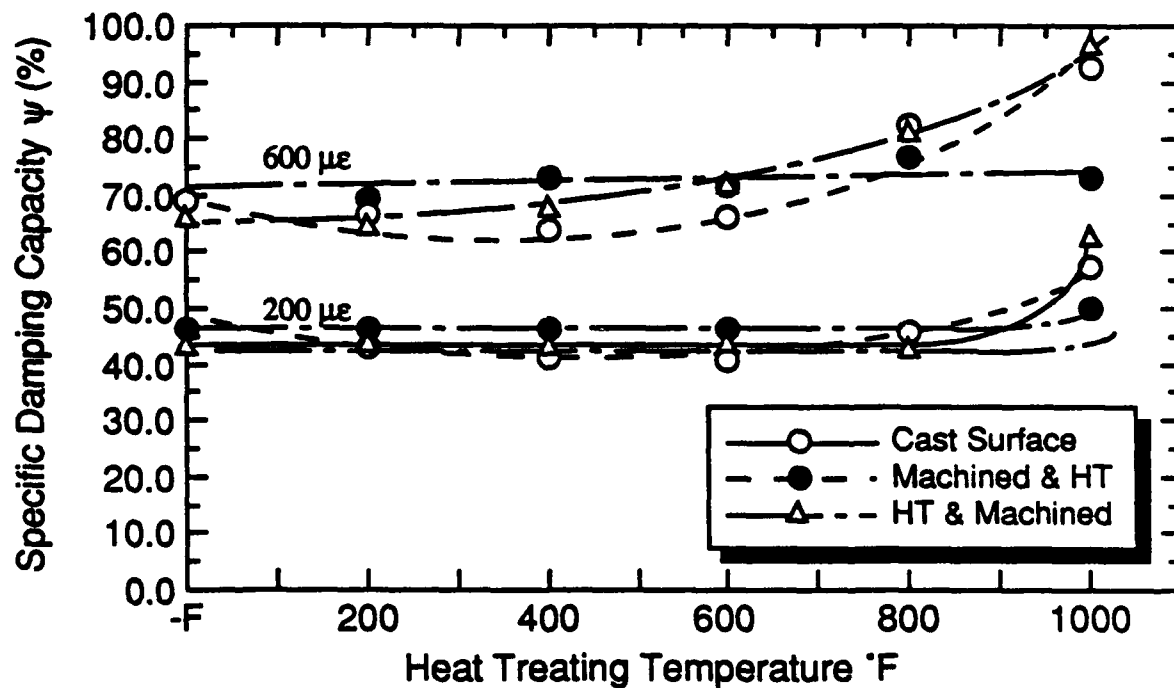
Figure 4.1-3 Damping Capacity of Sand Cast Mg-Zr (K1A) as a Function of Heat Treatment at Two Representative Strain Levels [Ref 4-3]

4.2 SUMMARY

Based on the damping data of Mg alloys in the literature, Mg-1.6% Zr, and Mg-1% Mn were selected as a high damping matrix for the composite. The damping capacity of these alloys varies between 30% - 80% at different strain levels and frequencies. It was recognized that their high damping was associated with a large equiaxed grain size ($\geq$ 20 µm) microstructure obtained by a casting process. If such a matrix microstructure could be retained in the cast composite, then the damping contribution from matrix will result in a high damping Gr/Mg composite.

4.3 REFERENCES

4-1 J.W. Jensen: "Damping Capacity - Its Measurement and Significance," Bureau of Mines Rept. of Inv. 5441, 1959, p 46.

4-2 D.F.Walsh, J.W. Jensen, and J.A. Rowland: "Vibration Damping Capacity of Magnesium Alloys", Proc. 14th Annual Convention, the Magnesium Association, Oct 1958, Pick Fort Shelby Hotel, Detroit.

4-3 D.F. Walsh, J.W. Jensen, and J.A. Rowland: "Vibration Damping Capacity of Various Magnesium Alloys," Bureau of Mines Rept. of Inv. 6116, 1962.

4-4 R.R. Nothdurft: "A Study of the Effect of the Crystal Orientation on the Internal Friction of Magnesium Single Crystals," Theses, University of Missouri, Rolla, MO, 1964, p 58.

4-5 J.W. Fredrickson: "Damping Capacity of K1A," Dow Chemical Company, Midland, Michigan, Report No. MT 17753-Final, Dec. 5, 1958.

4-6 K. Sugimoto, and K. Niiya: "A Study of Damping Capacity in Magnesium Alloys," Trans JIM Vol. 18, pp 277-288, 1977.

4-7 E.G. Hennecke and R.E. Green, Jr.: "Orientation Dependence of Dislocation Damping in Hexagonal Metals, Journal of Applied Physics, Vol. 40, No. 0, pp 3632-3641, August 1969.

4-8 K. Sugimoto, K. Matsui, Taira Okamoto, and K. Kishitake: "Effect of Crystal Orientation on Amplitude Dependent Damping in Magnesium," Trans JIM, Vol. 16, pp 647-655, 1975.

5.0 Damping of Gr/Mg Composites

CHAPTER 5.0
DAMPING CHARACTERISTICS OF Gr/Mg COMPOSITES

Fiber, matrix, and interfaces in metal matrix composites all influence the damping behavior of composites. From the fabrication point of view, any modifications in fiber and interfaces are somewhat limited, while an appropriate matrix alloy could be selected to enhance the composite damping. Among the magnesium alloys, Mg-0.6%Zr (K1A) and Mg-1.0%Mn (M1A) alloy exhibit high damping. These alloys exhibit high damping when in the cast condition where grain size is sufficiently large (> 20 μm) and elemental precipitates are fine and uniformly dispersed. If these microstructural conditions could be retained during composite fabrication, then it would yield a high damping Gr/Mg composite.

In the following sections, the fabrication of potentially high damping Gr/Mg composites are discussed. Damping behavior of these Gr/Mg composites measured as a function of temperature and strain amplitude are presented and analyzed. In addition, the methodology of increasing the damping capacity by microstructural modification using appropriate heat treatments are also discussed.

5.1   SPECIMEN FABRICATION AND CHARACTERIZATION

Using a vacuum investment casting technique unidirectional $[0]_8$ P55/K1A-Mg and P55/MIA [Ref 5-3] composite panels were fabricated by FMI, Inc. As cast flat panels were fragile and quite rough (Fig. 5.1-1), thereby required special handling. Panels were carefully hand-sanded to approximately 0.080 inch thickness to ensure good, even surfaces (Figs. 5.1-2). After sanding, areas of excessive relief were identified and avoided during specimen layout. Further selection of the panel sections chosen for specimen fabrication involved avoiding the few cracks and voids detected by x–radiography. After a layout was transferred to the panels, the specimens were cut out using a diamond wheel, and ends were hand-sanded to remove any burrs resulting from the cutting. Micrographs of Gr/K1A and Gr/M1A, shown in Figures 5.1-3 and 5.1-4 respectively, indicate good matrix infiltration and small grain size. Mechanical properties and fiber volumesfor the two materials were conducted prior to damping tests (Table 5.1-1).

A P55Gr/Mg - 1% Zr (FRONT) PANEL A: CAST **B** P55Gr/Mg - 1% Mn CAST: SPECIMENS 1 & 2
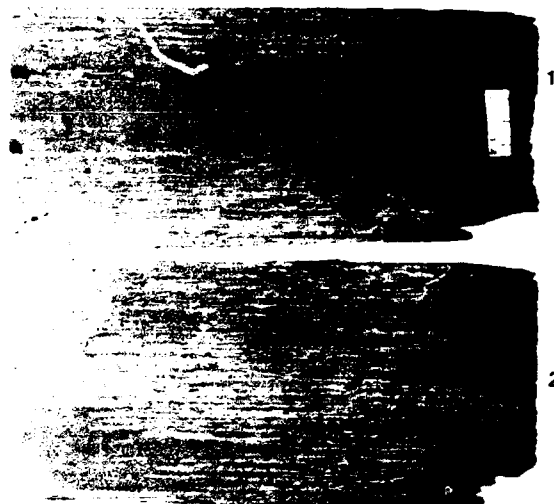
Figure 5.1-1 Photograph of Gr/K1A and Gr/M1A Panels in As-Fabricated Condition.
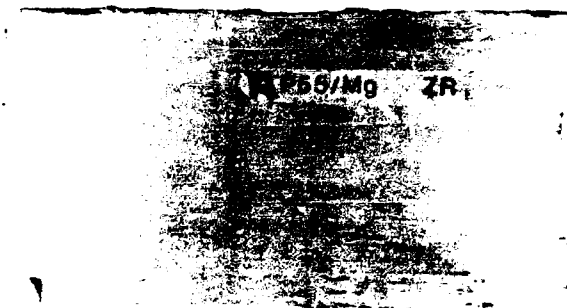
A CAST P55Gr/Mg-1%Zr PANEL A **B** CAST P55Gr/Mg-1%Zr PANEL A
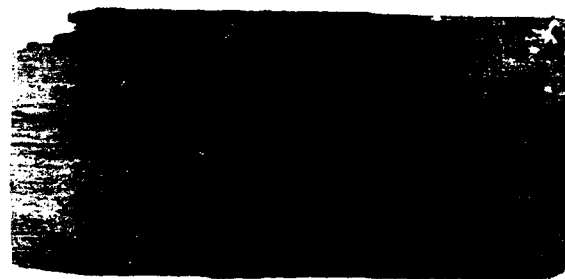
Figure 5.1-2 Photograph of Gr/K1A and Gr/M1A Panels After Hand Sanding.
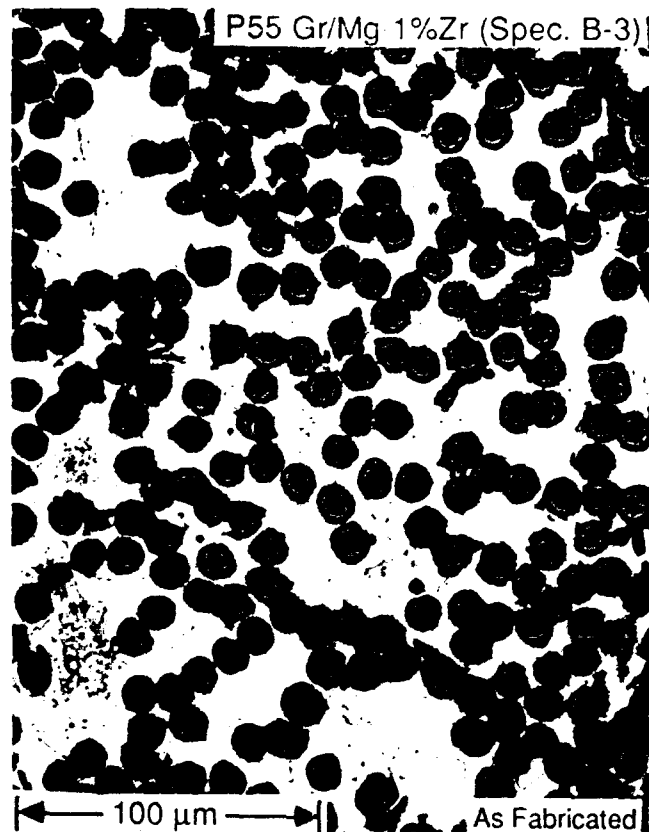
*Figure 5.1-3 Photomicrograph of Cast P55Gr/Mg-0.6%Zr (Gr/K1A) Indicating Good
Matrix Infiltration and Small Grain Size*
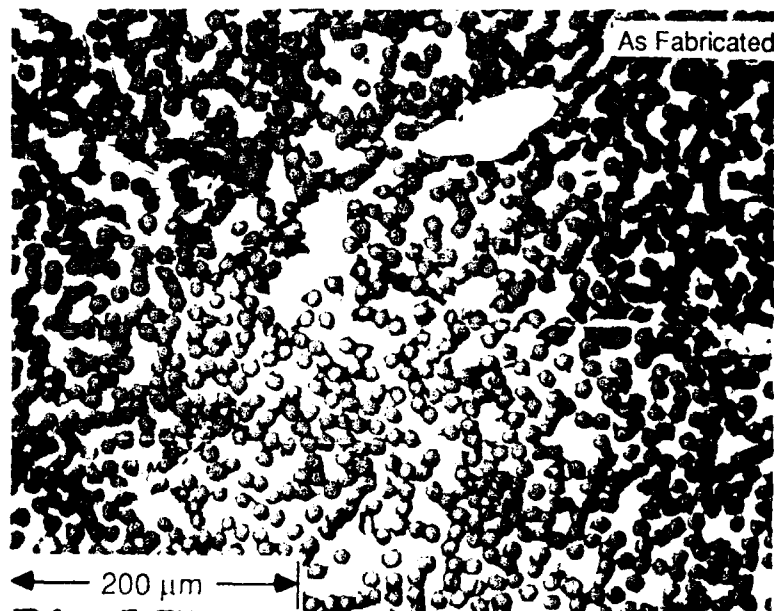
*Figure 5.1-4 Photomicrograph of Cast P55Gr/Mg-1.0%Mn (Gr/M1A) Indicating
Good Matrix Infiltration and Small Grain Size*

5-3

Table 5.1-1 Mechanical and Material Properties of Gr/M1A and Gr/K1A

Material	Density g/cm³ (lb/in³)	v/o %	Modulus GPa (msi)
[0°] P55Gr/Mg-0.6%Zr [0°] P55Gr/Mg-1%Mn	1.91 (0.0690) 1.89 (0.0683)	46.8 46.1	164.8 (23.9) 166.2 (24.1)
Mg-1%Zr Mg-1%Mn	1.74 (0.0629) 1.74 (0.0629)	— —	44.9 (6.51) 44.2 (6.41)

5.2   RESULTS

To characterize the damping of these composites fully, different test techniques were employed to measure damping over a wide range of frequencies, strain amplitudes, and vibration modes. Damping was measured in flexural, extensional, and torsional modes by the following techniques: 1) clamped-free flexure, 2) piezoelectric composite oscillator, and 3) torsional pendulum.

The damping response of each composite was determined as a function of strain amplitude and temperature. Strain amplitude dependence was measured in flexural (low-frequency clamped-free flexure) and extensional (resonant piezoelectric composite oscillator) modes of vibration at room temperature. Temperature dependence of these materials was determined using flexural (intermediate-frequency clamped-free flexure) and torsional (low frequency torsional pendulum) modes of vibration at very low strain amplitudes to remove any possible strain amplitude dependence.

5.2.1   Strain Amplitude-Dependent Damping of Gr/K1A and Gr/M1A Composites

Strain amplitude dependence of Gr/K1A and Gr/M1A composites were studied at low and high frequencies (1 Hz — 150 Hz and 80 kHz) and throughout a wide range of vibratory strain amplitudes (10⁻⁹ — 10⁻⁴) in both flexural and extensional modes. Both clamped-free and free-free flexure were used to measure damping in the flexural mode of vibration, while subresonant uniaxial tension-tension cycling and resonant piezoelectric composite oscillator were used for extensional mode. All strain amplitude dependent testing were conducted at room temperature, with flexural tests being conducted in vacuum to eliminate parasitic energy losses due to aerodynamic drag.

5-4

5.2.1.1 Flexural Damping Measurements of Gr/K1A and Gr/M1A Composites — Flexural

damping measurements as a function of strain amplitude were made by low-frequency clamped-free equipment described elsewhere [Refs 5-1 and 5-2]. Clamped-free flexure tests were conducted using both manual displacement and noncontact approaches.

These series of tests were conducted in vacuum utilizing either the noncontact apparatus at Texas A&M or the manual displacement equipment at Martin Marietta. Strain amplitude ranges for these tests were limited to no greater than 2×10^{-4} to minimize the possibility of damage during the free vibratory decay. Frequencies ranged from 10 Hz to 100 Hz, depending upon the length of the specimen available.

A comparison of damping of as-cast P55Gr/K1A and Gr/Al as a function of strain amplitude is shown in Figure 5.2.1.1-1. In every case, the damping response of Gr/K1A displays a higher overall damping, and more pronounced strain amplitude dependence, than the Gr/Al specimens although there is insufficient information regarding the strain amplitude independent region. Maximum damping values for the Gr/K1A system with this apparatus were nearly double of those for Gr/Al. A similar comparison of P55Gr/M1A and Gr/Al is shown in Figure 5.2.1.1-2. Once again , damping values for Gr/M1A were much greater than those of Gr/Al, and also a greater strain amplitude dependent damping region. In this case, the strain amplitude dependence of Gr/M1A was not as great as that observed for the Gr/K1A specimens.

Typical damping response of as-cast M1A specimens at $f = 109$ Hz using the clamped-free flexure apparatus at higher strain amplitudes is shown in Figure 5.2.1.1-3. This alloy shows significantly high strain amplitude independent damping ($\psi \approx 9.5\%$) and strong strain amplitude dependence. Damping reached a value of $\psi = 16.9\%$ at $\varepsilon \approx 1.35 \times 10^{-4}$. These values were far below those found in the literature, but significantly above those observed for the aluminum system. A comparison of damping values for Gr/K1A and Gr/M1A are shown in Figure 5.2.1.1-4. Damping values from Gr/M1A at the lower range of strain amplitude (2.0% @ 4.0×10^{-5}) agrees well with values shown earlier with the noncontact CFF apparatus at its highest strain amplitude range (2.25% @ 2.5×10^{-5}). Similar comparison of the Gr/K1A data did not fare as well (3.8% @ 1.3×10^{-5} compared to 1.8% @ 2.5×10^{-5}). This discrepancy may be the result of damage near the root of the mechanical CFF specimen or inhomogeneity in the microstructure. As illustrated in Figure 5.2.1.1-5, a specimen which exhibited extremely high damping and a strong strain amplitude dependence was found to be the result of a crack parallel to the fibers which may have contributed to frictional damping effects.
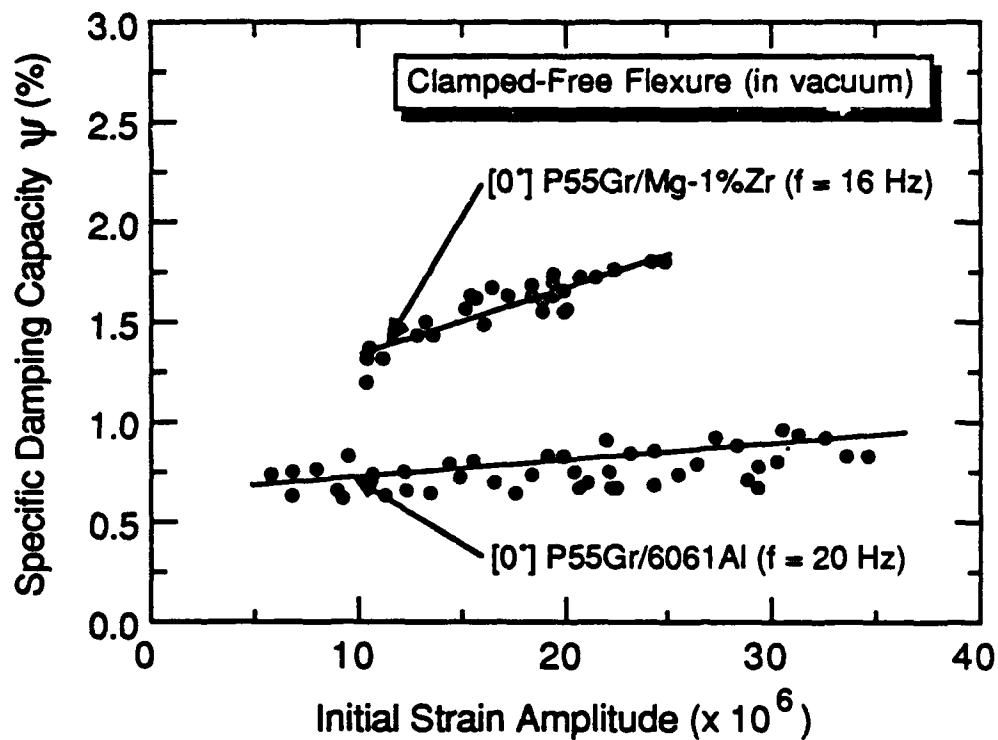
Figure 5.1.1.1-1 Comparison of the Damping Capacity of Gr/K1A and Gr/Al as a Function of Strain Amplitude (Clamped-Free Flexure in Vacuum)
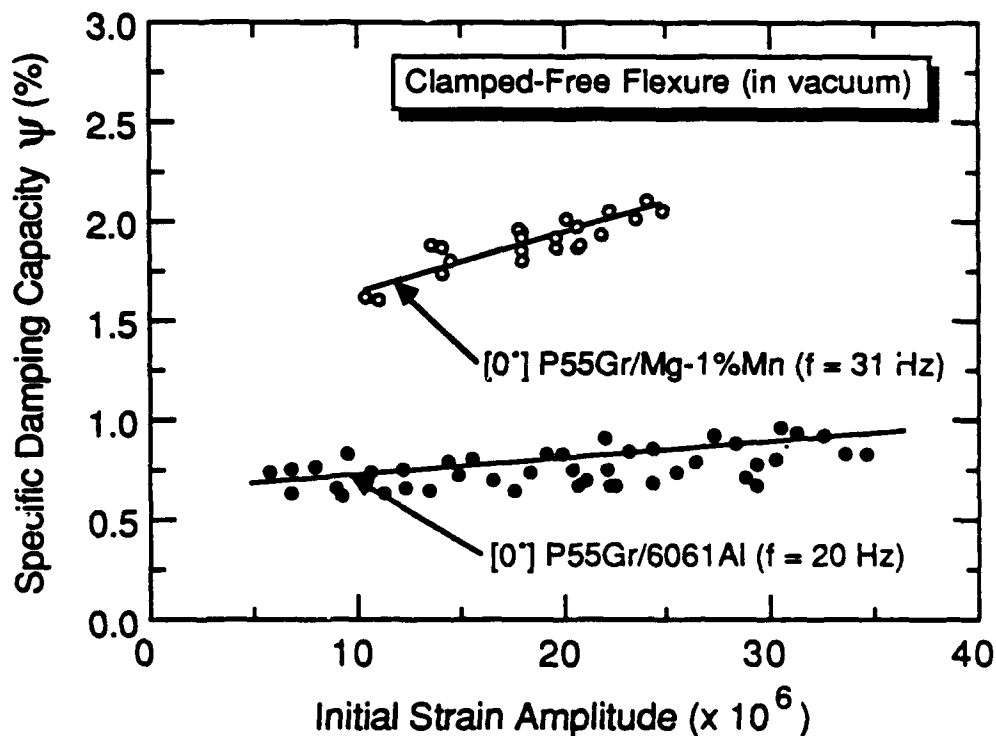
Figure 5.2.1.1-2 Comparison of the Damping Capacity of Gr/M1A and Gr/Al as a Function of Strain Amplitude (Clamped-Free Flexure in Vacuum)
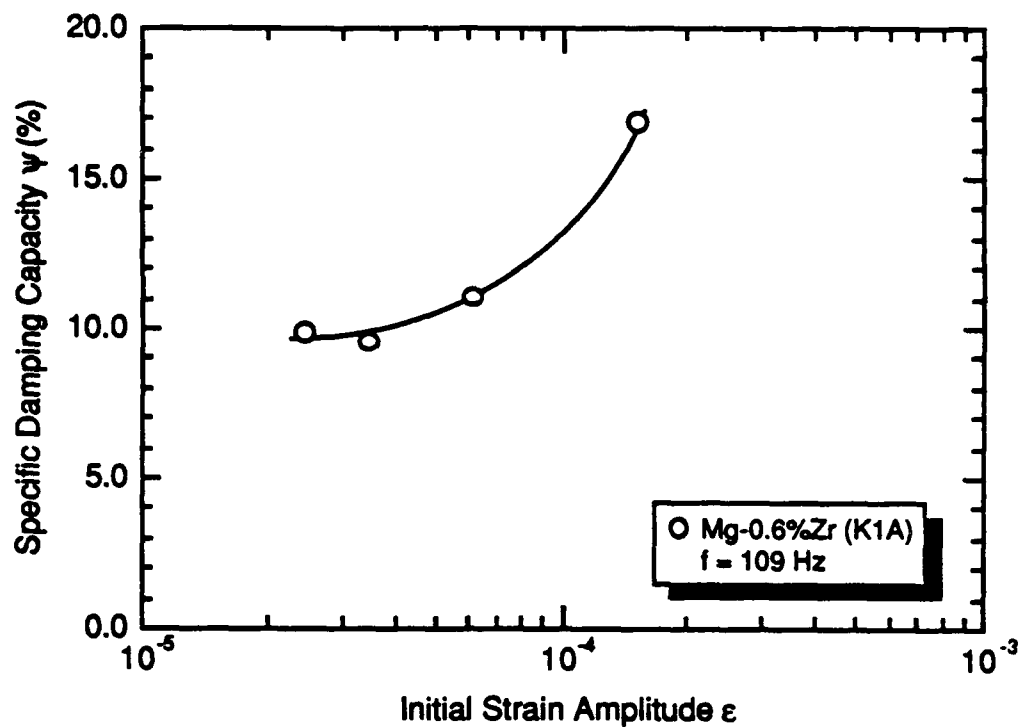
Figure 5.2.1.1-3 Damping Behavior of As-Cast Mg-0.6%Zr (K1A) as a Function of Strain Amplitude (Clamped-Free Flexure in Vacuum)
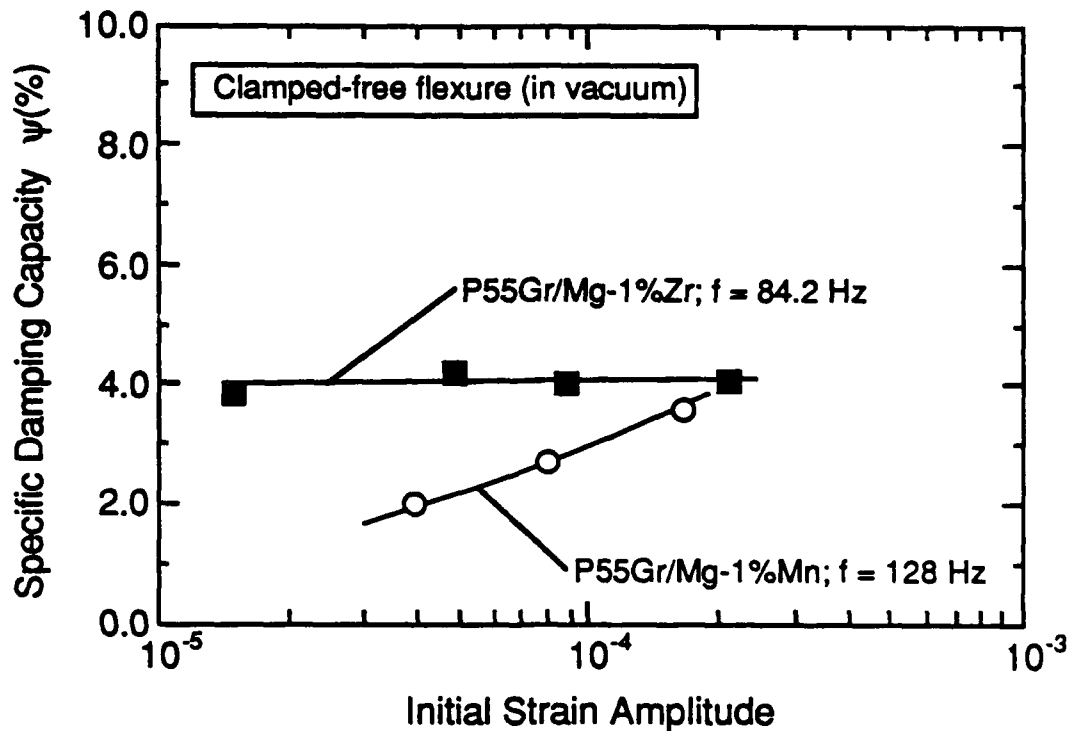
Figure 5.2.1.1-4 Comparison of Damping in Gr/K1A and Gr/M1A as Measured by the Mechanical Displacement Clamped-Free Flexure Apparatus (in Vacuum)
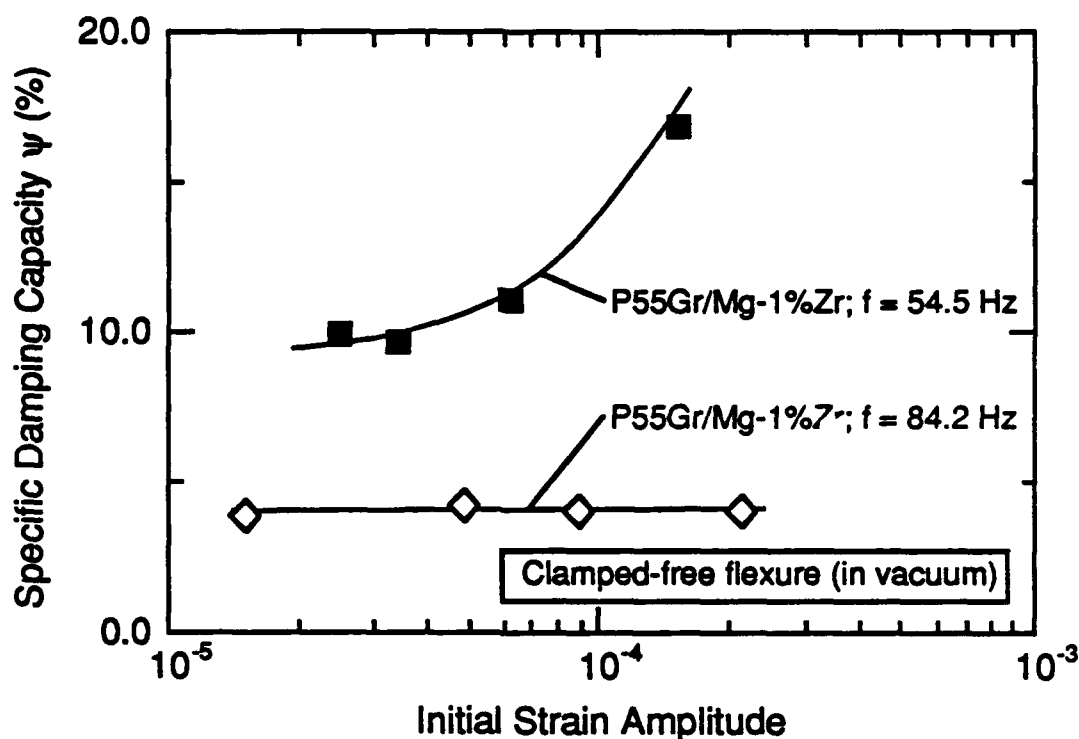
**Figure 5.2.1.1-5 High Damping in a Gr/K1A Specimen Indicating Damage
(Mechanical Displacement Clamped-Free Flexure Apparatus in Vacuum)**

5.2.1.2   Extensional Damping Measurements of Gr/K1A and Gr/M1A Composites — Damping measurements of Gr/K1A and Gr/M1A were made in extensional vibratory mode utilizing the resonant piezoelectric composite oscillator. A series of tests were conducted with the piezoele· ic composite oscillator for both the matrix alloy and the Gr/K1A and Gr/M1A composite specimens. For these tests, specimen width was typically 3.18 — 6.35 mm (0.125 — 0.250 in.) and the length carefully hand-polished to within 0.1% of $\lambda/2$ where λ is the wavelength of sound in the material, or 2.54 — 5.08 cm (1.0 — 2.0 in.), depending upon whether the specimen was the unreinforced alloy or a composite. Specimens of Mg-0.6%K1A with sufficient integrity were not available for testing.

As shown in Figure 5.2.1.2-1, the damping of M1A exhibited very low values in strain amplitude independent damping ($\psi \approx 0.8\%$), whereas the strain amplitude dependent damping was very pronounced. An interesting phenomenon was observed in the strain amplitude dependent damping, where a damping peak of $\psi \approx 7.8\%$ occurred at $\varepsilon_p \approx 3.9 \times 10^{-5}$. This type of behavior was not observed in any other previous test. Similar behavior was noted for both the as-cast Gr/K1A and Gr/M1A specimens (Fig. 5.2.1.2-2). Both systems exhibited strain amplitude independent and dependent damping, and both displayed the characteristic peak in strain amplitude dependence at ε_p

$\approx 3.1 \times 10^{-5}$ and $\varepsilon_p \approx 4.9 \times 10^{-5}$ for Gr/K1A and Gr/M1A respectively. Peak values, however, were much lower than that observed with the unreinforced material ($\psi \approx 3.4\%$ and $\psi \approx 3.8\%$ for Gr/K1A and Gr/M1A respectively).
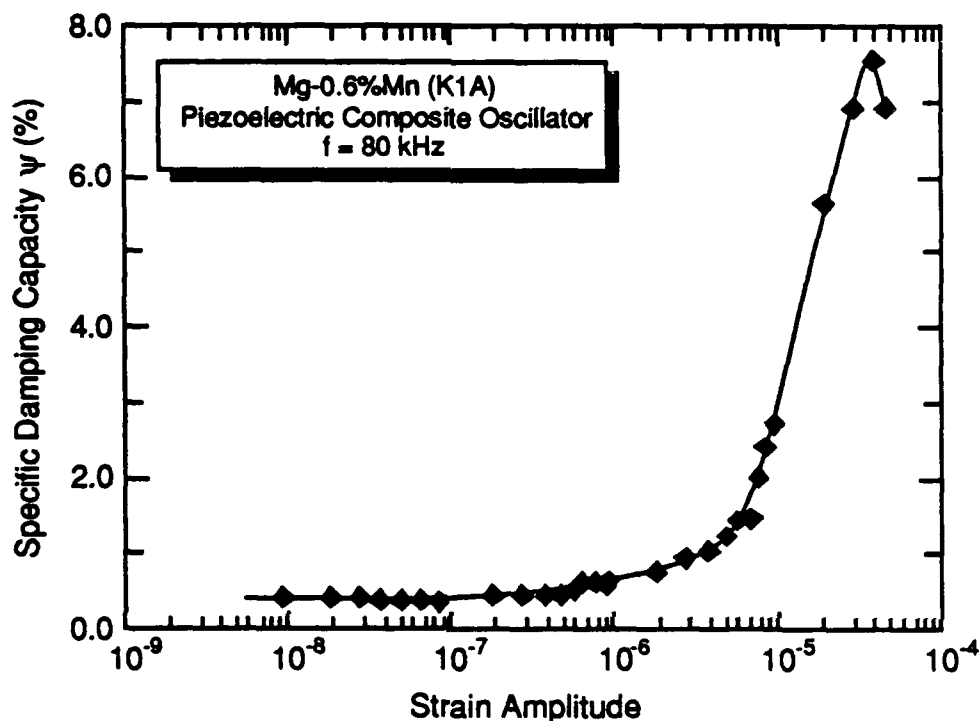
Figure 5.2.1.2-1 Damping Behavior of As-Cast Mg-0.6%Zr (K1A) as a Function of Strain Amplitude (Piezoelectric Composite Oscillator @ 80 kHz)

5.2.2   Temperature-Dependent Damping of Gr/K1A and Gr/M1A Composites

Temperature dependence of Gr/K1A and Gr/M1A composites as studied at low (< 1 Hz) and intermediate (≈ 2 kHz) frequencies. Above room temperature tests was possible with the torsional pendulum, while temperatures below and above room temperature were possible with the clamped-free flexure apparatus.

5.2.2.1   Torsional Damping Measurements — Damping measurements were made with the torsional damping apparatus at the University of Denver. This apparatus has been generally used for measurements of damping in wire geometry specimens as a function of temperature at strain ampli-

tude, levels less than 10-6. Gr/Mg precursor wire specimens for these tests were prepared by dipping air-stable coated pitch 55 fiber tows (2000 count) in molten Mg alloy. After fabrication and prior to testing, these wires were carefully hand-sanded to remove any extraneous matrix material from the surface.
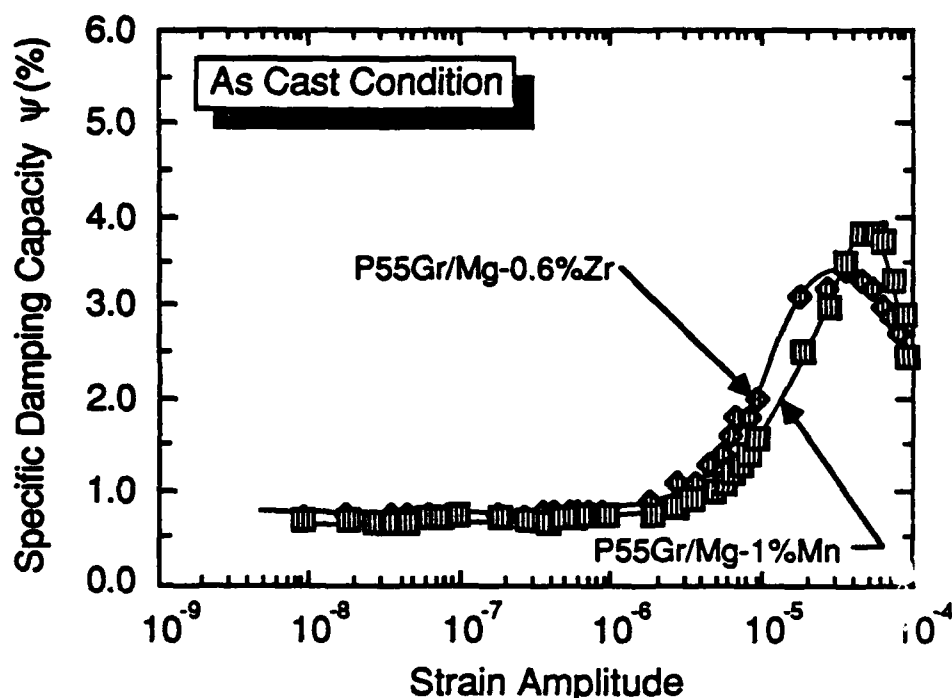
Figure 5.2.1.2-2 *Damping Behavior of As-Cast P55Gr/Mg-0.6%Zr (Gr/K1A) and P55Gr/Mg-1.0%Mn (Gr/M1A) as a Function of Strain Amplitude (Piezoelectric Composite Oscillator @ 80 kHz)*

As shown in Figure 5.2.2.1-1, two Gr/M1A specimen exhibited similar temperature dependence with a peak at about 441 K (335°F) of $\psi \approx 19\%$ for specimen #1, and 16.2%. However, specimen #2 showed a greater temperature-independent damping level of $\psi \approx 13$-15% after the peak, whereas specimen #1 exhibited nearly temperature-dependent behavior throughout the test. A local minima at $\psi \approx 8.5\%$ was observed in specimen #1, but no corresponding minima was recorded for specimen #2. Both specimens were cut from the same panel, but local differences in matrix infiltration could have caused this difference in damping behavior and also the overall high damping levels.

Thermal dependence of the damping of P55Gr/0.6%Zr (Gr/K1A) was also studied (Fig. 5.2.2.1-2) and this material exhibited quite different behavior than noted above. First, only a slight increase in

damping was observed in the Gr/K1A system compared to a distinct peak noted in the Gr/M1A material. Due to the lack of significant temperature dependence, the specimen was taken to much higher temperatures than reported above, but the maximum temperature of ≈ 547 K (525°F) was set to minimize the possibility of microstructural changes affecting the damping. A substantial temperature dependence was noted above 511 K (460°F) where the temperature continued to increase rapidly with increasing temperature, reaching a maximum value of ψ ≈ 19.6% at 547 K (525°F). Again, as was the case with Gr/M1A, the Gr/K1A specimen exhibited a local minima in damping of about ψ ≈ 5.3% occurring at 497 K (435°F).
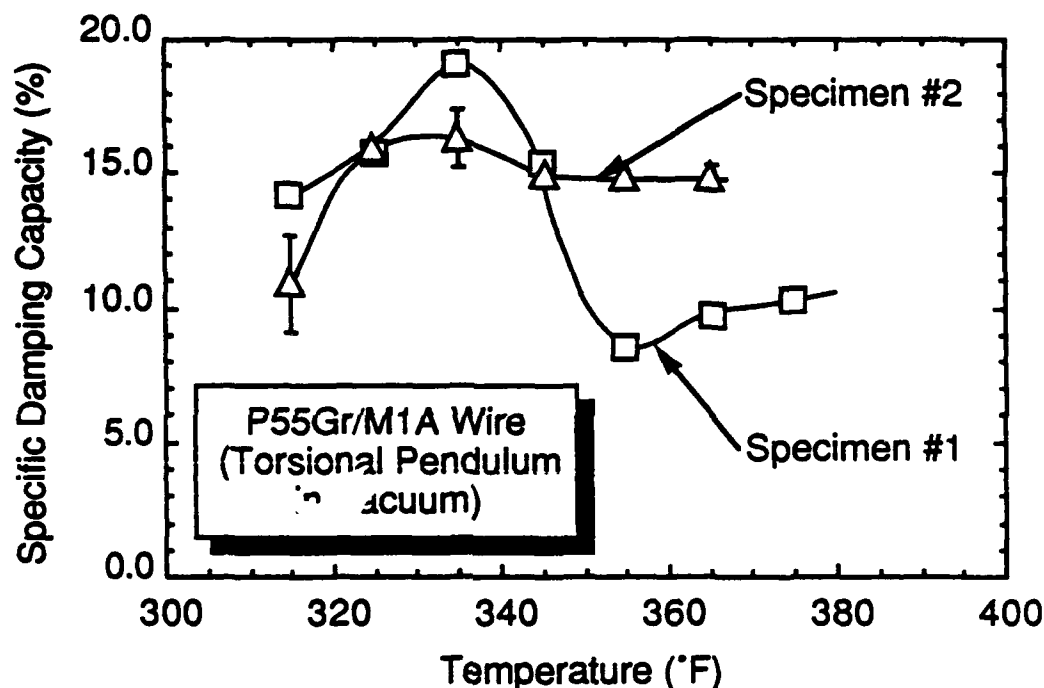
Figure 5.2.2.1-1 Thermal Dependence of the Damping in P55Gr/Mg-1.0%Mn (Gr/M1A) Precursor Wire Indicating a Peak at 441 K (335 °F)

Because the actual damping mechanism associated with the strong temperature dependence above 505 K was not known, the possibility existed that damage at these elevated temperatures could affect the damping. Consequently, the specimen was kept at the elevated temperature for 12 hours while the damping was observed. After the 12 hour soak, the damping was so high that the values could not be measured with the damping apparatus. Thus, the specimen was cooled to room temperature and the temperature dependence was then measured. As shown in Figure 5.2.2.1-3, the slight peak at lower temperatures now occurs at 447 K (345°F), but the strong temperature dependence

observed in as-fabricated specimens now occurred at 484 K (412°F), a much lower temperature than before. Because of the strong temperature dependence, a maximum temperature of only 519 K (475°F) was achieved within the limitations of the torsional pendulum.
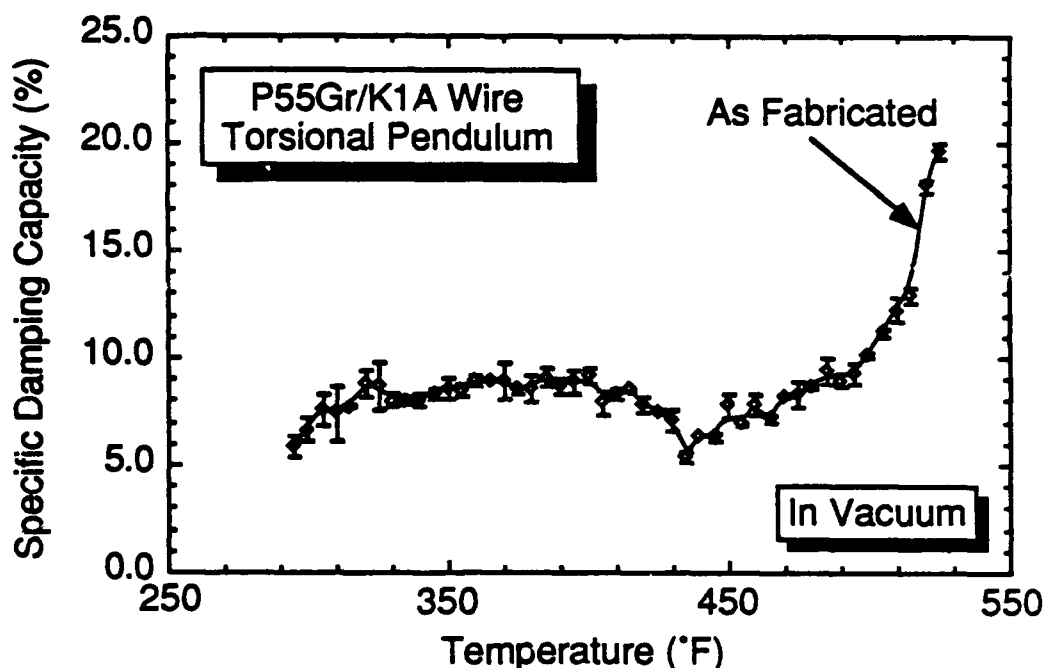
Figure 5.2.2.1-2 Thermal Dependence of the Damping in P55Gr/Mg-0.6%Zr (Gr/K1A) Precursor Wire Indicating a Strong Temperature Dependence Above 505 K (450 °F)

A final test on this specimen involved another damping test after a significant amount of time at room temperature to see if any of the thermally-induced effects were permanent. As shown in Figure 5.2.2.1-4, the original thermal dependence of the damping returned to the specimen after 144 hours at room temperature. This indicates that some reversible thermally-activated mechanism was responsible for this elevated temperature behavior. However, the local minima after the slight damping peak was eliminated by the thermal treatment.
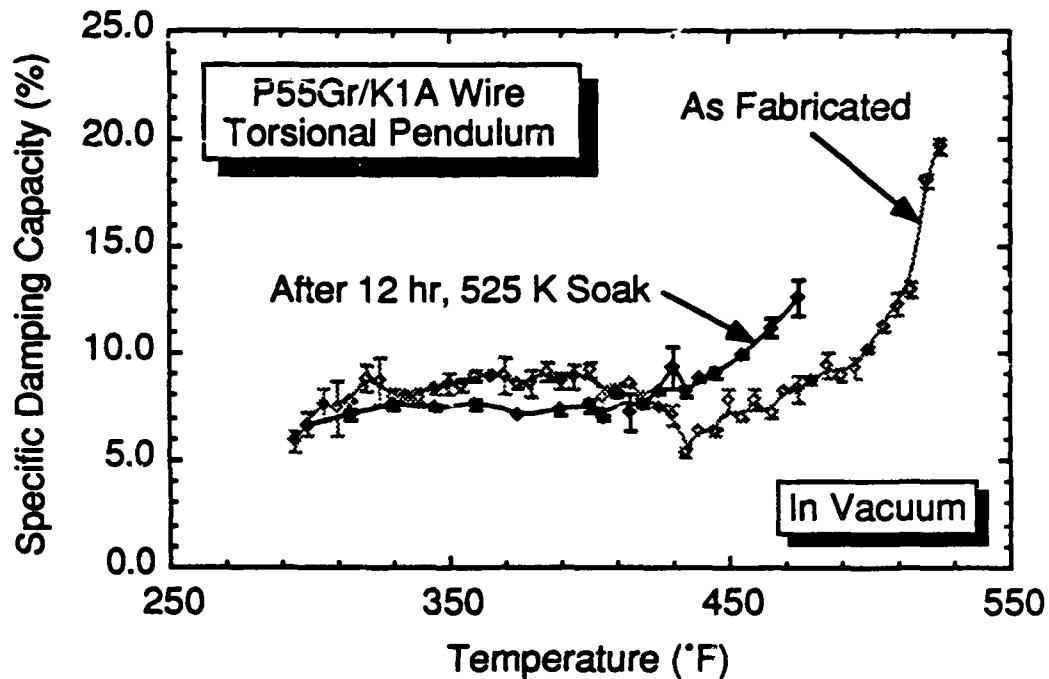
Figure 5.2.2.1-3 Thermal Dependence of the Damping in P55Gr/Mg-0.6%Zr (Gr/K1A) Precursor Wire After a 547 K (525 °F) Soak for 12 Hours, Indicating an Enhanced Temperature Dependence
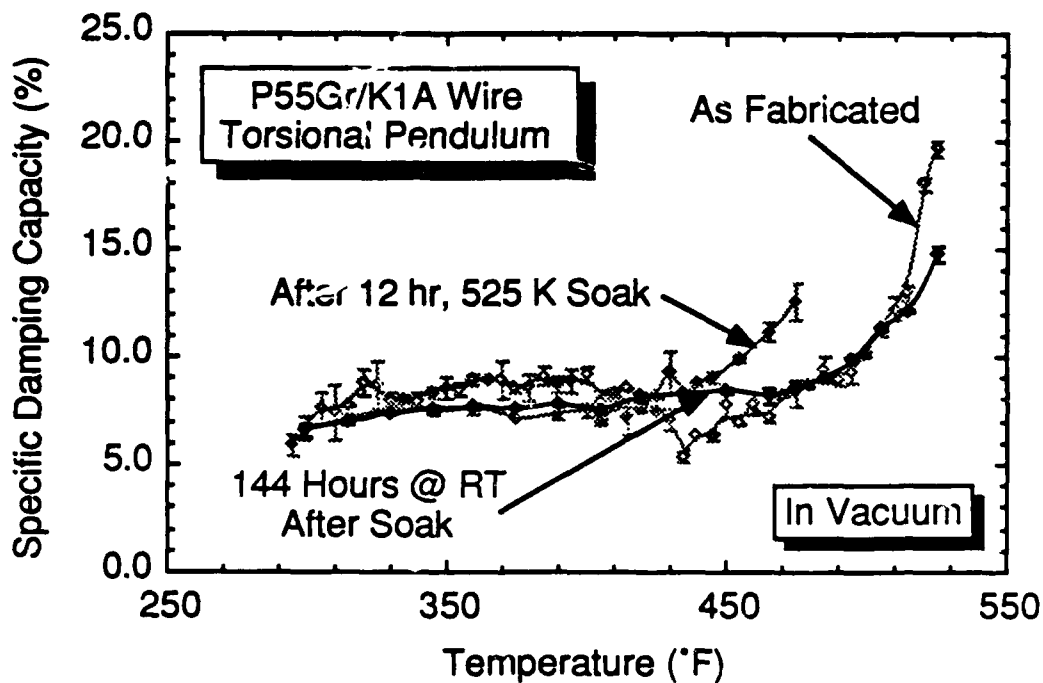
Figure 5.2.2.1-4 Thermal Dependence of the Damping in P55Gr/Mg-0.6%Zr (Gr/K1A) Precursor Wire After 144 Hours at Room Temperature Indicating Most of the Initial Temperature Dependence of the Specimen Returning

5.2.2.2 Clamped-Free Flexure Measurements — Damping measurements at intermediate frequencies ($\approx$ 2 kHz) were performed on a continuously-driven clamped-free flexure apparatus (in vacuum). All tests were conducted at very low strain amplitudes ($< 10^{-7}$) to ensure complete strain amplitude dependence. Temperatures ranged continuously from 73 K to 673 K (-328°F to 752°F).

As shown in Figure 5.2.2.2-1, damping values obtained at higher frequencies were far below those observed earlier in torsion by over an order of magnitude. As the specimens were cooled, a peak was observed at about 200 K, and when heated back to room temperature, the identical behavior was observed with the damping becoming a maximum at about $\psi \approx 0.72\%$. At about room temperature, damping was relatively independent of temperature, with values of $\psi \approx 0.45\%$. The presence of a local minima may exist at about 500 K (441°F) as was found in the previous tests, although insufficient data were taken near this temperature to substantiate its presence. Once again, temperature dependence was noted in these materials above 351°F, and these results were repeatable upon cooling to room temperature.
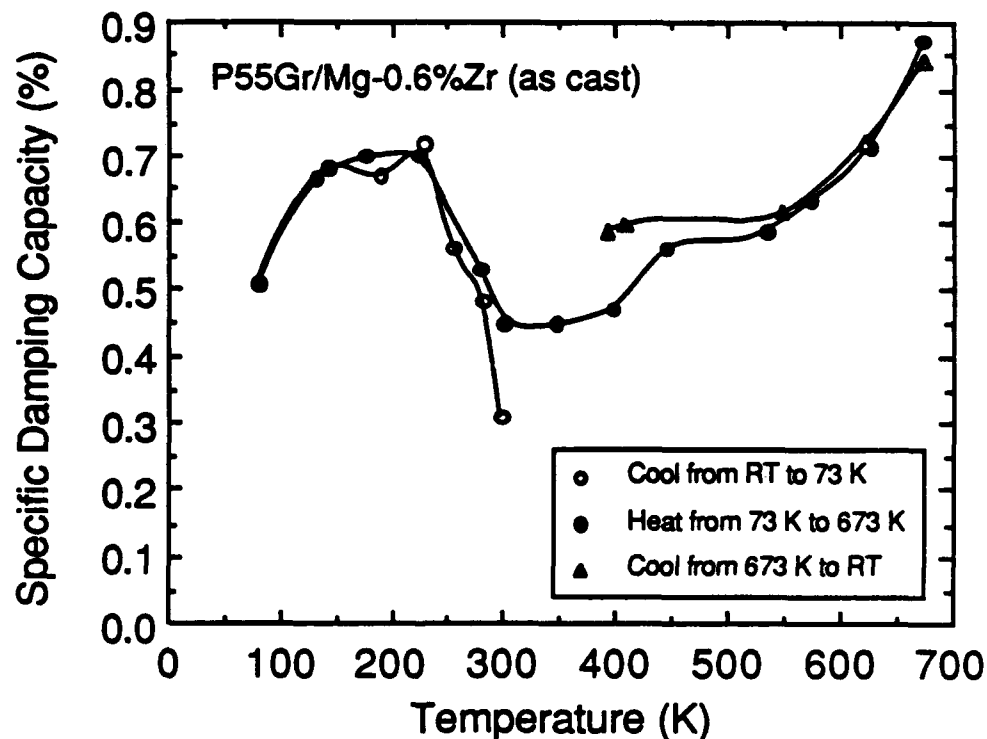
Figure 5.2.2.2-1 Thermal Dependence of the Damping in P55Gr/Mg-0.6%Zr (Gr/K1A) Flat Specimen Indicating a Peak at About 200 K and Strong Temperature Dependence Above Room Temperature.

5.3   DISCUSSION

5.3.1   Discussion of Strain Amplitude Independent Damping

Damping behavior of Gr/Al composites exhibit strain amplitude dependent behavior similar to that of metallic materials. Specific damping capacity of these composites is nearly strain amplitude independent below 10^{-5}, but exhibits strong strain amplitude dependence above 10^{-4}.

At low strain amplitude levels where material damping is nearly independent of strain, the energy dissipation is primarily attributed to anelastic relaxation mechanisms involving atomic diffusion, dislocation relaxation (Bordoni Peak), dislocation resonance, Zener thermoelastic effect, and phase transitions. At low temperatures, a peak was observed in Gr/Mg damping at about 200 K (–99.4 °F). This peak in the temperature dependence coincides with a damping peak in graphite corresponding to a phase transition from rhombohedral to hcp at 200 K. Damping measurements of graphite fiber alone as a function of temperature also exhibits a peak (Fig. 5.3.1-1), although at a slightly higher temperature (248 K). This peak is quite reproducible upon cooling and reheating.
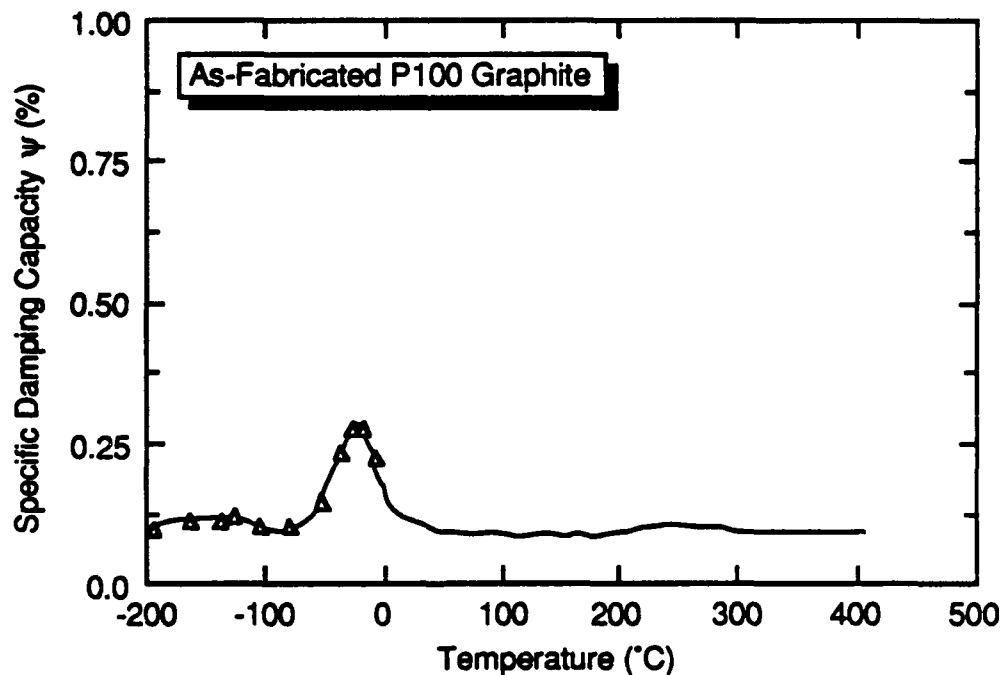
Figure 5.3.1-1 Thermal Dependence of the Damping in P100 Graphite Fiber Indicating a Peak at 253 K (-4.0 °F)

A number of other mechanisms not related to microstructural processes may occur, particularly in flexural testing. During flexural vibration the top and bottom surfaces of the composite beam undergo cyclic compressive and tensile stress states. The resulting strain is generally accompanied by a change in temperature; temperature rises under compressive loads, and declines under tensile loads. Energy dissipation processes resulting primarily from heat transfer due to thermal gradients within the specimen is referred to as Zener thermoelastic damping. Zener thermoelastic damping effects are maximum at a relaxation frequency where the period of applied stress is comparable with the time taken for heat to flow across the beam. However, at frequencies below 100 Hz, contribution from Zener relaxation in Gr/Mg was calculated to be below y = 0.03%, suggesting that anelastic relaxation processes operative within the constituent fiber and matrix must be the predominant mechanism for energy dissipation in Gr/Mg.

The dynamic response of a linear anelastic (or viscoelastic) composite in terms of their constituent properties can be predicted by Hashin theory [Ref 5-4]. Using a correspondence principal, Hashin has derived expressions to determine effective complex moduli of fiber-reinforced materials directly for the composite effective elastic modulus by replacing the elastic modulus of the phases by their complex moduli. For unidirectional composites, the axial specific damping capacity ψ_{11} can be expressed in the following form:

$$\psi_{11} = \left[\frac{E_f}{E_{11}}\right] \cdot \psi_f V_f + \left[\frac{E_m}{E_{11}}\right] \cdot \psi_m (1 - V_f) \tag{5-1}$$

where

E_f	$\equiv$	Fiber Modulus
ψ_f	$\equiv$	Fiber Damping
E_{11}	$\equiv$	Axial Composite Modulus
ψ_f	$\equiv$	Fiber Damping
ψ_m	$\equiv$	Matrix Damping
V_f	$\equiv$	Fiber Volume.

Graphite fibers behave in a nearly elastic fashion and is considered to have minimal damping as compared to the matrix. Given values for $\psi_m \approx 30\%$, and $\psi_f = 0.1\%$, Equation 5-1 yields ψ_{11} of 4.69%, which is far greater than that observed for any tests other than the torsional pendulum. Thus, the matrix is not contributing as much damping as possible.

The K1A and M1A alloys exhibit significant damping ($\psi > 30\%$) only when grain size is quite large (e.g. D > 20 μm). At intermediate grain size, (D $\approx$ 10 μm) damping for K1A were measured at only

$\psi = 13.8\%$. Using a fiber damping value of $\psi_f = 0.1\%$, Equation 5-1 yields ψ_{11} of 2.22%, as compared to the measured ψ_{11} value of 1.5% observed by various test methods. A major problem with these composites is that while large grain size is required for high damping, the average grain size in these composites is often less than 2 μm. Consequently, there are two possible approaches suggested by Equation 5-1 to improve the strain amplitude independent damping response of these materials, namely 1) to increase the damping contribution from the matrix by heat treatment, or to improve the damping contribution from the fibers where a significant amount of strain energy is concentrated.

5.3.2 Analysis of Strain Amplitude Dependent Damping

As shown in the previous section, strain amplitude dependence was observed in the Gr/Mg system. As with other materials, the total measured damping may be expressed as a sum of strain amplitude independent (ψ_i) and strain amplitude dependent (ψ_H,) or hysteretic, components, i.e. $\psi_{total} = \psi_i + \psi_H$. While strain amplitude dependence was noted in the Gr/Al system [Ref 5-1], the peak in damping found in Gr/Mg using the piezoelectric composite oscillator was not. It was essential that any explanation of the strain amplitude dependence of the damping should account for the presence of a peak.

As was found with the Gr/Al system, energy dissipation arising from dislocation breakaway from pinning points plays a predominant role in the strain amplitude dependent damping of many nonmagnetic alloys. To verify if this mechanism is responsible for the strain amplitude dependence in Gr/Mg, data from the piezoelectric composite oscillator tests were studied using the Granato-Lucke (G-L) theory, with some modifications as outlined in the literature [Refs 5-5 and 5-6]. G-L theory basically states that the stra.. amplitude dependent damping (ψ_h) of a material experiencing a strain ε may be described by the foll... ng relationship

$$\psi_H = \frac{C_1}{\varepsilon} \cdot \exp\left[\frac{-C_2}{\varepsilon}\right]$$

(5-2)

where C_1 and C_2 are material constants. For the analysis of the uniaxial tension-tension cycling data [Ref D-2], the strain amplitude throughout the length of the specimen was relatively uniform. Consequently, Equation 5-2 could be used in its original form. However, when the strain amplitude distribution throughout the length of the specimen is nonuniform, the form of the equation must change

to accommodate this distribution. Granato and Lucke describe the integration of Equation 5-2 over the length of a specimen whose strain amplitude is sinusoidal in nature, as is the case with the piezo-electric composite oscillator [Ref 5-6]. Remarkably, the equation has only minor outward changes in form, with minor changes in the constants C_1 and C_2 as shown below:

$$\psi_H = \frac{C_1}{\sqrt{\varepsilon}} \cdot \exp\left[\frac{-C_2}{\varepsilon}\right] \tag{5-3}$$

where:

$$C_1 = 2\Omega\Lambda L_N^3 \sqrt{\frac{2\kappa\eta^*a}{\pi^5 L_C^3}} \tag{5-4}$$

$$C_2 = \frac{\kappa\eta^*a}{L_C} \tag{5-5}$$

where Ω and K are orientational constants, Λ is the mobile dislocation density, L_N is the dislocation network length, η^* is the Cottrell misfit parameter, a is the lattice spacing, and L_C is the average dis-location loop length. Note that the only change in the functional dependence is the replacement of the inverse strain outside the exponential with an inverse square root strain. Therefore, a plot of ln $\psi_H e^{1/2}$ versus $1/\varepsilon$ should yield a linear fit if, indeed, the G-L strain amplitude dependence is observed. Constants C_1 and C_2 are the intercept and the slope of the G-L plot described above. As shown in Figure 5.3.2-1, a good linear fit is obtained with Gr/M1A data, with values $C_1 = 3.075$ x 10^{-4} and $C_2 = 3.936$ x 10^{-5}. Similar results were obtained for Gr/K1A as well, with $C_1 = 2.415$ x 10^{-4} and $C_2 = 1.635$ x 10^{-5}. Thus, it is reasonable to suggest that dislocation damping also plays an important role in the strain amplitude dependent damping of Gr/K1A and Gr/M1A.

In addition to the proper strain amplitude dependence, if one were to take the first and second derivative of Equation 5-3 as a function of strain amplitude, it is noted that a maxima in the damping should occur at a value $\varepsilon_p = 2C_2$. This result also coincides well with the data, as damping peaks are observed at approximately 3.0 x 10^{-5} and 6.0 x 10^{-5} for Gr/K1A and Gr/M1A respectively.

While the data exhibit the appropriate strain amplitude dependence for dislocation damping, it is imperative that predictions of mobile dislocation loop length and density be evaluated and compared to measured quantities to verify that dislocation breakaway is responsible for strain amplitude

dependent damping. Values for the average loop length between minor pinning points, L_C, are obtained directly from C_2. From the data presented above, with appropriate material constants, $L_C = 5.53 \times 10^{-8}$ m and 3.57×10^{-8} m for as-cast Gr/K1A and Gr/M1A respectively. These values appear to be reasonable for minor pinning point length. By substitution of other material constants and an approximation, $L_N/L_C = 100$, one obtains an approximate value for mobile dislocation density of 3.01×10^9 /m and 5.94×10^9 /m for Gr/K1A and Gr/M1A respectively. These values, while significantly higher than values observed for the monolithic alloys alone, are significantly lower than dislocation densities measured from various TEM images of $0.6 - 1.6 \times 10^{14}$ /m. This discrepancy can be explained due to slip being limited to the basal plane in hcp structures such as Mg, and therefore only a small portion of the measured dislocations are of proper alignment.
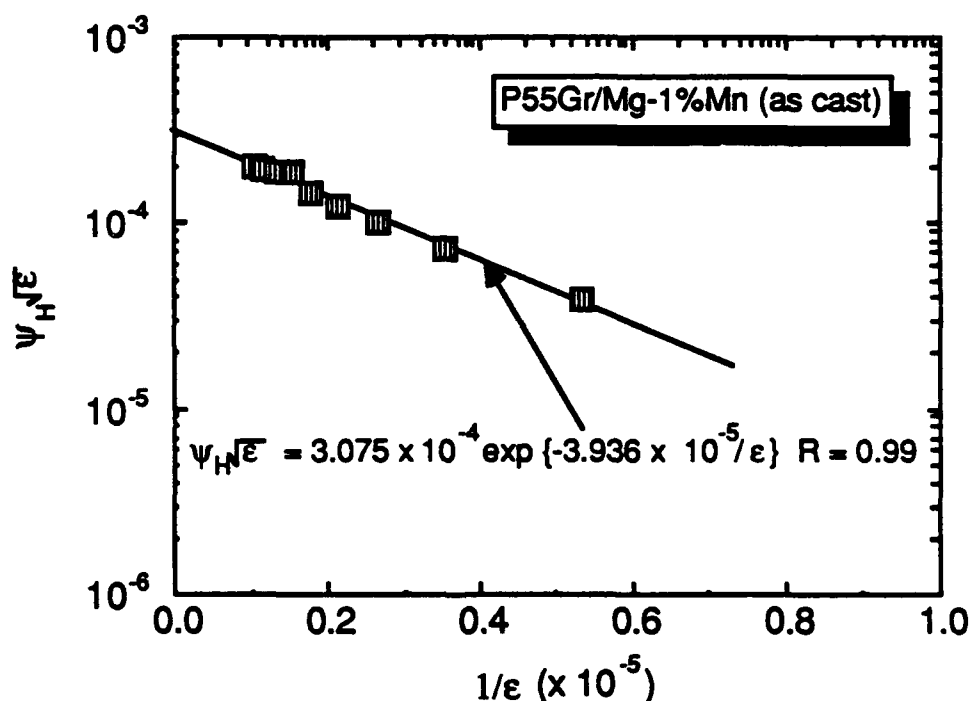
Figure 5.3.2-1 *Granato-Lucke Plot of Data from As-Cast Gr/K1A Indicating the Proper Strain Ampliutde Dependence for a Dislocation Damping Mechanism*

5.4 SUMMARY

Damping measurements of pitch 55 graphite fiber reinforcement in high-damping Mg-0.6%Zr (K1A) and Mg-1.0%Mn (M1A) alloys exhibited a transition from strain amplitude independent to dependent response at strain levels above 10^{-6}. The strain amplitude dependent response was explained in terms of the Granato-Lucke (G-L) model, suggesting that dislocation damping is the

likely energy dissipation mechanism. Also, mobile dislocation densities predicted by G-L theory were consistent with the average dislocation densities measured from various transmission electron micrographs near the fiber-matrix interface. The strain amplitude dependence also predicted the presence of the damping peaks, and gave a reasonable approximation for the dislocation loop length. After substitution of appropriate material constants, a four to five order of magnitude lower mobile dislocation density was observed than that measured by TEM, which was explained by the limited slip systems for dislocations in hcp metals, and consequently, the small percentage of total dislocations that are mobile under a low applied stress.

Damping measurements of these materials in the strain amplitude independent region as a function of temperature indicated a contribution from a phase transformation between rhombohedral and hcp structures in the graphite fiber at 200K (-99.4°F). Above room temperature, the temperature dependent damping response was typical of that found in the matrix alloy alone. Comparison of predicted and measured composite damping capacity at low strain amplitudes yielded an *in situ* matrix damping contribution of 9% which was substantially lower than the damping capacity of cast Mg alloys. Low *in situ* matrix damping in the composite could be attributed to the fine grain structure near the fiber-matrix interface.

5.5   REFERENCES

5-1   J.H. Armstrong, S.P. Rawal, and M.S. Misra: "Damping Measurements of Graphite-Aluminum Composites," Martin Marietta Report R86-48681-002, December 1986.

5-2   M.S. Misra, S.P. Rawal and J.H. Armstrong: "Damping Characteristics of Metal Matrix Composites," Final Report MCR-643, Office of Naval Research Contract N00014-85-C-0857, 1986.

5-3   S.P. Rawal, M.S. Misra, J. Jackson, and D. Goddard: "Novel Processing Techniques to Fabricate Gr/Mg Composites for Space Applications," Final Report MCR-88-635, Naval Sea Systems Command Contract N00024-84-C-5306, 1988.

5-4   Z. Hashin: "Complex Moduli of Viscoelastic Composites - II Fiber Reinforced Materials," International Journal Solids and Structures, Vol. 6, No. 6, p. 797 (1970).

5-5   A.V. Granato and K. Lucke: "Theory of Mechanical Damping Due to Dislocations," J. Appl. Phys., 27, 583 (1956a).

5-6   A.V. Granato and K. Lucke: Applications of Dislocation Theory to Internal Friction Phenomena at High Frequency," J. Appl. Phys., 27, 789 (1956b).

6.0 Heat Treatment of Gr/Mg

CHAPTER 6.0
EFFECT OF HEAT TREATMENT UPON DAMPING OF Gr/Al COMPOSITES

Strain amplitude independent damping contributions from the matrix were well below the levels anticipated. The low level of matrix damping contribution was attributed to the small grain size found in the as-cast composite. It was therefore the objective of this task to increase the grain size through heat treatment in hopes of increasing the overall contribution to the total damping from the matrix alloy.

6.1 TECHNICAL DISCUSSION

6.1.1 Specimen Preparation

Both [0°] P55Gr/Mg-0.6%Zr (Gr/K1A) and [0°] P55Gr/Mg-1.0%Mn (Gr/M1A) specimens were tested in the as-cast condition, as well as heat treatments of 450°F for 6 hours, and 800°F for 4,8, and 16 hours. All of the specimens were subjected to X-radiography and metallographic examination to verify the structural integrity. All heat treatments were conducted in an argon atmosphere to minimize contamination of the specimen surfaces.

6.1.2 Damping Test Technique

All specimens were tested using the piezoelectric composite oscillator technique. In each case, specimens were thoroughly cleaned after heat treatment and prior to mounting to the quartz bar system.

6.2 RESULTS

Damping of Gr/M1A as a function of strain amplitude for as-cast and heat treated specimens is shown in Figure 6.2-1. Damping of Gr/M1A increased systematically with heat treatment. Strain amplitude independent damping values were $\psi_i = 0.55\%$, 0.62% and 1.0% for as cast, 6 hours at 450°F and 4 hours at 800°F respectively. Strain amplitude dependence also changed with respect to heat treatment, with the position and height of the damping peak shifting to lower strain amplitudes

in conjunction with the increase in strain amplitude independent damping. Micrographs of a 6 hour, 450°F heat treated specimen (Fig. 6.2-2) indicates a growth in grain size to as large as 10 μm, often encompassing two or more fibers.
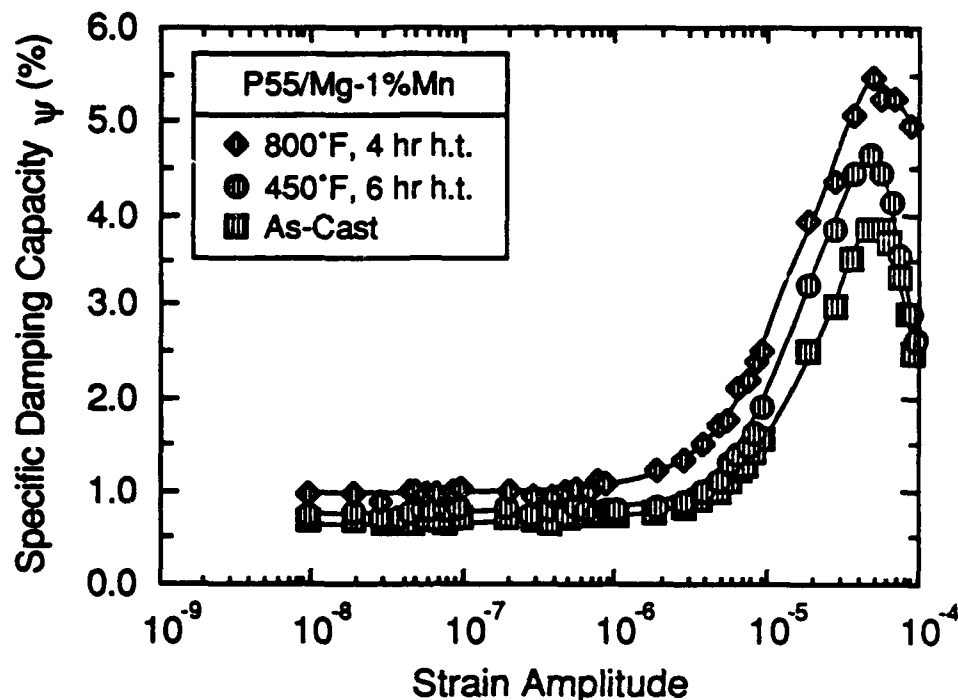
Figure 6.2-1 Damping of Gr/M1A Composite in As-Cast and Heat Treated Conditions, Indicating an Overall Increase in Both Strain Amplitude Independent and Dependent Damping

6.3   DISCUSSION

Strain amplitude independent internal friction can be attributed to anelastic mechanisms which can be separated into contributions from its constituent fiber and matrix. According to Hashin theory, internal friction of unidirectional composites (ψ_{11}) can be expressed as

$$\psi_{11} = \left[\frac{E_f}{E_{11}}\right] \cdot \psi_f V_f + \left[\frac{E_m}{E_{11}}\right] \cdot \psi_m (1 - V_f) \qquad (6\text{-}1)$$

where E_f, E_m, and E_{11} are the elastic moduli of the fiber, matrix and composite respectively, and ψ_f and ψ_m are the damping capacity values of the fiber and matrix respectively. Equation 6-1 has been

used successfully to predict strain amplitude independent damping values for Gr/Al [Ref 6-1] and B/Al [Refs 6-2, 6-3] in agreement with measured values. Given the strain amplitude independent damping for Gr/M1A mentioned earlier, the contribution from the matrix can be calculated as $\psi_m \approx$ 3.10%, 3.59%, and 6.24% for the as-cast and heat treatments respectively. This increase of matrix contribution to damping from heat treatment corresponds well with the noted growth in grain size. While the damping contribution increased, the values are still significantly below those values for sand-cast M1A and K1A found in the literature [Refs 6-4 and 6-5].
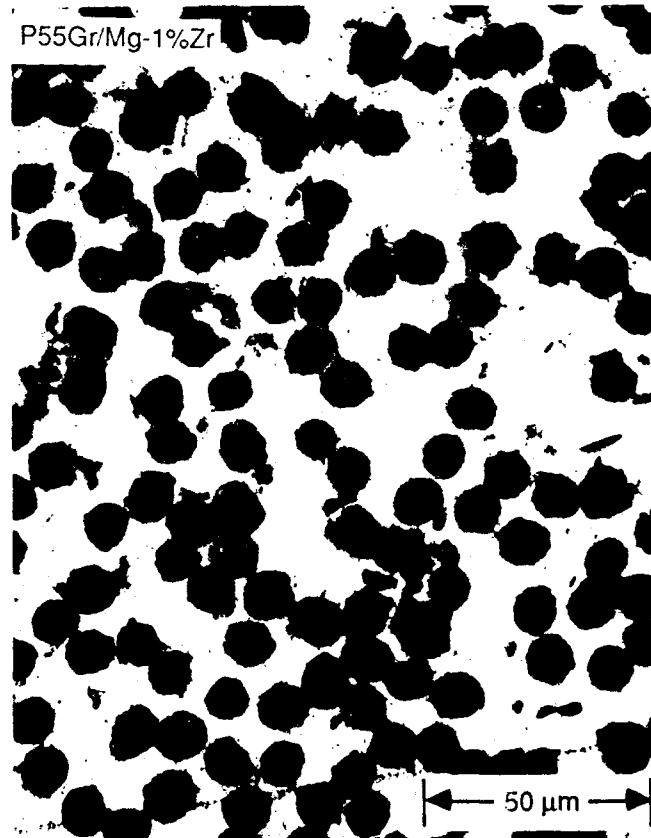
Figure 6.2-2 Micrograph of Heat Treated P55Gr/Mg-0.6%Zr Showing a Number of Grains in Excess of 10 μm Encompassing Two or More Fibers

In the case of graphite/aluminum [Ref 6-1], strain amplitude dependent damping was attributed to dislocation motion as described by Granato and Lucke (G-L) [Refs 6-6 and 6-7]. According to G-L theory, strain amplitude dependent damping (ψ_H) can be described as:

$$\psi_H = \frac{C_1}{\sqrt{\varepsilon}} \cdot \exp\left[\frac{-C_2}{\varepsilon}\right] \qquad (6\text{-}2)$$

where ε, the vibratory strain amplitude, is sinusoidal with respect to the specimen length (standing wave). For the standing-wave configuration, constants C_1 and C_2 are defined by the following

$$C_1 \cong 2\Omega\Lambda L_N^3 \sqrt{\frac{2\kappa\eta^* a}{\pi^5 L_C^3}} \qquad (6\text{-}3)$$

$$C_2 \cong \frac{\kappa\eta^* a}{L_C} \qquad (6\text{-}4)$$

where Ω and K are orientational constants, Λ is the mobile dislocation density, L_N is the dislocation network length, η^* is the Cottrell misfit parameter, a is the lattice spacing, and L_C is the average dislocation loop length. To investigate the possibility that damping from dislocation motion could be responsible for the strain amplitude dependence, a G-L plot ($\psi_H \varepsilon^{1/2}$ vs. $1/\varepsilon$) for the Mg-1.0%Mn alloy was performed as shown in Figure 6.3-1. These data show an excellent fit to the predicted G-L strain amplitude dependence. Least-squares fit of G-L plots for both Gr/K1A and Gr/M1A were performed, and each case, very good agreement with G-L theory was found. By substituting appropriate material constants of $a = 3.21$ Å, $\eta^*(\text{K1A}) = 0.141$, $\eta^*(\text{M1A}) = 0.219$, $K = 0.02$, $\Omega = 0.04$, and $L_N/L_C = 100$, values were obtained for L_C as shown in Table 6.3-1. Dislocation loop length increased and density increased systematically with heat treatment, which is indicative of reduction or redistribution of minor pinning points in the matrix. Confirmation of the dislocation density of heat treatment specimens was not possible because oxidation of the TEM specimens immediately after specimen preparation.

The damping peak visible in the strain amplitude dependent region could also be described in terms of the G-L theory. By taking the first and second derivatives of Equation 6-2, a maxima in damping is predicted at strain ε_p where $\varepsilon_p = 2C_2$. Predicted values from the G-L slopes are $\varepsilon_p = 7.872 \times 10^{-5}$, 5.908×10^{-5}, and 1.618×10^{-5} for as-cast and heat treated Gr/M1A respectively. The actual position is close to the predicted values, with the exception of the 800°F, 4 hr test which does not shift nearly as much as anticipated.

P55Gr/Mg-1%Mn (as cast)

$$\psi_H \sqrt{\varepsilon} = 3.075 \times 10^{-4} \exp\{-3.936 \times 10^{-5}/\varepsilon\} \quad R = 0.99$$
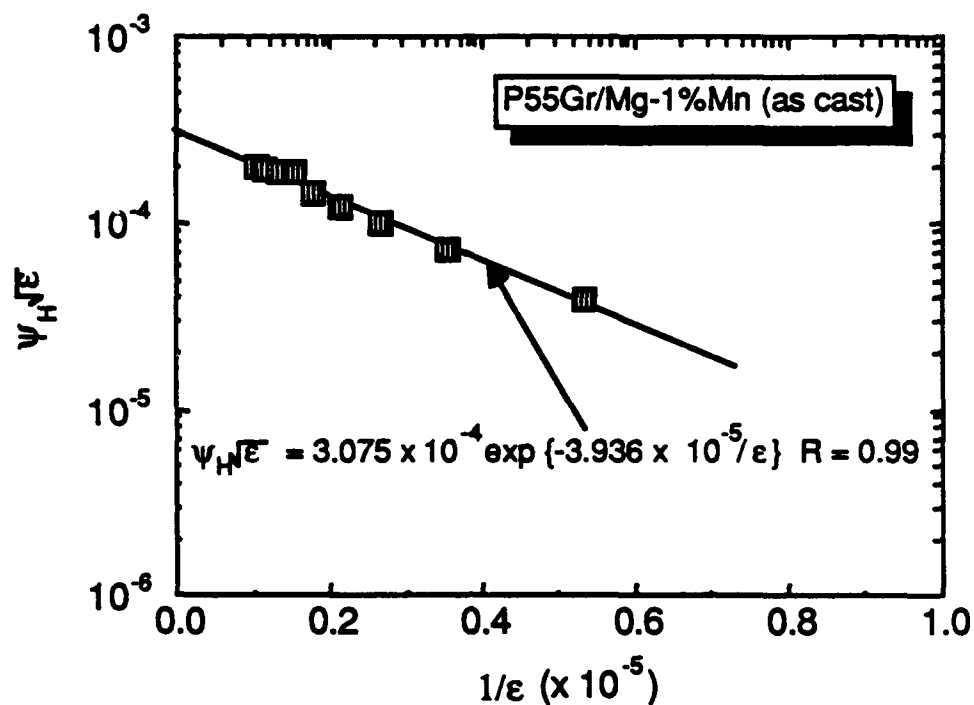
Figure 6.3-1 Granato-Lucke Plot of Gr/K1A Composite Indicating an Excellent Fit

Table 6.3-1 Result of Granato-Lucke Analysis of Strain Amplitude Dependent Damping of Gr/K1A and Gr/M1A

Material	Condition	$C_1 (\times 10^4)$	$C_2 (\times 10^5)$	$L_C (\times 10^8 m)$
P55Gr/Mg-0.6%Zr	As Cast	2.415	1.635	5.53
	450°F, 6 hr.	2.567	0.631	14.3
	800°F, 4 hr.	2.249	0.532	17.0
P55Gr/Mg-1.0%Mn	As Cast	3.075	3.936	3.57
	450°F, 6 hr.	3.107	2.954	4.76
	800°F, 4 hr.	4.227	0.809	17.4

6.4   SUMMARY

Damping measurements of as-cast $[0°]_8$ P55Gr/Mg-0.6%Zr (Gr/K1A) and P55Gr/Mg-1.0%Mn (Gr/M1A) composites exhibited a transition from strain amplitude independent to dependent damping at about $\varepsilon = 10^{-6}$. Damping of the Gr/K1A and Gr/M1A composites were higher than those measured for Gr/Al under similar circumstances. Unlike $[0°]$ P55Gr/6061Al specimens tested earlier, the Gr/K1A and Gr/M1A specimens possessed a peak in the strain amplitude dependent damping.

From the strain amplitude independent region, it was determined that the matrix contributed only 3.1% of the total specific damping capacity (ψ) for the Gr/M1A specimens, although damping values in the literature for these alloys were as high as $\psi = 30\%$. Metallographic analysis of these materials indicated that the grain size of the matrix was as low as $2 \mu m$, whereas the high damping exhibited in the literature was for a grain size in excess of $20 \mu m$. Therefore, Gr/Mg specimens were heat treated to increase the matrix grain size, thereby enhancing the contribution of the matrix to the total damping.

Prior to damping measurements, both Gr/M1A and Gr/K1A were heat treated at 450°F for 6 hours, and at 800°F for 4,8, and 16 hours in an argon atmosphere, followed by an oven cool. Damping test data analysis indicated that strain amplitude independent contributions from the matrix increased as a result of heat treatment (3.59% and 6.24% for 450°F, 6 hr and 800°F, 4 hr heat treatment respectively). Further heat treatments at 800°F for longer durations did not result in any significant increase in damping, although micrographs indicated a coarsening of elemental precipitates in the matrix.

Data analysis of the strain amplitude dependent damping of heat treated Gr/Mg indicated the strain amplitude dependent damping can be described by the Granato-Lucke theory of dislocation damping. Strain amplitude dependence is modeled by a dislocation breakaway from minor pinning points. Average dislocation loop length (L_C) between minor pinning points increased systematically with longer heat treatment (3.57×10^{-8} m, 4.76×10^{-8} m, and 17.4×10^{-8} m for as-cast, 450°F, 6 hr and 800°F, 4 hr heat treatment respectively). Approximate predicted values of mobile dislocation density was on the order of 6×10^9 $1/m^2$, which was far lower than the average dislocation density observed in various TEM images of 10^{14} $1/m^2$. This large difference can be attributed to the limited slip systems in hcp structure materials, consequently limiting the number of dislocations that can become mobile in response to an applied cyclic stress.

6.5   REFERENCES

6-1   S.P. Rawal, J.H. Armstrong, and M.S. Misra: "Interfaces and Damping in Metal Matrix Composites," Martin Marietta Report MCR-86-684, prepared for the Office of Naval Research, December, 1986.

6-2   J.A. DiCarlo and J.E. Maisel: "High-Temperature Dynamic Modulus and Damping Measurement of Aluminum and Titanium Matrix Composites," Advanced Fibers and Composites for Elevated Temperatures, I. Ahmad and B.R. Noton, eds., Conference Proceedings, Metallurgical Society of AIME, p. 55 (1979).

6-3   J.A. DiCarlo and J.E. Maisel: "Measurements of the Time/Temperature-dependent Dynamic Mechanical Properties of Boron/Aluminum Composites," Composite Materials: Testing and Design (Fifth Conference), ASTM STP 674, S.W. Tsai, ed., American Society for Testing and Materials.

6-4   J.W. Fredrickson: "Damping Capacity of K1A," Dow Chemical Corporation Report MT17753-Final, Dec. 1958.

6-5   K. Sugimoto, K. Niiya, T. Okamoto, and K. Kishitake: "A Study of Damping Capacity in Magnesium Alloys," Trans JIM, 18, pp 277-288, 1977.

6-6   A. Granato and K. Lucke: "Theory of Mechanical Damping Due to Dislocations," J. Appl. Phys., 27, p. 583 (1956)

6-7   A. Granato and K. Lucke: "Applications of Dislocation Theory to Internal Friction Phenomena at High Frequencies," J. Appl. Phys., 27, p. 789 (1956)

7.0 Residual Stresses and Damping

CHAPTER 7.0
ROLE OF RESIDUAL STRESSES IN DAMPING IN Gr/Al

During the fabrication process of graphite/aluminum (Gr/Al) composites, large residual stresses are generated in the matrix when the laminate is cooled from the consolidation temperature to room temperature. These residual stresses are induced as a result of the mismatch in the coefficient of thermal expansion (CTE) between the fiber and the matrix. In the case of P55 Gr/6061 Al, the matrix contracts (CTE = 23 ppm/K) and the fibers expand (CTE = -1.2 ppm/K) as the material cools, generating a tensile component of residual stresses in the matrix in the fiber direction [Ref 7–1]. At the microstructural level, the residual stresses are accommodated by the creation of dense and tangle dislocation networks near the interface. These residual stresses significantly influence the thermomechanical response such as fatigue life, CTE and damping of composites.

Damping measurements of as-fabricated graphite/aluminum composite specimens indicated that beyond a critical strain amplitude damping increased with the increasing strain amplitude. Because strain amplitude dependent damping is generally independent of frequency [Refs 7-2, 7-3 and 7-4], damping response was examined at both high and low frequencies (80 kHz and 1 Hz) over a wide range of strain amplitude. Data analysis in terms of Granato-Lucke dislocation damping theory [Ref 7-3], combined with transmission electron microscopy observations, suggested that mobile dislocations in the tangled network near the interfaces contribute to energy dissipation at vibrational strain levels greater than the critical strain amplitude. Therefore, any changes in residual stress state and associated changes in mobile dislocation density near the interface could influence the damping response of Gr/Al at different strain amplitude levels.

7.1 EXPERIMENTAL PROCEDURE

7.1.1 Material

Single-ply and four-ply unidirectional P55 Gr/6061 Al panels were obtained for damping measurements. Both composite panels were fabricated by diffusion-bonding technique at DWA Composite Specialties, Chatsworth, CA. For a single-ply panel, graphite/aluminum precursor wires were consolidated between 88.9 μm thick 6061 Al face sheets at 861 K and 24 kPa for 20 minutes, yielding a composite with 0.635 mm thickness and 39.2% fiber volume. Examination of the panels using X-radiography and optical microscopy indicated good bonding characteristics and fiber collimation. Elastic modulus for these composites was 158 GPa and ultimate tensile strength was 531 MPa.

From the P55/6061 Al composite panels, various test specimens were prepared for damping measurements at room temperature (RT) by a resonant piezoelectric ultrasonic composite oscillator technique (PUCOT), and subresonant tension-tension cycling techniques. The apparatus for the PUCOT consisted of piezoelectric quartz drive and gage crystals, and a specimen cut to precisely one-half of the resonant wavelength for the specific frequency chosen (Fig. 7.1.1-1) as documented in the literature [Refs 7-5—7-9]. In this application, each test specimen was vibrated in a longitudinal standing wave configuration at 80 kHz frequency and a preselected strain amplitude level between 10^{-9} and 10^{-4}. In the tension-tension cycling method, test specimens were subjected to a low frequency (0.1 - 4 Hz) sinusoidal oscillation in a servohydraulic machine between 1×10^{-5} - 6×10^{-4} strain [Ref 7–10]. Prior to damping tests, specimens were given different thermal treatments to modify the axial residual stress level from that of the as-fabricated state. For example, micromechanical analyses show that after a cryogenic quench to -240°F, the axial residual stresses at room temperature are near zero [Ref 7-11].
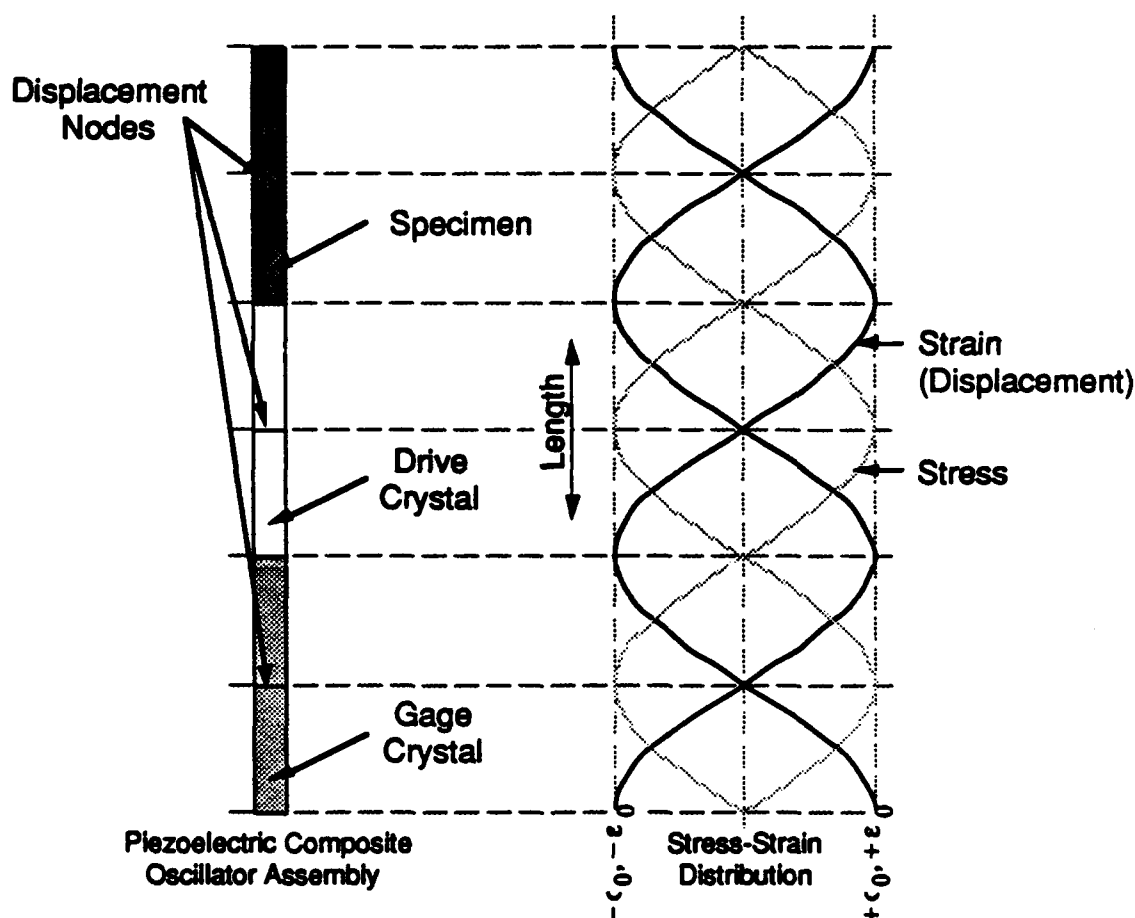
Figure 7.1.1-1 Schematic of the Stress and Strain (Displacement) Distribution of the Piezoelectric Ultrasonic Composite Oscillator Technique (PUCOT)

Five different types of test specimens were prepared with the processing condition and heat treatment described below:

a) as-fabricated

b) Stress-relieved (SR): As-fabricated specimens were slowly quenched in a liquid nitrogen (77 K) to induce interfacial matrix yielding to reduce the residual stresses,

c) -T6 condition: Specimens were solution annealed at 853 K for 0.5 hours, followed by a water quench at RT. Subsequent artificial aging was done at 444 K for 20 hours,

d) -T6/stress-relieved, and

e) Recreated as-fabricated condition: Stress-relieved specimens were heated to 853 K and air cooled to room temperature, thus recreating the consolidation conditions. As a result, the residual stress level in the specimen should be equivalent to the as-fabricated condition.

Four-ply composite specimens (in the as-fabricated and stress-relieved conditions) were used for piezoelectric composite oscillator tests because they were thick enough (2.0 mm) to be bonded to the drive quartz crystal using E910 adhesive. In tension-tension cycling technique, single-ply composite specimens in the as-fabricated, -T6/stress-relieved and recreated as-fabricated condition were tested to examine the effect of residual stresses on the damping capacity.

7.2   RESULTS AND DISCUSSION

Damping behavior of as-fabricated $[0°]_4$ P55/6061 Al specimens in piezoelectric composite oscillator tests at 80kHz between 10^{-8} - 10^{-4} strain amplitude levels is shown in Figure 7.2-1. These results indicated that within the 10^{-8} - 10^{-5} strain amplitude range, specific damping capacity of the test specimen is nearly uniform ($\psi \approx 0.55$ - 0.6%). Above 10^{-5} strain amplitude, damping capacity of as-fabricated specimen gradually increased with strain. The transition from the strain amplitude independent to dependent damping response in the as-fabricated specimens was similar to the typical damping behavior of $[0°]$ Gr/Al [Ref 7-12], $[0°]_8$ Gr/Mg [Ref 7-13] and discontinuous silicon carbide aluminum matrix composites [Ref 7-14].

Similar strain amplitude dependent damping response was also observed in the data obtained by the tension-tension cycling test technique between 1.5×10^{-4} and 3.5×10^{-4} at 1 Hz (Fig. 7.2-2). Subsequent tests at 0.4 and 4.0 Hz yielded damping values identical to the 1 Hz test above 10^{-4} strain amplitude. These results showed that average damping capacity of Gr/Al at these strain amplitude levels was significantly higher than those obtained by PUCOT at 10^{-4} strain amplitude. Comparison

of these data at other strain amplitude was not possible due to limitations of each technique. The higher damping observed by extensional tension-tension cycling at 10^{-4} strain amplitude could be attributed to its length-independent strain distribution compared to the sinusoidal strain distribution in PUCOT (Fig. 7.1.1-1), thereby resulting in an overall higher strain amplitude level. In the tension-tension cycling test method, the average damping capacity of a reference 6061-T625Al specimen was $\psi \approx 1.8\%$ between 1×10^{-4} and 4×10^{-4} (Fig. 7.2-2) compared to $\psi \approx 1.1\%$ for 6061-T6 as measured at 40 Hz by Whaley, et. al. using a double base excited cantilever beam apparatus [Ref 7-15]. Their experimental measurements showed that 6061-T6 exhibited constant damping capacity until 1.3×10^{-3} strain level had been reached. Above this strain value, damping increased with increasing strain amplitude. While 6061-T6 Al exhibits nearly strain amplitude damping between 10^{-5} and 10^{-4} strain levels, Gr/Al composites showed distinctively strain amplitude dependent damping behavior both by PUCOT and uniaxial tension-tension cycling techniques at 80 kHz and 1 Hz respectively. Lucke and Granato [Ref 7-16] identified that strain amplitude dependent response in metallic materials was basically independent of text frequency because of the operational energy dissipation mechanisms described later.
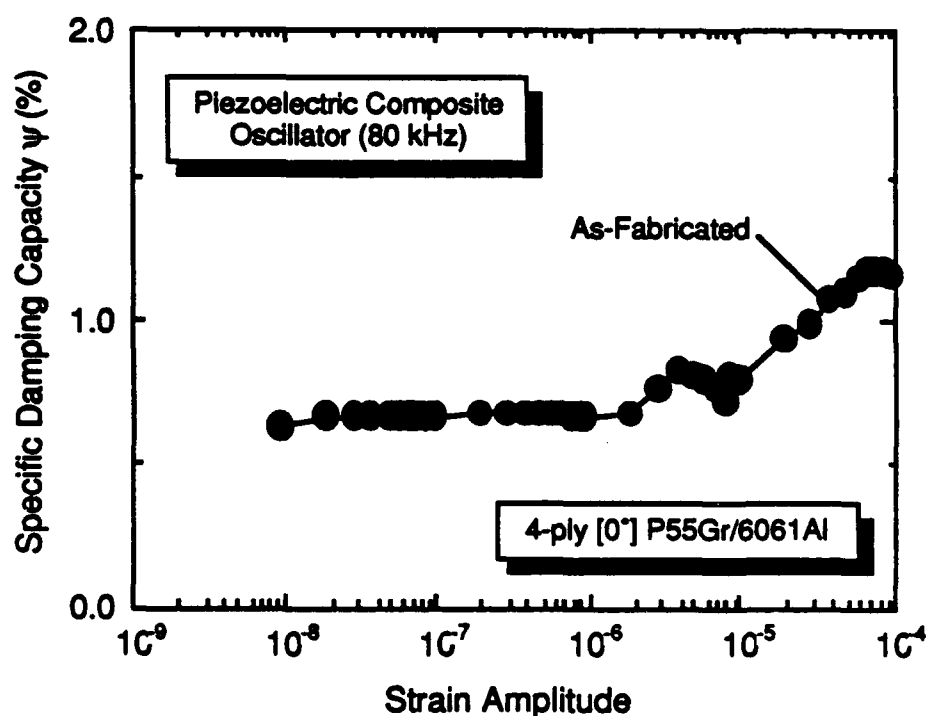
Figure 7.2-1 Damping Behavior of As-Fabricated [0°]₄ P55/6061 Al Specimens in Piezoelectric Composite Oscillator Tests at 80k Hz Indicating Both Strain Amplitude Independent and Dependent Response
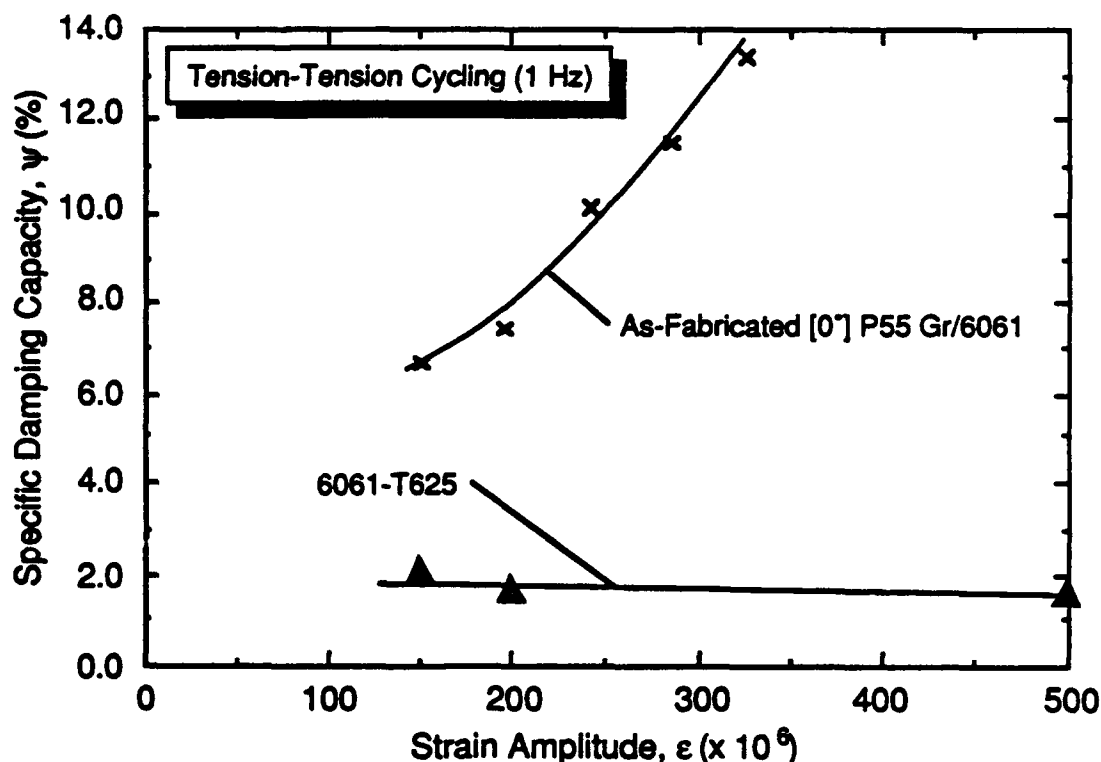
Figure 7.2-2 Damping Behavior of As-Fabricated [0°] P55/6061 Al Specimens in Tension-Tension Fatigue Tests Indicating Both Strain Amplitude Independent and Dependent Response and an Overall Greater Damping Capacity than Observed by Piezoelectric Composite Oscillator

The strain amplitude dependent damping behavior of Gr/Al composites has been examined by analytical models based on micromechanics, and microstructural features [Ref 7-12]. Micromechanical analysis suggested that, in the presence of residual axial tensile stress (about 20.7 MPa), microyielding could initiate in the matrix even at 10^{-4} strain level, while the composite behaves nearly in the elastic manner until the failure strain level of 3.4×10^{-3} has been attained. Various measurements of residual stresses by x-ray diffraction [Ref 7-17], acoustoelastic [Ref 7-18] and acoustic emission [Ref 7-19] indicated that in as-fabricated Gr/Al, axial residual stresses could be between 20.7 and 124.8 MPa. With these high residual stresses in the matrix, the damping response would exhibit transition at strain levels lower than 10^{-4}, as observed in Figure 7.2-1.

In addition to micromechanical approach, the strain amplitude dependent damping response has also been analyzed in terms of microstructural features (e.g., dislocations, second phase particle size and spacings) using the Granato-Lucke (G-L) model [Refs 7-2, 7-3, 7-16]. The G-L theory describes the response of a dislocation to an oscillatory stress as a vibrating string that is anchored between major

pinning points defined by tangles (or large precipitates) and impurities (or fine precipitates) are distributed as minor pinning points along the dislocation network. According to this model, dislocations vibrate about minor pinning points up to a critical strain amplitude beyond which dislocations break away from these minor pinning points and oscillate between major anchoring points, thereby providing hysteretic energy loss.

According to G-L theory, for a material subjected to the vibration in a uniform strain field, strain amplitude dependent contribution to the damping (ψ_H) is given by

$$\psi_H = \frac{C_1}{\varepsilon^n} \exp\left[\frac{-C_2}{\varepsilon}\right] \qquad (7\text{-}1)$$

where C_1 and C_2 are constants in terms of material parameters. In a plot of $\ln\{\psi_H\varepsilon\}$ versus $1/\varepsilon$ the slope C_2 provides a measure of pinning point density, and the intercept C_1 is indicative of mobile dislocation density. The exponent n depends upon the specimen length dependency of the oscillatory strain amplitude, i.e. $n = 1$ if strain amplitude is uniform (uniaxial tension-tension cycling) or $n = 1/2$ if strain amplitude is sinusoidal (piezoelectric composite oscillator). Figure 7.2-3 shows a typical G-L plot from the damping data obtained by tension-tension cycling tests. By introducing appropriate material constants, the calculated mobile dislocation density was $\Lambda \approx 6 \times 10^{13}$ $1/m^2$ for Gr/Al. This mobile value was quite consistent with the average dislocation density $\Lambda \approx 4 \times 10^{14}$ $1/m^2$ obtained by quantitative image analysis of various transmission electron micrographs [Ref 7-20]. Average dislocation density near the fiber-matrix interface was higher in the composite compared to the unreinforced 6061 aluminum alloy ($\Lambda \approx 8 \times 10^{12}$ $1/m^2$) suggesting that mobile dislocations in Gr/Al could trigger transition to strain amplitude dependence at lower strains than in an Al alloy. The high dislocation density was associated with the residual stresses that were generated during the consolidation process due to the mismatch in the CTE between the matrix and fiber. These residual stresses were accommodated by the creation of dense and tangled dislocation networks in the matrix, adjacent to the interface [Ref 7-21].

Both G-L theory and micromechanical analysis suggested that movement of dislocations or equivalently residual stresses in Gr/Al composite could be responsible for exhibiting strain amplitude dependent damping response at lower strain levels than required for 6061 aluminum alloys. Any modification of the residual stress state by appropriate heat treatment would also influence the damping response. Figure 7.2-4 shows that the [0°]₄ P55/6061 Al specimen, after a stress relieving treatment by cryogenic prestraining method, exhibited nearly strain amplitude independent damping

response even after 10^{-5} strain level in the PUCOT test. The absence of strain amplitude dependent damping compared to as-fabricated specimens (Fig. 7.2-3) could be attributed to the reduced residual stresses near the fiber-matrix interface. With a near zero residual stress state, the transition to strain amplitude dependent damping would shift to higher strain levels ($> 10^{-4}$) compared to as-fabricated specimens with tensile residual stress.

f = 1.0 Hz: $\varepsilon\psi = 0.000582 \exp (-0.00105/\varepsilon)$; R = 0.99
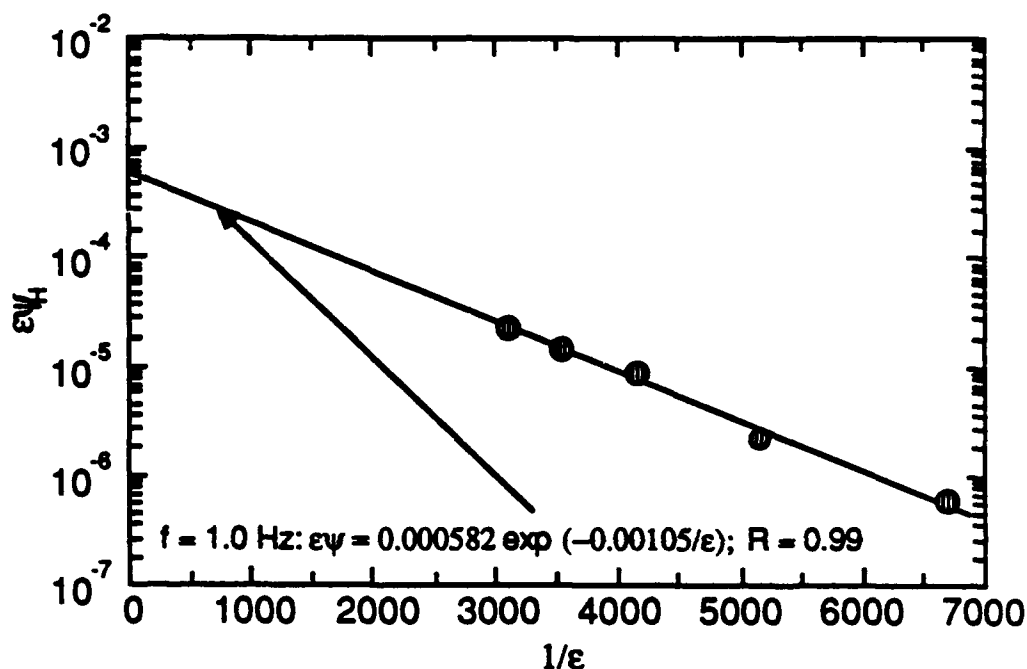
Figure 7.2-3 Granato-Lucke Plot of [0°] P55Gr/6061Al Indicating the Proper Strain Ampliutde Dependence

Similarly, damping measurements of [0°] P55/6061 Al specimens heat treated to -T6/stress-relieved condition (Fig. 7.2-5) showed the absence of strain amplitude dependence found in as-fabricated specimens. Both -T6 and -T6/stress-relieved composite specimens also exhibited similar damping response. The average damping capacity of -T6/stress-relieved composite specimens was higher than the unreinforced 6061-T625Al alloy ($\psi = 1.8\%$), although the strain amplitude independent nature of specimens was nearly identical. When the stress-relieved specimens were heat treated in accordance with the diffusion bonding process conditions, their measured damping capacity and strain amplitude dependence was found to be similar to the as-fabricated specimens. These observations of the reappearance of strain amplitude dependent damping within $1 \times 10^{-4} - 4 \times 10^{-4}$ strain amplitude suggested that the composite damping is clearly influenced by the magnitude of matrix

residual stress. The presence of the tensile residual stress state near the interface introduces a static load along the same direction as the applied force, thus triggering the strain amplitude dependent damping at low strains. By cryogenic quench treatment, the residual stress in the composite was relieved through matrix yielding, consequently the transition from strain amplitude independent to dependent damping shifted to high strain levels.
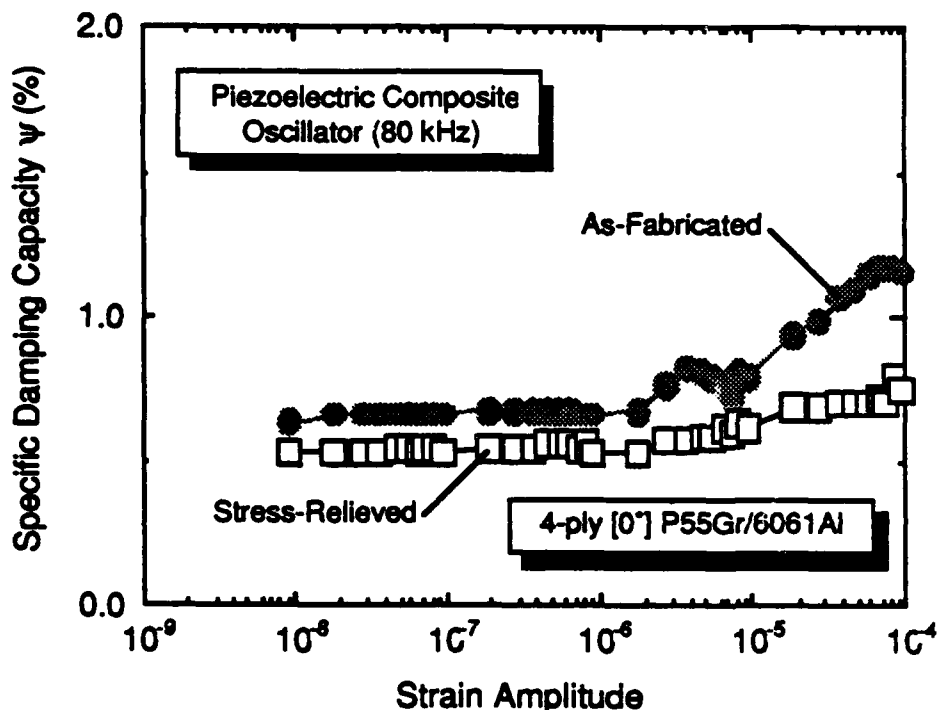
Figure 7.2-4 Damping Response of [0]₄ P55Gr/6061 Al by Piezoelectric Composite Oscillator Indicating a Lack of Strain Amplitude Dependence After Cryogenic Stress Relieving

7.3 SUMMARY

Damping measurements of as-fabricated unidirectional P55/6061 Al specimens indicated that beyond a critical strain amplitude, damping increased with increasing strain amplitude. Data analysis in terms of Granato-Lucke theory, combined with transmission electron microscopy observations, suggested that movement of dislocations in the tangled networks near the interfaces could provide the operative energy dissipation mechanism at these strain levels. These dense and tangled dislocation networks were associated with the thermal residual stresses that are generated by the differences in thermal expansion of graphite fiber and aluminum matrix.
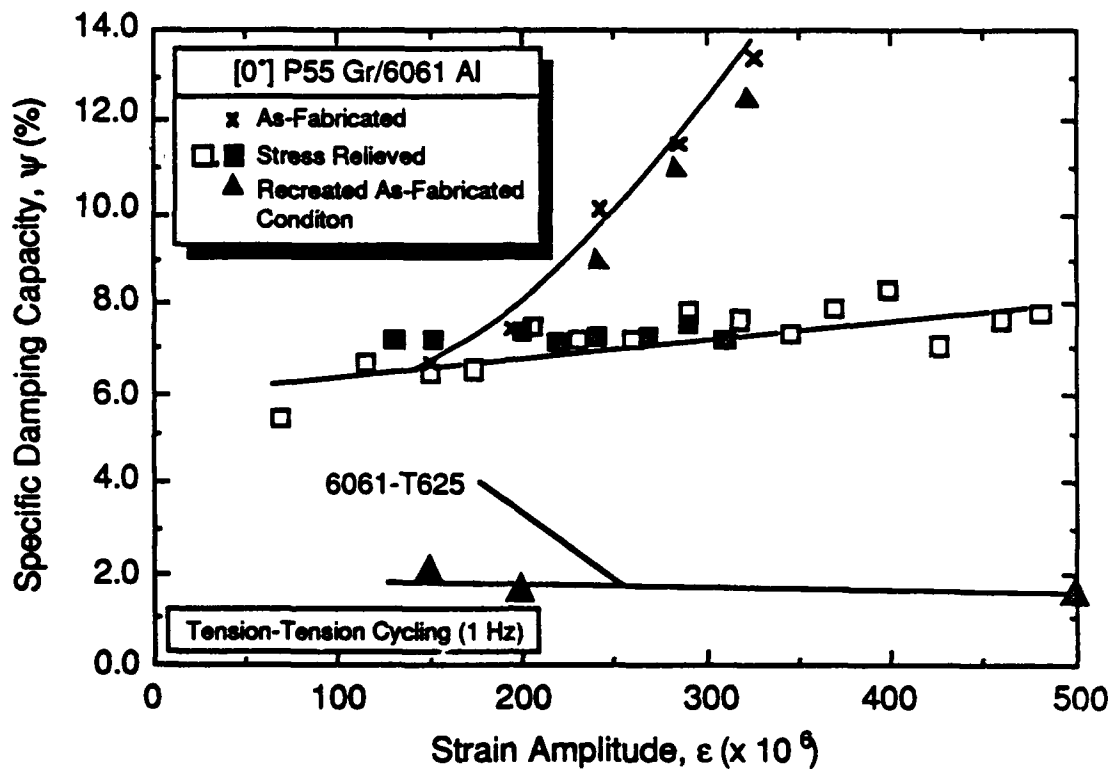
Figure 7.2-5 Damping Response of [0°] P55Gr/6061 Al by Tension-Tension Fatigue Indicating a Lack of Strain Amplitude Dependence After Cryogenic Stress Relieving and -T6 Heat Treatment

Residual stress state near the fiber-matrix interface was modified by appropriate heat treatment procedures. As-fabricated Gr/Al specimens subjected to cryogenic quench treatment to relieve residual stresses through matrix yielding showed the disappearance of strain amplitude dependent damping response when measured both by piezoelectric composite oscillator and uniaxial tension-tension cycling test methods. When the stress-relieved specimens were heated to diffusion-bonding process temperature (861 K) and slowly cooled to room temperature, their damping response exhibited the reappearance of strain amplitude dependent behavior at strains between 1×10^{-4} and 4×10^{-4}. The presence of residual stress along the axis of vibration induces strain amplitude dependent damping response at stress levels much lower than those observed in stress-relieved specimens. These observations of heat treated and as fabricated Gr/Al indicated that residual stresses play a significant role in the damping behavior of composites.

7.4   REFERENCES

7-1   M.H. Rice and G.A. Gurtman, "Residual Stresses and Thermomechanical Behavior of Metal Matrix Composites" (Report SSS-R-84-6534, Naval Research Lab, Washington, DC, Jan. 1984).

7-2   A.V. Granato and K. Lucke, "Theory of Mechanical Damping Due to Dislocations," J. Appl. Phys., 27 (1956), 583.

7-3   A.V. Granato and K. Lucke, "Applications of Dislocation Theory to Internal Friction Phenomena at High Frequency," J. Appl. Phys., 27 (1956), 789.

7-4   J.M. Roberts and N. Brown, "Low Frequency Internal Friction in Zinc Single Crystals," Acta Metall., 10 (1962).

7-5   J. Marx, Review of Scientific Instruments, 22 (1951), 503-509.

7-6   S.H. Carpenter and J.E. Fawks, "An Investigation of the Cathodic Charging of Pure Iron with Hydrogen by Modulus Measurements," Scripta Metall, 15 (1981), 699-704.

7-7   W.H. Robinson and A. Edgar, IEEE Transactions of Sonics and Ultrasonics, SU-21 (1974), 98-105.

7-8   M.R. Harmouche and A. Wolfenden, Journal of Testing and Evaluation, 13 (1985), 424-428.

7-9   J. Armstrong, "A Study of Hydrogen-Induced Cracking in Pure Iron" (Ph.D. dissertation, University of Denver, 1985).

7-10   A.K. Ray, V.K. Kinra, S.P. Rawal, and M.S. Misra, "Measurement of Damping in Continuous Fiber Metal Matrix Composites," Role of Interfaces in Material Damping, eds. B.B. Rath and M.S. Misra, ASM, Metal Park, OH, pp 995-102, 1986.

7-11   D. Barret and K. Buesking, "Temperature Dependent Nonlinear Metal Matrix Laminate Behavior" (NASA contractor report 4016).

7-12   M.S. Misra, S.P. Rawal and J.H. Armstrong, "Damping Characteristics of Metal Matrix Composites" (Final Report MCR-643, Office of Naval Research, 1986).

7-13   S.P. Rawal, M.S. Misra, and J.H. Armstrong, "Microstructure and Damping Characteristics/Relationships in Gr/Al and Gr/Mg Composites", (Paper presented at TMS/ASM-MSD Annual Meeting, Las Vegas, NV, February 28, 1989).

7-14   A. Wolfenden and M.R. Harmouche, "Anelastic and Elastic Measurements in Aluminum Metal Matrix Composites," (Paper presented at the Testing Technology of Metal Matrix Composites, sponsored by ASTM Committee D-30 on High Modulus Fibers and Their Composites, Nov. 1985).

7-15   P.W. Whaley, P.S. Chen, and G.M. Smith, "Continuous Measurement of Material Damping During Fatigue Tests," Experimental Mechanics, Dec. 1984, 342-348.

7-16   K. Lucke and A. Granato, "Dislocations and Mechanical Properties of Crystals," (ed. by J.C. Fisher, W.G. Johnston, R. Thomson and T. Vreeland, Jr., p. 425, Wiley, New York, 1957).

7-17   M.H. Rice, A. Maewal, G.A. Gurtman, and H.L. Marcus, "The Effects of Residual Stresses on the X-Ray Induced Response of Metal Matrix Composites," Final Technical Report (SSS-FTR-89-10219) Prepared for Director, Defense Nuclear Agency, Washington, DC.

7-18   S.N. Chatterjee, "Acoustoelastic Response of Unidirectional Fiber Composites," Journal of Composite Materials, 23 (1989), 588-576.

7-19   J.H. Armstrong, S.P. Rawal, and M.S. Misra, "Acoustic Emission Testing of Metal Matrix Composites" (Martin Marietta IR&D Project D-81R, Progress Report R86-48681-003).

7-20   L.F. Allard, S.P. Rawal, and M.S. Misra, "Characterization of Interfaces in Metal Matrix Composites," Journal of Metals, 38 (10)(1986), 40-42.

7-21   M. Vogelsand, R.J. Arsenault, and R.M. Ficher, "An In-Situ HVEM Study of Dislocation Generation at Al/SiC Interfaces in Metal Matrix Composites," Metallurgical Transactions A, 17A (1986), 379-389.

8.0 Acoustic Emission of MMC

CHAPTER 8.0
ACOUSTIC EMISSION FOR DAMAGE CHARACTERIZATION AND RESIDUAL STRESS MEASUREMENT OF METAL MATRIX COMPOSITES

Continuous graphite fiber-reinforced metal matrix composites (MMC) are candidate materials for use in large precision space structures (LPSS) due to their high specific mechanical properties, resistance to environmental attack, high thermal and electrical conductivities, near-zero coefficient of thermal expansion (CTE), and the potential for high damping. As with any composite, however, characterization of MMC structural integrity is more difficult than with monolithic alloys because of their complex nature. Of particular interest to investigators studying the damping response of these materials are the interfaces and the immediate surrounding region between the fiber reinforcement and matrix materials. Damping of metal matrix composites and interfacial phenomenon occurring during cyclic loading are interrelated in terms of dislocation substructure, interfacial rubbing, localized matrix yielding, and the residual stress state. Unfortunately, conventional techniques often are unable to detect or identify these phenomenon because they can only be observed *in situ*. As a result, greater emphasis is being placed on development of *in situ*, nondestructive evaluation techniques (NDE) to study composite interfaces.

Use of acoustic emission (AE) has become widespread in both industry and academia for characterization of the structural integrity of composites [Refs 8-1, 8-2 and 8-3]. Possible sources of AE in composites include matrix cracking, fiber breaking, interfacial shear and friction, interfacial bonding and extensive matrix plastic flow (Fig. 8.0-1). Applications range from research to quality control/production monitoring. In particular, AE has been used for the study of interfaces, primarily in polymeric matrix composites, but with increasing use in metal matrix composites. With the advent of computer-controlled AE data aquisition equipment and digital transient recorders, sophisticated data analysis techniques are now possible, allowing identification of damage in specimens with simple geometries [Ref 8-4].
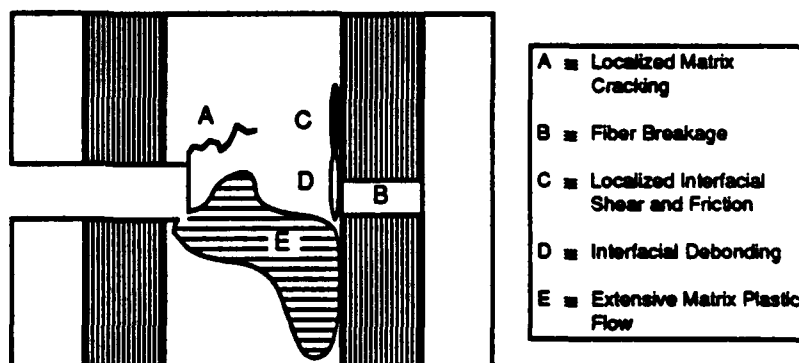
Figure 8.0-1 Schematic of Possible AE Sources and Associated Mechanisms in Metal Matrix Composites

A = Localized Matrix Cracking

B = Fiber Breakage

C = Localized Interfacial Shear and Friction

D = Interfacial Debonding

E = Extensive Matrix Plastic Flow

In this task, use of acoustic emission techniques was evaluated for unidirectional graphite fiber-reinforced metal matrix composites. Both aluminum and magnesium matrix systems were studied and the results compared to obtain unique signatures for these two types of materials. Damage initiation and progression were studied for both flat and wire specimen geometries, and deformation mechanisms were identified for metal matrix composites. Because of the identification of deformation mechanisms in these materials, a methodology was also developed for quantifying the residual stress state resulting from CTE mismatch during fabrication.

8.1   AE TERMINOLOGY

Acoustic emission is the measure of a stress wave propagating through a material resulting from a sudden release of stress. These stress waves are usually the result of cracking, dislocation breakaway, magnetic domain motion, and in composites, delamination and interfacial friction. Measurement of these stress waves is accomplished by a piezoelectric transducer that converts specimen motion (velocity or displacement) into an electrical signal. A schematic of an AE event is given in Figure 8.1-1. Some degree of noise exists in the signal as a result of amplification often as high as 100 db. Consequently, an electronic threshold is predetermined above which an AE event is detected. The number of times that this signal crosses the threshold is called counts and the peak amplitude reached is called its amplitude. With the advent of sophisticated, computerized analysis systems, a number of other parameters of the AE signal can be studied, such as the rise time of the signal (from first detection to peak amplitude) and event duration (from the signal arrival time to the time at which the signal last crosses the threshold). Further analysis can yield the energy of the event and the root-mean-square (RMS) voltage of the AE signal.
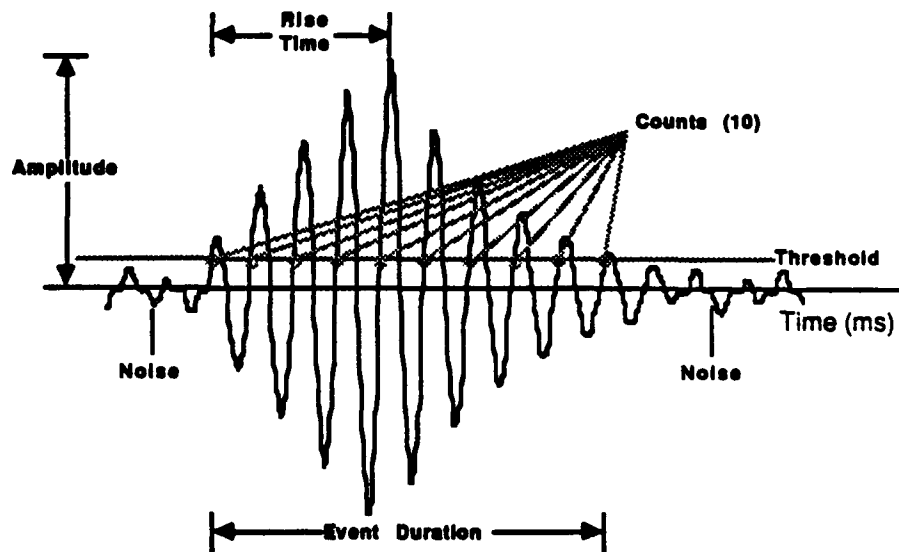
Figure 8.1-1 Schematic of an Acoustic Emission Signal Indicating Related Terminology

8-2

8.2   EXPERIMENTAL APPARATUS

8.2.1   Acoustic Emission Equipment

To measure acoustic emission from test specimens, Physical Acoustics Corporation (PAC) Micro30 piezoelectric transducers were attached to the specimen. These transducers produced an electrical signal in response to surface motion resulting from a sudden release stress within the specimen. Battery-powered Panametrics preamplifiers with switchable 20-40 db gain were used to amplify transducer signals. Coaxial cables were used throughout to minimize RF noise. Kron-Hite filters placed between the preamplifiers and the data acquisition system provided a bandpass of 100-300 kHz. A PAC 3000/3104 computer-based data acquisition system monitored the acoustic emission as a result of tensile testing. Four independent AE inputs were available and all parameters associated with AE analysis were either hardware or software-selectable. A block schematic of the parameters measured by the PAC system is shown in Figure 8.2.1-1. In addition to transducer inputs, a number of analog inputs were available. Load, strain (where possible) and rms voltage were recorded for each AE events detected. Data were digitized and stored both in internal memory and on floppy diskette. Consequently, in-depth analysis of AE data, such as energy, amplitude, count, etc. distributions can be accomplished after testing has been completed.
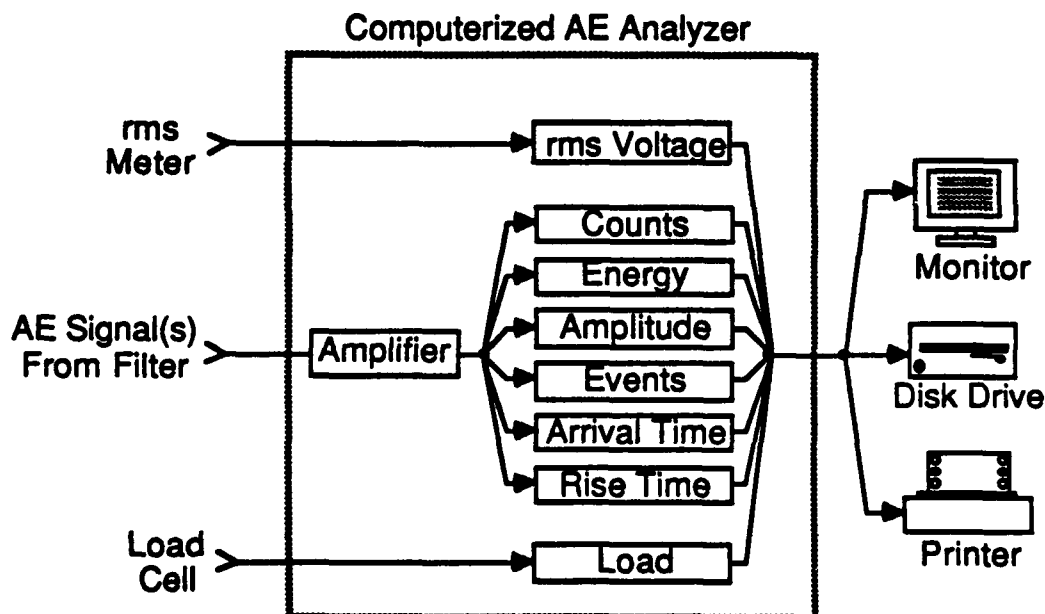
Figure 8.2.1-1 Block Diagram of Signal Inputs for the PAC3000 Acoustic Emission Data Acquisition and Analysis System

8-3

8.2.2   Mechanical Loading Apparatus

Stress necessary to activate AE mechanisms was supplied by uniaxial tensile loading. In both cases, a constant crosshead rate was maintained and a load cell monitored the resulting stress. As the experimental setups were different for the wire and flat specimen geometries, each will be discussed below.

8.2.2.1   Wire Specimen Geometry — Great care was taken so as to eliminate spurious acoustic emission and to ensure uniaxial loading of wire specimens. A 4.5 kN Instron tensile machine was used to apply load and a specially-designed gripping arrangement was used as shown in Figure 8.2.2.1-1. Cylindrical brass bearings and universal joints were used to allow rotation of the grips to ensure uniaxial loading. Special aluminum tabs were machined to allow for load transmittance to the specimen without stress concentration. Two AE transducers were placed onto the aluminum tabs with water-based acoustic couplant and held in place with constant-force spring clips. It was felt that the use of two transducers could allow AE source location. Output from the load cell was sent to the PAC 3000/3104 system. Because of the specimen geometry, it was not possible to measure the resultant strain during tensile testing.
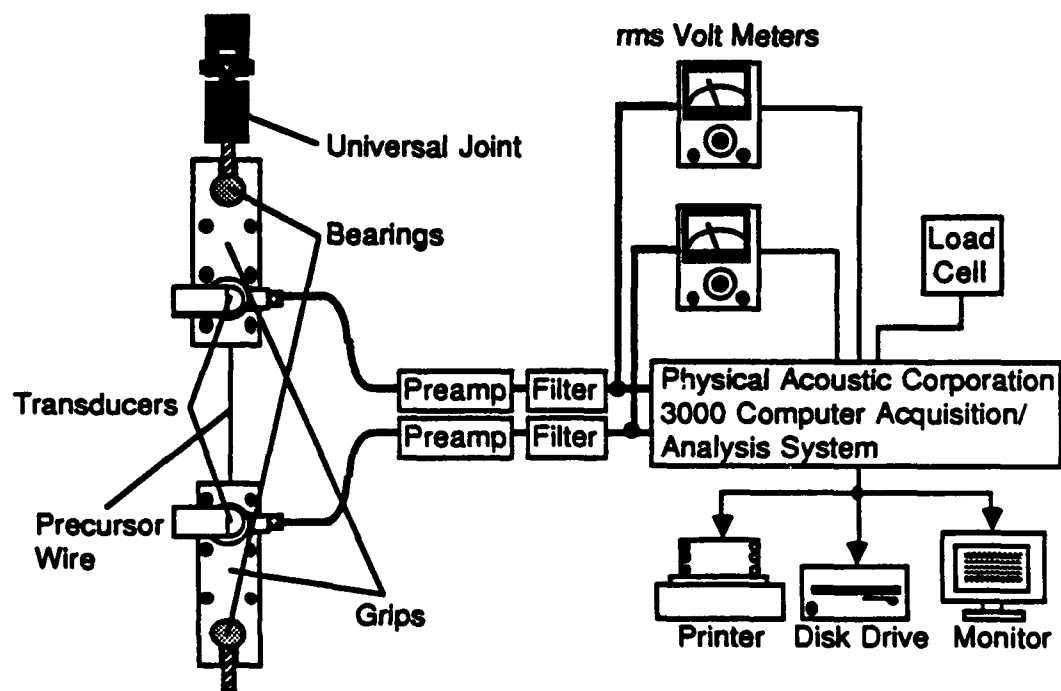
Figure 8.2.2.1-1 Schematic of the Testing Apparatus Used in the AE Analysis of Precursor Wire Specimens

8.2.2.2   Flat Specimen Geometry — In a similar fashion, flat specimen geometries were tested in tension by using a Dillon 45 kN tensile machine with a gripping arrangement shown in Figure 8.2.2.2-1. Load cell selection was dictated by the failure loads anticipated for a particular specimen type. Only one transducer was placed at the center of the gage length in each of the flat specimen tests as it was felt that there was insufficient resolution of arrival time differences to facilitate source location. As was the case with the wire geometry tests, universal joints were used to ensure uniaxial loading of the specimen. Mechanical clamp-type grips with allen head bolts secured the specimen, and the torque for each bolt was monitored during specimen mounting (22.6 N-m). RMS voltage, load cell and strain gage (standard wheatstone bridge apparatus) analog outputs were monitored by the PAC 3000/3104 system.
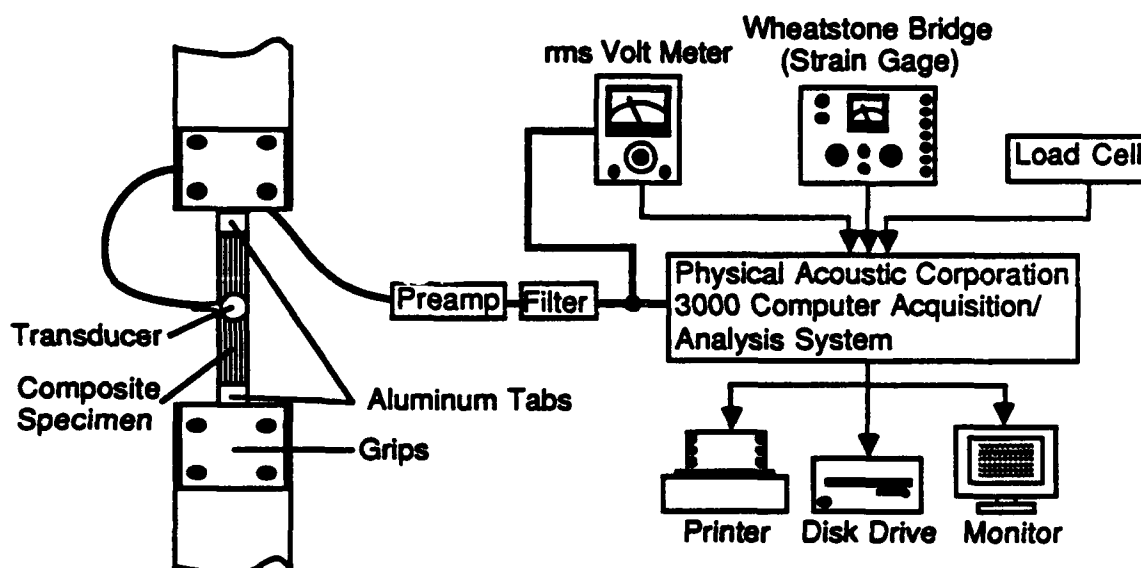
Figure 8.2.2.2-1   Schematic of the Testing Apparatus Used in the AE Analysis of Flat Specimens

8.3   SPECIMEN FABRICATION

As can be inferred from the previous section, different specimen geometries dictated different specimen fabrication procedures. However, there were techniques common to both types of specimens. A special acoustically-quiet adhesive, Dexter-Hysol EA9330.4 was used because of its lack of asbestos and its minimal binder volume (< 5%), both potential sources of spurious acoustic emission. Care was taken in both cases to minimize excess adhesive. In addition, this adhesive cured at room temperature (48 hour minimum before testing) to minimize possible thermal effects noted ear-

lier for these metal matrix composites. Specimen surfaces were hand-sanded to provide a better bonding surface. In both cases, care was exercised to ensure tab and specimen alignment during bonding and curing operations. Below the specimen fabrication procedures specific to each specimen geometry are discussed.

8.3.1 Wire Specimen Geometry Fabrication

Precursor wires of Pitch 55 Graphite and 6061 Aluminum were fabricated by Materials Concepts, Inc. from Union Carbide Thornel 2000 filament count fiber bundles. Some of the specimens were subjected to shear deformation accounting for 50% and 35% reductions. Metallographic analysis was used to determine structural integrity for both as-fabricated and shear deformed specimens. Material properties for these precursor wires are given in Table 8.3.1-1.

Material	Units	P-55S 2K (bundle)	P55Gr/6061Al (precursor)
Density	gm/cm³	2.0	2.77
Tensile Modulus	GPa	379.0	217.9*
Tensile Strength	GPa	1.72	1.02
Filament Diameter	μm	10	10
Filaments/Strand	—	2000	2000
Fiber Volume	%	—	47.98

*calculated from rule of mixtures

Table 8.3.1-1 Material Properties of P55Gr/6061Al Precursor Wires and Its Constituents

Aluminum tensile tabs for the precursor wire specimens were fabricated from 6061-T6 as shown in Figure 8.3.1-1. One section of the tabs was threaded to allow for the matching section to be bolted in place, thus securing the specimen in the tabs during bonding and to provide a mechanical bond. Alignment of the specimen to the aluminum tabs during bonding/curing operations was accomplished by an alignment jig as shown in Figure 8.3.1-2. Bottom sections (threaded) of the tabs and alignment pins were placed in the jig, adhesive was applied to the knurled surface and the specimen was placed in the alignment pins. Hold down pins were placed in the alignment pins and pressure was applied by clamps while slight tension on the specimen was maintained. Finally, adhesive was applied around the wire specimen and the top portions of the tabs were bolted into position. Pressure from the hold down pins was not remove until the adhesive had cured.

To ensure that additional damage to the specimen was not introduced during handling, an aluminum support bar was bolted to the grips prior to clamp removal. This support bar was not removed until the specimen secured in the tensile apparatus described previously in Figure 8.2.2.1-1.

Threaded Tab
Specimen
Knurled Surface
Unthreaded Tab
Allen Head Bolts
Adhesive
Bearing Surfaces
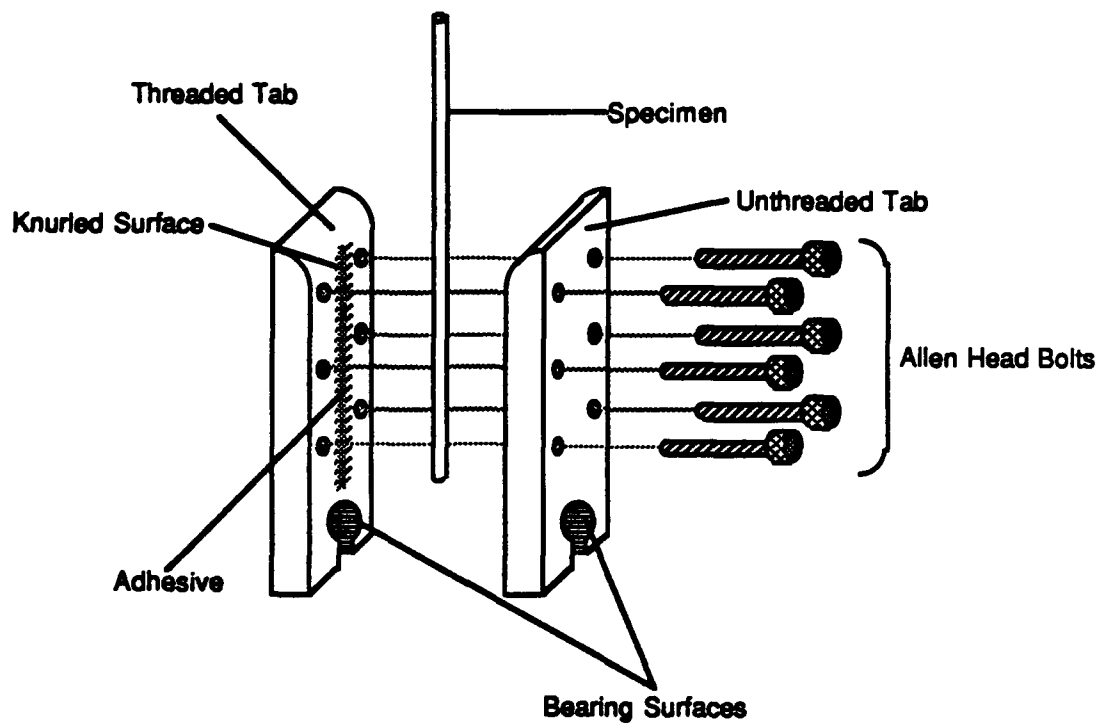
Figure 8.3.1-1 Schematic of the Aluminum Tensile Tabs Used in This Investigation for Precursor Wire Specimens

Clamp
Tabs
Specimen

Clamp
Hold Down Pin
Allen Head Bolts
Alignment Dowel
Top Tab
Specimen
Bottom Tab
Jig

Cross-Sectional View
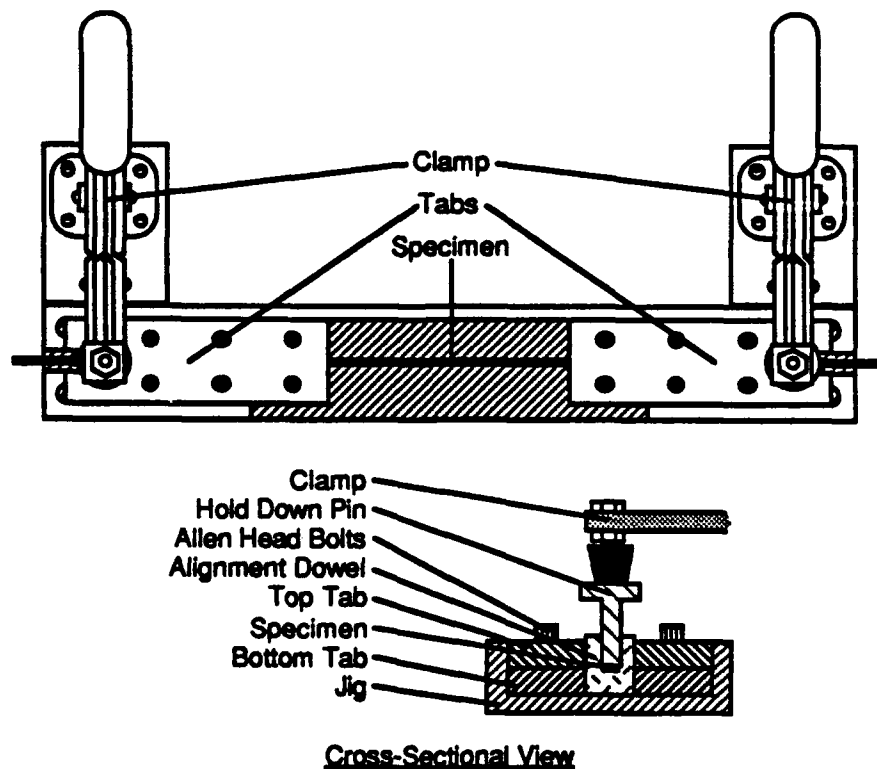
Figure 8.3.1-2 Schematic of the Alignment Jig to Ensure Proper Bonding of the Precursor Wire Specimens

8-7

8.3.2 Flat Specimen Geometry Fabrication

Single-ply unidirectional panels were cut from flat panels utilizing state-of-the-art fabrication techniques. Aluminum matrix composites were fabricated by diffusion bonding techniques by DWA Specialties, Chatsworth, CA, and magnesium matrix composites were fabricated by vacuum investment casting techniques. Specimens were tested in the as-fabricated conditions and material properties for each type of specimen are given in Table 8.3.2-1.

Table 8.3.2-1 Material Properties for Continuous Graphite Reinforced Metal Matrix Composite Flat Specimens

Material	Density (gm/cm³)	Fiber Volume (%)	Elastic Modulus (GPa)	Ultimate Strength (MPa)
Single-Ply P55 Gr/6061 Al — [0°] — [90°]	2.413	39.23	157.9 38.2	530.9 30.5
P100 Gr/6061 Al — [0°] — [90°]	2.463	34.0	255.9 37.24	640.0 57.9
P100 Gr/AZ91C/AZ31B Mg — [0°] — [90°]	1.854	26.5	223.5 33.1	573.8 100.7

Tensile tabs were fabricated from 6061 aluminum tensile tabs to minimize stress concentrations and ensure a specimen gage length of 7.6 cm. A schematic of the tensile tabs is shown in Figure 8.3.2-1. In each case, tab widths were machined to match precisely the width of the specimen which was nominally 1.3 cm. Surfaces of the specimen within the tab were hand sanded and inner surfaces of the tabs were sand-blasted to ensure proper bonding surfaces. Bond line thickness was maintained at 76 μm through the use of thermocouple wires placed along the specimen perpendicular to the loading axis. Teflon blocks were used to align the specimen and tabs during bonding and all excess adhesive was removed prior to adhesive curing. Total specimen/tab thickness was kept to 6.45 ± 0.13 mm to ensure alignment with the gripping arrangement described earlier.

0.003 Inch diameter Wires   Composite Specimen

6061-T6 Aluminum Tabs Dexter-Hysol EA9330.4 Adhesive
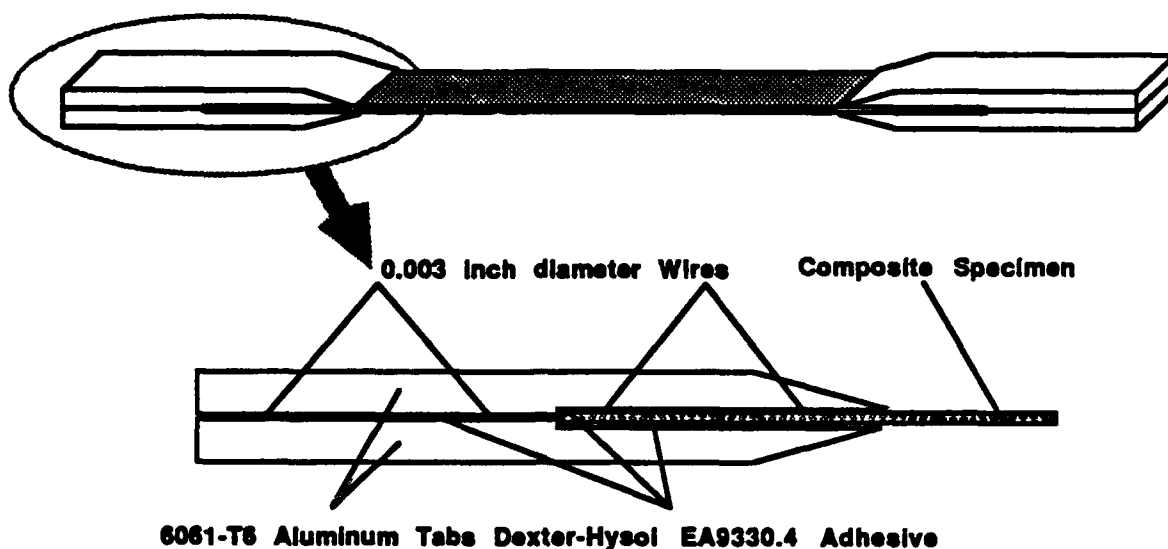
Figure 8.3.2-1 Schematic of the Aluminum Tensile Tabs Used in This Investigation for Flat Composite Specimens

8.4   RESULTS AND DISCUSSION

Initial investigations into AE of metal matrix composites focused upon damage characterization and identification of the AE sources. After sufficient information was obtained for both Gr/Al and Gr/Mg systems, this technique was employed to study the residual stress state generated during fabrication by monitoring matrix yielding.

8.4.1   Damage Initiation and Progression

AE data from both precursor wire and flat specimen geometry were obtained to monitor the initiation and propagation of damage in metal matrix composites. Both Gr/Al and Gr/Mg composite systems were utilized.

8.4.1.1   Precursor Wire Geometry — Preliminary investigations into tensile behavior of wire specimens indicated a propensity for inter-grip failure, thereby negating any useful mechanical and AE information. A "feathering" of a softer adhesive from the gage length to 1.3 cm (0.5 in.) within the tabs was shown to enhance the probability of failure within the gage length. Subsequently, only data from tests with inter-gage failure were considered for evaluation.

Acoustic emission amplitude distribution for as-fabricated precursor wire as a function of failure
stress during constant rate tensile loading (@ 0.40 N/min) is shown in 8.4.1.1-1. A low-amplitude
AE peak at approximately 33 mV appeared almost immediately upon loading and continued to grow
throughout the test. Some AE activity was observed at higher amplitudes after 50% failure stress
has been reached, resulting in a peak at 66 mV evident after 75% failure stress, which corresponds
to 447.4 MPa (64.9 ksi). After failure, the first peak amplitude was over twice that of the higher
amplitude peak.
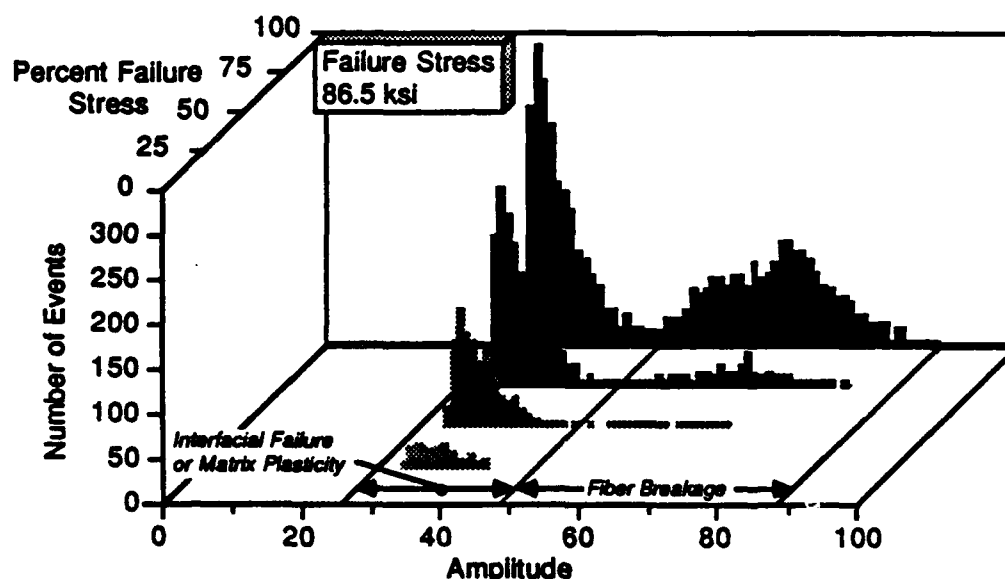
*Figure 8.4.1.1-1 Amplitude Distributions for As-Received P55Gr/6061Al Precursor
Wire Specimens at 25%, 50%, 75% and 100% Failure Stress Showing the Develop-
ment of the Two Amplitude Peaks*

Also of interest is the progression of damage in a composite when some damage is present in the
material prior to testing. This "pre damaging" of the specimen was accomplished by shear deforma-
tion of the precursor wire. Micrographs of these specimens, shown in Figures 8.4.1.1-2 and 8.4.1.1-
3 for as-received and shear deformed to 0.18 mm respectively, indicate increasing void volume and
fiber breakage with increasing shear deformation.

A comparison of amplitude distributions from Gr/Al specimens for as-fabricated and shear-
deformed conditions is given in Figure 8.4.1.1-4. Shear deformed specimens exhibited only a low
amplitude peak, while the as-received specimens exhibited both a low and high amplitude peak.

This twin peak has also been observed in the B/Al system as well [Ref 8-2]. Typical AE event summation with respect to time for as-received and shear deformed specimens is shown in Figure 8.4.1.1.5. Shear deformed specimens exhibited a higher event summation rate, but failed at a lower stress, thereby resulting in an overall lower number of total counts.
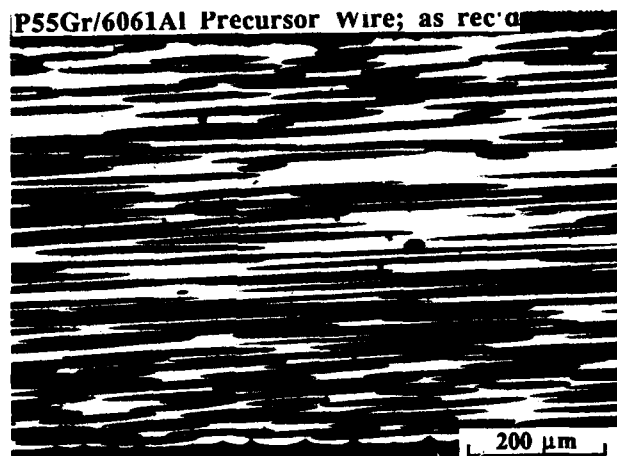
Figure 8.4.1.1-2 Photomicrograph of a Transverse Section of As Received P55Gr/6061Al Precursor Wire Indicating Good Fiber-Matrix Interfacial Bonding and No Fiber Breakage

An attempt was made to locate AE sources along the specimen gage length from arrival time differential of the two transducers. However, measurements indicated that insufficient resolution existed with these high modulus, low density materials, which in turn relates to a high velocity of sound. Possible corrections include a larger specimen gage length or a redesign of the grips, allowing for placement of the transducers in-line with the specimen axis and thereby enhancing AE transmission to the transducer. Both of these items are being addressed for future tests.
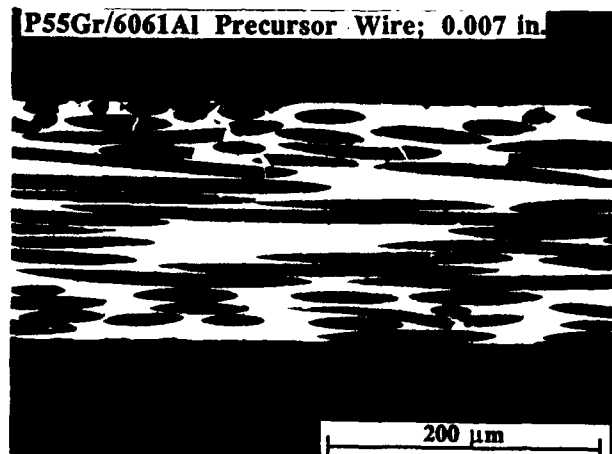
Figure 8.4.1.1-3 Photomicrograph of a Transverse Section of P55Gr/6061Al Precursor Wire Shear Deformed to 0.18 mm (0.007 in) Indicating Degredation of the Fiber-Matrix Interface and Significant Fiber Breakage

8.4.1.2   Flat Specimen Geometry — As was observed with precursor wire tests, a number of specimens fractured near or within the aluminum tabs, and thus were eliminated from further consideration. Both aluminum (diffusion bonded) and magnesium (both diffusion bonded and vacuum investment cast) matrix composites were studied in this investigation.

8.4.1.2.1 Graphite/Aluminum Matrix Composites — Damage sites in diffusion bonded P100Gr/6061Al were initiated by thermal cycling for 100 and 1000 cycles between ±250°F. Typical stress-strain behavior and corresponding RMS voltage of the AE from diffusion-bonded P100Gr/6061Al composites after 100 thermal cycles are shown in Figure 8.4.1.2.1-1. Gr/Al composites exhibit burst-like AE behavior beginning at about 1200 microstrain and RMS liftoff occurring after 1500 microstrain. Little AE activity was observed until substantial load was applied, with failure occurring at 502.8 MPa (72.9 ksi). Very little difference in the mechanical properties and the AE were observed between the 100 and 1000 thermal cycle tests as is evidenced by little change in AE rate (Fig. 8.4.1.2.1-2), indicating that no appreciable change in the damage was made by thermal cycling.

8-12
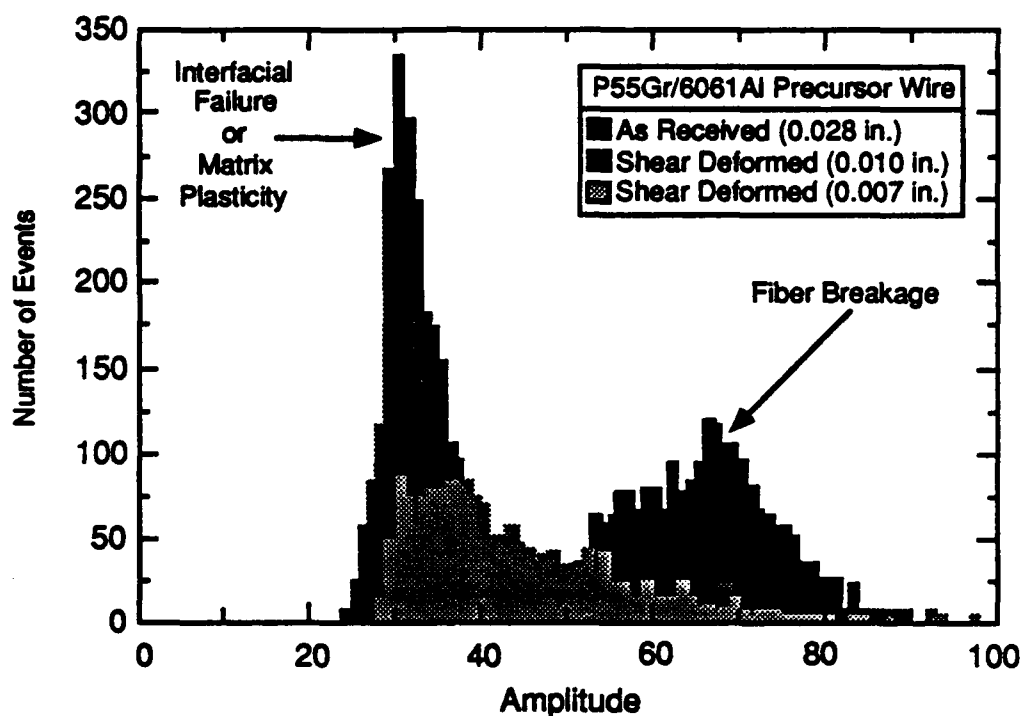
Figure 8.4.1.1-4 *Comparison of Amplitude Distributions at Failure for As Received and Shear Deformed Precursor Wires, Indicating the Elimination of the High Amplitude Peak*
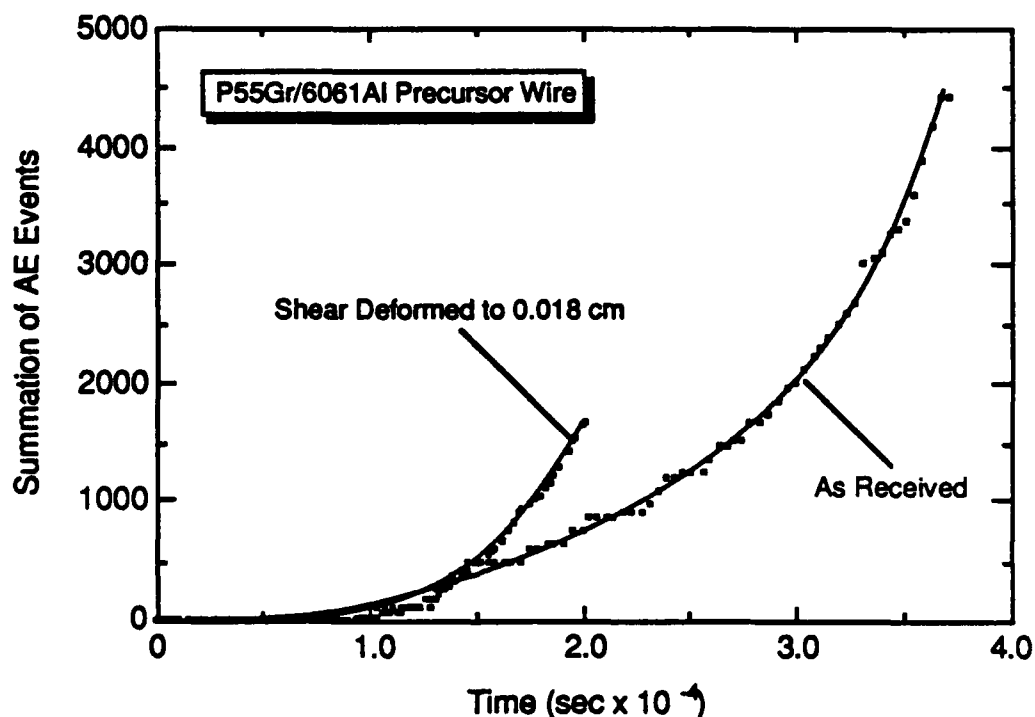
Figure 8.4.1.1-5 *Comparison of AE Event Rate for As Received and Shear Deformed Precursor Wires, Indicating a Greater AE Event Rate for Damaged Specimens*

Figure 8.4.1.2.1-1 *Stress-Strain and Corresponding rms Voltage Behavior of P100Gr/6061Al Indicating Little AE Activity at Low Stresses and rms Lift-off Near Failure*

Amplitude distributions from the 100 thermal cycle test are shown in Figure 8.4.1.2.1-3 for 50% and 100% failure stress. As was observed previously in Figure 8.4.1.2.1-1, very AE activity was observed as late as 50% failure stress. Unlike the two-peak amplitude distribution obtained for the precursor wire tests, however, the flat composite specimens exhibited a uniform distribution throughout the observed amplitudes for both 50% and 100% failure stress.

8.4.1.2.2 Graphite/Magnesium Matrix Composites — The stress-strain behavior for P100 Gr/AZ91C/AZ31B Mg (Fig. 8.4.1.2.2-1) exhibited nonlinearity until a significant stress was applied, and unlike the Gr/Al specimen tested earlier, notable AE activity was observed at lower stress levels. RMS liftoff was not as significant in the Gr/Mg composites as it was in the Gr/Al composites. A slight difference was noted in the AE event rate for the Gr/Mg system as a result of thermal cycling (Fig. 8.4.1.2.2-2) with the 1000 thermal cycle specimen having the higher event rate similar to the behavior noted in the Gr/Al precursor wire specimens.

8-14
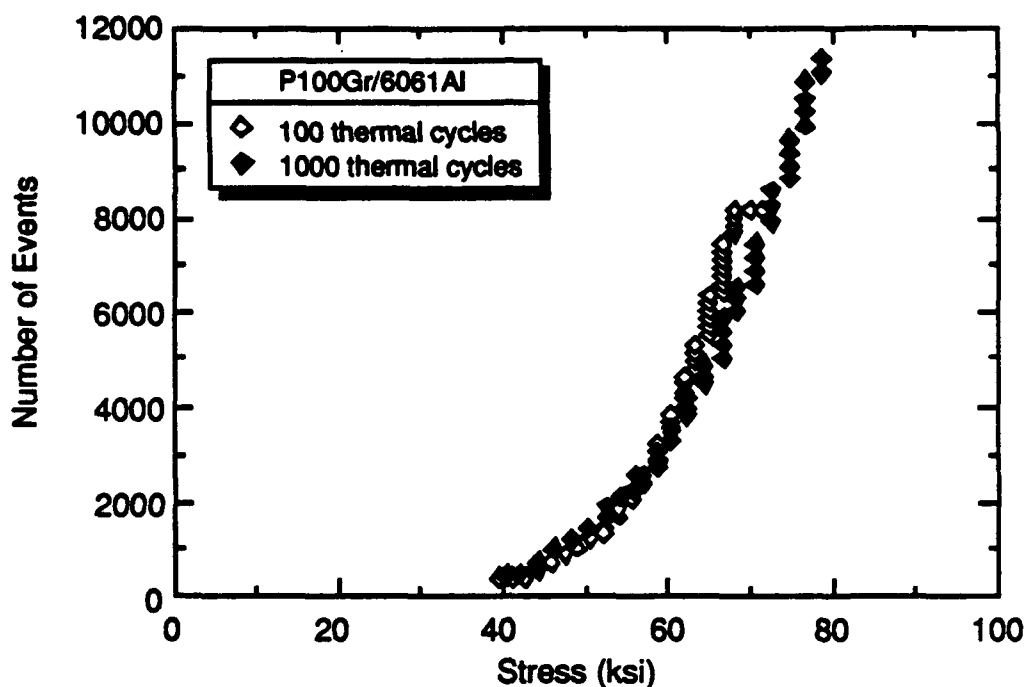
Figure 8.4.1.2.1-2 AE Event Rate for Single-Ply [0°] P100Gr/6061Al Subjected to 100 and 1000 Thermal Cycles Between ±250 °F Indicating No Discernable Change in the Damage State

Amplitude distributions for the P100 Gr/AZ91C/AZ31B Mg specimen subjected to 100 thermal cycles is shown in Figure 8.4.1.2.2-3. Unlike the Gr/Al flat specimens, a notable, lower amplitude peak was observed after 50% failure stress similar to the low amplitude peak noted in the Gr/Al precursor wire specimens. However, unlike the Gr/Al system, no distinguishable high amplitude peak was observed. At failure, the magnitude of the peak was nearly twice that of the flat distribution observed with the Gr/Al flat specimens.

8.4.2   Discussion of AE and Related Damage Mechanisms

It is reasonable to suggest that the high amplitude peak observed in precursor wire specimens was due to fiber breakage. Awerbuch, et.al. have shown single-fiber boron to exhibit only a high amplitude peak at failure, while B/Al composites exhibit both a low and high amplitude peak [Ref 8-2]. Furthermore, one would expect that the higher amplitude events would result from the breakage of the fibers which possess a significantly higher modulus than the surrounding matrix and as such

8-15

carry more strain energy to release at fiber failure. Further support for this hypothesis is given in the micrographs shown earlier (Figs. 8.4.1.1-2, 8.4.1.1-3 and 8.4.1.1-4) which show good matrix infiltration and fiber integrity for as received specimens, but shear deformation indicates significant fiber breakage which causes more load to be carried by the matrix and thus lowering the strain energy released when breakage occurs.
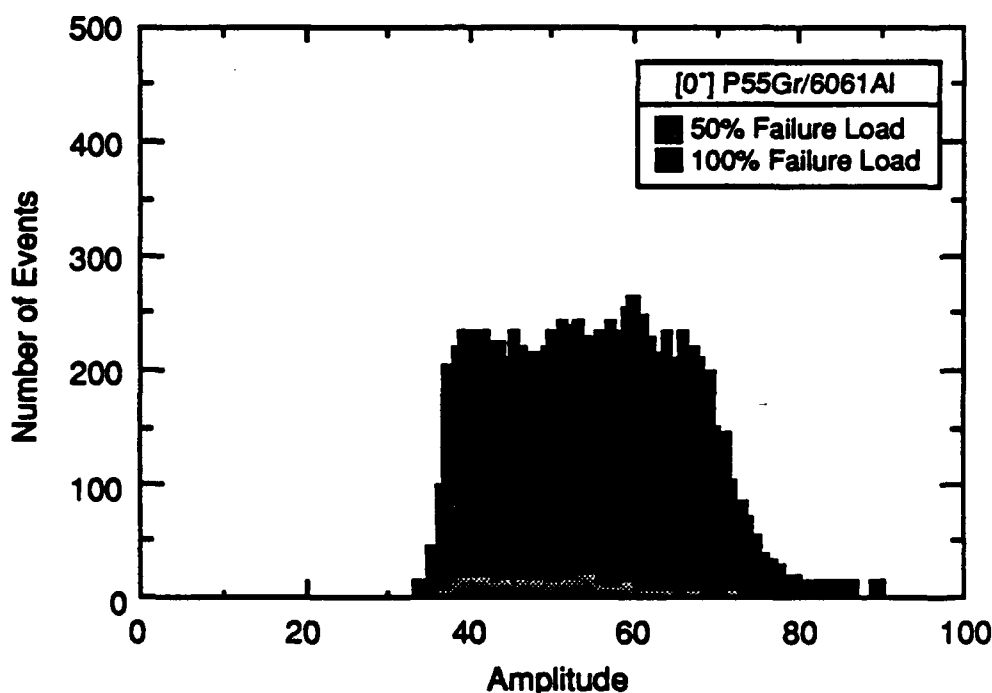
Figure 8.4.1.2.1-3 Amplitude Distribution of 2-ply P100Gr/6061Al for
50% and 100% of Failure Stress Indicating a Uniform Amplitude Distru-
bution which is Independent of Stress

The low amplitude peak observed in the Gr/Al system appears almost immediately after loading, not simultaneously with the appearance of the high amplitude peak observed in the B/Al system [Ref 8–2]. Appearance of this peak at lower stresses is an indication of residual stresses in the matrix due to a mismatch between the coefficient of thermal expansion (CTE) of the fiber (negative CTE) and matrix (positive CTE). A component of the residual stress along the fiber direction in the matrix is tensile; consequently the static residual stress in the matrix is added to the applied tensile load. Thus, within the same matrix alloy system, stress-induced AE mechanisms to appear at much lower applied stresses than found in composites with lower levels of residual stress. These AE mechanisms include matrix plasticity and interfacial failure. Moire interferometry conducted for Martin Marietta by Dr. J.S. Epstein, Idaho National Engineering Laboratory, Idaho Falls, Idaho [Ref 8-5]

showed matrix plasticity to exist near the fiber matrix interface during deformation. Also, because the interface in these composites are inherently weak, it is also logical that AE would detect the deterioration of this area.
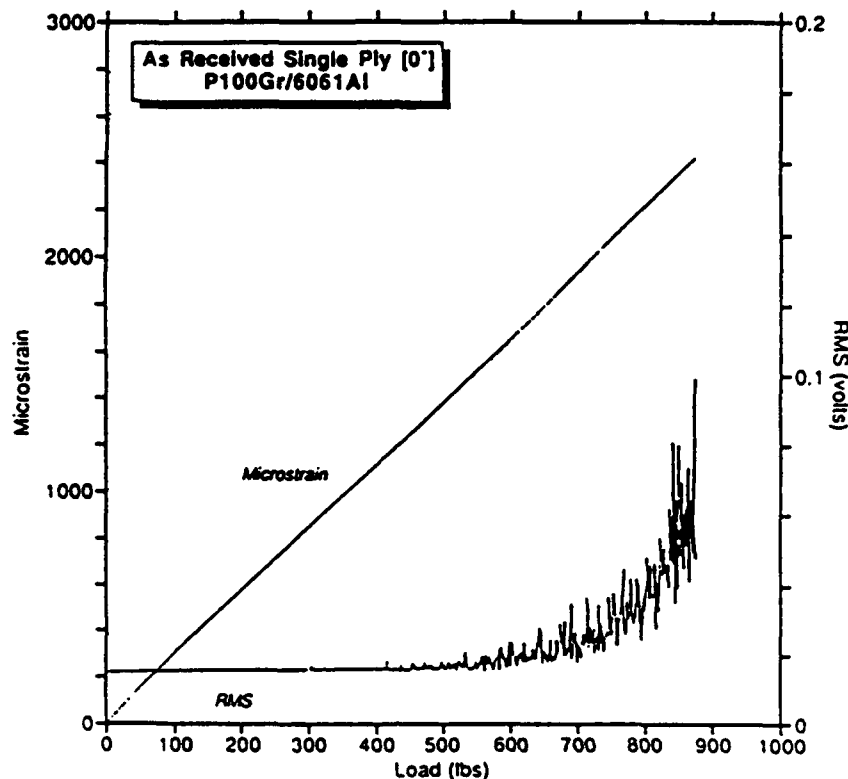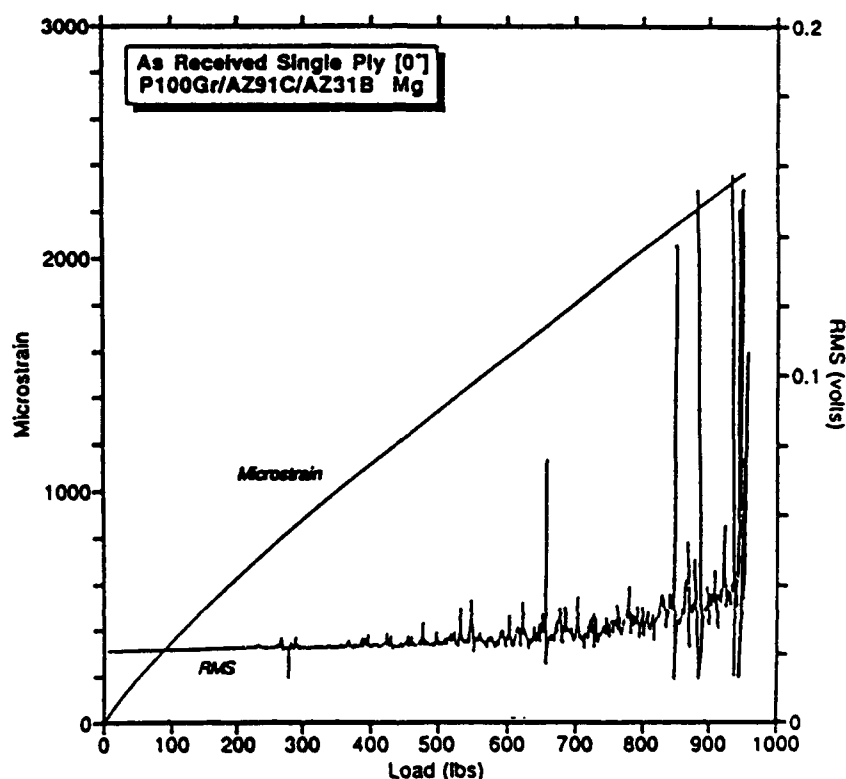

Figure 8.4.1.2.2-1 Stress-Strain and Corresponding rms Voltage Behavior of P100Gr/AZ91C/AZ31B Mg Indicating AE Activity at Low Stresses and Only Slight rms Lift-off Near Failure

Other differences between these tests can be observed. Lack of a definite two-peak amplitude distribution in the Gr/Al flat specimens may indicate that deterioration of the diffusion-bonded interface not found in the precursor wire tests. Presence of a middle amplitude peak, when added to lower amplitude peaks from interfaces and matrix plasticity, and higher amplitude peaks from fiber breakage, could obscure the two-peak behavior observed in the simpler system. Also, the larger low-amplitude peaks observed in the Gr/Mg specimens could be due to the differences in the AE behavior of aluminum and magnesium. While most of the AE behavior of aluminum occurs at yield, it is possible in certain orientations for magnesium to exhibit burst-like AE behavior at stresses far below yield [Ref 8-6].
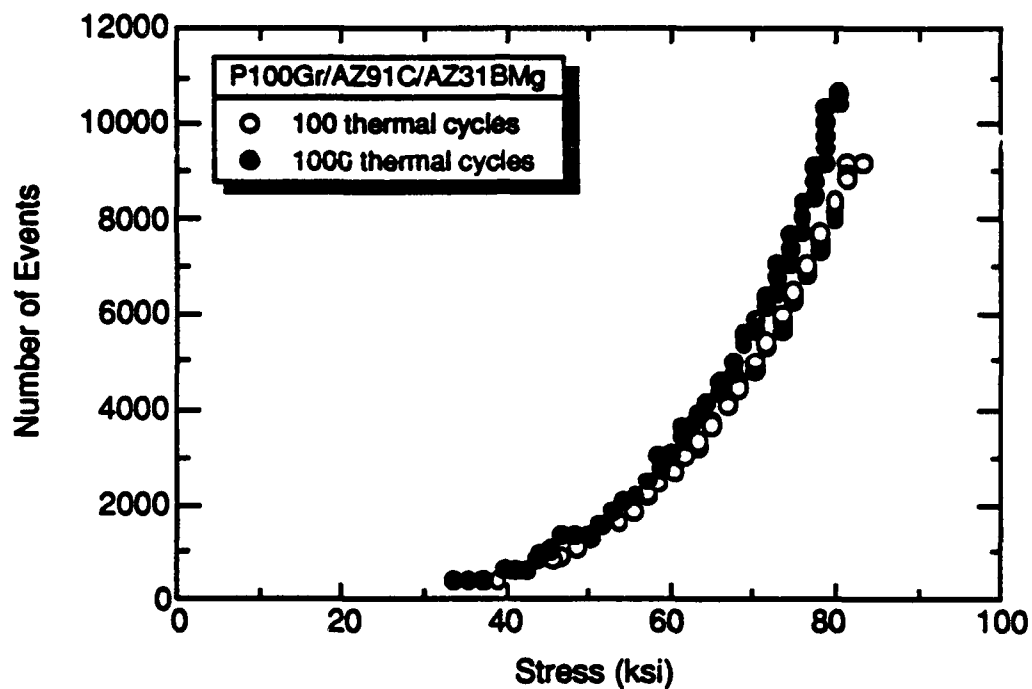
Figure 8.4.1.2.2-2 AE Event Rate for P100Gr/AZ91C/AZ31B Mg for Both 100 and 1000 Thermal Cycles Indicating a Slight Increase in AE Activity for the 1000 Thermal Cycle Specimen
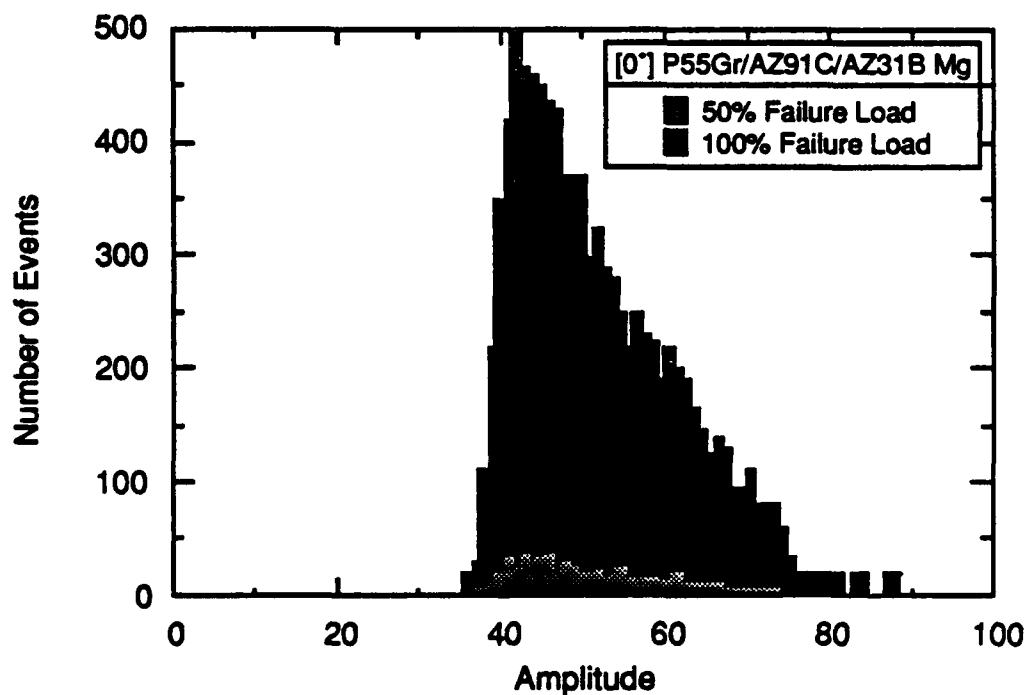
Figure 8.4.1.2.2-3 Amplitude Distribution of P100Gr/AZ91C/AZ31B Mg for 50% and 100% of Failure Stress Indicating a Peak at 43 mV

8.4.3   Measurement of Residual Stress Using AE Technology

Residual stresses in metal matrix composites can affect their mechanical and dynamic response. Of particular interest for this investigation is the interaction between residual stresses and damping. Residual stresses can significnatly affect the strain amplitude dependent damping response. Also, as discussed above, the amount of residual stress in the matrix material can affect the amount of external applied stress required to activate AE mechanisms, particularly those in the matrix alloy. For example, if the presence of an rms peak at matrix yield typical of 6061 alloys [Ref 8-7] can be observed, the amount of stress required for yield in the monolithic alloy minus the amount of stress borne by the matrix when yielding is detected should indicate the amount of tensile residual stress in the matrix. Thus, it was the intent of this part of the investigation to monitor this AE processes that can be used to identify the amount of residual stress in metal matrix composites.

8.4.3.1 Modifications to Equipment — The conventional AE setup for composite materials shown earlier in Figure 8-3.2.2-1 did not detect the presence of a peak in rms at low stresses which would be indicative of matrix yielding. Lack of detection of this phenomenon is primarily due to the fact that low gain amplification typically used with composites to minimize data "clipping" may not be sufficient to detect this peak. Thus, a slight modification to the equipment is necessary.

To ensure the detection of any low-amplitude phenomenon without losing high amplitude data, a second rms meter circuit was added (Fig. 8.4.3.1-1). Furthermore, a high-speed AET Phoenix IBM AT-controlled AE data acquisition and analysis system was used in lieu of the slower PAC 3000 system. In addition to the obvious advantage of speed, the Phoenix system allows digitized rms data to be recorded, thereby allowing comparison of two simultaneous signals at different gain.

8.4.3.2 Material Selection — For this investigation, as-fabricated 4-ply unidirectional diffusion bonded P55Gr/6061Al, and 8-ply vacuum investment cast P55Gr/Mg-1.0%Mn (Gr/M1A) and P55Gr/Mg-0.6%Zr (Gr/K1A) composites were chosen. In each case, X-radiography was used prior to AE testing to verify collimation of fiber tows, fiber integrity and matrix infiltration.

8.4.3.3 AE Analysis — Stress-strain behavior of diffusion-bonded flat [0°] P55Gr/6061Al with the resultant rms voltage from acoustic emission is shown in Figure 8.4.3.3-1. The presence of a small peak in rms was observed, beginning at about 8 ksi applied stress. A higher gain plot (100 db) is shown in Figure 8.4.3.3-1 (inset). Aside from this rise in rms, AE activity was relatively low, similar to behavior observed earlier (Fig. 8.4.1.2.1-1).
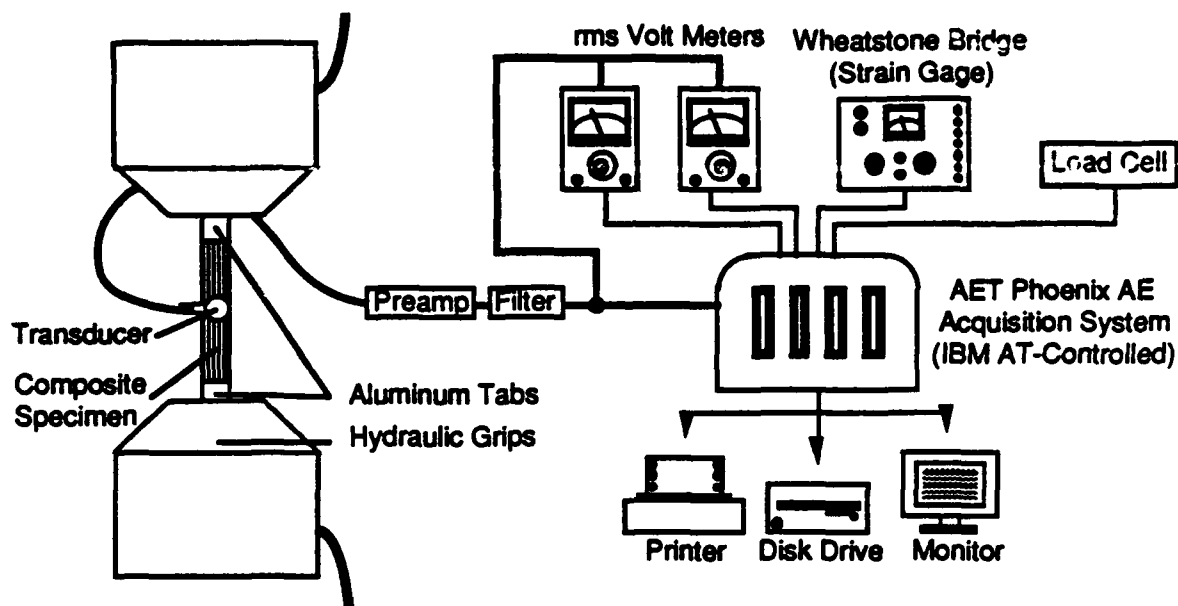
Figure 8.4.3.1-1 Schematic of the AE Apparatus Used to Quantify the Residual Stresses in Gr/Al and Gr/Mg
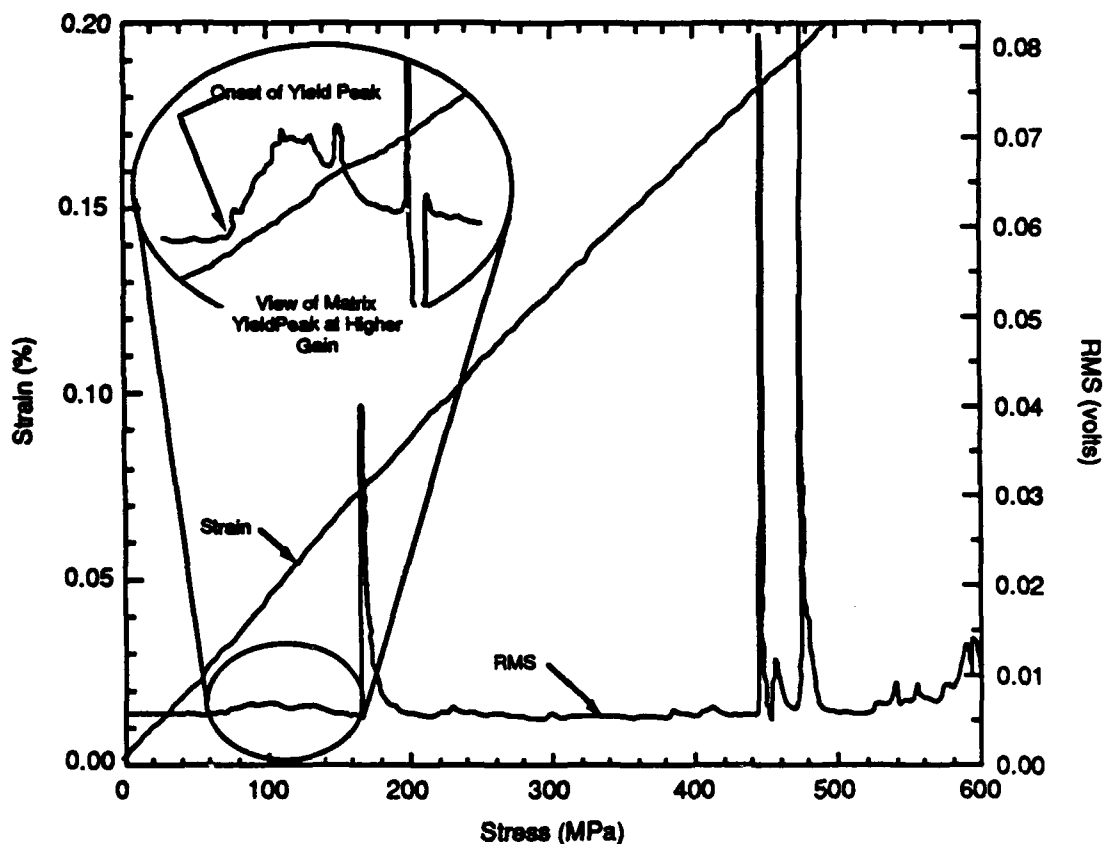
Figure 8.4.3.3-1 Stress-Strain and rms Behavior of 4-ply [0°] P55Gr/6061Al Displaying a Slight rms Liftoff and the Presence of an rms Peak Beginning at Approximately 8 ksi Stress. Inset Shows Same Peak at Higher Gain

In comparison, testing of Gr/K1A specimens under identical conditions did not result in any sort of rms peak (Fig. 8.4.3.3-2), although some liftoff is noted along with burst-type behavior at approximately 38 ksi applied stress. Most of the AE activity throughout the test was of the burst variety, with some activity occurring as low as 10 ksi.
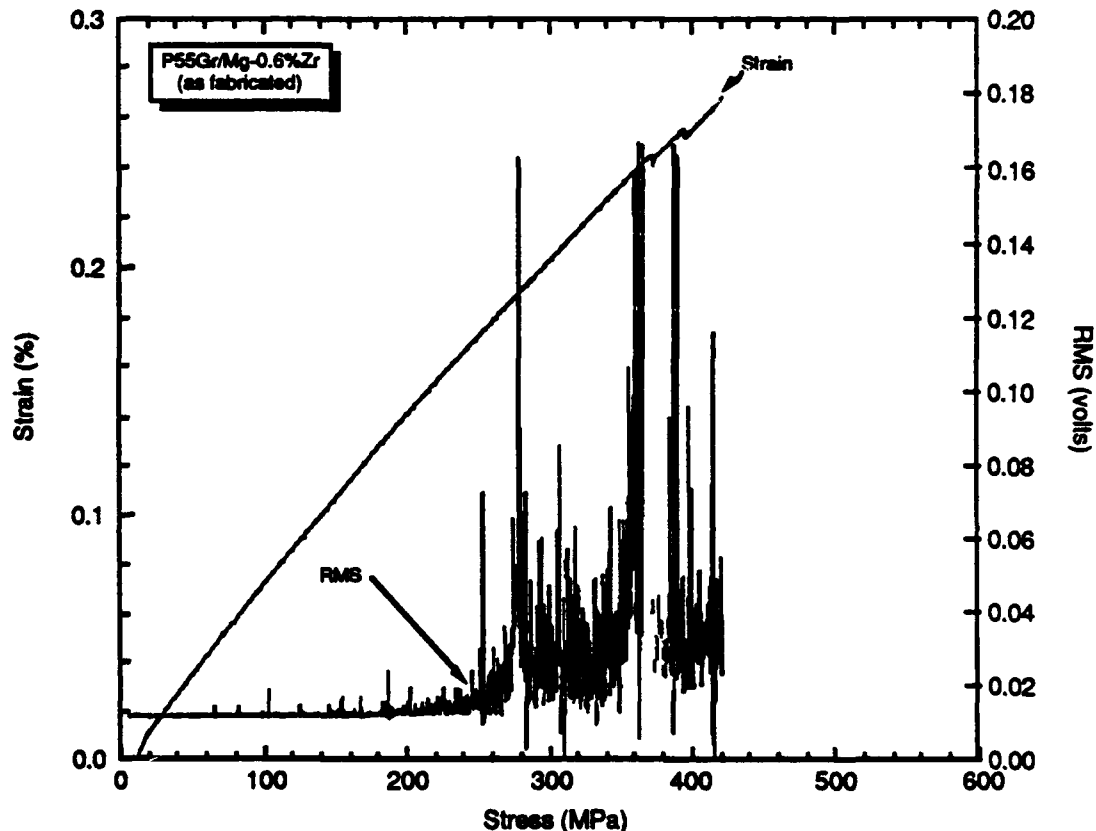
Figure G5.3.3-2 Stress-Strain and rms Behavior of Cast [0°] P55Gr/Mg-0.6%Zr Displaying a Slight rms Liftoff at Higher Stresses than Observed in the Gr/Al System, Indicating Lower Residual Stresses are Present

8.4.3.4 Determination of Residual Stress — The premise behind the use of acoustic emission to determine the axial component of the residual stress is that any stress-related mechanisms (such as matrix yielding, interfacial failure, etc.) are affected by the biasing stress supplied by the residual stress. Provided that (1) the chosen stress-related mechanism can be detected by AE, (2) this phenomenon can be measured in the monolithic matrix alloy as well, and (3) the stress borne by the matrix can be determined, then AE can be used to quantify the residual stresses by noting the differences between the activation stresses in the alloy and the composite.

8-21

Given that the strain in the fiber and matrix should be continuous at the fiber-matrix interface (good interface), then the stress borne by the fiber can be related to that of the matrix by the follow ing relationship:

$$\sigma_f = \sigma_m \frac{E_f}{E_m} \tag{8-1}$$

where E_f = elastic modulus of the fiber, and E_m = elastic modulus of the matrix. In addition, the following relationship between the stress components and the fiber volume V_f can be obtained from a free-body diagram:

$$\sigma_f = \frac{\sigma - \sigma_m \left(1 - V_f\right)}{V_f} \tag{8-2}$$

where σ is the total composite stress. These two equations can be solved simultaneously to obtain the relationship between the applied stress and the stress borne by the matrix

$$\sigma_m = \sigma \left[\frac{E_m}{E_f V_f + E_m \left(1 - V_f\right)} \right] \tag{8-3}.$$

Given the values of E_m = 69.0 GPa (10 Msi), E_f = 379.2 GPa (55 Msi), and V_f = 39.2%, this indicates that σ_m = 36.2% σ for Gr/Al. With the onset of the rms peak occurring at a composite stress of 55.2 MPa (8 ksi), suggesting that the matrix is experiencing a stress of 20 MPa (2.9 ksi).

In precipitation-strengthened aluminum alloys, two types of AE behavior are observed. Heiple, Carpenter, and Carr [Ref 8-7] have identified the mechanisms of acoustic emission for precipitation-strengthened alloys, including 6061 Al, as a function of matrix heat treatment. The first type of behavior observed is a peak in acoustic emission rms voltage coinciding with the onset of plastic flow. In these materials, Cottrell atmospheres provide unpinning of dislocations which result in the sudden release of energy as dislocations avalanche at the onset of plastic flow. A second AE mechanism in precipitation-strengthened aluminum alloys is the inclusion fracture and/or debonding. As shown in Figure 8.4.3.4-1, AE and yield stress of 6061 Al is affected by heat treatment. Acoustic emission in these materials decreases with aging because growth of the precipitates reduces the solute concentration, thereby reducing the Cottrell atmospheres. Accordingly, yielding of the mono-lithic 6061 aluminum alloy occurs at a variety of different stresses, depending upon the temper of
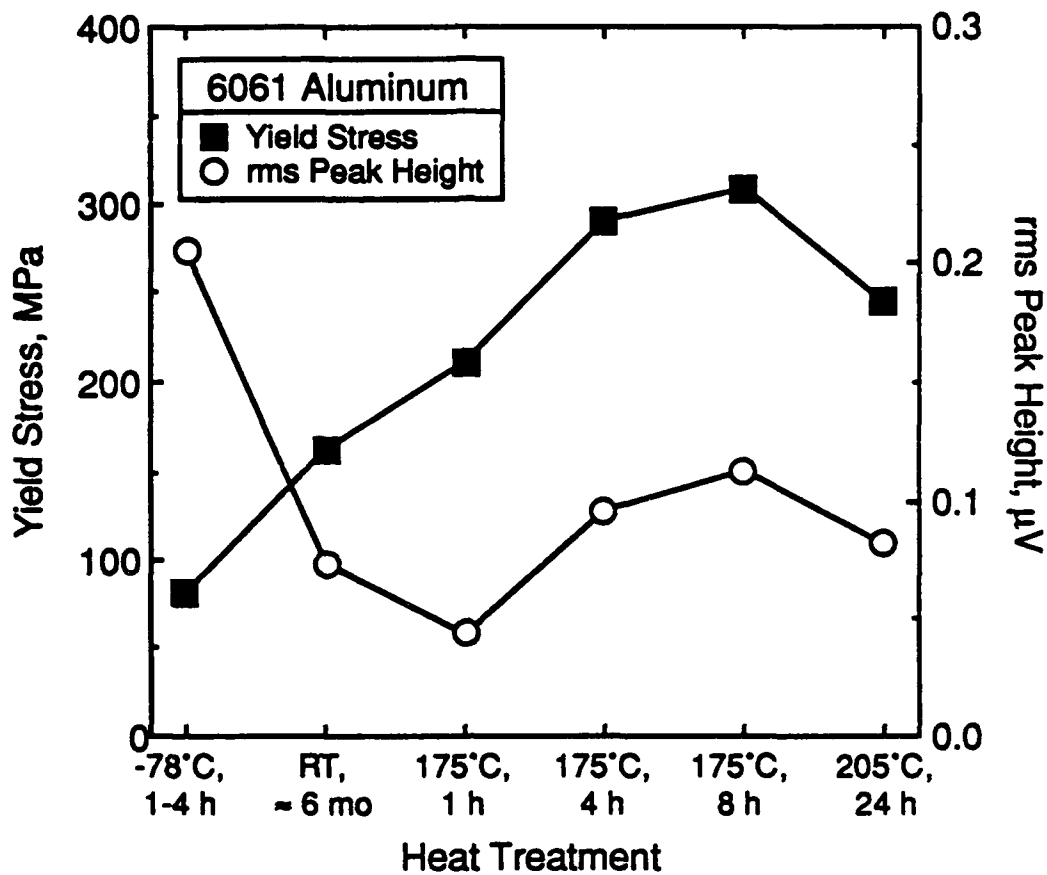
Figure 8.4.3.4-1 Acoustic Emission and Yield Strength of 6061 Aluminum as a Function of Heat Treatment

the matrix. For example, yielding occurs at 55.2 MPa (8 ksi) for 6061-0 and 144.8 MPa (21 ksi) for 6061-T4 (solution heat treated, naturally aged). While there is discussion as to the actual temper of the matrix in a composite, it is possible that either 6061-0 [Ref 8-8] or 6061-T4 from natural ageing could be the condition of the matrix. Because the matrix stress is well below either of the yield stresses of the monolithic alloys, the axial component of the residual stress (tensile) must contribute to the applied axial stress during tensile testing to cause matrix yielding. Thus, the axial component of the residual stress would range from 35.2 MPa to 124.8 MPa (5.1 ksi to 18.1 ksi), depending on matrix temper (6061-0 or 6061-T4 respectively). These results , particularly the higher range of values, coincide well with other measurements and calculations of the residual stresses in metal matrix composites [Ref 8-8].

Unlike the Gr/Al test, the Gr/K1A specimen did not exhibit a distinct rms peak at low stress levels. Acoustic emission from magnesium alloys is highly orientationally dependent [Ref 8-6], and as such may not exhibit the distinct matrix yielding peak observed in the Gr/Al system. However, some rms liftoff did occur at 262 MPa (38 ksi). With an average fiber volume of 46.1%, and a matrix modulus of 44.2 GPa (6.41 Msi), Equation 8-3 yields a matrix-borne stress of only 22.3% σ. Therefore, at the appearance of this rms peak, the matrix is experiencing a stress of 58.4 MPa (8.47 ksi). With a yield strength of 83.0 MPa (12 ksi) for die-cast K1A alloy, the matrix-borne stress must have been assisted by a residual stress of 24.6 MPa (3.53 ksi). This low residual stress is not surprising, as residual stresses in these materials from CTE mismatch during fabrication should be low due to the low matrix elastic modulus and low yield stress. Furthermore, it would be expected for cast composites to have inherently lower residual stresses than those fabricated by a diffusion-bonding process.

8.5   SUMMARY

Acoustic emission (AE) technology has been utilized to monitor the initiation and progression of damage in Gr/Al and Gr/Mg composites. During tensile loading, operative damage mechanisms include matrix yielding, interfacial degradation, and fiber breakage. A low amplitude AE rms voltage peak which appears immediately after loading was indicative of matrix yielding and interfacial degradation. Initiation of this peak in Gr/Al composite wires at low loads was possible because of a static tensile preload contributed by residual stresses. A higher amplitude rms peak was attributed to fiber breakage. This two-peak behavior changed dramatically as damage was introduced into the specimens by shear deformation, where the event rate increased by virtue of the weaker fiber-matrix interface. Fiber breakage was virtually eliminated as an AE mechanism as evidenced by the elimination of the second, high amplitude peak.

Residual stresses are an important aspect in metal matrix composites because they affect their mechanical and dynamic behavior. Because AE mechanisms in metal matrix composites are stress-activated, phenomenon such as residual stresses near the fiber-matrix interface can affect AE response of deformation mechanisms. By using a reproducible AE mechanism such as matrix yielding, attempts were made to quantify the amount of residual stresses in the composite. Estimated residual stress values for the [0°] P55Gr/6061Al system ranged from 35.2 MPa to 124.8 MPa (5.1 ksi to 18.1 ksi), depending on matrix temper (6061-0 or 6061-T4 respectively). The higher range of

8-24

residual stress values agree well with results from the literature. Similar analysis of the [0°] P55Gr/Mg-0.6%Zr (Gr/K1A) resulted in a residual stress value of only 24.6 MPa (3.53 ksi). These experiments suggested that AE analysis can be used to provide a reasonable estimate of residual stresses in metal matrix composites where yielding of the matrix alloy produces a distinct AE signature.

8.6   REFERENCES

8-1   R.B. Clough, F.S. Biancaniello and H.N.G. Wadley, "Measurement of Fiber Fracture and Fiber-Matrix interface Shear Strengths in Metal Matrix Composites," Proceedings of Non-destructive Testing and Evaluation of Advanced Materials and Composites Conference, U.S. Air Force Academy, Colorado Springs, CO 1986, pp. 91-102.

8-2   J. Awerbuch, "Fatigue Damage Progression in Metal-Matrix Composites," presented at SDIO/IST Advanced Composites Program Review, Woods Hole Study Center, June 2-3, 1986.

8-3   M.A. Hamstad, "Quality Control and Nondestructive Evaluation Techniques for Composites - Part VI: Acoustic Emission - A State-of-the-Art Review," AVRADCOM Report # TR83-F-7, May 1983.

8-4   J.B. James, Ph.D. Dissertation, Department of Physics, University of Denver, August 1985.

8-5   M.S. Misra, S.P. Rawal and J.H. Armstrong, "Damping Characteristics of Metal Matrix Composites," Martin Marietta Denver Aerospace Report MCR-86-634, November 1986.

8-6   M.A. Friesel, "Acoustic Emission in Magnesium and Titanium," Ph.D. Dissertation, University of Denver, Denver, CO, August, 1982.

8-7   C.R. Heiple, S.H. Carpenter, and M.J. Carr, "Acoustic Emission from Dislocation Motion in Precipitation-Strengthened Alloys," Metal Science, Vol 15, pp. 587-598 (1981).

8-8   M.H. Rice and G.A. Gurtman, "Residual Stresses and Thermo-Mechanical Behavior of Metal-Matrix Composites," Naval Research Laboratory Report SSS-R-84-6534, January, 1984.

9.0 High Damping Pitch Gr Fibers

CHAPTER 9.0
HIGH DAMPING PITCH GRAPHITE FIBERS

Vibrational energy dissipation processes in a composite include contributions from different operative mechanisms in its constituent phases, namely fiber, matrix and interfaces. The dynamic response of a linear anelastic (or viscoelastic) composite in terms of their constituent properties can be predicted by Hashin theory [Ref 9-1]. Using a correspondence principal, Hashin has derived expressions to determine effective complex moduli of fiber-reinforced materials directly for the composite effective elastic modulus by replacing the elastic modulus of the phases by their complex moduli. For unidirectional composites, the axial specific damping capacity ψ_{11} is expressed as the sum of contribution from fiber and matrix:

$$\psi_{11} = \left[\frac{E_f}{E_{11}}\right] \cdot \psi_f V_f + \left[\frac{E_m}{E_{11}}\right] \cdot \psi_m (1 - V_f) \qquad (9-1)$$

where
E_f = Fiber Modulus
ψ_f = Fiber Damping
E_{11} = Axial Composite Modulus
ψ_f = Fiber Damping
ψ_m = Matrix Damping
V_f = Fiber Volume.

In this moduli weighted rule of mixture, damping contribution from fiber constitutes the dominant term because E_f/E_m ratio is often between 5-15. During cyclic loading of Gr/Al or Gr/Mg composites, most of the vibrational strain energy is stored in the high modulus pitch fibers. Therefore improvements in energy dissipation from fibers would significantly influence the damping response of composite.

Recent measurement of fiber damping at NASA Lewis Research Center [Refs 9-2,9-3] indicated that P55, P100, and P120 fibers generally exhibit low damping. For example, P55 graphite fibers tested at room temperature at 207 Hz exhibited a damping of $\psi \approx 0.15\%$. Typical damping response of pitch fibers between -200°C and 400°C (Fig. 9.0-1) shows baseline response and a characteristic peak @ about -70°C, that can be attributed to microstructural transformation from rhombohedral structure to hexagonal close-packed structure [Refs 9-4, 9-5].
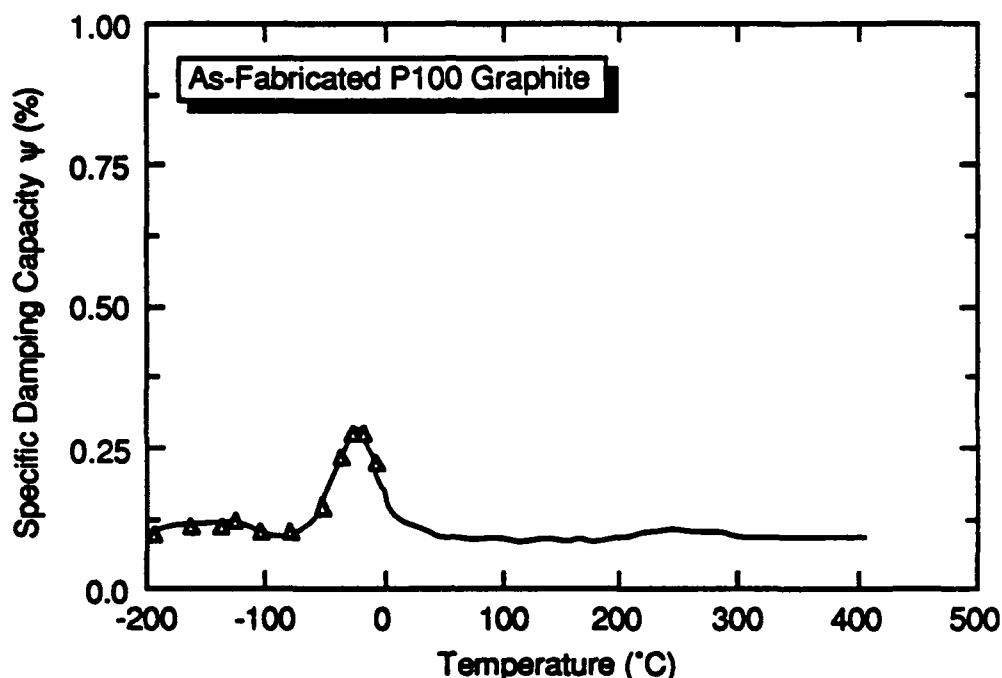
Figure 9.0-1 Typical Damping Response of As-Received Graphite Fibers

In terms of the role of damping capacity of constituents, an improvement in fiber damping provides an effective approach to enhance damping capacity of composite. For example, the modulus-weighted rule of mixture for damping described by Equation 9-1 indicates that a contribution of ψ = 2.0% from the fiber is equivalent to the contribution from matrix damping capacity of 30.8% (based on P100Gr/Al). Among the lightweight metallic materials, only pure magnesium with large grain size ($\geq$ 40 μm) exhibits such high damping at these relatively low strain amplitudes ($\sim10^{-5}$). However, magnesium matrix grain size is small ($\leq$ 5 μm) when incorporated in a composite because it is governed by the interfiber spacing, and as such the in-situ matrix damping capacity is generally less than 10%. Therefore, the most effective approach would be to enhance fiber damping and sustain that level in the composite. Fiber damping measurements by Leisutre et al [Ref 9-3] indicate that intercalated Gr fibers do exhibit improvements in damping.

9.1   INTERCALATION OF GRAPHITE FIBERS

Intercalation is the systematic insertion of guest atoms or molecules between the graphene (hexagonal) planes in a graphite host material. Often strong oxidizing agents such as nitric acid or bromine are used to chemically modify the pitch fibers [Refs 9-6,9-7]. The intercalate species serve as either

9-2

a donor or acceptor, greatly increasing the number of carriers in the graphene planes while the carrier mobility is reduced to a lesser degree. As a result of intercalation, the thermal, electrical, and mechanical properties of the graphite host can be altered significantly. For example, by selecting the proper intercalate, the electrical conductivity of the graphite host can be increased by more than a factor of 20 [Ref 9-8].

It appears that mobile carrier species associated with increased interplanar spacing may provide a mechanism of damping in pitch graphite fibers. Leisutre et. al. [Ref 9-3] observed that pitch fibers modified by intercalation process exhibit an order of magnitude increase in damping as compared to as-processed pitch 100 fibers (Fig. 9.1-1). Damping response of intercalated fibers also shows the characteristic rhombohedral to hcp peak at low temperature (-70°C) and a high temperature (200°C) peak that could be associated with intercalant movement or sliding between the graphene planes. But after heating the fiber above 300°C, the measured damping gradually drops down to baseline level because the intercalant tends to escape from the pitch fibers. Because temperatures well in excess of this will be experienced during consolidation, an innovative process must be developed to seal in the intercalants before these high damping fibers can be incorporated into metal matrix composites.
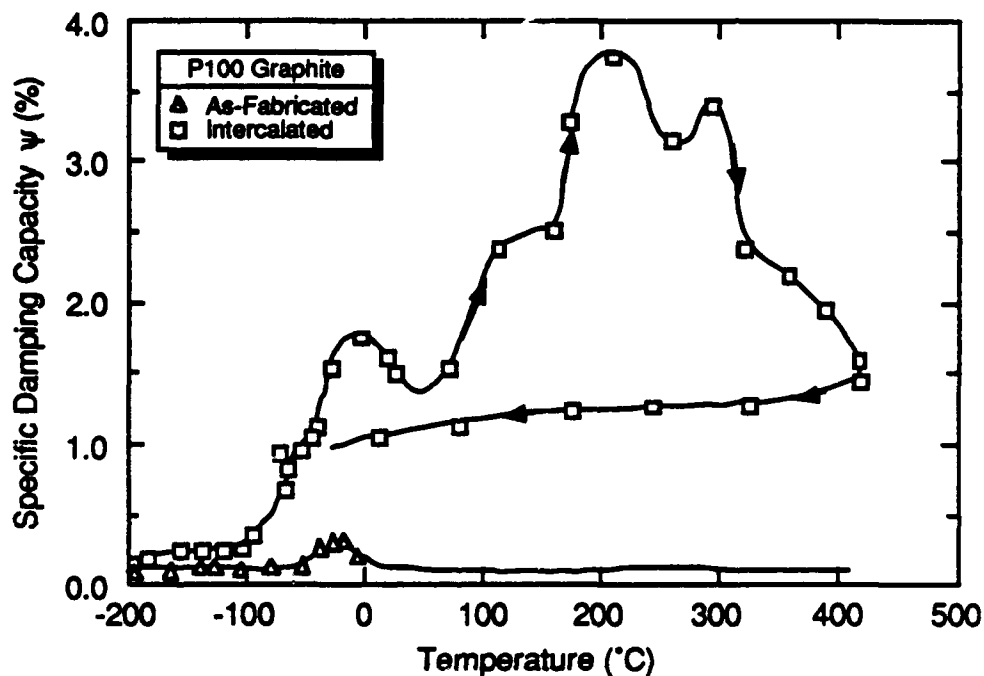
Figure 9.1-1 Damping Response of Intercalated Graphite Fibers Indicating a Significant Increase in Damping

9.2 FABRICATION AND TESTING OF HIGH-DAMPING FIBERS

In an attempt to seal the intercalants, brominated pitch fibers were plated with electroless nickel at Martin Marietta. An average plating thickness on each fiber was 75Å, and the temperature of plating bath was maintained below 100°C. Damping capacity of the plated-intercalated fiber was measured in the flexural test setup at NASA Lewis Research Center [Ref 9-9]. Preliminary test measurement at different temperature indicated that baseline damping capacity of coated fiber was comparable to unintercalated fibers, and still showed the characteristic peak at about -70°C (Fig. 9.2-1). The low damping could be due to the nickel sheath which experiences the maximum strain during flexural vibration. Also, it is likely that residual intercalant level in the coated fiber is less than as-brominated fiber, if the intercalant had escaped slowly, even at 100°C. Therefore, to exploit the high damping of intercalated fibers in a composite, innovative methodologies must be developed to seal the carrier species within the fiber, before incorporation into a metallic matrix.
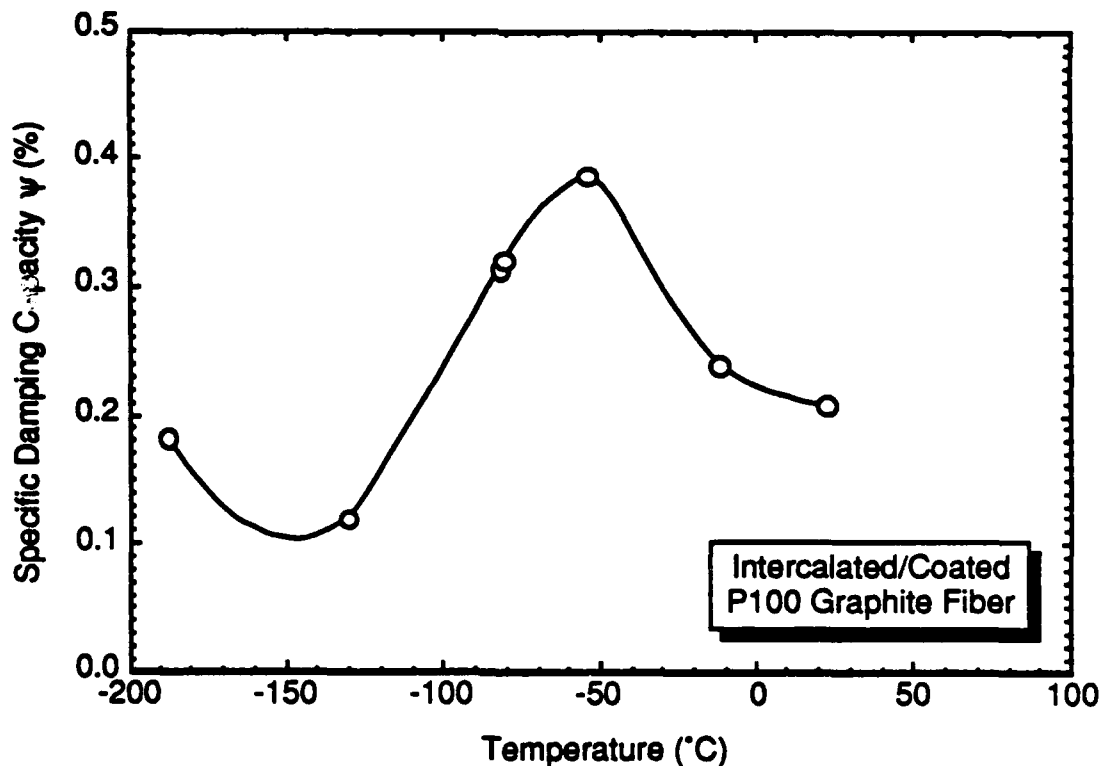
Figure 9.2-1 Damping Behavior of Intercalated/Nickel Coated Fibers Exhibiting Low Damping Response

9.3 SUMMARY

An increase in fiber damping would provide a significant contribution to the total damping of a graphite fiber reinforced metal matrix composite because the fibers are sites of the highest strain energy. Preliminary experiments have indicated that intercalated (brominated) graphite fibers exhibit an order of magnitude increase in damping when compared to as-processed pitch fibers. Brominated pitch fibers were plated with electroless nickel at Martin Marietta in an attempt to seal the intercalants at low temperatures prior to preparing precursor wires. Damping capacity of the plated-intercalated fiber was measured in the flexural test setup at NASA Lewis Research Center. Preliminary test measurement at different temperature indicated that baseline damping capacity of coated fibers were comparable to unintercalated fibers, and still showed the characteristic peak at about -70°C. The low damping could be due to the nickel sheath which experiences the maximum strain during flexural vibration. Also, it is likely that residual intercalant level in the coated fiber is less than as-brominated fiber, if the intercalant can escape slowly even at 100°C. Therefore, to exploit the high damping of intercalated fibers in a composite, innovative methodologies must be developed to seal the carrier species within the fiber, before incorporation into a metallic matrix.

9.4 REFERENCES

9-1   Z. Hashin: "Complex Moduli of Viscoelastic Composites - II Fiber Reinforced Materials," International Journal Solids and Structures, Vol. 6, No. 6, p. 797 (1970).

9-2   J.A. DiCarlo: NASA Lewis Research Center, private communication, Jan. 15, 1987.

9-3   G.A. Leisutre, A.E. Eckel, and J.A. DiCarlo: "Temperature Dependent Damping of Some Commercial Fibers," presented at 12th Annual Conference of Composite Materials and Structures, Cocoa Beach, FL, Jan. 21, 1988.

9-4   P. Millet, R. Schaller, and W. Benoit: Journal De Physique, Collogue C9, Suppliment au n°12, Tomme 44, pp C9-511, Dec. 1983.

9-5   R. Shcaller and W. Benoit, Material und Technik, 13, 1985, pp 63-71.

9-6   D.A. Jaworske, J.R. Gazer, C.C. Hung, and B.A. Banks: "Properties and Potential Applications of Brominated P100 Carbon Fibers," SAMPE quarterly, Vol. 18, No. 1, October 1986, pp 9-14.

9-7   J.R. Baier: "Stability of Bromine Intercalated Graphite Fibers," NASA TM-86859, 198

9-8   J. Shioya, H. Matsubara, and S. Murakima: "Properties of AsF_5 - Intercalated Vapor Grown Graphite," Synth Met., 14, pp 113-123, 1986.

9-9   A. Eckel, NASA Lewis Research Center, OH, Private communication Nov. 7, 1988.

10.0 Characterization of Interfaces in Metal Matrix Composites

CHAPTER 10.0
CHARACTERIZATION OF INTERFACES IN METAL MATRIX COMPOSITES

The interface consists of the bond between fiber and matrix, and the immediate region adjacent to the bond. Various micromechanical models of a composite assume no fiber-matrix reaction, zero thickness and a strong bond at the interface. In reality, the interfacial region has finite thickness with a chemical, electrical or mechanical-type of bond. In metal matrix composites (MMC), fiber surfaces are often modified by a coating to promote bonding, while still maintaining both physio-chemical and mechanical compatibility with the matrix. On the basis of these considerations, the interface is defined as "the region of significantly changed chemical composition that constitutes the bond between the matrix and reinforcement for transfer of loads between these members of the composite structure" [Ref 10-1].

The interfacial bond and its stability are affected by different thermal treatments and fabrication processes such as diffusion bonding and casting. In Gr/Al composites, heat treatment at temperatures above 550°C results in an interfacial chemical reaction leading to formation of carbides, and the degradation of graphite fibers and mechanical behavior of composites [Refs 10-2, 10-3, and 10-4].

Fabrication methods also introduce voids disbonds, and the residual stress state at the interfaces. Residual stresses are generated because of differences in coefficients of thermal expansion between the fiber and matrix, and lead to the creation of dense dislocation networks adjacent to the interface. During the fabrication process, roughness of the fiber surface may entrap gases that eventually diffuse through the matrix and lead to the formation of voids at the interface. Thus, fiber-matrix interfaces in MMC are a unique site of residual stresses, associated dislocation substructure, and the microstructural features such as voids, disbonds, impurities, and second-phase precipitates.

These interfacial features may also be various sources of energy dissipation mechanisms during cycling loading. Therefore, interface structure needs to be examined to identify specific sources of damping mechanisms in metal matrix composites. Analytical transmission electron microscopy (TEM) with its capabilities for high-resolution imaging, electron microdiffraction, and energy-dispersive spectroscopy for elemental analysis of particles and phases, is an excellent tool for microstructural characterization of composites. TEM has been used to study interfacial characteristics, such as aluminum carbide formation in heat-treated Gr/Al [Ref 10-4], composite microstructure [Ref 10-5], dislocation generation at interfaces in discontinuous SiC/Al composites [Refs 10-6 and 10-7] and dislocation substructure in both diffusion-bonded and cast Gr/Mg composites [Ref 10-8].

Therefore, TEM was used to examine inte. facial integrity, precipitate morphclogy and dislocation substructure in both diffusion-bonded Gr/Al and cast Gr/Mg composites. A methodology was also developed to determine dislocation densities near the interfaces by weak-beam imaging technique, because dislocation motion plays a significant role in damping mechanisms [Refs 10-9, 10-10, and 10-11].

10.1   EXPERIMENTAL PROCEDURE

10.1.1 Material

Test specimens of Pitch 55 Gr/6061 Al composite were prepared from single-ply unidirectional diffusion-bonded flat plate fabricated by DWA Composite Specialties, Inc., CA. During the fabrication process, Gr/Al precursor wires were consolidated between 0.0035-in. thick 6061 aluminum face sheets at 588°C temperature and 3.5 ksi applied pressure for 20 minutes, yielding a composite plate of 39% fiber volume. Similarly, test specimens of P55Gr/Mg-0.6% Zr (Gr/K1A) and P55Gr/Mg-1% Mn (Gr/M1A) were also prepared from eight-ply unidirectional flat plates that were fabricated by Material Concepts, Inc., Columbus, OH, using a vacuum casting technique.

10.1.2 TEM Specimen Preparation

Thin-plate Gr/Al and Gr/Mg composites were prepared for transmission electron microscopy by first preparing a "sandwich" from three slices, nominally 5.0 mm wide, cut from a single plate, using Torr-Seal epoxy to bond the slices. The sandwich was clamped together and heated to 60°C for 2 hours to cure the Torr-Seal. Wafers, nominally 300-microns thick, were cut from these sandwiches, using a slow-speed, diamond-wafering saw. All wafers were cut so the carbon fiber axis was extended in the plane of wafer. These specimens were attached to a support planchet using a low-temperature melting wax, and were precision ground, first on 30-micrometer then on 15-micrometer diamond-impregnated disks, using a precision polishing attachment for the Buehler Mini-Met polishing device. With this technique, parallel-sided specimens could be obtained that were less than 100-microns thick. Three-millimeter disks were cut from these thin slices using a slurry coring drill, and the disks were dimpled using amond pastes down to 1-micron size to form a specimen that was nominally 20-microns thick at the center of the dimpled region. A single-hole graphite washer was then attached to the dimpled specimen, using Torr-Seal with a 24-hour cure to provide support for the delicate specimens during further handling. These specimens were milled to perforation in a

Gatan Dual-Ion Mill, using 5-kV argon ions at 12-degrees incidence angle. These conditions were found to be critical to produce many interface regions in a typical specimen that were electron transparent in both graphite fiber and matrix regions.

Each test specimen contained relatively smooth matrix regions and did not exhibit the formation of an uneven or "hillock" surface structure which is typical of ion-milled metal specimens. During all stages of the specimen preparation process, care was taken to minimize any mechanical deformation or specimen heating that might change bulk dislocation structures. Dislocation characteristics of bulk structures can be retained in such thin specimens by minimizing mechanical or thermal trauma [Refs 10-6, 10-7, and 10-12]. A Philips 420T analytical transmission electron microscopy (TEM), operated at 120 kV was used for all microstructural observations.

10.2   RESULTS AND DISCUSSION

Ion-milled thin specimens of Gr/Al and Gr/Mg composites were examined by TEM to characterize graphite fibers, second-phase precipitates, interfaces, and the attendant dislocation substructure.

10.2.1   Pitch Graphite Fiber

The high-resolution image (Fig. 10.2.1-1) of graphite fiber in both diffusion-bonded Gr/Al and Gr/Mg composites revealed a typical turbostratic structure [Ref 10-13] of pitch-based carbon fibers showing sheet-like distribution of crystalline domains. These domains are sheets of graphite with 0.34-nm lattice spacings consistent with the (002) basal plane spacings as indicated by the properly oriented electron diffraction pattern (inset) in Figure 10.2.1-2. Such crystalline sheets are distributed throughout the fiber, essentially extending parallel to the fiber axis, and are 3 to 10-nm wide, separated by generally amorphous carbon as indicated by the dark field image of the same region (Fig. 10.2.1-2).

10.2.2   Interface Structure

A typical interface in a Gr/Al composite is shown in Figure 10.2.2-1, adjacent to the matrix that contains mostly equiaxed precipitate particles. This image suggests that the specimen surface is relatively smooth and clearly electron transparent over large specimen regions. Near the interface, the

graphite fiber is very thin, increasing in thickness toward the center of the fiber. The thin dark band directly at the interface is the original surface coating applied by a chemical vapor deposition (CVD) technique to act as a bonding layer. In various Gr/Al specimens examined by TEM, no voids have been observed at the fiber-matrix interface, indicating good microstructural integrity. Most of the TEM images of graphite fiber structure do not exhibit defects, although Figure 10.2.2-1 reveals an unusual void in the fiber. A narrow matrix region bordered by two graphite fibers is shown in Figure 10.2.2-2a, revealing a dark plate-like precipitate at the fiber-matrix interface. Also, the dark field image of the same interface region shows the fine grainy appearance of CVD layer (Fig. 10.2.2-2b).
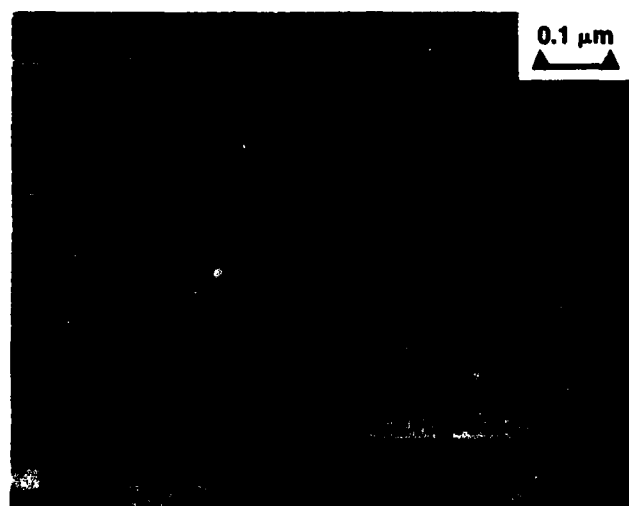
Figure 10.2.1-1 The Graphite Structure Showing Crystalline Sheets Parallel to the Fiber Axis and a Properly Oriented Diffraction Pattern Inset Indicating the Orintation of the Basal Planes Relative to the Fiber Surface

Figure 10.2.1-2 Transmission Electron Microphotograph of a Crystalline Sheet in Graphite Fiber Showing 0.34 nm Basal Plane Lattice Fringes (a Properly Oriented Diffraction from this Region is Shown in Inset)

Fiber Matrix Interface ➔

1µm
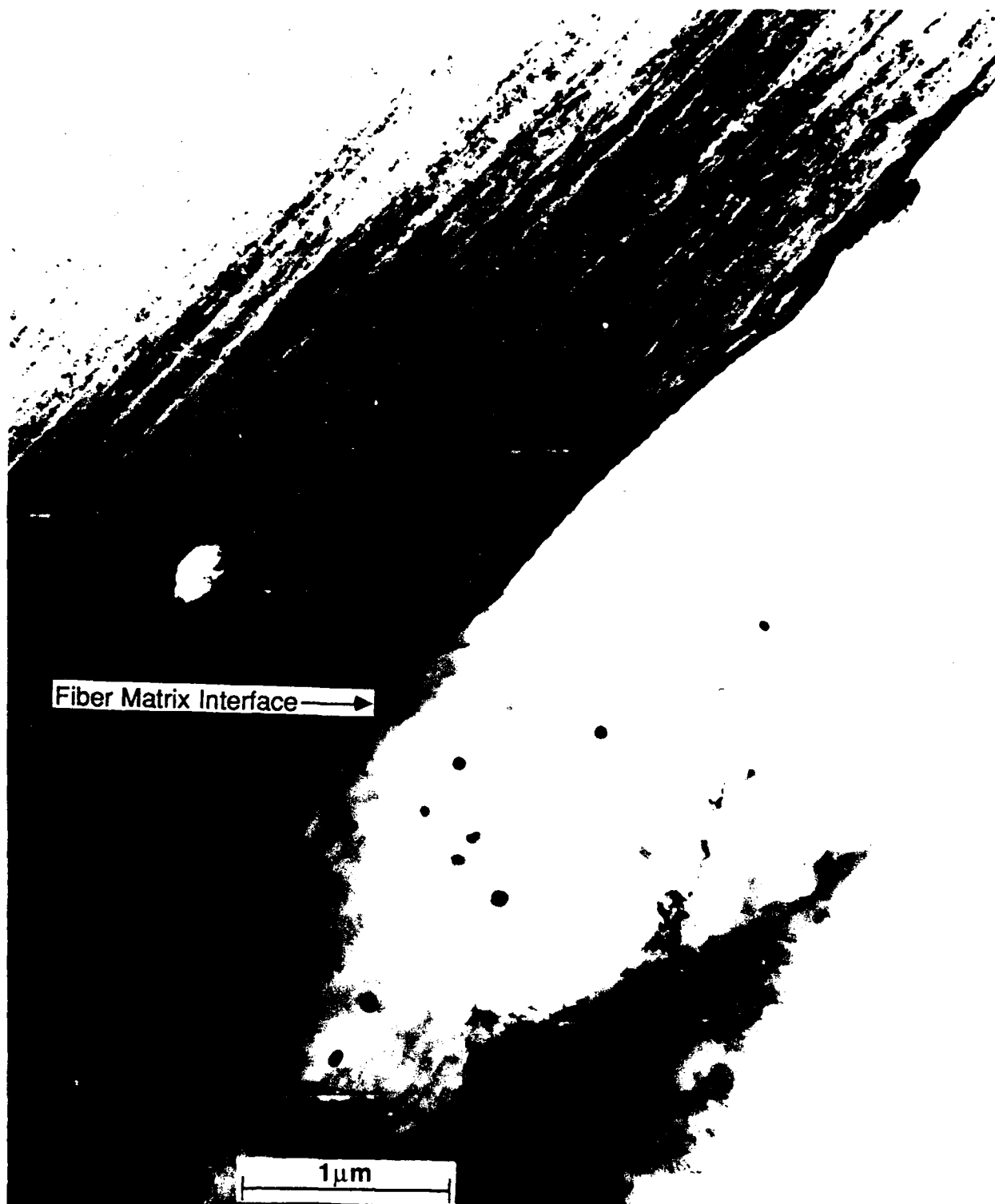
Figure 10.2.2-1 TEM Micrograph Showing a Typical Fiber-Matrix Interface in Gr/Al Composite — Note an Unusual Void-Like Defect in the Graphite Fiber

(a) Bright-Field Image
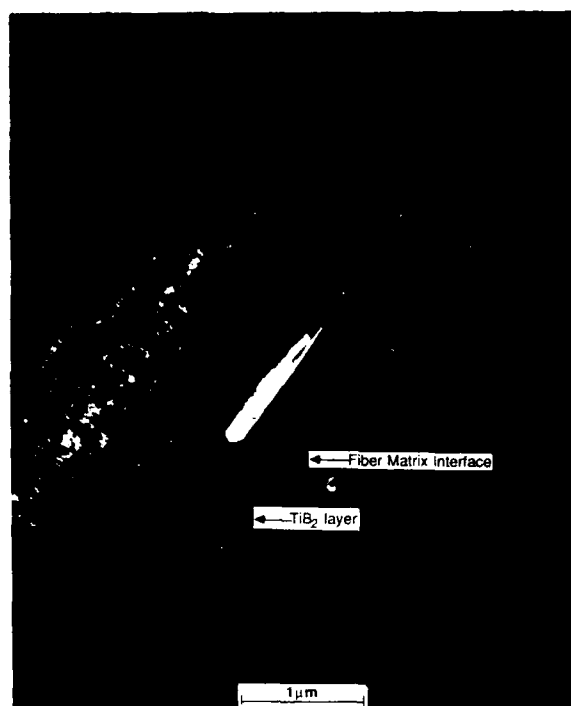
(b) Dark-Field Image

Figure 10.2.2-2 TEM Micrograph Showing a Narrow Matrix Region between the Two Graphite Fibers — Lamellar Feature at the Interface is Part of Ti-B Coating on the Graphite Fibers

Chemical analysis of microstructural areas such as the matrix, graphite fiber, and interface was performed with energy dispersive x-ray spectroscopy (EDS), by using the microscope scanning system with a 10-nm beam in point mode on the specimen. An EDS spectra obtained from a general matrix region, a CVD coating layer, and graphite fiber near the interface is shown in Figure 10.2.2-3. The matrix shows only Al and the graphite fiber shows Al, Mo, and Ar. While Al and Ar are artifacts caused by the ion-milling process, molybdenum may be an impurity in the original fiber. Here the CVD layer at the interface is primarily Ti (boron cannot be detected by the EDS detector used), with traces of several impurity elements. The strong Al peak in the spectrum results from excitation of the matrix.

One of the specimens underwent interfacial separation during ion milling as evidenced in Figure 10.2.2-4. In this case, EDS analysis of the fiber, matrix, and interface regions is identical to Figure 10.2.2-3. The nature of interfacial separation indicates that the titanium-boron layer is adherent to the aluminum matrix rather than to the graphite fiber, providing a clue to the failure mechanism or debonding in Gr/Al composites.
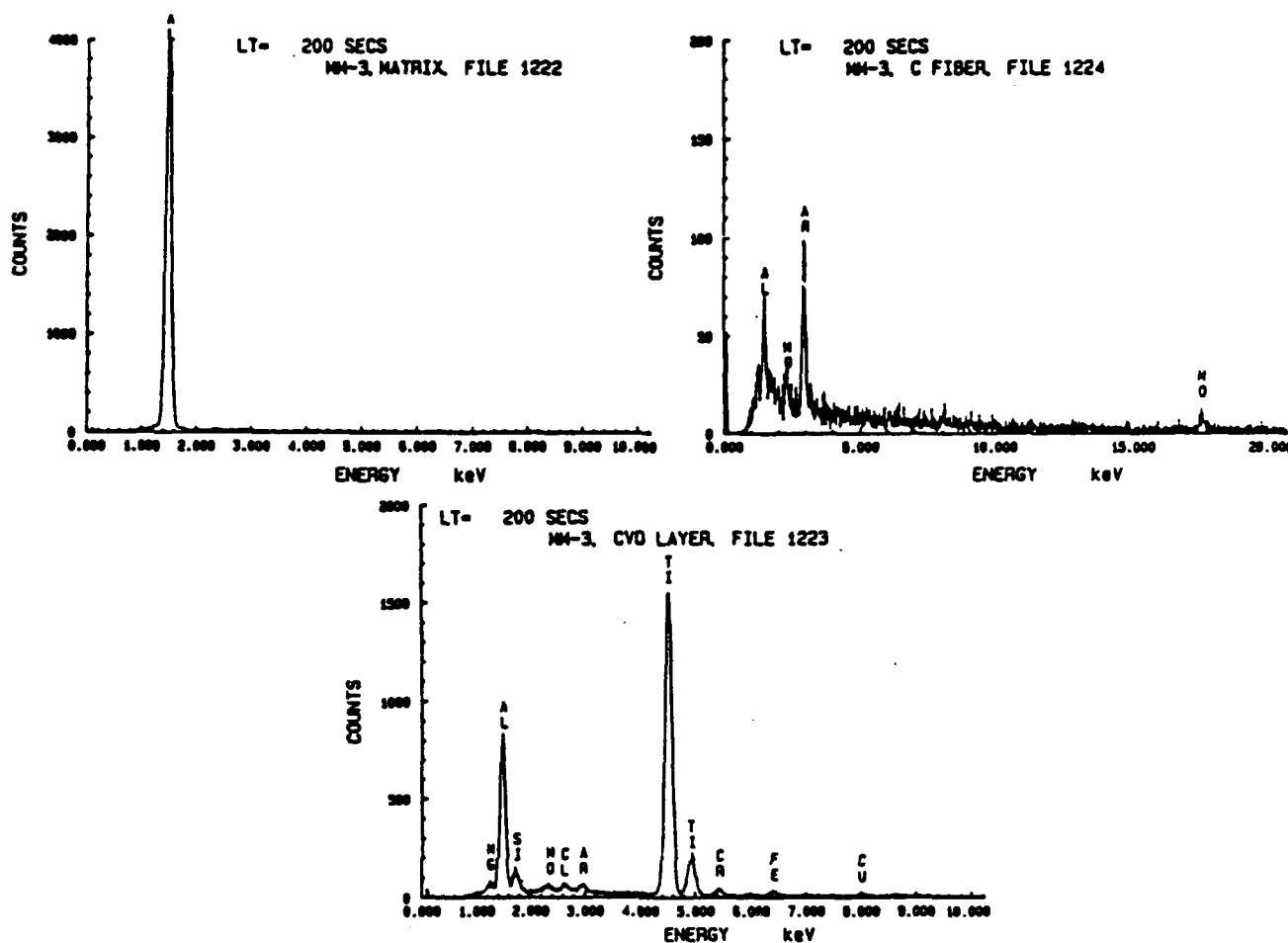
Figure 10.2.2-3 EDS Spectra from the Matrix (Top), Graphite Fiber Near the Interface (Middle), and the CVD Bonding Layer (Bottom) in Gr/Al Composite

Fiber-matrix interfaces were also examined in cast Gr/K1A and Gr/M1A composites, where an SiO_2 coating was applied on graphite fibers, as compared to Ti-B coating in diffusion bonded Gr/Al and Gr/Mg composites. During TEM investigation of both Gr/K1A and Gr/M1A, ion milled specimens were quickly brought to the microscope to study the interface structure, otherwise the Mg matrix would oxidize in air within 15 minutes, particularly along the grain boundary and near the interface. A typical micrograph (Fig. 10.2.2-5) of the interface region in Gr/Mg composite shows fine precipitates within 20Å distances from Gr fiber, and equiaxed grains in the adjacent matrix. These precipitates were identified as Mg_2Si and MgO compounds which form during a chemical reaction between the fiber coating (SiO_2) and Mg matrix [Ref 10-14]. Even after the reaction, a thin layer of SiO_2 remains adherent with the fiber [Ref 10-14]. Various micrographs of interfaces indicated good microstructural integrity of the fiber-matrix bond, though during ion-milling a Gr/Mg specimen also showed an interfacial separation (Fig. 10.2.2-6) similar to the Gr/Al specimen shown earlier. Again,

EDS analysis indicated that the coating formed a more adherent bond with the matrix than with the graphite fiber. In the matrix grain adjacent to the fiber, grain boundaries were generally perpendicular to the interface (Fig. 10.2.2-7), and in a few cases subgrains lay at random angles to the interface. Figure 10.2.2-7 also shows second phase precipitates along the grain boundary, and dislocation substructure near the interface.

Figure 10.2.2-4 TEM Micrograph Showing that Interfacial Ti-B Layer is Adherent to the Matrix (Interfacial Separation During Specimen Preparation)

10.2.3 Dislocation Substructure

In metal matrix composites, fabrication process parameters, residual stress state at the interface, and precipitate morphology do affect the associated dislocation structure significantly. Also, for TEM imaging of the microstructural features, specimen orientation with respect to the electron beam is very important, particularly to reveal dislocations.
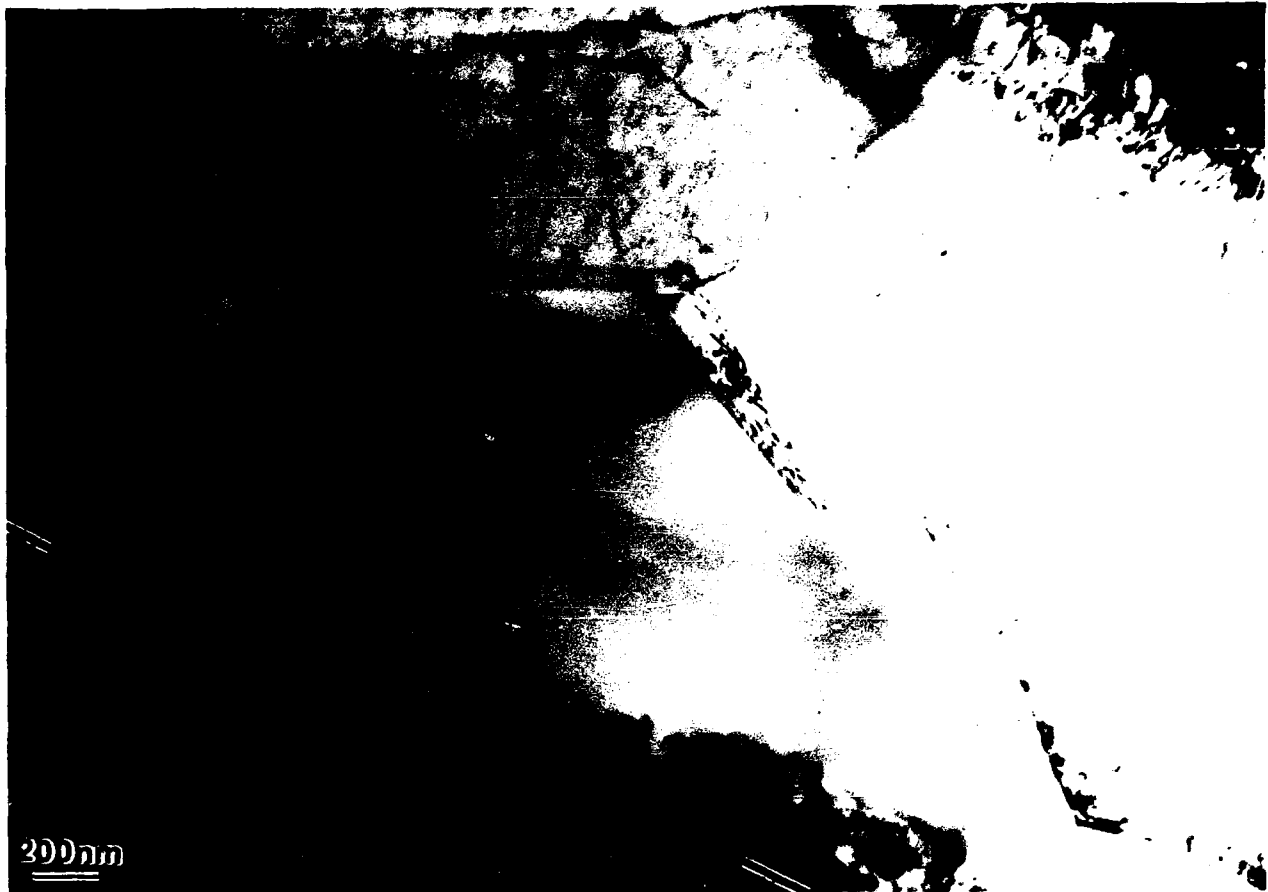
*Figure 10.2.2-5 TEM Micrograph Showing Fine Precipates and Equiaxed Grains Near the
Interface in Cast Gr/Mg Composite*

In Figure 10.2.3-1a, a diffusion-bonded Gr/Al specimen is tilted so the dense dislocation tangles adjacent to the interface are in dark contrast, while a slightly different tilt shown in Figure 10.2.3-1b is sufficient to take the dislocations out of contrast and reveal fine precipitates in the matrix. Another pair of TEM images of a narrow interfiber region of matrix also shows dense tangled dislocation substructure in dark contrast (Figs. 10.2.3-2a and 10.2.3-2b). This dense dislocation network at the fiber-matrix interface is primarily caused by the residual stress state generated from differences in thermal expansion between graphite fiber and aluminum matrix [Refs 10-3, 10-4, and 10-14]. Dislocations in Gr/Al correspond to the Burgers Vector a/2 [110], and the networks are made of the different variants.
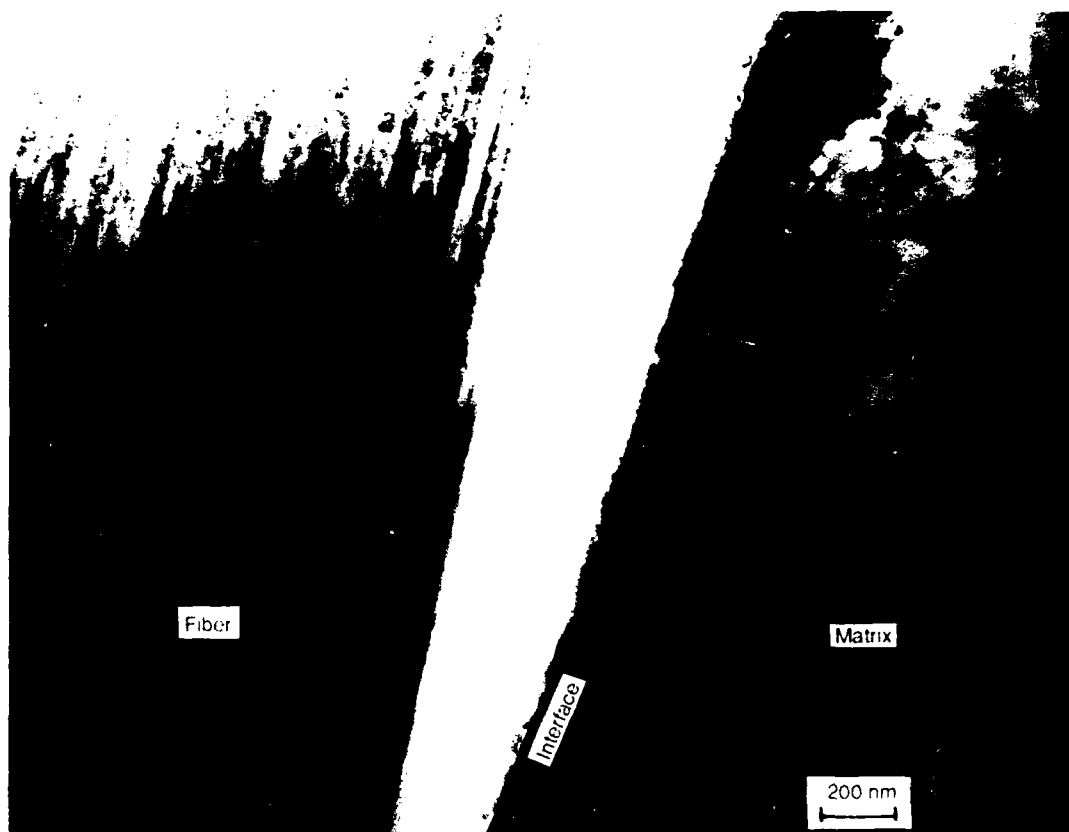
Figure 10.2.2-6 TEM Micrograph Showing Interfacial Separation in Cast Gr/Mg Composite

TEM examination of cast Gr/Mg composites reveals a generally linear dislocation substructure near the fiber-matrix interface as evidenced in Figure 10.2.3-3a and 10.2.3-3b. These characteristic dislocation configurations, such as linear in Gr/Mg and tangled network in Gr/Al composites are a result of differences in available slip systems in hcp Mg and fcc Al matrix, respectively. Linear dislocations in Figure 10.2.3-3 do bear a crystallographic orientation in the matrix region, indicating that active slip systems in hcp Mg matrix are primarily along basal planes. Figure 10.2.3-3b, also shows that the presence of a fine second-phase precipitate perturbs the attendant dislocation structure, as it acts as a potential barrier or source of dislocations.

10-11

Figure 10.2.2-7 TEM Micrograph Showing Grain Boundary (gb) Nearly Perpendicualr to the Interface, and Associated Dislocation Substructure in Gr/Mg Composites

Because dislocations play a key role in the damping mechanism in metals, it is believed that such differences in dislocation substructure may suggest the differences in the damping behavior of composites. For example, under cyclic stress the linear dislocation substructure resulting from active basal glide systems in an Mg alloy matrix may less likely undergo intersections as compared to dislocations in an Al alloy matrix which are predominantly tangles near the interface. Furthermore, in the presence of cyclic stress amplitude different density of dislocations may be mobile to contribute to damping mechanism in each MMC.
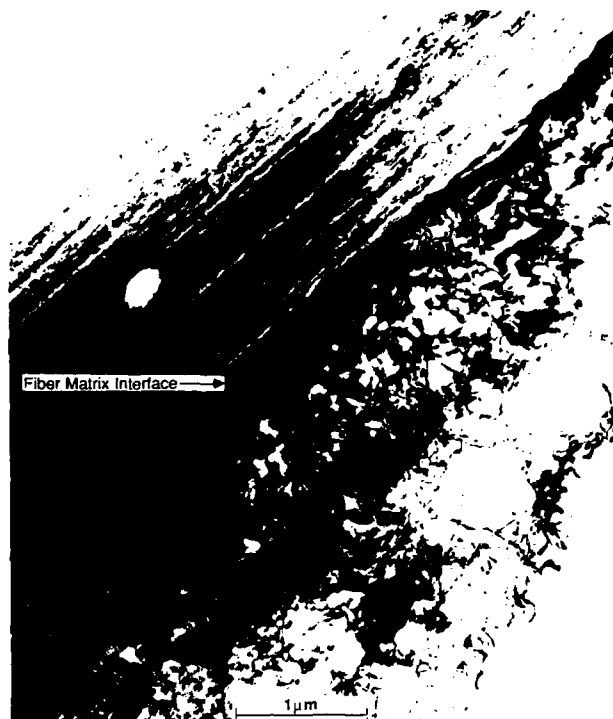
(a) Oriented to Reveal the Dislocation Structure
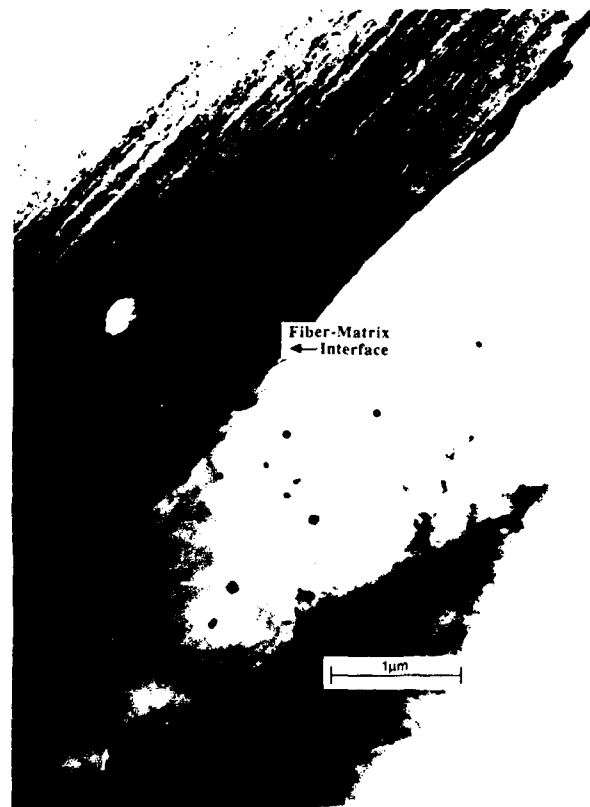
(b) Tilted Slightly to Take the Dislocations Out of Contrast

Figure 10.2.3-1 Matrix Region Adjacent to the Fiber-Matrix Interface in Gr/Al Composites

(a)
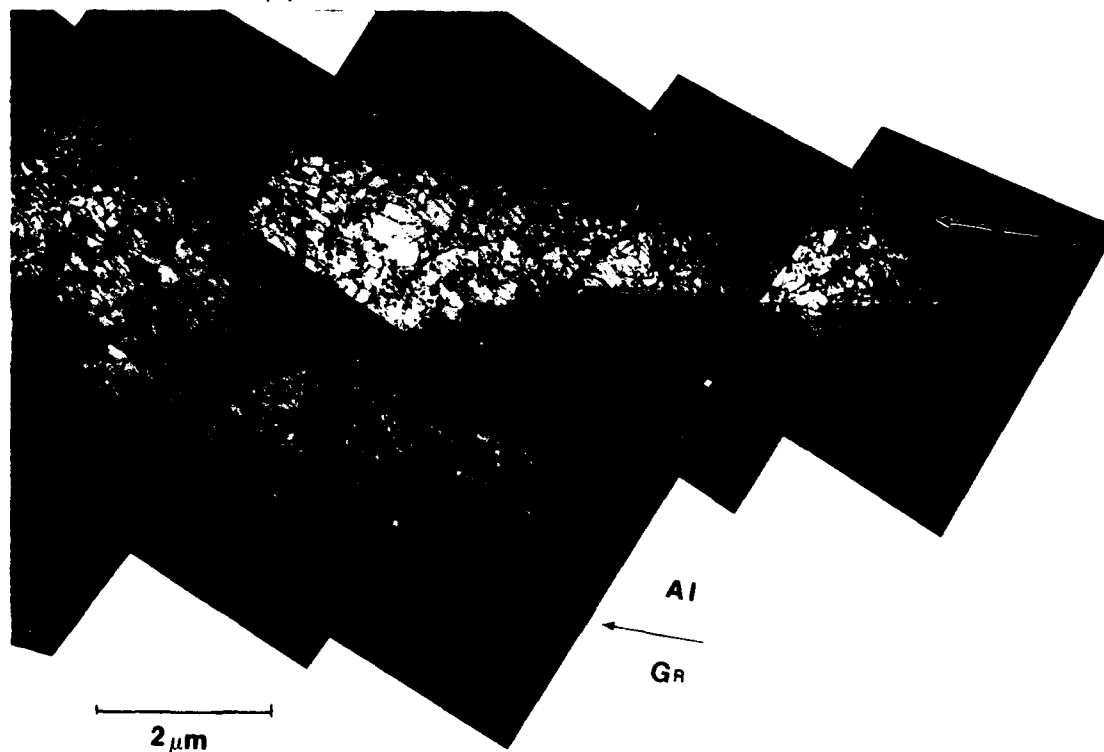
(b)

Figure 10.2.3-2 Dislocation Substructure in the Narrow Interfiber Matrix Region in Gr/Al Composites
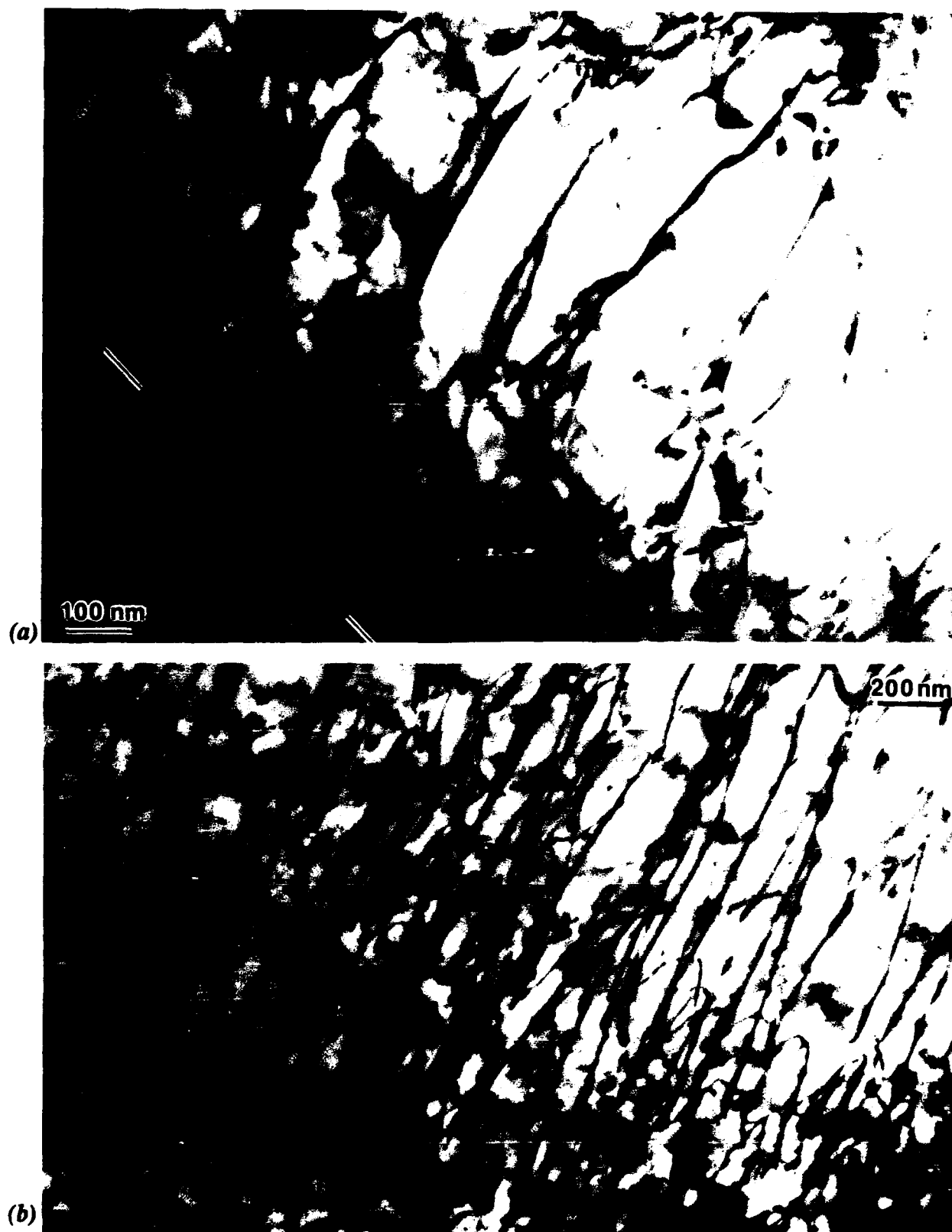
Figure 10.2.3-3 Nearly Linear Dislocation Substructure Near the Interface in Cast Gr/Mg Composites

10.2.4 Dislocation Density Measurements

Dislocation networks and tangles near the interfaces can be characterized by using the weak-beam imaging technique. From the various TEM images, few photomicrographs were suitable for quantitative image analysis and for dislocation density determination in Gr/Al and Gr/Mg composites.

Figure 10.2.4-1 shows tangled dislocations in a narrow matrix region between two adjacent fibers. Here the specimen is oriented in a two-beam condition with the [200] (+g) reflection, highly excited in an [h00] systematics orientation as shown by the inset diffraction pattern. In this pattern, the direct beam [000] is on the electron optical axis. Although dislocation tangles in this region are not as dense as those seen in previously Figure 10.2.3-1a, individual dislocations are still difficult to identify unambiguously. Such an image is not suitable for quantitative image analysis.

Figure 10.2.4-1b is a dark-field image taken after tilting the illumination to bring the [200] (+g) reflection onto the optical axis. In this orientation, the [600] (+3g) reflection becomes strongly excited, and the [200] (+g) reflection is weakened. This is the so-called "g(3g)" condition for weak-beam imaging of dislocations [Ref 10-16], and the dark-field image clearly shows the dislocations imaged as individual bright lines that are suitable for image analysis. Another dark field image of dislocation network in the narrow interfiber-matrix region is shown in Figure 10.2.4-2. To obtain quantitative information on dislocation densities in such specimens so that the role of dislocation structures in material damping can be appropriately analyzed, it is necessary to examine a significant number of different specimen matrix regions, each oriented to an identical g(3g) imaging condition. In this way, the effects of sample orientation on the dislocation contrast are minimized, and reliable dislocation density estimates are obtained.

These dislocation density measurements have special significance, particularly in reference to damping mechanisms related to movement of dislocations. An energy-dissipating mechanism involving breakaway of dislocations from its minor pinning points as envisioned in Granato-Lucke model [Refs 10-9, 10-10] describes the stress amplitude damping behavior of Gr/Al and Gr/Mg composites. Quantitative analysis of transmission electron micrographs indicate a dislocation density ~ $4\times10^{14}/m^2$ in Gr/Al and 6×10^{13} - $1.6\times10^{14}/m^2$ in cast Gr/Mg composites. These average dislocation density values in composites are significantly higher than the dislocation density in corresponding metallic matrix.

(a) Bright-Field, Two-Beam Image
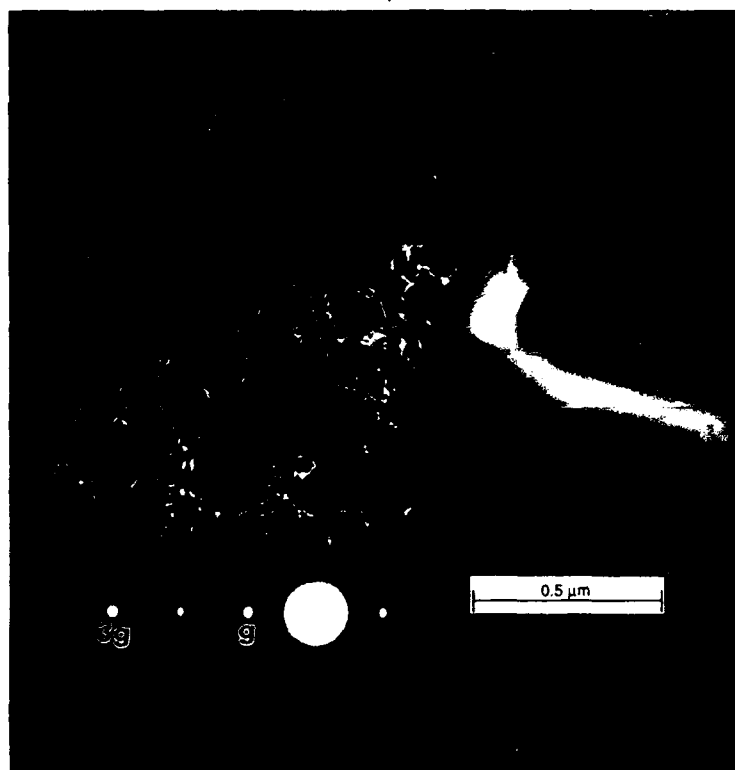
(b) Dark-Field, Weak Beam "g (3g)" Image

Figure 10.2.4-1 Dislocation Tangles Near the Fiber-Matrix Interface
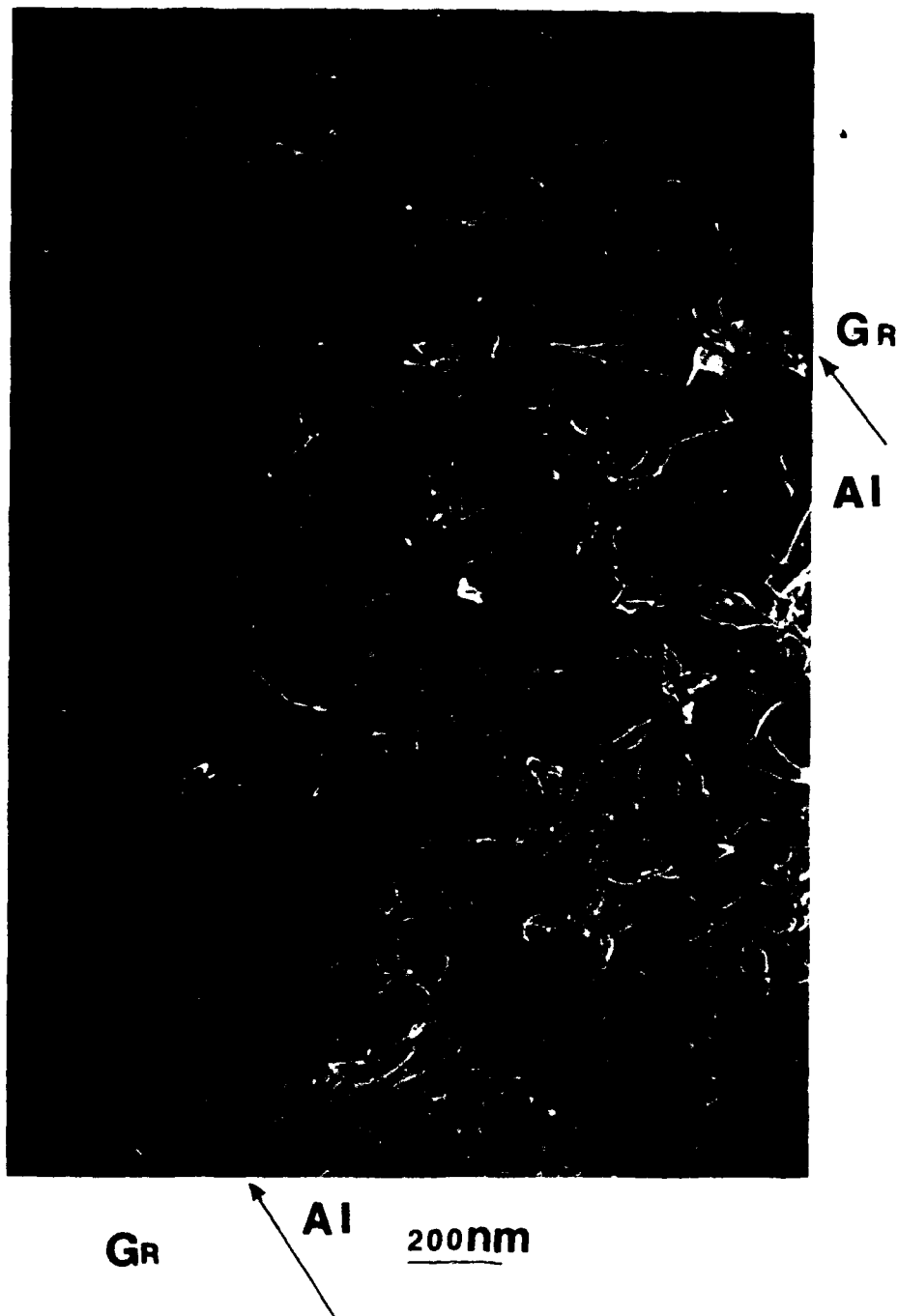
Figure 10.2.4-2 *Dark-Field Image of Dislocation Tangles in the Narrow Interfiber Matrix Region*

10.3 CONCLUSIONS

Fiber-matrix interfaces in metal matrix composite include voids, impurities, second phase precipi-
tates and dense dislocation substructure. These interfacial features could also provide various
sources of vibrational energy dissipation during cyclic loading.

Interfacial regions in diffusion bonded Gr/Al and cast Gr/Mg composites were successfully exam-
ined by transmission electron microscopy. Various TEM images revealed the nature of interfacial
bond, where the fiber coating was far more adherent to the matrix as compared to the fiber, during
interfacial separation or debonding. Interface region in both composites also revealed dislocation
substructure which are associated with residual stresses generated due to differences in thermal
expansion between fiber and matrix during composite processing conditions. In Gr/Al composite,
these dislocations have the characteristic Burger's Vector a/2 [110] for the face centered cubic Al
system, and the dense tangled networks are made of the different variants. Near the interface in
Gr/Mg composite, dislocations are generally linear and correspond to available basal slip systems in
hcp Mg matrix. Dislocation density measurements were made using the weak beam imaging tech-
nique, and an average dislocation density in Gr/Al was 4×10^{14} $1/m^2$ and Gr/Mg composites between
1.6×10^{13} and 1.6×10^{14} $1/m^2$. These measurements of dislocation density indicate that enough
mobile dislocations are present to contribute to the damping mechanisms (Granato-Lucke model) in
each composite.

10.4 REFERENCES

10-1   Arthur G/ Metcalfe: "Physical Chemical Aspects of the Interface", Interfaces in Metal
       Matrix Composites, Academic Press, pp 65-123, 1974.

10-2   J. Lo, D. Finello, M. Schmerding, and H.L. Marcus: "Interface Structure of Heat-Treated
       Aluminum-Graphite Fiber Composites", Mechanical Behavior of Composites, eds. J.E. Hack
       and M.F. Amateau, pp 77-81, 1983.

10-3   G.L. Steckel, R.M. Flowers, and M.F. Amateau: Transverse Strength Properties of Graphite-
       Aluminum Composites, Final Report for 1 Oct 1977 - 30 Sept 1978, Naval Surface Weapons
       Center, TOR-0078 (3726-03)-4, Sept 30, 1978.

10-4   H.L. Marcus: Interface Character of Aluminum-Graphite Metal Matrix Composites, Final
       Technical Report UTMSE-83-1, ONR Contract N00014-78-C-0094, Jan 1983.

10-5   S.R. Nutt and R.W. Carpenter: Precipitate Phases in Al-SiC Composites", Proceedings of the 42nd Annual Meeting of the Electron Microscopy of America, ed. G.W. Bailey San Francisco Press, San Francisco, CA, pp 490-491, 1984.

10-6   M. Vogelsang, R.J. Arsenault, and R.M. Ficher: "An In-Situ HVEM Study of Dislocation Generation at Al/SiC Interfaces in Metal Matrix Composites", Metallurgical Transactions A, 17A, pp 379-389, 1986.

10-7   R.J. Arsenault and N. Shi: "Dislocation Generation Due to Differences Between the Coefficients of Thermal Expansion", Materials Science and Engineering, 81, pp 175-187, 1986.

10-8   S.P. Rawal, L.F. Allard, and M.S. Misra, "Microstructural Characterization of Interfaces in Diffusion-Bonded and Cast Gr/Mg Composites", presented at 115th TMS Annual Meeting, New Orleans, Louisiana, in press 6 March 1986.

10-9   A.V. Granato and K. Lucke, "Application of Dislocation Theory to Internal Friction Phenomena at High Frequencies", Journal of Applied Physics, 27(7), pp 789-805, 1956.

10-10   A.V. Granato and K. Lucke: "Theory of Mechanical Damping Due to Dislocations", Journal of Applied Physics, 27(6), pp 583-593, 1956.

10-11   A.V. Granato and K. Lucke: "Temperature Dependence of Amplitude-Dependent Dislocation Damping", Journal of Applied Physics, 51(12), pp 7136-7142, 1981.

10-12   G. Dupouy: Proc. 3rd Int. Conf. on High-Voltage Electron Microscopy, eds. P.R. Swann, C.J. Humphreys and M.J. Gorings, Academic Press, London, p 447, 1974.

10-13   J.B. Donnet and R.C. Bansal: Carbon Fibers, New York, Marcel Dekker, Inc. Chapter 2, 1984.

10-14   S.P. Rawal and M.S. Misra, "Interfacial Bonds in Cast Gr/Mg Composites, Interfaces in Polymer, Ceramic and Metal Matrix Composites", ed. H. Ishida, pp 179-187, 1988.

10-15   K.K. Chandler and M. Metzger: J. Mater. Sci., 7, p 34, 1972.

10-16   J. B. VanderSande: Introduction to Electron Microscopy, eds J.J. Hren et. al., New York, Plenum Press, Chapter 20, 1979.

11.0 Interlaboratory Damping Tests

CHAPTER 11.0
DAMPING TEST DATA COMPARISON: INTERLABORATORY TESTING

Damping is defined as the inherent ability of a vibrating material to dissipate its vibrational energy, even when the material is isolated and energy losses to surroundings are negligible. Various experimental techniques can be used to measure material damping capacity at different frequencies and strain amplitudes, but no single method can be used over the entire frequency range ($10^{-2} - 10^{10}$ Hz) of interest to the aerospace community. The experimental procedures and their limitations are well documented in the literature [Ref 11-1 — 11-6].

Material damping is primarily a low energy loss process, therefore the major problem in measurement involves extraneous energy losses in the apparatus because of support friction, air drag, acoustic radiation, transducer mounting, and wire movement. In all the damping measurement the specimen support, the excitation device, and the vibration monitoring equipment also play an extremely important role. Therefore extraneous energy losses in any damping test technique must be minimized to obtain inherent damping values of material.

Because damping is measured in a number of ways, and the efforts made to minimize extraneous energy losses vary, it is essential that data from reference and test specimens be compared to validate particular experimental setups. To eliminate any anomalies in damping data for specimens tested in different vibratory modes, tests must be conducted at sufficiently low strain amplitudes to ensure that measured damping is nearly constant.

11.1 LABORATORIES AND TESTING PARAMETERS

To compare the damping capacity values, test specimens of Gr/Al and Gr/Mg were sent to different laboratories that are involved in the damping measurements of advanced composites. These laboratories and their principal investigators are:

1)   Texas A&M University, College Station Texas; Prof. V.K. Kinra
2)   University of Idaho, Moscow, Idaho; Prof. R. Gibson]
3)   NASA Lewis Research Center; Dr. J. DiCarlo
4)   Aerospace Corporation; Dr. G. Steckel

Damping test method and parameters for each laboratory are listed in Table 11.1-1. In each case, the specimens sent to each laboratory were cut from the same panels. X-radiography of each panel confirmed the consistency of each specimen sent to the external laboratories for investigation. Each test was conducted at sufficiently-low strain amplitudes to ensure completely strain amplitude independent damping response. Data for Gr/Al and Gr/Mg specimens are given in Tables 11.1-2 and 11.1-3 respectively. Test results from each laboratory show that at low strain amplitude ($< 10^{-5}$), the damping capacity of Gr/Al [0], varies between 0.5 - 1%ψ. Similarly, measured damping of Gr/Mg at these strain levels varies between 1.14 - 2.45 over a wide frequency range.

Table 11.1-1 Institutions Involved in Interlaboratory Testing and Experimental Parameters

Location	Material	Flexural		Extensional	
		ε	f (Hz)	ε	f (Hz)
Martin Marietta	Gr/Mg, Gr/Al	10^{-4}	10 — 120	—	—
Texas A&M University	Gr/Mg, Gr/Al	10^{-6}	10 — 120	—	—
University of Idaho	Gr/Mg, Gr/Al	10^{-5}	60 — 80	10^{-6}	2,000
NASA Lewis	Gr/Mg	$10^{-7} — 10^{-6}$	2,000	—	—
Aerospace Corp.	Gr/Mg	10^{-6}	56	—	—

Table 11.1-2 Damping Results for Gr/Al Composites

P55Gr/Al (Flexure)

Laboratory	Strain Amplitude (x 10^{6})	Frequency (Hz)	Loss Factor η (x 10^{3})	Specific Damping Capacity ψ (%)
University of Idaho	7	77.3	0.759	0.477
	7	497.5	2.158	1.356
Texas A&M	5	20	1.030	0.647
	34	20	1.663	1.045
Martin Marietta	43.46	63.97	0.880	0.553
	138.1	63.97	3.371	2.118
	297.8	63.97	4.471	2.809
	587.5	63.97	4.690	2.947

Table 11.1-3 Damping Results for Gr/Mg Composites

P55Gr/Mg

Laboratory (Test Method)	Strain Amplitude (x 10^6)	Frequency (Hz)	Loss Factor η (x 10^3)	Specific Damping Capacity ψ (%)
University of Idaho (extensional)	<1	60.358 82.996 118.927	3.649 2.363 3.580	2.293 1.485 2.249
Aerospace Corporation* (clamped-free flexure)	4.8	55	2.392 ± 0.057	1.503 ± 0.036
NASA (clamped-free flexure)	≤1	2350 2446	1.81 2.05	1.14 1.29
Texas A&M (clamped-free flexure)	10.34 24.51 10.49 25.27	16 16 31 31	1.942 2.885 2.572 3.341	1.220 1.813 1.616 2.099
Martin Marietta (clamped-free flexure)	13.5 202.0	128 128	3.963 6.589	2.49 4.14

*Data Averaged over Five (5) Tests

At low strain amplitudes, damping is typically a function of temperature and frequency. However, measured damping from the different test equipment within the frequency range (16 < f < 2500 Hz) and strain amplitude range less than 10^{-5} are quite comparable. At higher strain amplitudes, both Gr/Al and Gr/Mg composite exhibit strain increase in damping with increasing strain amplitude.

11.2 SUMMARY

Damping capacity of MMC at low strain amplitudes is quite small. Therefore, extraneous losses during the damping measurement must be minimized to obtain reliable data. Damping measurements of test specimens from the same Gr/Al and Gr/Mg panes were performed at five different laboratories that are involved in determining the dynamic response of metal matrix composites. These measurements were performed within the frequency range (16 < f < 2500 Hz) and strain amplitude range (1 x 10^{-6} — 200 x 10^{-6}). At low strain levels when damping is a function of temperature and frequency only, measured values from all of these test sites were in excellent agreement.

11.3   REFERENCES

11-1   R.F. Gibson and R. Plunkett: The Shock and Vibration Digest, Vol 9, No. 2, pp 9-17 (1977).

11-2   S.A. Suarez, R.F. Gibson, and L.R. Deobald: Experimental Techniques, Vol 8, No. 5, pp 19-24 (1984).

11-3   B.J. Lazan: Damping of Materials and Members in Structural Mechanics, Pergamon Press, Ltd., Oxford (1968).

11-4   A.K. Ray, V.K. Kinra, S.P. Rawal, and M.S. Misra: "Measurement of Damping in Continuous Fiber Metal Matrix Composites," Role of Interfaces in Material Damping, eds. B.B. RAth and M.S. Misra, ASM, Metal Park, OH, pp 995-102, 1986.

11-5   A.S. Nowick and B.S. Berry: Anelastic Relaxation in Crystalline Solids, Academic Press, New York (1972).

11-6   I. G. Ritchie and H.L. Rosinger: Dynamic Elastic Properties of Materials, Materials Research in AECL, AECL-4842, Summer 1974.

12.0 Centrifugal Casting of Gr/Mg Composite Tubes

CHAPTER 12.0
DEVELOPMENT OF CENTRIFUGAL CASTING TECHNIQUES TO FABRICATE Gr/Mg TUBES

Graphite (Gr) fiber reinforced magnesium (Mg) matrix composites offer low mass, high stiffness, and near zero coefficient of thermal expansion (CTE), which makes them ideal candidates for large precision reflectors, antenna towers, and support truss structures. While Gr/Mg exhibits attractive material properties, dimensional stability and potential for high damping capacity, a major concern is the fabrication of large tubes needed as basic structural elements for boom-type structures. In the current fabrication processes such as diffusion bonding, pultrusion and filament winding-vacuum casting (FWVC), 1-2 in. dia, 50-in. long Gr/Mg tubes have been produced, but scale-up to produce larger tubes greater than 3-in. dia and 5-ft long would be difficult and extremely expensive. For example, large vacuum chambers will be required for diffusion bonding and large expensive casting molds will be needed in the FWVC process. The pultrusion process is still in the development stages, and it is limited to the production of unidirectional and low angle ply laminate tubes. Therefore, a fabrication process needs to be developed that could be easily scaled-up to produce large Gr/Mg tubes.

Conventional filament winding (FW) offers flexibility in designing a composite with the desired fiber lay-up, and centrifugal casting (CC) is used commercially to produce large metallic tubes. Both filament winding and centrifugal casting processes can be easily sized to produce tubular components with desired dimensions and fiber layup. Therefore, this task was directed to develop a fabrication process combining filament winding and centrifugal casting (FWCC) techniques to produce Gr/Mg tubes. Various experiments in the development of FWCC process were performed in this joint project with Mr. A.P. Divecha and Ms. S. Karmakar of Naval Surface Warfare Center (NSWC), Silver Spring, MD. Figure 12.0-1 shows the flowchart of the filament winding centrifugal casting process. Three major technologies involved in the FWCC process are:
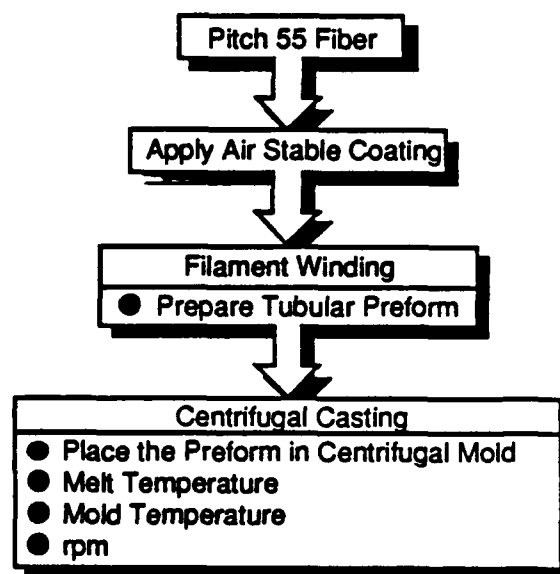

Figure 12.0-1 FWCC Task Flowchart

1)   Application of Air Stable Coating

2)   Filament Winding, and

3)   Centrifugal Casting

High modulus pitch graphite fibers are coated with an air stable silicon dioxide (SiO_2) coating to facilitate wetting with molten magnesium [Refs 12-1, 12-2, and 12-3]. Subsequently, the coated fibers are filament wound to produce tubular preforms and prepared for centrifugal casting. The technical details of air stable coating and conventional filament winding are well established [Ref 12-4], therefore, the theoretical and experimental aspects of centrifugal casting of Gr/Mg tubes were examined as described below.

12.1   CENTRIFUGAL CASTING

The centrifugally casting is a dynamic process where the process parameters such as mold rotational speed, melt temperature, mold temperature, etc., influence casting quality. Centrifugal force provides an efficient way to distribute liquid metal over the surface of the mold, to form a tube, and centrifugal pressure arising from the rotation, in conjunction with directional solidification assist feeding, and accelerates separation of nonmetallic inclusions and gases. These centrifugal casting principles for metallic tubes could be applied to produce Gr/Mg tubes, where both the centrifugal and infiltration processes occur simultaneously (Fig. 12.1-1). Initially, the basic processing conditions and parameters were identified and subsequently 2-in. dia 6-in. long tubular components were cast; thus demonstrating the feasibility of producing Gr/Mg tubes by the FWCC process.

Therefore in preliminary theoretical analysis, the centrifugal casting conditions were identified to obtain the operational pressure required to infiltrate molten Mg into the network of Gr fiber preform.

12.2   THEORETICAL ASPECTS

The centrifugal force (F_c) acting on the metal inside a rotating mold is the product of the mass (m), the radius (R), and the square of the angular velocity (ω):
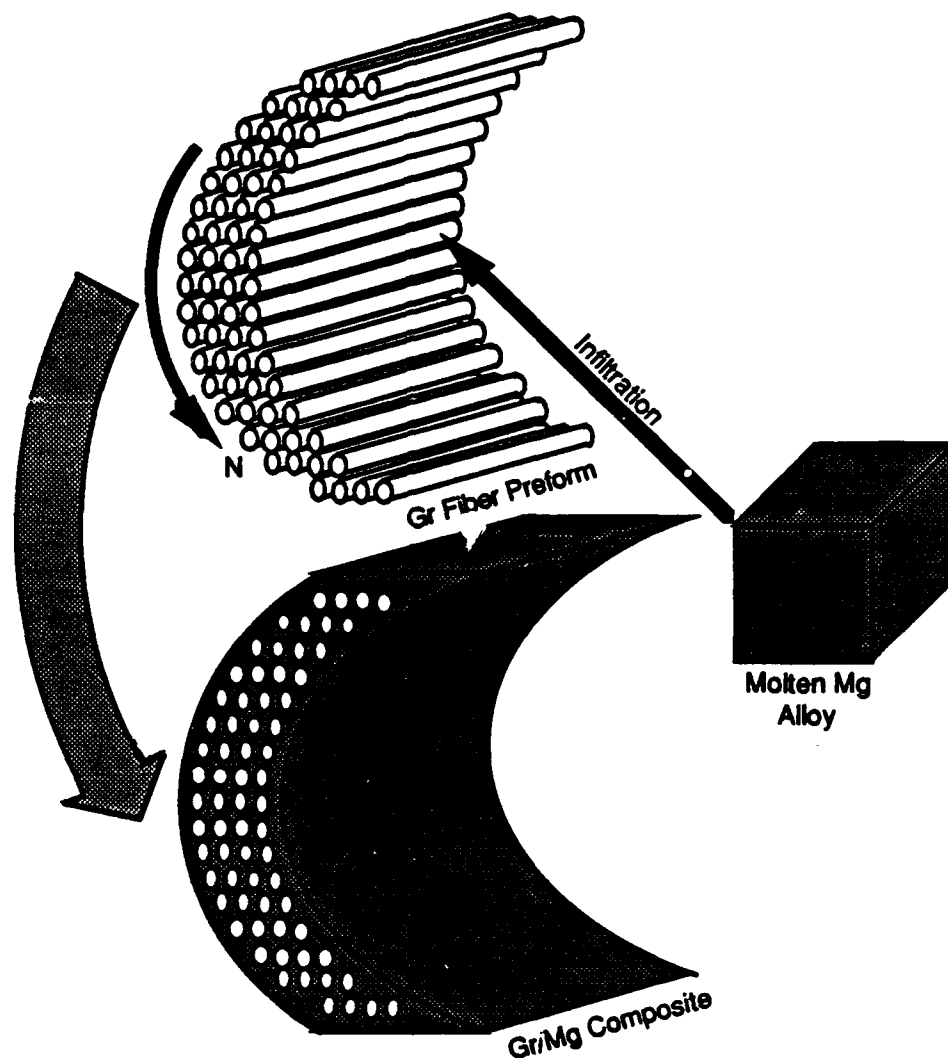
$$F_c = mR\omega^2 \tag{12-1}$$

*Figure 12.1-1 Schematic Illustration of a Centrifugally Cast Gr/Mg
Tubular Section. Molten Mg Alloy Infiltrates into a Graphite Fiber
Preform Rotating at N Revolutions per Second*

the gravitational force (F_g) on the same mass would be given by:

$$F_g = m \cdot g \tag{12-2}$$

where g = acceleration due to gravity. Generally, the centrifugal force on the metal is expressed in terms of a G factor, which is the ratio of centrifugal force to gravitational force:

$$G = \frac{F_c}{F_g} = \frac{R\omega^2}{g} \tag{12-3}$$

12-3

Expressed in more convenient speed units of revolution per minute N ($\omega = 2\pi N/60$), Equation 12-3 becomes:

$$G = \frac{R}{g} \cdot \left(\frac{\pi}{30}\right)^2 \cdot N^2 = \frac{0.011RN^2}{g} \qquad (12-4).$$

Expressing 12-4 in terms of N, one obtains

$$N = 42.3 \left(\frac{G}{D_m}\right)^{1/2} \text{ where D = rotational diameter (meters)} \qquad (12-5)$$

or

$$N = 265 \left(\frac{G}{D_{in.}}\right)^{1/2} \text{ where D = rotational diameter (inches)} \qquad (12-6).$$

These relationships between rotational speed, diameter, and centrifugal force in terms of the G factor are illustrated in a monograph (Fig. 12.2-1) that is normally used to select the speed in accordance with the magnitude of centrifugal force required. Thus a rotational speed of about 1500 rpm should be sufficient to develop about 100 G feeding force for a 4-in. dia (ID) casting, providing an even distribution of metal over the inside surface of the mold.

There is no standard criterion for selection of the required force. In true, or open bore casting, centrifugal motion is imparted from mold to metal by frictional forces at the mold surface and within the liquid. In horizontal axis casting, the metal entering the mold must acquire sufficient velocity rapidly to prevent instability and 'raining' as it passes over the upper half of its circular path. The dashed line in Figure 12.2-1 indicates the rotational speed necessary to present raining or fall of metal droplets from the top surface of the mold.

The centrifugal feeding pressure ($\Delta P_{feeding}$) provided by the rotation of the mold is given by:

$$\Delta P_{feeding} = \rho \omega^2 \left(R_2^2 - R_1^2\right) / 2 \qquad (12-7)$$

12-4

$$\Delta P_{feeding} = \rho \pi^2 N^2 \left(R_2^2 - R_1^2 \right) / 1800 \tag{12-8}$$

where ρ is the density, R_1 is the bore radius (i.e., cast tube ID), and R_2 is the radius of rotation at the point where the feeding pressure is to be calculated. In practice, high feeding pressures can be attained using an optimum combination of R_1, R_2, and N. High feeding pressure could assist the matrix infiltration into the graphite fiber network, while the air stable coating on Gr fiber will provide wettability with molten magnesium. With this theoretical background, centrifugal casting experiments were performed (at the laboratory scale) to infiltrate Mg matrix into Gr fiber preforms.
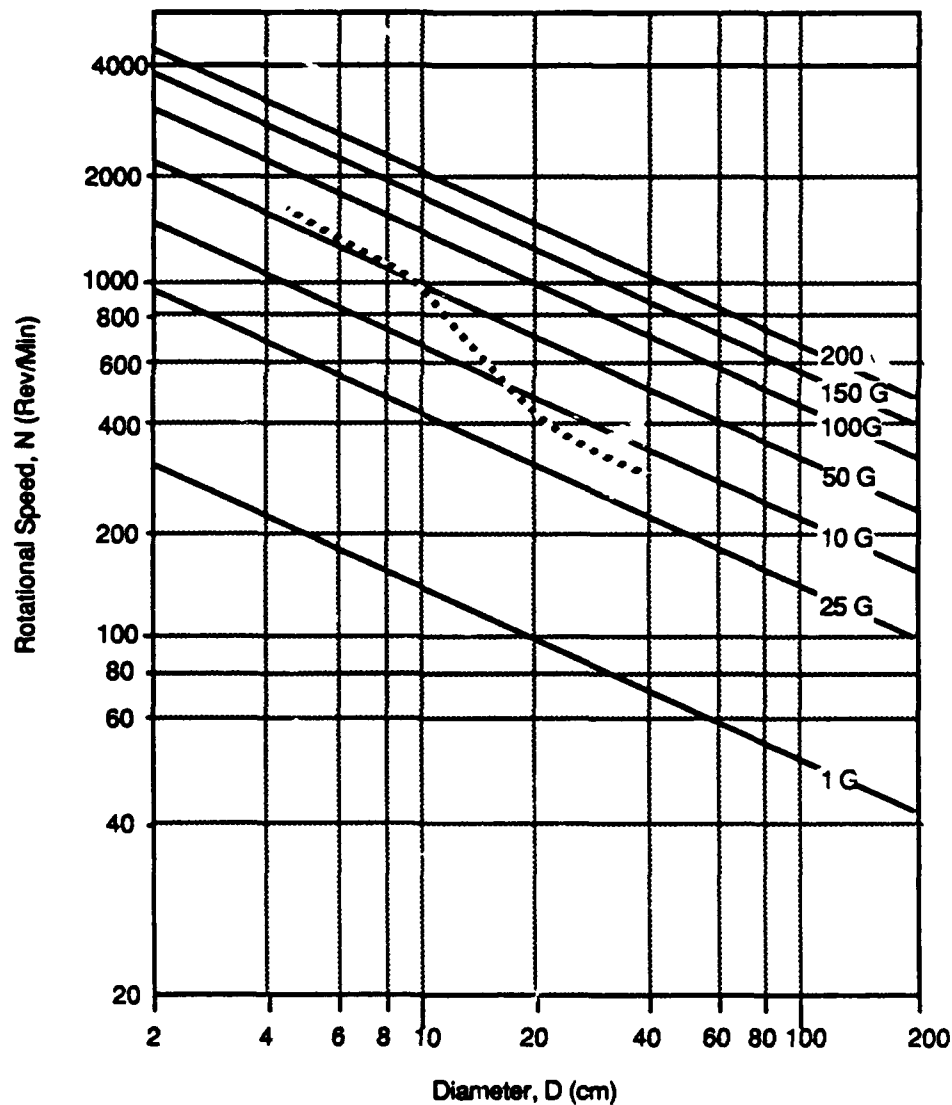

Figure 12.2-1 Relationship between Rotational Speed and Inside Diameter of a Casting for Various Amounts of Centrifugal Force (G-Force)

12.3 EXPERIMENTAL DETAILS

High modulus P55 and P100 graphite fibers were coated with silicon dioxide and filament-wound to prepare tubular preforms. For these preforms, fiber layup of $[\pm16°]_s$ was selected because it provides a zero CTE with high modulus (33 Msi) in P100/Mg tube at 37% fiber volume [Ref 12-4]. The filament winding was performed on 48-in . long, 4-in. dia. aluminum mandrels, and the fugitive binder was applied to prevent movement of fibers during preform removal oft the mandrel. Using P55 fibers, a final hoop wrap was also filament wound to constrain the radial displacement of fibers during centrifugal casting. From 48-in. long tubular preforms, 6-in. long sections were cut for centrifugal casting experiments.

12.3.1 CENTRIFUGAL CASTING TEST SETUP

Figure 12.3.1-1 shows the schematic of a centrifugal casting set up. An 8-in. long steel tube was designed as a mold and held directly on a lathe machine for mold rotation. A steel shroud was placed around the mold-tube with inlets for argon gas and a pouring spout for molten magnesium. The 4-in. dia. Gr fiber tubular preform with end sleeves (Fig. 12.3.1-2) was held against the inside diameter of the mold. The preform was anchored with half-inch wide steel rings to prevent the collapse and disintegration of the preform when the binder was removed. These end sleeves prevent collapsing and minimize fiber movement during mold rotation.
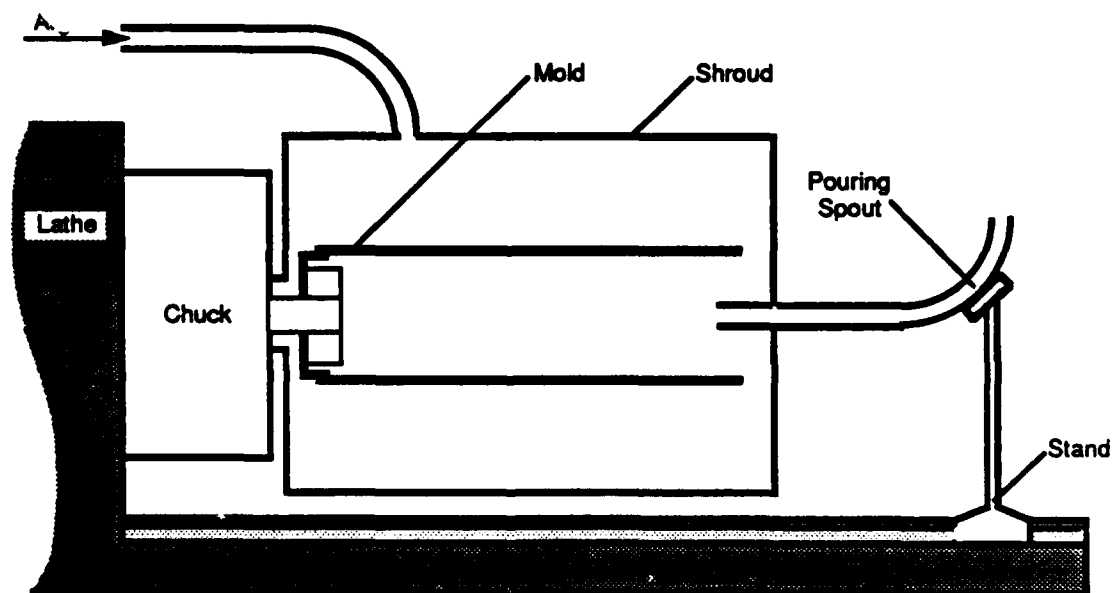

Figure 12.3.1-1 Schematic of the Laboratory Scale Centrifugal Casting Fabrication Apparatus
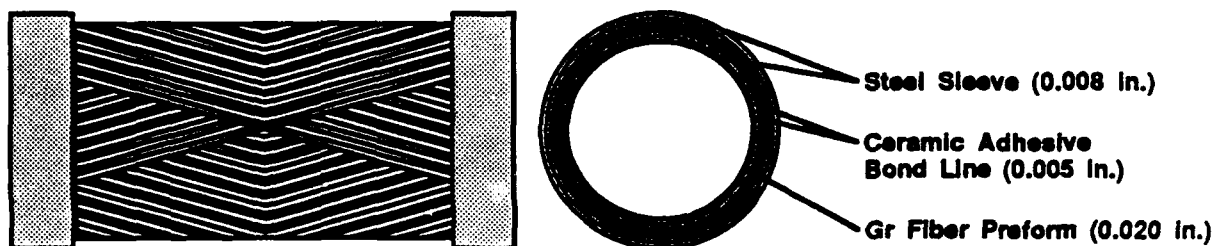
Figure 12.3.1-2 A Schematic of the 4-in. Diameter Gr fiber Tubular Preform with End Sleeves

Prior to centrifugal casting, fugitive binder was removed off the preform by heating the mold outer surface with an oxy-acetylene flame. At the same time, hot argon was introduced to minimize degradation of fiber coating. After fifteen minutes when all the fumes due to the binder had escaped, the mold was rotated at 2900 rpm, and molten magnesium at 1350°F temperature was introduced through the pouring spout into the mold. The cast tube was released from the mold and examined to determine the extent of matrix infiltration.

Visual examination revealed few cold shuts and stringers indicating that magnesium had chilled at few spots due to insufficient mold preheat or melt superheat temperature. Photomicrographs from various regions of the casting showed a few localized regions where the molten magnesium had infiltrated into the fiber network, though the fiber-matrix distribution was not uniform because of the likely fiber movement during casting (Fig. 12.3.1-3). Based on the observations of these castings, the following problems were identified:

— Mold preheat temperature dropped significantly before pouring molten Mg alloy
— Steel sleeves anchoring the preform at either end slipped due to vibration of the mold/preform/sleeve assembly
— Pouring temperature of molten AZ91C Mg alloy was not high enough
— Thermal losses in pouring spout
— Incomplete binder removal
— Likely degradation of fiber coating, and
— Presence of oxidative atmosphere that could inhibit the wetting of fibers with molten magnesium.
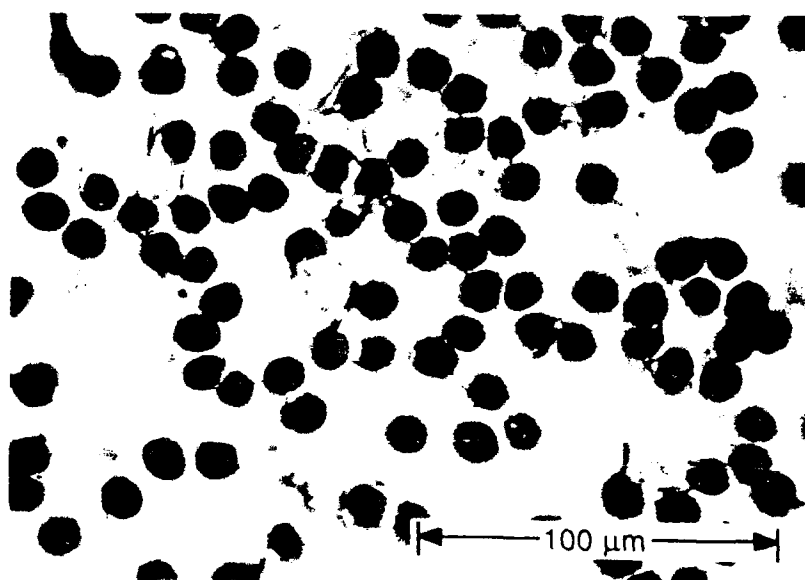
*Figure 12.3.1-3 Photomicrograph of the Centrifugally-Cast Gr/Mg Tube
Showing a Few Localized Regions where the Molten Magnesium had
Infiltrated into the Fiber Network*

In the next few attempts, the mold/preform assembly was heated from outside prior to pouring the molten magnesium, and argon gas was continuously flushed around the mold to provide the protective atmosphere.

The outer surface of the cast tube showed no evidence of chilling, suggesting that thermal conditions were adequate during solidification. Subsequent microstructural examination revealed the extent of matrix infiltration had increased slightly, while the fibers in the remaining areas were still trapped between magnesium. From these uninfiltrated regions, a few fibers were examined by scanning auger microprobe to evaluate any contamination of the coating due to incomplete binder removal. Auger elemental analysis, combined with microstructural observations, indicated that a carbonaceous residue from the binder removal remained around the fibers and inhibited wetting. These results suggested that the preform should be heated for longer duration in the presence of an inert atmosphere to ensure complete binder removal with degradation of fiber coating.

Mold/preform heating methodology was modified by replacing oxy-acetylene flame with the glow-bar heating elements. These resistive heating elements consisted of two semicircular pieces that were placed around the mold with a small gap to allow the mold rotation. The preform was held at about 500°F for 45 minutes to ensure complete binder removal. Heating elements were shutoff and molten magnesium was poured into the rotating mold. Again, visual examination revealed good magnesium surface finish, and microstructures from different areas showed various regions with good matrix infiltration and remaining tube where the fibers were trapped inside the matrix. Figure K12.3.1-4 shows that in the infiltrated regions, fiber matrix distribution was quite uniform and the casting appeared to be of good quality.
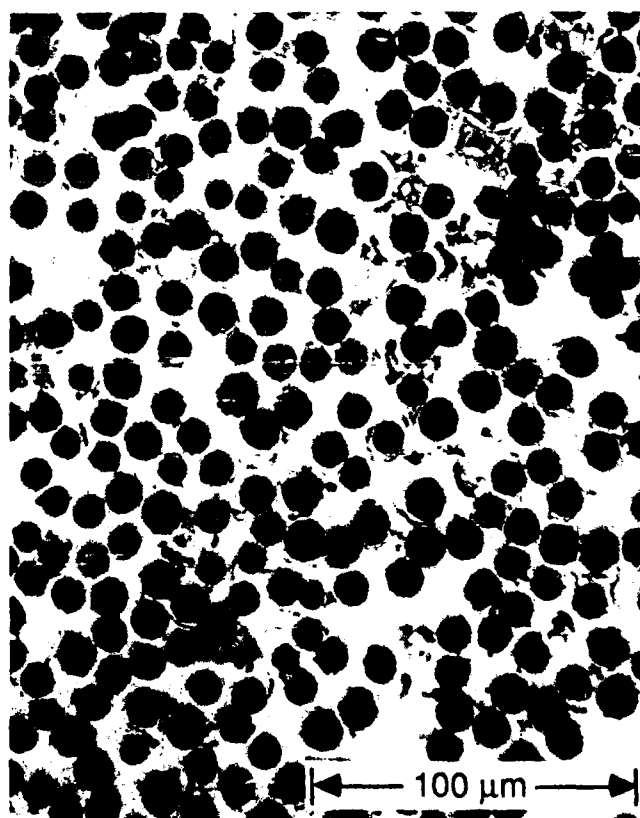

Figure 12.3.1-4 Photomicrograph of the Centrifugally-Cast Gr/Mg Tube Utilizing a Glow-Bar Approach for Preheating the Mold/Preform, Indicating Good Matrix Infiltration

12.4 CONCLUDING REMARKS

Fabrication processes such as diffusion bonding, pultrusion and filament winding-vacuum casting have been successfully used to produce 1-3 in. dia. 50-in. long tubes. But any scaleup to produce large tubes from these will be very tedious and expensive. Therefore, a fabrication process combining two well established technologies: 1) filament winding and 2) centrifugal casting was evaluated because it has potential to produce large tubes using state-of-the-art equipment.

Laboratory scale experiments were conducted to demonstrate the feasibility of fabricating tubes by filament winding-centrifugal casting (FWCC) process. Filament wound P55 fiber tubular preforms were placed inside a centrifugal mold setup that was held on a lathe machine for mold rotation. In each casting experiment, Gr/Mg tube had various regions that showed excellent matrix infiltration and in the remaining tube fibers were trapped between the molten magnesium. The visual and microstructural observations indicated that if binder was completely removed without any degradation of coating, and optimum combination of melt superheat and mold-preform temperature was maintained then the casting showed good matrix infiltration. With an improved design to preheat the preform under the protective atmosphere, good matrix infiltration could be attained in the entire tube. Therefore, the observations of well infiltrated regions in the cast tube demonstrate that filament winding centrifugal casting technique could be developed to produce large Gr/Mg tubes.

12.5 REFERENCES

12-1   H.A. Katzman, "Carbon-Reinforced Metal-Matrix Composites," U.S. Patent 4,376,803 (1983).

12-2   H.A. Katzman, "Fiber Coatings for the Fabrication of Fiber-Reinforced Magnesium Composites," Journal of Material Science, Vol. 22, pp 144-148, February 1987.

12-3   D.M. Goddard, Metal Progress, Vol. 498, pp. 125, 1984.

12-4   S.P. Rawal, M.S. Misra, D. Goddard, and J. Jackson, "Novel Processing Techniques to Fabricate Gr/Mg Composites for Space Applications," Martin Marietta Denver Aerospace Report #MCR-88-635, October, 1988.